Parreira, Pedro Miguel Raimundo (2015) Nanocharacterisation of zirconia based RRAM devices deposited via PLD. PhD thesis.

http://theses.gla.ac.uk/6877/

Nanocharacterisation of zirconia based RRAM devices deposited via PLD

Pedro Miguel Raimundo Parreira

Presented as a thesis for the degree of Ph.D. at the

School of Physics and Astronomy, University of Glasgow, June 2015 *para a avó Graça e para o avô Nano,*

esta tese é para vocês

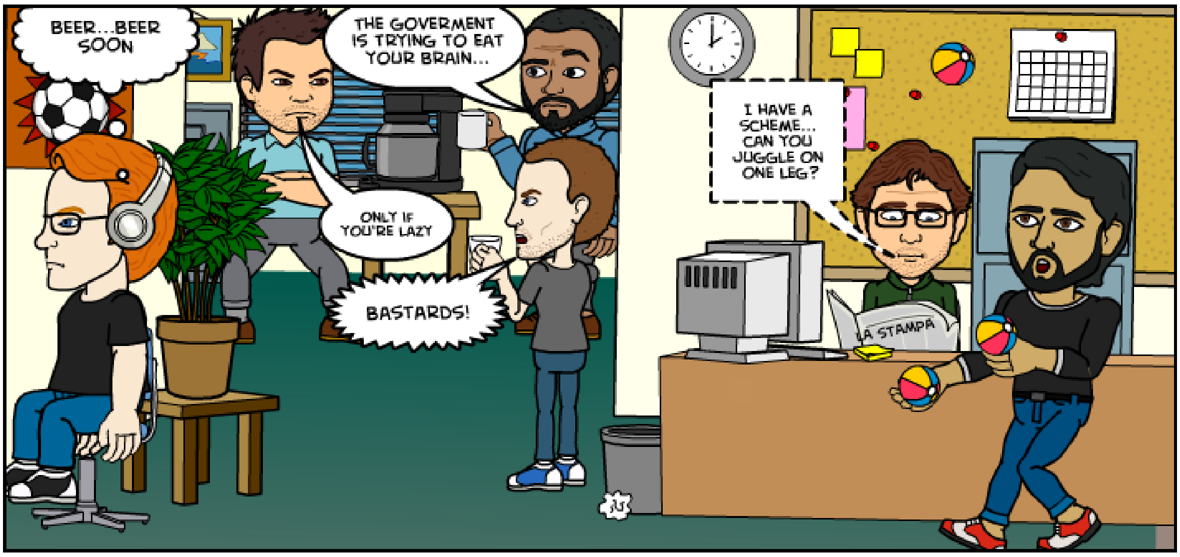

countless conversations over coffee

Abstract

With CMOS technology reaching fundamental scaling limitations, innovative data storage technologies have been a topic of great academic and industrial interest. Emerging technologies, not all based in semiconductors, that exploit new variables like spin, polarisation, phase and resistance, are being investigated for their feasibility as data storage devices. One very promising technology is resistive switching random-access memory (RRAM). In RRAM devices memory operation relies on the change in resistance of a metal-insulator-metal structure, typically induced by ion migration combined with redox processes. Here, RRAM devices based on amorphous and crystalline zirconia have been prepared by means of pulsed laser deposition (PLD). The thesis starts with an overview of the commissioning of a new PLD system, with a focus on characterisation of the laser ablation plume, reduction of the density of "droplets" and development of the optimal system parameters, like temperature, oxygen pressure and laser fluence, for the preparation of zirconia based RRAM devices. For both amorphous and crystalline devices, titanium was used as an active electrode as it promotes the introduction of oxygen vacancies which are responsible for inducing resistive switching. In addition, growth of epitaxial Nb doped strontium titanate (Nb:STO) via PLD was achieved, as the high temperatures used during growth hinder the use of metallic bottom electrodes. Both types of RRAM devices have good performance figures, with ON/OFF ratios of 10^3 and 10^4 and endurance of more than 10^4 cycles. Conduction mechanisms point to two different types of resistive switching: insulator-to-metal transition and trapping and de-trapping at the metal-oxide interfaces. Surprisingly, both conduction mechanisms were found to coexists on amorphous devices. Scanning transmission electron microscopy and electron energy loss spectroscopy were used to investigate how interfaces can influence resistive switching. Results indicate that titanium, in addition to introducing oxygen vacancies, creates an ohmic interface with zirconia which forces the resistive switching to take place on the inert metal-oxide Schottky interface, which was not described so far.

Acknowledgements

First and foremost I would like to thank my supervisors Dr Donald MacLaren and Dr Stephen McVitie for all the support during the last four years. Their guidance, encouragement and countless suggestions literally made this PhD thesis possible. It was a real pleasure working under your supervision and I feel very fortunate to have been given a chance to do so. I am also truly grateful for the assistance provided by Dr Sam McFadzean, not only during the countless microscopy sessions, but for also for always having an answer and pointing me in the right direction. Many thanks to Billy Smith and Colin How for the very enjoyable microscopy training sessions and for making sure all the equipment was in pristine condition (not to mention all those football matches!). Thanks must also go to Dr Ian McLaren and Dr Damien McGrouther for all the fruitful discussions, regarding EELS analysis and in-situ sample preparation using the focused ion beam. Thanks to everyone at JWNC for assisting me during the nanofabrication stages on my project. Thanks also to Dr Liam Cunningham at IGR, not only for allowing access to the facilities, but also for the fruitful discussions regarding substrate preparation. Of course none of the work presented here would've been possible without the help of my fellow PhD office mates, Ciaran, Francisco, Shabir, Marco, Aaron and Colin who made sure I never got (too) overwhelmed! Those countless conversations over coffee are surely going to be missed. I would also like to thank Dr Kerry O'Shea, Dr Gary Paterson and Dr Maria José Benitez for the all the support, helpful discussions and guidance during my time in Glasgow.

A very genuine thanks to my parents Rui and Manela and to my sister Margarida, who besides listening to my complaints over the years, always supported and encouraged me to pursue my objectives - even the odd and (maybe?) not so good ones - I promise I'll make it up to you with some physics chat over the next family dinners. Finally, a special and heartfelt thanks to Silvia who on very short notice agreed to start a new life in Glasgow, which was challenging in earlier times (to say the least). Now that we're both just about to commence a new chapter in our life together, I sincerely hope it was worth it!

Declaration

This thesis is a record of the work carried out by myself in the Materials and Condensed Matter Group of the School of Physics and Astronomy at the University of Glasgow during the period 2011 - 2015. The work described herein is my own with the exception of the LabView code that runs the probe station, which was develop by Dr. Gary Paterson and the STEM EELS data acquisition on chapter 6 that was performed by Dr. Donald MacLaren.

Some of the work reported in this thesis can be found in the following publication:

1. P. Parreira, S. McVitie and D.A. MacLaren, "Resistive switching in ZrO_2 films: Physical mechanism for filament formation and dissolution", Journal of Physics: Conference Series 522 (1) 012045 (2014)

Contents

List of Figures

List of Tables

Chapter 1

Introduction

This thesis will start with a brief comparison between some of the existing emerging technologies and resistive switching (RS) devices, followed by the description of their main switching mechanisms. In chapter 2 a description of fabrication and characterisation techniques will provided, focusing on the pulsed laser deposition (PLD) system and on the transmission electron microscope (TEM). Chapter 3 will cover the preparation of amorphous ZrO_2 thin films via PLD with the adequate physical properties to be integrated in RRAM devices. Chapter 4 will focus on the preparation of $SrTiO_3$ (STO) substrates, followed by a description regarding the epitaxial growth of Nb:STO thin films via PLD, to be used as electrodes in crystalline ZrO_2 based devices. Fabrication details, electrical and TEM characterisation of amorphous and poly-crystalline devices is presented in chapter 5, together with a description of the proposed RS model. Devices with epitaxial Nb:STO and crystalline ZrO_2, as well as $PrCaMnO_3$ (PCMO) based devices prepared by collaborators, will be characterised spectroscopically in chapter 6. Finally, chapter 7 will summarise all conclusions and outline future work that should be implemented in the development of this research field.

1.1 Technology Overview

Computing platforms, ranging from handheld devices to large supercomputers, require systems for storing data [1]. Beginning with punch cards that stored a few bytes of data with holes in a sheet of card, storage systems have reached multi-terabytes of capacities in less space and consuming less power by using semiconductors [1]. Semiconductor memories are classified based on how many times they can be rewritten into random access memories (RAMs) and read-only memories (ROMs). ROMs are normally used to permanently stored information that is going to be read many times. These memories can be re-written significantly less times than can be read, and the *write* process takes much longer than the *read*. RAMs, on the other hand, have the same speed for both cycles and there is no limit to how many times they can be re-cycled [2]. Additionally, memory can be volatile or non-volatile: in volatile memories, the information eventually fades when the power supply is turned off. On the other hand, unpowered non-volatile memories retain the stored information for periods of years [1]. There are many types of volatile and non-volatile memory technologies within a modern computer system, regardless of its size and application. Static RAM (SRAM), is the fastest memory technology, with write/read speeds of the order of 0.1 ns, and is used when access times are critical. On the other hand, dynamic RAM (DRAM) is over one order of magnitude slower, and is used as main memory, temporarily holding data to and from storage. The reason behind these two classes of volatile memory is linked to their device architecture. SRAM is significantly more complicated and costly to fabricate, and memory cells are much bigger when compared to DRAM [2]. The established FLASH, and the emerging technologies like magnetic RAM (MRAM), ferroelectric RAM (FeRAM) and resistive RAM (RRAM), are examples of non-volatile memories. In terms of performance, FLASH is so much slower than SRAM or DRAM that it is mostly used to archive data. It is important to note that the concept of "memory" usually means computation, whereas "storage" is linked to archival of information. In figure 1.1 the memory technologies most commonly used are categorised according to their purpose.

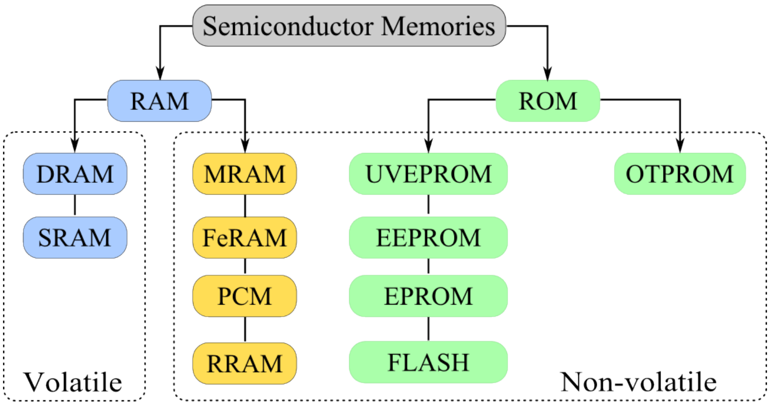

Figure 1.1: Standard semiconductor and emerging memory technologies categorised. Adapted from [2].

It is interesting that, in figure 1.1, new technologies like MRAM, FeRAM, PCM and RRAM are non-volatile but are categorised as RAM. This is important as emerging technologies are now approaching the performance of SRAM and DRAM but have the benefit of being non-volatile, which is a recent achievement. In fact, the ideal memory device would satisfy simultaneously four requirements: high speed, high density, low power consumption and non-volatility [1–3]. The development of such technologies has been a topic of great academic and industrial interest over the past decades [4, 5], as existing technologies are facing huge scalability challenges i.e. increase in storage capacity and performance cannot be achieved by further reducing device dimensions or packing density [4]. In addition, the drive to develop new memory technologies is also linked to the rising gap in speeds between the processing power of modern CPUs and the hard disk drives required for information storage, as illustrated in figure 1.2a.

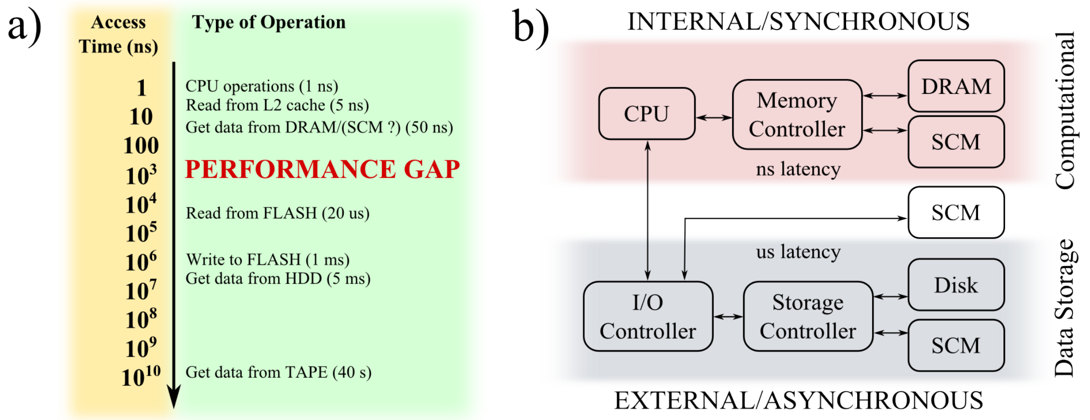

Figure 1.2: a) Comparison between the time needed for several computing processes and data retrieval. b) Flow chart illustrating the use of SCM in both computational processes and data storage. Adapted from [6].

This gap arises normally from the very slow access times of hard disk drives (2-4 ms) which have remained more or less constant over the past decade [7]. In fact, as CPU cores become both faster and more numerous, the limiting factor for most programs is memory access times [8]. One possible solution is the development of a class of devices that can be used for computational processes and data storage indistinguishably. Such class of devices has been termed *storage class memory* (SCM) by IBM in the last decade. SCM can be internal (synchronous, faster) or external (asynchronous, slower) according to figure 1.2b. In other words, it can be used as SRAM and DRAM (memory) while satisfying the non-volatility of hard disk drives (storage). In addition, memory developers and producers are also interested in the development of alternative fabrication processes that are scalable beyond the 20 nm lithography limit. Ultimately, this can be achieved by using a cross-point memory array that can be fabricated in multiple layers forming a stacked 3D memory, as seen in figure 1.3 [1]. It is expected that in the future, this is what the device architecture will tend to be like regardless of the technology used because such a design has the highest packing density. However, this architecture represents a challenge to existing technologies because of the need to address individual memory cells using additional transistor circuitry. However, for true cross-point 3D stacks with very high density, the use of additional addressing circuitry is not possible as it substantially increases the size of individual cells.

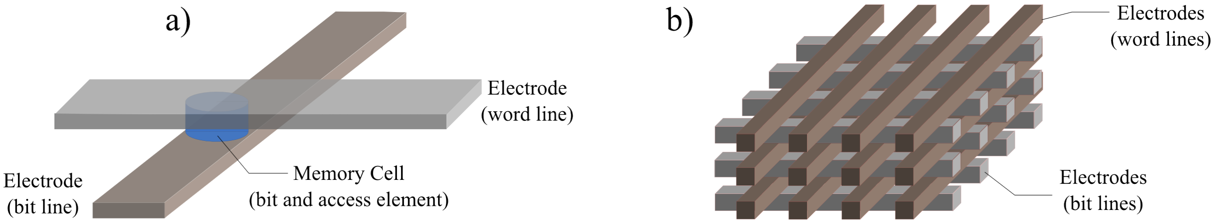

Figure 1.3: a) Memory bit in a cross-point architecture and b) high density 3D stack of memory bits without access elements. Adapted from [1].

Emerging memory concepts have been pursued extensively in the hope of finding suitable technologies for SCM [3, 9]. Amongst the emerging technologies such as magnetoresistive random access memory (MRAM), ferroelectric RAM (FeRAM), phase change memory (PCM) and in comparison to the existing like SRAM, DRAM and FLASH, resistive RAM (RRAM) has attracted increasing attention more recently. This section will focus on briefly describing the working principle of these technologies, giving examples and explaining why RRAM is the best candidate for SCM.

FLASH memory is without any doubt the most established non-volatile memory technology [1]. It was originally developed by Toshiba in the early 1980s and is credited to Masuoka *et al.* [10, 11], although the idea of using a floating gate (FG) device to produce nonvolatile memory was suggested for the first time in 1967 by Kahng and Sze at Bell Labs [12]. The working principle of a FLASH memory cell is closely based on a metal-oxide semiconductor field effect transistor, MOSFET, but with two gates (floating and control) instead of one. Figure 1.4 illustrates a simplified schematic of a typical FLASH cell.
FLASH stores data as isolated charge in the floating gate of a MOSFET, where the control gate will require different voltages to drive the transistor depending on the charge on the floating gate, because of screening by the charges in the floating gate. The logic state of these devices can be sensed by current flowing through the transistor when a small

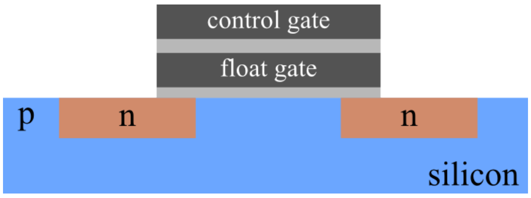

Figure 1.4: Simplified schematic of a typical FLASH cell, where n regions represent the source and drain electrode. Adapted from [1].

voltage is applied to the control gate. It is worth remembering that figure 1.4 illustrates the simplest case, different from what happens in real FLASH memories nowadays, which have much more complex architectures. In fact, the level of optimisation of FLASH memories is a good example of how much semiconductor memory technologies have matured since the 1970s [1, 3]. A conventional FG memory device must have a tunnel oxide layer thickness of 8 nm to prevent charge loss and to make 10 years' data retention certain. This necessity will limit scalability for FLASH memory devices [1]. But perhaps the major limitation facing FLASH memories is the high voltage required for their operation. It is expected that the entire semiconductor industry will progressively change from 5 V to 3.3 V, 1.1 V and finally 0.5 V for its logic operations [1, 13]. Although such change will greatly impact FLASH technology, it would have less of an effect on emerging technologies like MRAM, FeRAM, PCM and hardly any on RRAM, as explained in the next sections.

Figure 1.5 illustrates a typical MRAM cell, which is based on a Magnetic Tunnel Junction or MTJ [3, 7]. The spin-polarised current tunnelling through the barrier separating two magnetic layers is dependent on their relative magnetisation, an effect termed tunnelling magnetoresistance (TMR) [3, 14, 15]. One of the layers has its magnetisation pinned by the AF layer, whereas the second can be flipped (or *written*) under an external event [3], as illustrated in figure 1.5. Devices will have low resistance when the layers have parallel magnetisation, and high resistance when anti-parallel. This results in two distinct resistance states that can be used for binary logic [16].

Various companies such as Samsung, IBM, Hitachi, Toshiba, and TSMC are actively developing variant technologies of MRAM chips. In regards to performance, MRAM competes favourably with other existing memories such as FLASH and DRAM, with an access time of a few nanoseconds [17, 18]. However, MRAM suffers from scalability issues due to the spread of the magnetic field to neighbouring cells [1], especially during the *writing* operation [1, 17, 18]. In addition, the high current (> 1 mA) needed for *writing* has also been identified as a limitation. Despite this, and as an example, 4 and 16 Mb MRAM

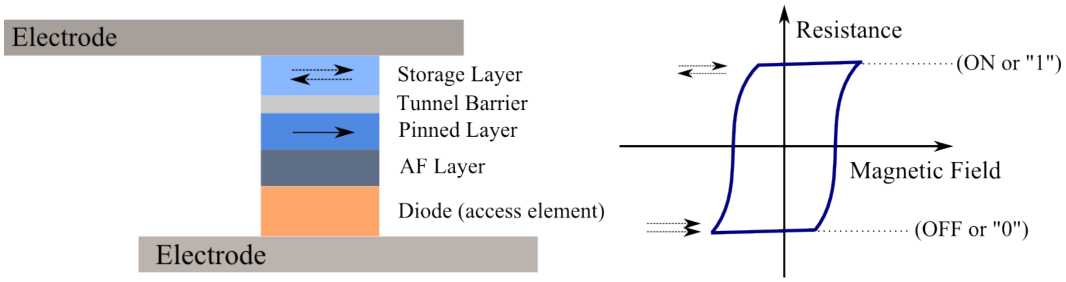

Figure 1.5: Schematic of a MRAM cell. The antiferromagnetic layer (AF) pins the switching layer responsible for two resistance states. Adapted from [3, 16].

chips by *Everspin Technologies* have replaced SRAM and FLASH memories in the flight control computers of the new Airbus A350 civilian aircraft [7, 19]. Another application of MRAM chips is in power fail safe control modules of BMW superbike engines due to their excellent high temperature reliability [7, 19, 20]. The reason behind using MRAM relates to the “instant ON” capability provided by non-volatility with almost SRAM-like speed, a useful feature in the event of power-losses in dynamic situations [19]. During the next decade, it is suggested that MRAM will be the technology with the fastest growth in commercial applications, when compared to competing emerging memories [1].

FeRAM is a non-volatile memory technology that uses ferroelectrics in a capacitor-like structure, as depicted in figure 1.6. Ferroelectrics are a class of materials that possess spontaneous polarisation, in one or more axis, which is reversible by the application of an external field [3, 21]. In addition, ferroelectric materials exhibit bistable polarisation states that are retained in the absence of an applied external field [21]. The most common material used in FeRAM cells nowadays is lead zirconate titanate, PZT. In FeRAM devices, the polarisation can be sensed (or *read*) by measuring the voltage given by polarisation reversal or the non-reversal current [3, 21]. FeRAM also satisfies all speed requirements but suffers from a destructive *read* cycle. This means that the cell must be *re-written* after every time it is *read* therefore slowing the task. On top of this, the main drawback is perhaps the loss in reliability when ultra small structures are fabricated in a 3D architecture.
However, FeRAM achieved commercial success in 1993 and current FeRAM chips are already faster than FLASH memories [1, 21]. Nowadays FeRAM chips are used in high quality products, mainly within Mercedes, BMW, Ford and Porsche automobiles [7]. Perhaps the best example of FeRAM utilisation is RFID smartcards and authentication devices. Even if FeRAM suffers from scalability issues that prevent its mainstream commercialisation, because of its remarkable low power operation, FeRAM is likely to be used in very specific

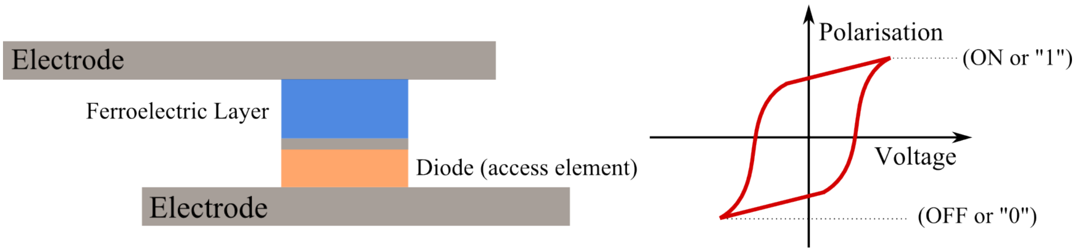

Figure 1.6: Schematic of a FeRAM cell. Voltage induces changes on the polarisation of ferroelectric layer that changes its resistance. Adapted from [16].

niche applications [21].

Another emerging technology currently under great development is phase change memory (PCM). These memory cells explore the difference in electrical resistance of certain chalcogenides, when these are amorphous (high resistance) or crystalline (low resistance). Normally these devices are fabricated in a low resistance state because growth temperature required during fabrication, normally yields crystalline switching layers. By applying a large but fast current pulse, the crystalline region is melted and quickly quenched, making it amorphous. By applying a smaller and longer current pulse, so that enough heat is generated to crystallise the layer, the low resistance state is achieved again [22]. A simplified schematic of a PCM memory cell is illustrated in figure 1.7. Even though this technology was developed during the 1960s, it was only with the discovery of GeSbTe alloy that significant advances in consumer products were seen. The GeSbTe alloy can be changed (or programmed) to be either GeTe or Sb_2Te_3, which have different electrical and optical properties [1, 22].

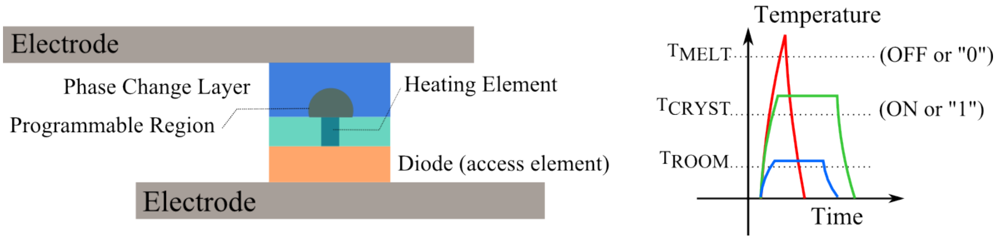

Figure 1.7: Simplified schematic of a PCM cell, illustrating how the structure change is induced. Adapted from [22]

.

The best example of phase-change non-volatile memories are perhaps optical storage media, such as RW-DVD and Blu-ray discs, that recently achieved 100 GB capacity. The difference in optical contrast between the amorphous and crystalline states, can be easily sensed and used as data bits. When it comes to performance, solid-state PCM memory cells are as fast as MRAM, but already much faster than FeRAM and FLASH [23, 24]. It is expected that PCM technology will (at best) match DRAM speeds, but due to the rather large sized cells, scalability is hindered. In addition to this, the high power used to write and erase data, even for state-of-the-art devices, has been identified as the major issue impeding mass fabrication [24].

For the emerging memories described so far, it should be noted that the four required properties for SCM, as explained in page 2, are not met on a single technology. Normally, performance requirements are met, like for MRAM, but scalability or high power requirements limit mass production and implementation. Additionally, MRAM, FeRAM and PCM technologies cannot be called "emerging" as commercialisation started during the mid 90s for all of them. On the contrary, resistive switching devices (RRAM) fulfil all SCM requirements, and can be termed truly emerging as research on it has seen a exponential increase in the last few years. Furthermore, the enhancement of computing capacity to cope with the complex real-time data environment is severely impeded by the von Neumann bottleneck, which refers to the limited data transfer rate between the central processing unit and the memory in the traditional computing architecture. The feasibility of combining the information storage and processing, eliminating the bottleneck, has been demonstrated in RRAM devices using a neuromorphic computing approach, based on which new parallel computing architectures can be envisioned [25].

RRAM devices rely on an insulating layer that can switch between resistance states upon the application of a voltage or current pulse. They are non volatile and require very low power [2, 26–28]. In fact, the reason for the growing interest in RRAM is the fact that unique properties like fast write/read operation (preferably <10 ns), high resistance ratio (>10), endurance (preferably $> 10^{10}$ cycles), CMOS compatibility and retention time greater than 10 years have already been demonstrated in laboratory devices [4, 27]. In addition, the performance can be dramatically increased by the use of materials or architectures that can provide multi-bit operation. In others words, there is the potential for further increase in data storage densities by the existence of more logic levels than those in binary systems (*0* and *1* or *on* and *off*). A simplified schematic of a RRAM device is illustrated in figure 1.8.

It is suggested that RRAM is a disruptive technology that will revolutionise the performance of products in many areas, ranging from consumer electronics to automotive applications [1]. In fact, it is one of the most promising emerging memory technologies and has the potential

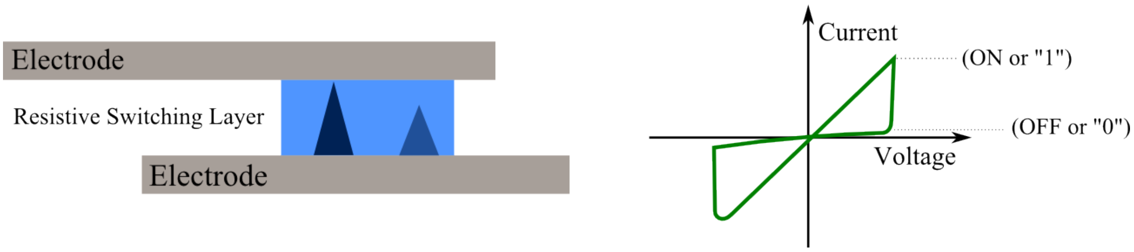

Figure 1.8: Schematic of a typical RRAM cell and its electrical response, illustrating two distinct switching events and resistance states.

.

of being a universal storage class memory technology [1, 29]. It should be noted that the universal character of RRAM SCM allows it to be used anywhere in a computer system, as depicted in figure 1.2 on page 3. Recently, the incorporation of RRAM devices using true 3D cross-point architectures and without any addressing circuitry was demonstrated [30]. As a matter of fact, in 2013 Panasonic started the production of RRAM for low power consumption microcomputers [31]. At the same time, a small start-up company called Crossbar recently released a statement announcing the fabrication of a 1 TB RRAM non-volatile memory in a 200 mm^2 chip [32]. When it comes to the working principle, the most common mechanism for RS is the formation and dissolution of a conductive filament between the two electrodes surrounding the switching layer, as illustrated by the coloured triangles in figure 1.8. Indeed, the greatest challenge to the mass integration of this technology and its use as SCM is the fact that the switching mechanisms are yet to be completely understood, especially at the nanoscopic level, which is the main motivation of the research described in this thesis. To add to this, the overwhelming number of materials systems investigated have different resistive switching mechanisms, which makes them particularly challenging to characterise. In fact, the large number of combination of materials and architectures being investigated is in conflict with the focusing of efforts needed to compete with mainstream memories [33]. Lastly, coexisting resistive switching mechanisms have been identified in the same devices, further illustrating just how difficult experimental characterisation can become [34]. The next sections will focus on linking RRAM behaviour with memristor theory as well as presenting detailed models of several types of resistive switching mechanisms.

1.2 Memristor Theory

It is interesting to realise that the resistive switching behaviour of RRAM is linked to memristors, which were predicted by Leon Chua as the "fourth basic circuit element" because they complete a conceptual symmetry with the resistor, inductor and capacitor [27, 29, 35]. In 1971, Leon Chua [29] postulated the existence of the fourth missing fundamental circuit element, which comes in the form of a passive two-terminal device called the memristor, short for memory-resistor. More specifically, Chua noted that there are six different mathematical relations connecting pairs of the four fundamental circuit variables: electric current i, voltage v, charge q and magnetic flux φ [5]. He also proved that memristor behaviour could not be duplicated by any circuit built using the other three elements, which is why memristors are truly fundamental [36]. A memristor behaves as a nonlinear resistor with memory depending on the past history of the current or voltage in the device. Five years after Chua's pioneering publication, Chua and Kang postulated that memristors are in fact a particular class of devices belonging to a larger class, termed *memristive systems* [35]. Initially, Chua's equations meant that the flux was solely dependant on charge, but this is not the case for *memristive systems*, where the stimulus can be voltage, for instance. A memristor is thus defined to be any dynamic electronic circuit element that obeys, independent of the underlying physics of the system, the following memristor equations [36, 37]

$$v = R(w, i)i, \tag{1.1}$$

$$\frac{dw}{dt} = F(w, i). \tag{1.2}$$

The first equation is the quasi-static resistance equation, or state-dependent Ohm's law, and the second is a dynamical equation that describes the temporal evolution of the state variable (or variables) w as a function F of w and possibly electric current [5, 36, 37]. The most important property of equations 1.1 and 1.2 is that the centre of $(v(t), i(t))$, due to any periodic current or voltage source, on both polarities, must always cross at the origin, in the sense that $(v, i) = (0, 0)$, as seen in the *pinched* I-V curve example in figure 1.8. Equations 1.1 and 1.2 also imply that the pinched hysteresis loop phenomenon of any memristor must hold for any periodic signal, $v(t)$ or $i(t)$, that assumes both polarities, as well as for any condition used to integrate the differential equations to obtain the corresponding steady state $i(t)$ and $v(t)$, respectively. Another unique property shared by all memristor hysteresis loops for every given periodic $i = f(t)$ (where f assumes both positive and negative values) and for any initial state $x(0)$, is that the area enclosed within the pinched loop on quadrants 1 and 3 of the I-V plane shrink as the frequency increases (figure 1.8), tending to a single-value function through the origin as frequency approaches infinity [35–37]. In other words, as the programming frequency approaches infinity the hysteresis tends to disappear, implying that a minimum programming time is required to induce memristive behaviour. This description is particularly useful when multibit level resistance or even analogue values are to be stored and processed [27]. The motivation for this being the recent advancements in memristive devices that have provided a strategic opportunity for advancing the development in neuromorphic engineering. This is attributed to the unique properties of the memristor including non-volatile storage, nano-scale dimensions, but, most importantly, its analog behaviour and its ability to remember the history via the modulation of its internal state. To perform the human brain's cognitive functions, electronic devices that can mimic biological neurons and synapses are the crucial basic elements [25]. The large number of transistor-based electronic synapses consume most of the power and area and hinder the further scaling of traditional very-large-scale integrated circuits (VLSI) neuromorphic chips. In view of many advantages, such as ultrafast synaptic function operation, ultra-low power consumption, sub-10 nm scalability, over 10^{10} endurance, and high connectivity of up to 4D architecture [38], memristor-based neuromorphic chips may provide a promising approach to realise large scale brain-inspired computing [25, 39, 40].

The link between Chua's theoretical work and the body of literature on resistance switching memory devices was first pointed out by Williams *et al.* in 2008 [5, 27]. Williams successfully prepared and characterised TiO_2/TiO_x based devices that were shown to obey Chua's memristor equations. This not only sparked enormous research interest in the field, but also linked memristive behaviour to a substantial body of evidence on resistive switching done over the previous few decades. More recently, it has been suggested that not all of the mechanisms identified to date can be accurately described as memristors because the driving forces behind electrochemical reactions are voltage dependant and not charge (or current) dependant [2]. However, Chua's equations successfully describe an overwhelming variety of resistive switching mechanisms published recently, in different material systems, as being memristive [37]. Chua's description of memristive systems is perhaps best explained and experimentally identified, by the shape of the current-voltage loop, illustrated in figure 1.8. If the hysteresis loop is pinched on the origin of the axis, then, regardless of the technology, materials system or driving force, the system is said to be memristive [29, 35–37].

1.3 Resistive Switching Mechanisms

Independent of the material system used, resistive switching (RS) consists of SET and RESET processes that change a material's high resistance state (HRS) to a low resistance state (LRS) and vice-versa, each change usually induced by an applied voltage. Resistive switching devices can be classified based on their switching mechanisms, switching materials or switching polarities. Very different classifications and categories of resistive switching behaviour can be found in the literature, especially in more recent work. In fact, there has been so many competing resistive switching mechanisms described in the literature, that linking the observed electrical response to a particular phenomenon is particularly challenging. Figure 1.9 illustrates categories of RS mechanisms according to Waser *et al.* [27].

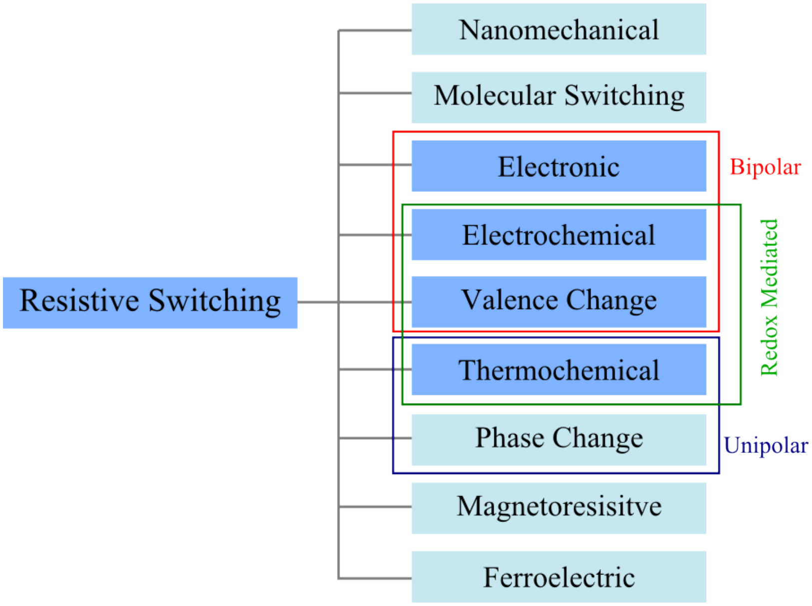

Figure 1.9: Categories of resistive switching mechanisms according their switching polarity and physical phenomenon. Adapted from [26].

Resistive switching that is mediated by redox reactions are of particular interest to RRAM, [27, 41] as redox reactions have been used to explain RS in electrochemical, valence change and thermochemical memories, as illustrated in figure 1.9. This is the reason for explaining these mechanisms in detail in the following section. In order to better understand the switching mechanisms we need to distinguish between three very different behaviours in respect to the polarities required for the resistive switching. Devices that switch independent of the polarity of an applied bias are called unipolar devices. These typically have symmetric I-V characteristics and have both SET and RESET occurring on both polarities, as depicted in figure 1.10a. In the same figure, the dashed line represents the current limit during the SET transition, required to prevent the devices from hard breakdown.

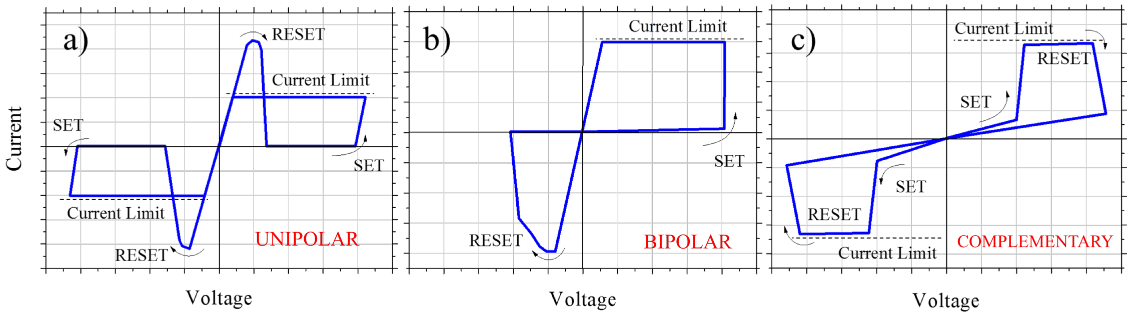

Figure 1.10: The three different modes of operation according to the polarities needed for the resistive switching. a) Unipolar behaviour where the switching occurs for both polarities. b) In bipolar devices different polarities must be used to switch from HRS to LRS and vice-versa. c) complementary switching, SET followed by RESET transitions in both polarities.

For unipolar resistive switching it is worth pointing out that the RESET voltages are always lower than the SET voltages (figure 1.10a) for both polarities. Similarly, the currents needed for RESET are always higher than those allowed by the current limit in the SET process. In contrast, devices that require one polarity for the SET process and the opposite for the RESET are called bipolar, as illustrated in figure 1.10b. For bipolar resistive switching, a current limit is only needed for the SET transition, and this limit is generally lower than the current needed for RESET. A third type of switching, called complementary switching and depicted in figure 1.10c, was described more recently and is characterised by a SET and a RESET event on both polarities [42]. Interestingly it is complementary RS that enables the fabrication of true 3D cross-point array with very high density, mentioned in the previous section. It was originally achieved by fabricating two bipolar memristors back-to-back, so that the polarity needed to switch ON the first memristor, turns the second OFF [30]. However, complementary switching has been observed in single devices and in different material systems. Systems where the mode of operation can be changed between unipolar and bipolar by different operation conditions are normally termed non-polar. In non-polar resistive switching systems, thermal effects are usually dominant [43]. Of course in real systems, where many phenomena need to be factored in, the shape of these curves may deviate considerably from the ones presented above.

RRAM devices possess attractive performance figures, especially long retention times ($\geq$ 10 years) and fast switching speeds ($\approx$ 10 ns). For FLASH based devices, having both properties is not a problem, because programming (*write*) is done the control gate, whereas the sensing (*read*) is done using source/drain electrodes i.e. FLASH devices have 3 terminals, as seen in figure 1.11a. However, in the simple MIM RRAM device this poses a problem because *read* and *write* are performed using the same 2 terminals, as depicted in figure 1.11b. Schroeder *et al.* suggested that in a purely electronic, passive, non-volatile 2 terminal device satisfying both long retention and short switching poses a dilemma, termed *voltage-time dilemma*. This happens because in the LRS and during *read*, a 2 terminal RRAM stack behaves like a leaky capacitor [27, 36, 44, 45]. Figure 1.11 illustrates the differences between FLASH and RRAM devices when programming and sensing the resistance state.

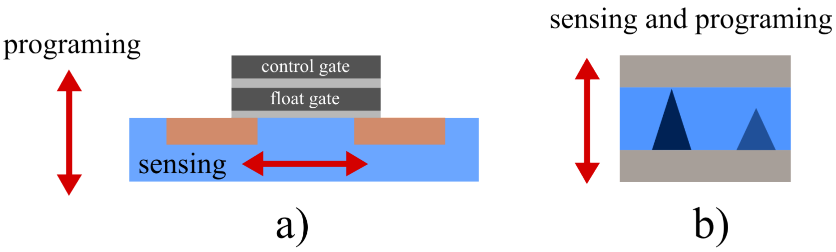

Figure 1.11: Different types or devices architecture for a) FLASH cell and b) RRAM cell. Note how the sensing and programing current paths are different for FLASH but not for RRAM. Adapted from [44]

One example illustrating such dilemma is trapping-detrapping of electronic charge at immobile traps in insulators as a mechanism for a nonvolatile resistive switching in MIM thin films stacks [27, 44, 46, 47]. A very high retention time (10 years) calls for sufficient barriers to suppress the escape of the trapped electronic charge by thermally activated or tunnelling processes [44]. However, because of high current densities, during *read* operation the non-equilibrium charge state of the traps is severely affected, and thus unstable on time scales which are many orders of magnitude smaller than the required retention time. Indeed, in common RRAM devices, the ratio between *write*/*read* voltages is approximately 10, but this ratio needs to give rise to an acceleration of the switching kinetics between *retention*/*write* times of 10^{16}. In other words, ultra fast switching and long term retention cannot be explained by electron trapping-detrapping alone [36]. This has an important implication: unless the application of a voltage or current across the device leads to nano-structural changes within the active layer or interfaces, non-volatility and ultra fast switching are not possible in MIM stacks. Interestingly enough, evidence of trapping-detrapping conduction mechanisms has been seen for all the ZrO_2 based devices characterised in this thesis. This topic will be addressed and explained in more detail in the next sections and also in chapters 5 and 6, when presenting the electrical characterisation of amorphous and crystalline RRAM devices. Nevertheless, the voltage-time dilemma suggest that purely electronic effects, like trapping-detrapping, cannot fully explain resistive switching behaviour, substantiating the importance of redox mediated processes [27, 44].

Resistive switching has been observed in devices based in binary metal oxides such as NiO [48–50], TiO_2 [51–54], ZrO_2 [55–57], ZnO [58–60], Cu_xO [61, 62], Al_2O_3 [63–65], HfO_2 [55, 66–68], TaO_x [69], $BiFeO_3$ [70], Co:$BaTiO_3$ [71] and more recently even in organic systems like PEDOT:PSS [72] and spirofluorene [73]. The material systems used for device fabrication will, in the majority of times, dictate which mechanism(s) is responsible for RS during electrical characterisation. The next sections will focus on the electrochemical (ECM), valence change memories (VCM) and thermochemical (TCM) resistive switching mechanisms. The reason for expanding on these three mechanisms is linked to the overwhelming number of materials systems whose RS is redox mediated. In other words, the resistive switching is presumed to be a combination of physical, chemical and thermal effects.

1.3.1 Electrochemical Metallisation Cell, ECM

The electrochemical metallisation cell (ECM), also called Programmable Metallisation Cell (PMC) or "cation devices" in the literature, uses electrochemical metal crystallisation and dissolution reactions to perform resistive switching [27]. In simple terms, a solid electrolyte merely transfers ions between electrodes but need not be chemically affected. One characteristic of these devices is that one electrode (AE) is made of an electrochemically active material like Cu or Ag that can be readily reduced. Alternatively, the intentional doping of the electrolyte layer with these elements was shown to work as well. Another characteristic is a chemically inert electrode (IE) made usually of either Pt or Au [4, 27, 74–77]. In earlier times the electrolyte (or insulator) layer was usually either a sulphide (As_2S_3, Cu_2S or Ag:Ge_xS_y), an iodide (AgI or $RbAg_4I$) or a selenide (Ag:Ge_xSe_y). The reason behind such materials has to do with their very high ionic solubility, especially when compared to other alloys. In recent work, more and more binary oxides (Ta_2O_5, $SrTiO_2$, TiO_2, ZrO_2, HfO_2, Al_2O_3, CuO_x, SiO_2 and WO_3) have been employed. It is worth mentioning that the change from the conventional solid-electrolytes to doped or undoped metal oxides increases the operating voltages from below 0.3 V to voltages just higher than those used on CMOS devices making them suitable candidates for non-volatile operations in large scale integrated circuits [43]. The reason for higher voltages relates to the fact that binary metal oxide are normally either insulators or n-type semiconductors. Figure 1.12a illustrates the initial stages of electroforming, the process responsible for switching from the as-deposited pristine state (IRS) to the LRS for the first time. In summary this process involves the following steps [27]:

1) Anodic dissolution of the AE metal (M) according to the reaction:

$$M \rightarrow M^{z+} + ze^-. \tag{1.3}$$

2) Migration under high electric field of the M^{z+} across the solid-electrolyte.

3) Cathodic deposition and electrocrystallisation at the IE surface according to:

$$M^{z+} + ze^- \rightarrow M. \tag{1.4}$$

Electroforming is an important step in ECM RRAM because the active layer is usually electrically insulating with only a few free charge carriers available for conduction. The electroforming step is believed to introduce defects that not only lower the active layer's resistance but could also be responsible for promoting additional switching events.

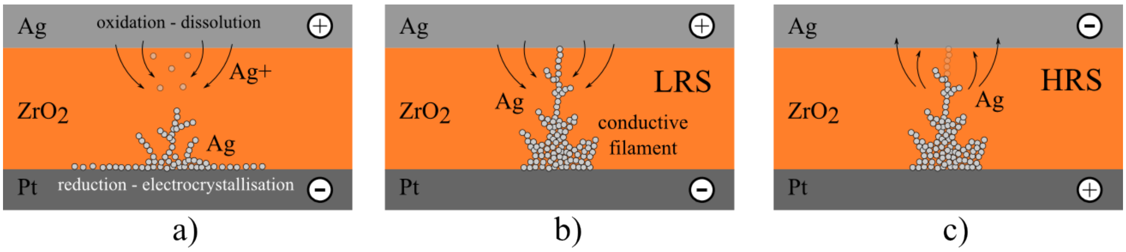

Figure 1.12: Schematic of an ECM RRAM stack with ZrO_2 as solid electrolyte during a) Forming b) SET and c) RESET transitions. Ag ions dissolve (oxidise) from the Ag electrode and travel to the Pt electrode where crystallisation (reduction) takes place.

A positive voltage oxidises the Cu or Ag atoms from the AE into Cu^+ or Ag^+ cations that dissolve into the electrolyte, as illustrated in figure 1.12a. Assuming that no other ionic species are present, M^{z+} cation transport on the amorphous solid-electrolyte layer, is described by Mott and Gurney model for electric field driven, thermally activated ion hopping [27]. This is important as device operation leads to Joule heating, enhancing cation transport. The dissolved cations are reduced and electrocrystallised at the inert contact. Eventually a conductive filament (CF) made of Cu or Ag (-M^{z+}-M^{z+}-) grows towards the active electrode. The ECM cell will achieve the LRS or turn ON as soon as the filament bridges the two electrodes, as depicted in figure 1.12b. Anodic dissolution, migration and electrocrystallisation, will immediately stop at this point because of the sudden decrease in the electric field as electrodes are now connected. Metal deposition at the inert electrode can be described by the Butler-Volmer relation, and is governed by the electrochemical overpotential, which is given by the difference between the Nernst potential and the effective electrode potential [27]. Once the polarity (or electric field) is reversed, electrochemical dissolution will take place at the active electrode interface, turning the cell OFF or to the HRS, illustrated in figure 1.12c. The vast majority of ECM cells are bipolar devices meaning that electric field is likely the dominating effect, however there are reports of ECM devices with unipolar behaviour [43]. Figure 1.10b (on page 13) illustrates a typical I-V sweep for ECM RRAM devices. The asymmetry in switching voltages has been a matter of some debate, because it was unclear why RESET and SET transitions happened for different voltages [78]. It was concluded that the asymmetry in voltage arises from geometric differences in morphology i.e. dendritic conductive filament with a sharp tip contacting a planar electrode, as seen in figure 1.12b [78]. Bipolar RS normally requires a current limit (compliance) during SET transition to protect devices against hard breakdown. The SET current compliance is used to limit the amount of current allowed through the dendrite shaped filament, thus governing its geometry. Interestingly, one can use the current compliance to control the conductance of the filament, directly controlling the ON/OFF ratio of ECM cells. For Ag/GeSe and Cu/SiO_2, the ON resistance can be controlled over 8 orders of magnitude just by controlling the current compliance during SET transitions [78]. This is of importance because it points towards the possibility of development of multi-bit devices, where current compliance dictates logic levels. Furthermore, in ECM cells a clear exponential relationship between the switching voltage and the sweep rate is observed, as well as a critical threshold SET voltage. These dynamic characteristics, together with the redox mediated RS model presented, can help explain how the voltage-time dilemma was overcome for ECM cells.

The choice of material systems is crucial when designing ECM cells. Reactions will be much easier at electrochemically active electrodes (like Cu or Ag for instance) that have lower work functions and higher ionic solubility but one must not neglect the influence of the active layer's properties and interface effects. As an example, the structural order of a metal oxide layer will dictate the density of grain boundaries, that by acting like preferential fast migration paths, directly influence device behaviour [27, 43]. In summary, even though complete consensus has not been reached, it is at least clear that ECM resistive switching models more accurately describe their experimental behaviour, when compared to VCM or TCM models. Perhaps not surprisingly, commercial applications mention in the introductory section (page 9), are based on ECM RRAM devices [32].

1.3.2 Valence Change Memory, VCM

In contrast to the largely inert insulator of ECMs, many nanoionic RRAM devices rely on electrochemical activity of the insulator itself. First reports which seem to fall into this category go back to the 1960s when Nb/NbO$_x$ thin film cells were studied [27, 79]. Also essential for VCM resistance switching is the choice of electrode material used in the MIM stack. Usually, one electrode is made from a metal that that does not oxidise easily (eg. Au or Pt), and the other from a metal that is easily oxidised (eg. Ti or Al), although symmetric devices have also been described [27]. There are many electronic and ionic phenomena that can explain resistive switching of a material system based purely on electronic effects [27, 41]. One possibility is the charge-trap model, where charges are injected by Fowler-Nordheim tunnelling across the metal-insulator interface, and become trapped at defect sites, changing the electrostatic barrier of the MIM structure. One other alternative is trapping at interface states, which affects the adjacent Schottky barrier, and hence the overall response of the stack. Finally, changes in a strongly correlated electron system of a transition metal oxide, in which injected electronic charges act like dopants, and can induce a transition from an insulator to a metal in perovskites oxides like Cu:SrTiO$_3$, or (Pr,Ca)MnO$_3$ [27]. However, for pure electronic mechanisms, it is not clear how the voltage-time dilemma can be overcome as explained in the previous section. In contrast to purely electronic mechanisms, many researchers have, over the years, suggested that the transport of anions plays a vital role in resistive switching. Indeed, valence change memories (VCM), also known as "anion devices", make use of the oxygen anion movement for the resistive switching. The movement of oxygen anions changes the valence of the transition metal (cations) and thus induce resistance change. Reduction of transition metal ions results in an increase in electron population in the conduction band, implying that the reduction reaction increases the number of free electrons and the conductivity [2]. By contrast, the oxidation of the reduced transition metal ions, empties the conduction band, decreasing the conductivity (see equation 1.5). It seems that for reliable resistive switching of VCM type devices the defects play a crucial role and recent work has focused on the engineering aspects of defect introduction and control [43]. Taking TiO_2 as an example, the equilibrium point defect concentration for oxygen vacancies is given by equation 1.6.

$$ne^- + Ti^{4+} \rightleftharpoons Ti^{(4-n)+}, \tag{1.5}$$

$$O_O^{2-} \rightharpoonup \frac{1}{2}O_2(g) + V_{\ddot{O}} + 2e^-, \tag{1.6}$$

where O_O^{2-} and $V_{\ddot{O}}$ indicate oxygen ions on regular lattice sites and vacancies, respectively [27]. As such, for most n-type metal oxides oxygen vacancies can be regarded as positively charged donor-type centres [26, 27, 78]. In addition, oxygen ions are much more mobile than metal cations, and influence the *electronic* conductivity by affecting the valence state of the transition metal cation i.e. redox reactions. Temperature dependent oxygen vacancy mobility is given by combining the Arrhenius law of diffusion with the Nernst-Einstein relation, yielding:

$$\mu_{vo} = \frac{z_{vo}\epsilon_o}{kT} D_0 e^{(-W_D/kT)}, \tag{1.7}$$

where $z_{vo} = 2$ for oxygen vacancies and W_D is the activation energy of the oxygen vacancy diffusion, ϵ_o is the permittivity of free space, z_{vo} the number of vacancies, k is Boltzmann's constant and T is the absolute temperature [27]. At this point, it is important to remember that there is not a consensus on the mechanisms responsible for RS due to valence change [41]. This is especially true because of the overwhelming number of resistive switching behaviours studied and characterised over the years. Similarly to ECM cells, valence change memories also require an electroforming step prior to stable bipolar resistive switching. Two slightly different electroforming mechanisms will be described, where the valence change of the transition metal cation is thought to account for the resistive switching observed. The choice of a symmetric device for this example is important, as a comment on electroforming in asymmetric MIM stacks is presented and discussed later in the section.

Figure 1.14 illustrates the initial stages of CF formation (i.e. electroforming) in a VCM type cell, according to Waser et al. [27].

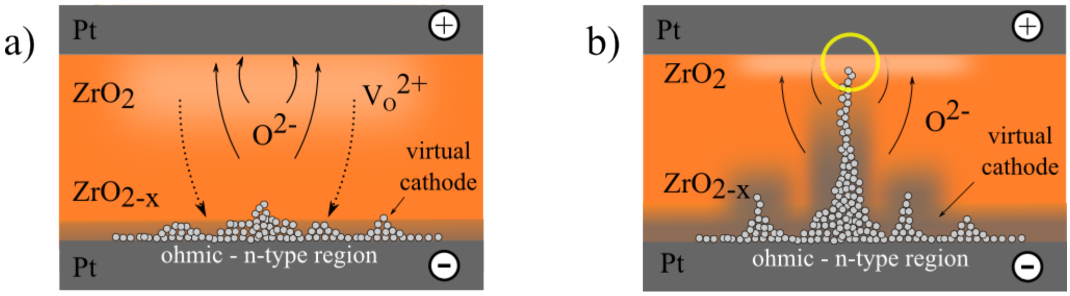

Figure 1.13: Schematic of a RRAM stack during electroforming, with ZrO_2 as the resistive switching layer and with platinum bottom and top electrodes. a) Virtual cathode propagates towards the anode under applied bias and b) Virtual cathode growth stops at the vicinity of the anode due to electrostatic repulsion. The yellow circle denotes where RS will take place. Adapted from [26, 27].

When a positive bias is applied to the top electrode, negatively charged oxygen ions will be attracted and drift towards that interface, oxidising it. This oxidation reaction may lead to the diffusion of oxygen through the surrounding regions or even lead to the evolution to oxygen gas [4, 80]. The electroforming process in metal oxides is an electroreduction where oxygen vacancies are created in the process, caused by high electric fields and enhanced by Joule heating. In comparison to oxygen ions, positively charged oxygen vacancies, will drift towards the bottom interface (cathode), giving rise to a n-type conducting region normally called *virtual cathode*, as seen in figure 1.13a. With continuation of the applied bias this *virtual cathode* propagates toward the anode until the gap between it and the anode is reduced to, normally, a few nanometres [27]. At this point, the oxygen vacancies that compose the *virtual cathode* will be repelled by the positively polarised anode and the propagation is hindered, as illustrated in figure 1.13b (yellow circle). Due to the accumulation of oxygen ions at the top interface, this region is now very insulating giving rise to a rectifying interface i.e. Schottky diode. It is in this very thin, but insulating, region that bipolar resistive switching is believed to take place in. Figure 1.14 illustrates the following steps, responsible for filament formation and rupture, or in other words, resistive switching.

When the *virtual cathode* is in close proximity to the anode, it takes a negative polarity applied to the top electrode to attract a few oxygen vacancies, bridging the electrodes. Once this happens, the VCM cell switches to the LRS. When the opposite voltage is applied to the top electrode, positively charged oxygen vacancies will be repelled from it, and the

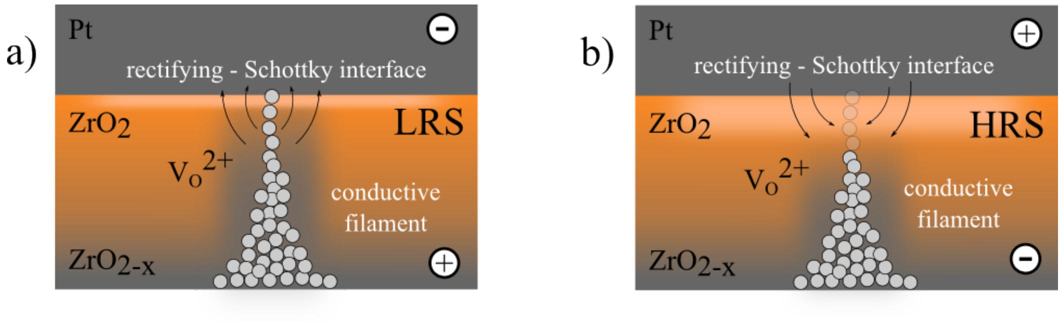

Figure 1.14: Close-up of a RRAM stack with ZrO_2 as the resistive switching layer focusing on the last stages of filament formation and dissolution. a) SET and b) RESET transitions. Oxygen ions will either reduce or oxidise the conduction filament depending on the applied voltage. Arrows indicate the oxygen ions movement, depending on the bias polarity.

conducting filament is broken, turning the cell to the HRS. This process is reversible and is the basis of bipolar resistive switching. It is important to mention that this description is not necessarily valid for all cases where valence-change mechanisms have been observed. In fact, many material systems have been described where the electroforming and bipolar switching have opposite polarities. To add to the complexity, Waser *et al.* [27] has also proposed that different electroforming conditions can influence the polarity and mechanisms responsible for resistive switching. In other words, the polarity of the bipolar RS is not completely obvious as many factors influence where and which redox reactions take place. Properties like the work function, oxygen affinity of the electrode materials and the use of different elements for the contacts will have an influence on the polarity of the resistive switching.

Asymmetric MIM stacks preferentially show bipolar resistive switching in comparison to symmetric ones, and the electroforming step is also different. The use of electrode materials with a low work function and high oxygen affinity, such as titanium, gives rise to a naturally formed ohmic interface with an oxygen depleted zirconia layer. In such devices, the “creation” of oxygen vacancies through *bubbling* is not necessary, making the forming process easier (where *bubbling* refers to oxygen literally bubbling out through one of the platinum electrodes i.e. oxygen is removed from the device stack). Similar to symmetric devices, the existent vacancies will be attracted to the cathode, and with continued applied bias filament formation will take place, turning the cell ON, as illustrated in figures 1.15a and 1.15b.

By inverting the polarity, the filament is oxidised, turning the device OFF as depicted in figure 1.15c. It should be noted that devices characterised and presented in chapter 5 fall

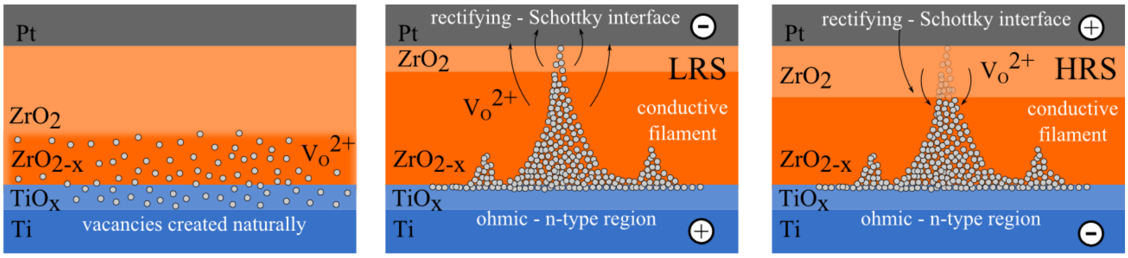

a) b) c)

Figure 1.15: Schematic of an asymmetric RRAM stack with Ti and Pt as electrode materials and zirconia as the switching layer. a) oxygen vacancies are created during fabrication. b) SET transition and c) RESET transition.

into this category.

In comparison with filamentary devices, another resistive switching VCM mechanism takes place at the metal/oxide interface, but over the entire device area [27, 41]. Such a mechanism is called homogeneous bipolar resistive switching and was originally explained by Sawa *et al.* [81–83]. It should be noted that such RS mechanism is normally described in crystalline systems such as perovskite oxides, like for instance Fe:$SrTiO_3$ (Fe:STO) or $PrCaMnO_3$ (PCMO), that are known for being anion deficient (n-type, like STO) or cation deficient (p-type, like PCMO) perovskites. Independent of the charge carrier type, it is assumed that such perovskite structures have *some* free charge carriers, as illustrated in figure 1.16a. The application of a voltage bias to the electrodes will give rise to oxygen vacancies drifting across the insulator.

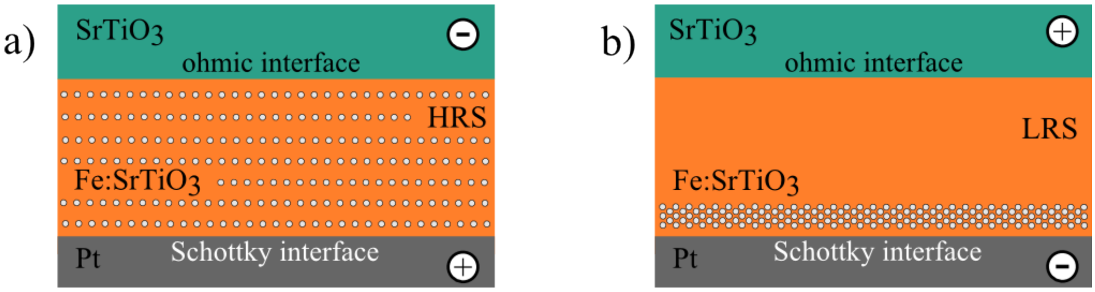

Figure 1.16: Schematic of a RRAM stack with Fe:$SrTiO_3$ as the resistive switching layer when the device is a) OFF and b) ON. Oxygen vacancies will either be confined to the undoped $SrTiO_3$ electrode or be homogeneously distributed over the RS layer, depending on the applied voltage. Note how the polarities are different when compared to filamentary ECM and VCM models.

If vacancies are brought towards the Schottky interface, the potential barrier will be reduced, and the device switches to the LRS, as depicted in figure 1.16b [84]. By inverting the polarity, oxygen vacancies can be homogeneously distributed again on the insulator layer, increasing the depletion region at the Schottky interface, and switching the device to the HRS [84, 85], as seen on figure 1.16a. One important outcome of Schottky barrier mediated RS is that in such devices only one interface is responsible for switching. As mentioned before, RS has been identified in most metal oxides. However, almost all of the reports of homogeneous or interface switching have been described for single crystal or highly crystalline materials. It is not surprising, that the PCMO based devices characterised in chapter 6 are believed to be homogeneous RS devices. By contrast, filamentary RS is very common with amorphous or polycrystalline materials, as presented in chapter 5. This is interesting and points to the fact that the structural order can dramatically influence the behaviour of resistance switching devices. This can be explained by different density of grain boundary or other structural defects in polycrystalline and crystalline layers, that act like fast migration paths for oxygen ions.

1.3.3 Thermochemical Memory Effect, TCM

So far the models described cation based (ECM) or anion based (VCM) RS mechanisms. This section focuses on cation *and* anion based RS, normally described as thermochemical memory effect (TCM) [86]. The TCM mechanism is similar to ECM and VCM type cells, where resistive switching is attributed to localised effects i.e. the formation of a conductive filament. This filament may be composed of the electrode metal transported into the insulator, or carbon from residual organics, or decomposed insulator material such as sub-oxides [87]. The contribution of anionic and cationic thermodiffusion on filament formation is dependant on which materials systems are involved. However, the driving forces, essentially for the RESET transition, are induced by thermal gradients and not electric field as in ECM or VCM cells. Figure 1.17 illustrates the SET and RESET transitions for TCM cells.

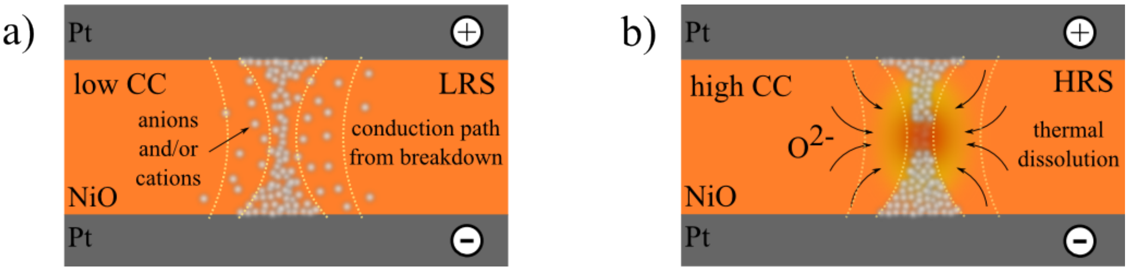

Figure 1.17: Schematic of a RRAM stack with NiO as the resistive switching layer during a) SET transition where CF is formed with oxygen vacancies, impurities or dopants within the oxide layer and b) RESET transition where thermal dissolution is responsible for the RESET transition.

In TCM cells, the LRS is achieved by applying a voltage without any particular polarity. Current flow through the oxide will cause Joule heating that increases the conductivity of the switching layer, and with the increase in voltage the switching material suffers from electrical breakdown, typically induced by thermal runaway [27]. A “low” current compliance (low CC) insures that a “controlled” breakdown gives rise to conduction paths, made from sub-oxides, metal cations from the electrodes or dopants, turning the cell to the LRS as depicted in figure 1.17a. The abrupt temperature gradient between the hot filament and the surrounding regions causes a significant thermodiffusion of oxygen anions out of the filament and/or cations in the opposite direction [7]. The negative free energy of formation, common to all the stable oxides, is the driving force that supports lower valence states at higher temperatures [27]. In the LRS, and with a “high” current compliance (high CC), Joule heating will be enough to thermally dissolve the filament, and the device switches back to HRS, as illustrated in figure 1.17b. With the application of a higher voltage (with the same polarity, but lower current compliance) the CF is formed again i.e. the LRS is achieved again. Hence, these devices are typically characterised by unipolar resistive switching , as opposed to bipolar observed for ECM and VCM cells [27, 86]. A typical example of an I-V sweep with unipolar behaviour can be seen in figure 1.10a in page 13. One characteristic that might help explain unipolar behaviour is the use of symmetric architectures, such as Pt/NiO/Pt [88] or Pt/TiO_2/Pt [89]. Another difference when compared to ECM and VCM is the number of filaments formed. Whereas in ECM and VCM cells *one* filament is formed, reports on Pt/NiO/Pt TCM cells show by C-AFM that *multiple* conductive filaments are in fact formed [90]. Surprisingly, in such studies, the HRS showed leakage current regions which are located at the grain boundaries. However for the LRS, point current images in the C-AFM image indicate discrete formations of filaments which are formed at the grain boundary regions as well as the non-grain boundary regions [90], which substantiates the importance of a controlled breakdown of the insulating oxide. Furthermore, Jeong *et al.* have shown that Pt/TiO_2/Pt MIM stacks exhibit bipolar RS (see VCM section before), that can be turned into unipolar by setting a higher current compliance value [78, 91]. One possible explanation is that field dominating RS effects, described for ECM and VCM devices, are only stable within a temperature window. With increased Joule heating, generated with higher current compliances typical of TCM devices, thermal effects better explain the RS behaviour.

1.3.4 Conduction mechanisms

So far the discussion has focused on how and why the resistance of RRAM devices changes with an applied polarity. Even if very little has been said about which conduction mechanisms are involved, these are of crucial importance when designing new material systems and device architectures [46, 47]. Furthermore, analysis of conduction mechanisms provide another source of information, and is a valuable tool in identifying RS phenomena in RRAM devices. One of the main switching mechanisms is based on the formation and rupture of a CF that bridges the two electrodes in a MIM structure and thus switches devices from a HRS to a LRS. Whether this switching event is closely related to ECM or VCM behaviour, the most prominent feature in the filament model is the linear relationship between current and voltage in the LRS i.e. an ohmic characteristic once the CF are formed [47]. However, for the HRS there are several conduction mechanisms that have been suggested and experimentally confirmed: space-charge limited conduction (or SCLC), trap charging and discharging, Schottky emission and Pool-Frenkel emission [43, 46, 47]. It has been suggested that in RRAM devices the second most important conduction mechanism is SCLC, which is controlled by defects [43, 46, 47]. This is interesting as the first step required in RRAM operation is electroforming, which is expected to introduce some structural disorder or defects, at the interface or within the insulating layer, which results in the formation of charge trapping centres [92]. Hence, SCLC behaviour can be described by the trap-controlled space charge limited (SCL) conduction mechanism where a threshold voltage, V_{TFL}, marks the transition from a trap-unfilled to trap-filled SCL regimes. Upon decreasing the voltage, the current retains the higher value indicating that the trapped carriers are not released from the trap centres, which result in the SET process. With the application of the reverse bias voltage the trapped carriers are releases from the traps, which results in the RESET process [92].

The conduction mechanisms that take place in a device can be inferred by the typical I-V plot characteristics, and in the case of SCLC the plot consists of two different regions. For low voltages the I-V characteristics exhibit ohmic conduction (i.e. $I \propto V$), but once the voltage exceeds V_{TFL}, the I-V curve fits a Child's square law (where $I \propto V^2$). One characteristic that suggests the trap charging and discharging model for electrical conduction is the presence of a negative differential resistance (NDR), and the existence of a N-shaped characteristic in the I-V semilog plot (usually for positive bias) [47]. Poole-Frenkel emission is the combination of SCLC and trap charging and discharging and is due to the field-enhanced thermal excitation of trapped electrons in the conduction band. The current density can be written as:

$$J = Eexp\Big[\frac{-q(\phi_B - \sqrt{qE/\pi\epsilon_i}}{kT}\Big] \tag{1.8}$$

meaning the current is very dependent on the electric field. This behaviour can be inferred by the linear fitting of the plot log (I-V) $\propto$ V^2 [27, 43, 46, 47]. Analysis of the conduction mechanisms that were observed in zirconia based devices is presented in chapters 5 and 6.

1.3.5 Summary of RS mechanisms

In the previous sections a description of resistive switching mechanisms, that covers RS behaviour in a wide range of material systems, was presented. The vital property, common to all mechanisms, is the introduction of defects (cations or anions) that change the as-deposited properties of the switching layer. However, resistive switching depends on so many parameters that identifying which RS mechanism governs a device is not straightforward. Therefore, the switching mechanisms presented in the previous section are summarised in table 1.1.

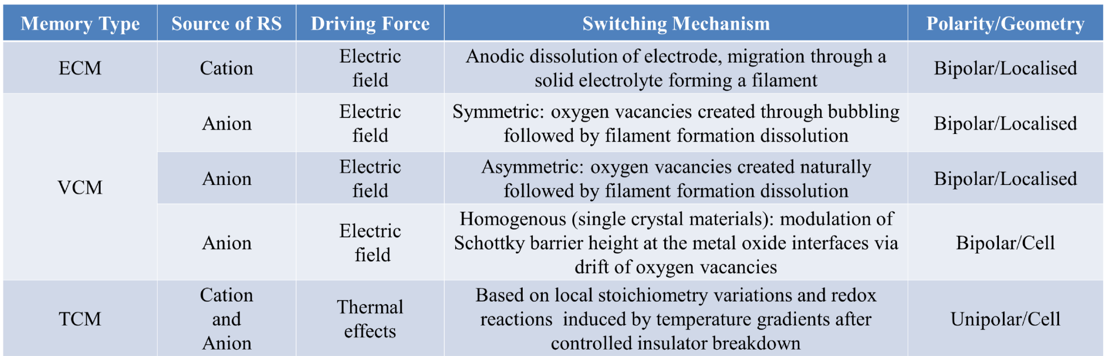

Memory Type	Source of RS	Driving Force	Switching Mechanism	Polarity/Geometry
ECM	Cation	Electric field	Anodic dissolution of electrode, migration through a solid electrolyte forming a filament	Bipolar/Localised
VCM	Anion	Electric field	Symmetric: oxygen vacancies created through bubbling followed by filament formation dissolution	Bipolar/Localised
	Anion	Electric field	Asymmetric: oxygen vacancies created naturally followed by filament formation dissolution	Bipolar/Localised
	Anion	Electric field	Homogenous (single crystal materials): modulation of Schottky barrier height at the metal oxide interfaces via drift of oxygen vacancies	Bipolar/Cell
TCM	Cation and Anion	Thermal effects	Based on local stoichiometry variations and redox reactions induced by temperature gradients after controlled insulator breakdown	Unipolar/Cell

Table 1.1: Summary of the three resistive switching mechanisms described in the previous section.

It should be remembered that there are many more resistive switching mechanisms described in the literature, as seen in figure 1.9. However, the ones presented in table 1.1 are enough to suggest something critical regarding RRAM devices: it is very unlikely that a particular device will be governed by only one of the effects described herein. Indeed, it will be shown in chapter 5 that, in real devices, multiple RS mechanisms can coexist.

1.4 Zirconium oxide as RS material

The polymorphic nature of zirconia is well known. Zirconium oxide has at least three crystallographic phases at atmospheric pressure: fluorite-type cubic from its melting point (≈ 2680 °C) down to ≈ 2370 °C, tetragonal from that temperature to ≈ 1150 °C, and monoclinic for lower temperatures [93–95]. Moreover, ZrO_2 exhibits two additional polymorphs, orthorhombic-I and -II, at lower temperatures with increasing pressure. Most of the applications of ZrO_2 are, strictly, structural dependent. Unfortunately, most stable (monoclinic) phase of ZrO_2 has limited practical applications due to its 3–5% volume expansion during cooling from the tetragonal phase [96]. Therefore, tetragonal and/or cubic phases of ZrO_2 have been paid much attention to fulfil the ever-increasing demand of high performance solar cells, sensors, novel catalyst, bioimaging and inert fuel matrix inside the core of nuclear reactors and accelerators [97]. In addition, ZrO_2 has been extensively investigated, mainly due to its high-k dielectric constant, useful for substituting SiO_2 as the gate oxide in MOSFETS [98]. It is well known that the dielectric constant (k) of ZrO_2 is a function of its crystalline structure. Average static values are 20, 37, and 47 [99], respectively, for monoclinic, cubic, and tetragonal phases [98–100].

Use of ZrO_2 for resistive switching (RS) device applications was first proposed by Lee et al. in 2005 [101]. Most of the reports on ZrO2- based devices were fabricated from sputter deposited ZrO2 thin films [99]. Different electrodes such as p^+-Si [101], n^+-Si [102–104], Al [57, 105, 106], Pt [107, 108], Ag [109], Au [110],Ti [106, 108, 111, 112],TiN [113], etc. have been studied for ZrO_2-based MIM RRAM devices [99]. As mentioned in the previous section, the polarities and resistive switching mechanisms change with architecture (symmetric/asymmetric), electrode material, deposition methods and with the intrinsic properties of the zirconia layer, namely, its electrical conductivity and structure. Unipolar RS was observed mostly on symmetric devices, which is in agreement with the literature. By contrast, bipolar response is usually achieved by employing two different materials for the electrodes. Although much work has been done for zirconia based devices, their switching mechanisms are still not perfectly described. Two examples were chosen from literature to illustrate such discrepancies.

One case in particular, where unipolar behaviour was observed for $Ti/ZrO_2/Pt$, was presented by Zhang et al. [112] in 2013. The zirconia films were prepared by sol-gel route, which require thermal treatments not only to evaporated the solvents, but also to improve the structural order of the films. XRD results presented by Zhang et al. were shown to be highly polycrystalline after thermal treatments up to 700 °C. This work is interesting due to the voltage polarity used. According to the authors, RS was performed with the Ti top electrode grounded, meaning the bias was applied to the Pt electrode. The application of a positive bias to the Pt electrode promotes the migration of oxygen vacancies, which are positively charged as seen in previous sections, towards the Ti electrode. Although this is in agreement with the RS mechanisms explained in detail in previous sections, it is contradictory when compared to the remaining published work on ZrO_2 based RRAM. One example of such contradiction is presented with the next example.

Wang et al. [111] also presented and described Ti/ZrO_2/Pt devices, but in contrast with the previous example, such devices are bipolar. The vast majority of work found in the literature, report on bipolar behaviour when Ti is used as an electrode material. As mentioned when describing VCM behaviour, metals with a low work function and high oxygen affinity, where Ti is the prime example, act like oxygen reservoirs capable of sourcing/sinking oxygen anions depending on the voltage bias [27, 80, 106, 108, 111, 112]. However, from all the studies presented where ZrO_2 is the active layer a few considerations should be made. The first comment has to do with the lack on characterisation of the metal/interface in zirconia based RRAM devices. Even though the majority of published work mentions oxygen vacancies and filament formation, the nature of the interfaces is mostly disregarded. Furthermore, it is suggested that the oxidation of the Ti electrode at the interface is responsible for filament formation and rupture, as the oxygen ions are sinked or sourced, respectively. The ohmic, quasi-ohmic and Schottky-like types of interfaces are not mentioned or linked to RS mechanisms. Additionally, the overwhelming majority of published work refers the application of positive voltages applied to the Ti electrode during SET transitions. In fact, RRAM devices presented in chapters 5 and 6 also exhibit such characteristic. This is contradictory to the models described in the literature where RS is said to be happening at the Ti/ZrO_2 interface, as oxygen vacancies should be electrostatically repelled from the positive metal electrode. Clearly, the atomistic mechanisms that explain and completely describe resistive switching in zirconia based devices are yet to be presented.

In the following chapters a detailed description of ZrO_2 based devices is going to be presented. First, insight is given on the preparation methods, and specially, on how preparation parameters influence material properties that will influence device response. Namely, how pulsed laser deposition (PLD) can be used to prepare thin films with adequate chemical and structural properties to be integrated in devices. This is of particular importance because controlling the oxygen vacancy density or the density of structural defects in thin films is a possibility with PLD. Second, chemical, morphological and structural characterisation on ZrO_2 RRAM devices is going to presented in detail. This was achieved by using transmission electron microscopy, and particularly electron energy loss spectroscopy (EELS). Electrical characterisation was also performed and focus will be given to the variability observed in Ti/ZrO_2/Pt devices. A model is proposed for zirconia based RRAM devices, explaining how different device architectures and material properties influence their behaviour. Finally, PCMO based devices fabricated by collaborators in Jülich, will be analysed by STEM EELS, and an electrochemical model that explains RS behaviour is proposed.

Bibliography

[1] Jagan Singh Meena, Simon Min Sze, Umesh Chand, and Tseung-Yuen Tseng. "Overview of emerging nonvolatile memory technologies." In: *Nanoscale research letters* 9.1 (Jan. 2014), p. 526. DOI: `10.1186/1556-276X-9-526`.

[2] Doo Seok Jeong et al. "Emerging memories: resistive switching mechanisms and current status". In: *Reports on Progress in Physics* 75 (2012). DOI: `10.1088/0034-4885/75/7/076502`.

[3] G W Burr, B N Kurdi, C H Lam, and Shenoy R S. "Overview of candidate device technologies for storage-class memory". In: *IBM Journal of Research and Development* 52.4 (2008), pp. 449–464.

[4] Shimeng Yu, Byoungil Lee, and H S Philip Wong. *Functional Metal Oxide Nanostructures*. Ed. by Junqiao Wu, Jinbo Cao, Wei-Qiang Han, Anderson Janotti, and Ho-Cheol Kim. Vol. 149. Springer Series in Materials Science. New York, NY: Springer New York, 2012, pp. 303–335. DOI: `10.1007/978-1-4419-9931-3`.

[5] Dmitri B Strukov, Gregory S Snider, Duncan R Stewart, and R Stanley Williams. "The missing memristor found." In: *Nature* 453.7191 (May 2008), pp. 80–3. DOI: `10.1038/nature06932`.

[6] http://researcher.watson.ibm.com/researcher/files/us-gwburr. 2013.

[7] RZ Mendioroz. "Resistive switching in Hafnium Oxide". In: *PhD Thesis* Universidad del País Vasco (2014).

[8] Ulrich Drepper. "What every programmer should know about memory". In: *Red Hat, Inc* 3 (2007), p. 114. DOI: `10.1.1.91.957`.

[9] M.H. Kryder. "After Hard Drives—What Comes Next?" In: *IEEE Transactions on Magnetics* 45.10 (Oct. 2009), pp. 3406–3413. DOI: `10.1109/TMAG.2009.2024163`.

[10] F. Masuoka, Masamichi Asano, Hiroshi Iwahashi, Teisuke Komuro, and Shinichi Tanaka. “A new flash E2PROM cell using triple polysilicon technology”. In: *1984 International Electron Devices Meeting* 30 (1984), pp. 464–467. DOI: `10.1109/IEDM.1984.190752`.

[11] F. Masuoka, M. Momodomi, Y. Iwata, and R. Shirota. “New ultra high density EPROM and flash EEPROM with NAND structure cell”. In: *1987 International Electron Devices Meeting* 33 (1987), pp. 552–555. DOI: `10.1109/IEDM.1987.191485`.

[12] D. Kahng and S M Sze. “A Floating Gate and Its Application to Memory Devices”. In: *Bell System Technical Journal* 46.6 (1967), pp. 1288–1295. DOI: `10.1002/j.1538-7305.1967.tb01738.x`.

[13] Chia-hong Jan. “10 years of transistor innovations in System-on-Chip (SoC) era”. In: *2014 12th IEEE International Conference on Solid-State and Integrated Circuit Technology (ICSICT)*. 2014, pp. 1–4. DOI: `10.1109/ICSICT.2014.7021244`.

[14] R. Meservey and P.M. Tedrow. “Spin-polarized electron tunneling”. In: *Physics Reports* 238.4 (Mar. 1994), pp. 173–243. DOI: `10.1016/0370-1573(94)90105-8`.

[15] C Hui-yu, F Yong-jia, and S Chang. “Giant Magnetic Tunneling Effect in 81NiFe/Al2O3/Fe Junction”. In: *Chinese physics letters* 139 (1997), pp. 94–97.

[16] By Jian-gang Zhu. “Magnetoresistive Random Access Memory: The Path to Competitiveness and Scalability”. In: *Proceedings of the IEEE* 96.11 (Nov. 2008), pp. 1786–1798. DOI: `10.1109/JPROC.2008.2004313`.

[17] P.K. Naji, M. Durlam, S. Tehrani, J. Calder, and M.F. DeHerrera. “A 256 kb 3.0 V 1T1MTJ nonvolatile magnetoresistive RAM”. In: *2001 IEEE International Solid-State Circuits Conference. Digest of Technical Papers. ISSCC (Cat. No.01CH37177)* (2001), pp. 2000–2001. DOI: `10.1109/ISSCC.2001.912570`.

[18] S. Tehrani et al. “Recent developments in magnetic tunnel junction MRAM”. In: *IEEE Transactions on Magnetics* 36.5 (2000), pp. 2752–2757. DOI: `10.1109/20.908581`.

[19] http://www.everspin.com/.

[20] http://www.businesswire.com/.

[21] T Eshita, T Tamura, and Y Arimoto. *Advances in Non-Volatile Memory and Storage Technology*. Elsevier, 2014, pp. 434–454. DOI: `10.1533/9780857098092.3.434`.

[22] By H Philip Wong et al. "Phase Change Memory". In: *Proceedings of the IEEE* 98.12 (2010), pp. 2201–2227.

[23] M Boniardi et al. "Optimization metrics for Phase Change Memory (PCM) cell architectures". In: *2014 IEEE International Electron Devices Meeting.* c. 2014, pp. 29.1.1–29.1.4. DOI: `10.1109/IEDM.2014.7047131`.

[24] Min Zhu et al. "Uniform Ti-doped Sb2Te3 materials for high-speed phase change memory applications". In: *Applied Physics Letters* 104.5 (2014), pp. 1–6. DOI: `10.1063/1.4863430`.

[25] Yi Li et al. "Activity-dependent synaptic plasticity of a chalcogenide electronic synapse for neuromorphic systems." In: *Scientific reports* 4 (Jan. 2014), p. 4906. DOI: `10.1038/srep04906`.

[26] Rainer Waser and Masakazu Aono. "Nanoionics-based resistive switching memories." In: *Nature materials* 6.11 (Nov. 2007), pp. 833–40. DOI: `10.1038/nmat2023`.

[27] Rainer Waser, Regina Dittmann, Georgi Staikov, and Kristof Szot. "Redox-Based Resistive Switching Memories - Nanoionic Mechanisms, Prospects, and Challenges". In: *Advanced Materials* 21.25-26 (July 2009), pp. 2632–2663. DOI: `10.1002/adma.200900375`.

[28] Stephan Menzel et al. "Origin of the Ultra-nonlinear Switching Kinetics in Oxide-Based Resistive Switches". In: *Advanced Functional Materials* 21.23 (Dec. 2011), pp. 4487–4492. DOI: `10.1002/adfm.201101117`.

[29] Leon Chua. "Memristor - The Missing Circuit Element". In: *IEEE Transactions on Circuit Theory* c.5 (1971).

[30] F. Nardi, S. Balatti, S. Larentis, and D. Ielmini. "Complementary switching in metal oxides: Toward diode-less crossbar RRAMs". In: *2011 International Electron Devices Meeting* (Dec. 2011), pp. 31.1.1–31.1.4. DOI: `10.1109/IEDM.2011.6131647`.

[31] http://news.panasonic.com.

[32] http://www.crossbar-inc.com.

[33] Livio Baldi, Roberto Bez, and Gurtej Sandhu. "Emerging memories". In: *Solid-State Electronics* 102 (Dec. 2014), pp. 2–11. DOI: `10.1016/j.sse.2014.06.009`.

[34] Ruth Muenstermann, Tobias Menke, Regina Dittmann, and Rainer Waser. “Coexistence of filamentary and homogeneous resistive switching in Fe-doped SrTiO3 thin-film memristive devices.” In: *Advanced materials (Deerfield Beach, Fla.)* 22.43 (Nov. 2010), pp. 4819–22. DOI: `10.1002/adma.201001872`.

[35] Leon Chua and Sung Kang. “Memristive Devices and Systems”. In: *Proceedings of the IEEE* 64.2 (1976), pp. 209–223.

[36] R Tetzlaff. *Memristors and Memristive Systems*. Springer Science & Business Media, 2014, p. 5.

[37] Leon Chua. “Resistance switching memories are memristors”. In: *Applied Physics A: Materials Science & Processing* January (2011), pp. 765–783. DOI: `10.1007/s00339-011-6264-9`.

[38] Dmitri B Strukov and R Stanley Williams. “Four-dimensional address topology for circuits with stacked multilayer crossbar arrays.” In: *Proceedings of the National Academy of Sciences of the United States of America* 106.48 (2009), pp. 20155–20158. DOI: `10.1073/pnas.0906949106`.

[39] Wei He et al. “Enabling an Integrated Rate-temporal Learning Scheme on Memristor.” In: *Scientific reports* 4 (Jan. 2014), p. 4755. DOI: `10.1038/srep04755`.

[40] Ting Chang, Sung-Hyun Jo, and Wei Lu. “Short-term memory to long-term memory transition in a nanoscale memristor.” In: *ACS nano* 5.9 (Sept. 2011), pp. 7669–76. DOI: `10.1021/nn202983n`.

[41] J. Joshua Yang, Isao H. Inoue, Thomas Mikolajick, and Cheol Seong Hwang. “Metal oxide memories based on thermochemical and valence change mechanisms”. In: *MRS Bulletin* 37.02 (2012), pp. 131–137. DOI: `10.1557/mrs.2011.356`.

[42] Eike Linn, Roland Rosezin, Carsten Kügeler, and Rainer Waser. “Complementary resistive switches for passive nanocrossbar memories”. In: *Nature Materials* 9.5 (2010), pp. 403–406. DOI: `10.1038/nmat2748`.

[43] J Joshua Yang, Dmitri B Strukov, and Duncan R Stewart. “Memristive devices for computing.” In: *Nature nanotechnology* 8.1 (Jan. 2013), pp. 13–24. DOI: `10.1038/nnano.2012.240`.

[44] Herbert Schroeder et al. “Voltage-time dilemma of pure electronic mechanisms in resistive switching memory cells Voltage-time dilemma of pure electronic mechanisms in resistive switching memory cells”. In: *Journal of Applied Physics* 054517.2010 (2011). DOI: `10.1063/1.3319591`.

[45] Zengtao Liu, Chungho Lee, Venkat Narayanan, Gen Pei, and Edwin Chihchuan Kan. “Metal Nanocrystal Memories — Part I : Device Design and Fabrication”. In: *IEEE Transactions on Electron Devices* 49.9 (2002), pp. 1606–1613.

[46] Chih-Yang Lin, Sheng-Yi Wang, Dai-Ying Lee, and Tseung-Yuen Tseng. “Electrical Properties and Fatigue Behaviors of ZrO[sub 2] Resistive Switching Thin Films”. In: *Journal of The Electrochemical Society* 155.8 (2008), H615. DOI: `10.1149/1.2946430`.

[47] YingTao Li et al. “An overview of resistive random access memory devices”. In: *Chinese Science Bulletin* 56.28-29 (Sept. 2011), pp. 3072–3078. DOI: `10.1007/s11434-011-4671-0`.

[48] Takashi Fujii, Masashi Arita, Kouichi Hamada, Yasuo Takahashi, and Norihito Sakaguchi. “In-situ transmission electron microscopy of conductive filaments in NiO resistance random access memory and its analysis”. In: *Journal of Applied Physics* 113.8 (2013), p. 083701. DOI: `10.1063/1.4792732`.

[49] Guokun Ma, Xiaoli Tang, Zhiyong Zhong, Huaiwu Zhang, and Hua Su. “Effect of Ni3+ concentration on the resistive switching behaviors of NiO memory devices”. In: *Microelectronic Engineering* 108 (Aug. 2013), pp. 8–10. DOI: `10.1016/j.mee.2013.03.043`.

[50] Seung Wook Ryu, Young Bae Ahn, Hyeong Joon Kim, and Yoshio Nishi. “Ti-electrode effects of NiO based resistive switching memory with Ni insertion layer”. In: *Applied Physics Letters* 100.13 (2012), p. 133502. DOI: `10.1063/1.3697691`.

[51] Deok-Hwang Kwon et al. “Atomic structure of conducting nanofilaments in TiO2 resistive switching memory.” In: *Nature nanotechnology* 5.2 (Feb. 2010), pp. 148–53. DOI: `10.1038/nnano.2009.456`.

[52] K Szot et al. “TiO2–a prototypical memristive material.” In: *Nanotechnology* 22.25 (June 2011), p. 254001. DOI: `10.1088/0957-4484/22/25/254001`.

[53] Liang Zhao, Seong-Geon Park, Blanka Magyari-Köpe, and Yoshio Nishi. "First principles modeling of charged oxygen vacancy filaments in reduced TiO2–implications to the operation of non-volatile memory devices". In: *Mathematical and Computer Modelling* 58.1-2 (July 2013), pp. 275–281. DOI: `10.1016/j.mcm.2012.11.009`.

[54] Li Qingjiang et al. "Memory Impedance in TiO2 based Metal-Insulator-Metal Devices." In: *Scientific reports* 4 (Jan. 2014), p. 4522. DOI: `10.1038/srep04522`.

[55] a. Salaün et al. "Investigation of HfO2 and ZrO2 for Resistive Random Access Memory applications". In: *Thin Solid Films* 525 (Dec. 2012), pp. 20–27. DOI: `10.1016/j.tsf.2012.10.070`.

[56] Jonggi Kim et al. "Effect of thermal annealing on resistance switching characteristics of Pt/ZrO2/TiN stacks". In: *Materials Chemistry and Physics* 142.2-3 (Nov. 2013), pp. 608–613. DOI: `10.1016/j.matchemphys.2013.08.003`.

[57] X. Wu et al. "Reproducible unipolar resistance switching in stoichiometric ZrO[sub 2] films". In: *Applied Physics Letters* 90.18 (2007), p. 183507. DOI: `10.1063/1.2734900`.

[58] Dinglin Xu, Ying Xiong, Minghua Tang, and Baiwen Zeng. "Coexistence of the bipolar and unipolar resistive switching behaviors in vanadium doped ZnO films". In: *Journal of Alloys and Compounds* 584 (Jan. 2014), pp. 269–272. DOI: `10.1016/j.jallcom.2013.09.073`.

[59] Vadim Sh Yalishev, Shavkat U Yuldashev, Yeon Soo Kim, and Bae Ho Park. "The role of zinc vacancies in bipolar resistance switching of Ag/ZnO/Pt memory structures." In: *Nanotechnology* 23.37 (Sept. 2012), p. 375201. DOI: `10.1088/0957-4484/23/37/375201`.

[60] Santosh Murali et al. "Resistive switching in zinc–tin-oxide". In: *Solid-State Electronics* 79 (Jan. 2013), pp. 248–252. DOI: `10.1016/j.sse.2012.06.016`.

[61] F. Yang, M. Wei, and H. Deng. "Bipolar resistive switching characteristics in CuO/ZnO bilayer structure". In: *Journal of Applied Physics* 114.13 (2013), p. 134502. DOI: `10.1063/1.4821237`.

[62] R. Dong et al. "Reproducible hysteresis and resistive switching in metal-Cu[sub x]O-metal heterostructures". In: *Applied Physics Letters* 90.4 (2007), p. 042107. DOI: `10.1063/1.2436720`.

[63] Wen-Hsien Tzeng et al. “Resistive switching characteristics of multilayered (HfO2/Al2O3)n n=19 thin film”. In: *Thin Solid Films* 520.8 (Feb. 2012), pp. 3415–3418. DOI: `10.1016/j.tsf.2011.10.118`.

[64] Ye Zhang et al. “Study of conduction and switching mechanisms in Al/AlOx/WOx/W resistive switching memory for multilevel applications”. In: *Applied Physics Letters* 102.23 (2013), p. 233502. DOI: `10.1063/1.4810000`.

[65] Seisuke Nigo et al. “Conduction band caused by oxygen vacancies in aluminum oxide for resistance random access memory”. In: *Journal of Applied Physics* 112.3 (2012), p. 033711. DOI: `10.1063/1.4745048`.

[66] S Balatti, S Larentis, D C Gilmer, and D Ielmini. “Multiple memory states in resistive switching devices through controlled size and orientation of the conductive filament.” In: *Advanced materials (Deerfield Beach, Fla.)* 25.10 (Mar. 2013), pp. 1474–8. DOI: `10.1002/adma.201204097`.

[67] Haowei Zhang et al. “Gd-doping effect on performance of HfO[sub 2] based resistive switching memory devices using implantation approach”. In: *Applied Physics Letters* 98.4 (2011), p. 042105. DOI: `10.1063/1.3543837`.

[68] B Gao et al. “Oxide-Based RRAM : Uniformity Improvement Using A New Material-Oriented Methodology”. In: *2009 Symposium on VLSI Technology Digest of Technical Papers* (2009), pp. 30–31.

[69] V. Y.-Q. Zhuo et al. “Band alignment between Ta2O5 and metals for resistive random access memory electrodes engineering”. In: *Applied Physics Letters* 102.6 (2013), p. 062106. DOI: `10.1063/1.4792274`.

[70] Qingqing Ke et al. “Oxygen-vacancy-mediated negative differential resistance in La and Mg co-substituted BiFeO3 thin film”. In: *Journal of Applied Physics* 124102.110 (2011). DOI: `10.1063/1.3668119`.

[71] S. Li, H. Z. Zeng, S. Y. Zhang, and X. H. Wei. “Bipolar resistive switching behavior with high ON/OFF ratio of Co:BaTiO3 films by acceptor doping”. In: *Applied Physics Letters* 102.15 (2013). DOI: `http://dx.doi.org/10.1063/1.4802209`.

[72] Jong Yun Kim, Hu Young Jeong, Jeong Won Kim, Tae Hyun Yoon, and Sung-Yool Choi. “Critical role of top interface layer on the bipolar resistive switching of Al/PEDOT:PSS/Al memory device”. In: *Current Applied Physics* 11.2, Supplement (2011). International Symposium on Next Generation Terabit Memory Technology

CAP/ 2010 {ISNGTMT} Supplement, e35–e39. DOI: `http://dx.doi.org/10.1016/j.cap.2010.12.038`.

[73] Frank Verbakel et al. "Reproducible resistive switching in nonvolatile organic memories". In: *Applied Physics Letters* 91.19 (2007). DOI: `http://dx.doi.org/10.1063/1.2806275`.

[74] Qi Liu et al. "Real-time observation on dynamic growth/dissolution of conductive filaments in oxide-electrolyte-based ReRAM." In: *Advanced materials (Deerfield Beach, Fla.)* 24.14 (Apr. 2012), pp. 1844–9. DOI: `10.1002/adma.201104104`.

[75] Xiao-Jian Zhu, Jie Shang, and Run-Wei Li. "Resistive switching effects in oxide sandwiched structures". In: *Frontiers of Materials Science* 6.3 (July 2012), pp. 183–206. DOI: `10.1007/s11706-012-0170-8`.

[76] H.-S. Philip Wong et al. "Metal–Oxide RRAM". In: *Proceedings of the IEEE* 100.6 (June 2012), pp. 1951–1970. DOI: `10.1109/JPROC.2012.2190369`.

[77] Yuchao Yang et al. "Observation of conducting filament growth in nanoscale resistive memories." In: *Nature communications* 3 (Jan. 2012), p. 732. DOI: `10.1038/ncomms1737`.

[78] Rainer Waser. "Electrochemical and thermochemical memories". In: *Technical Digest - International Electron Devices Meeting, IEDM* (2008), pp. 2–5. DOI: `10.1109/IEDM.2008.4796675`.

[79] W. R. Hiatt and T. W. Hickmott. "BISTABLE SWITCHING IN NIOBIUM OXIDE DIODES". In: *Applied Physics Letters* 6.6 (1965), pp. 106–108. DOI: `http://dx.doi.org/10.1063/1.1754187`.

[80] J Joshua Yang et al. "The mechanism of electroforming of metal oxide memristive switches." In: *Nanotechnology* 20.21 (2009), p. 215201. DOI: `10.1088/0957-4484/21/33/339803`.

[81] Akihito Sawa. "Resistive switching in Rapid advances in information technology rely on high-speed and". In: *Materials Today* 11.6 (2008), pp. 28–36.

[82] Isao H. Inoue and Akihito Sawa. "Resistive Switchings in Transition-Metal Oxides". In: *Functional Metal Oxides*. Wiley-VCH Verlag GmbH & Co. KGaA, 2013, pp. 443–463. DOI: `10.1002/9783527654864.ch16`.

[83] T. Fujii et al. "Hysteretic current–voltage characteristics and resistance switching at an epitaxial oxide Schottky junction SrRuO3 SrTi0.99Nb0.01O3". In: *Applied Physics Letters* 86.1 (2005), p. 012107. DOI: `10.1063/1.1845598`.

[84] Jinho Park, Deok-hwang Kwon, Hongwoo Park, C U Jung, and M Kim. "Role of oxygen vacancies in resistive switching in Pt/Nb-doped SrTiO3". In: *Applied Physics Letters* 105.18 (2014), p. 183103. DOI: `10.1063/1.4901053`.

[85] W Jiang et al. "Mobility of oxygen vacancy in SrTiO3 and its implications for oxygen-migration-based resistance switching". In: *Journal of Applied Physics* 110.3 (2011), p. 034509. DOI: `10.1063/1.3622623`.

[86] Ilia Valov. "Redox-Based Resistive Switching Memories (ReRAMs): Electrochemical Systems at the Atomic Scale". In: *ChemElectroChem* (Dec. 2013), n/a–n/a. DOI: `10.1002/celc.201300165`.

[87] Rainer Waser. "Microelectronic Engineering Resistive non-volatile memory devices (Invited Paper)". In: *Microelectronic Engineering* 86.7-9 (2009), pp. 1925–1928. DOI: `10.1016/j.mee.2009.03.132`.

[88] D. C. Kim et al. "Electrical observations of filamentary conductions for the resistive memory switching in NiO films". In: *Applied Physics Letters* 88.20 (2006), pp. 2–4. DOI: `10.1063/1.2204649`.

[89] I.G. Baek et al. "Highly scalable nonvolatile resistive memory using simple binary oxide driven by asymmetric unipolar voltage pulses". In: *IEDM Technical Digest. IEEE International Electron Devices Meeting, 2004.* (2004), pp. 587–590. DOI: `10.1109/IEDM.2004.1419228`.

[90] J. Y. Son and Y.-H. Shin. "Direct observation of conducting filaments on resistive switching of NiO thin films". In: *Applied Physics Letters* 92.22 (2008), p. 222106. DOI: `10.1063/1.2931087`.

[91] Doo Seok Jeong, Herbert Schroeder, and Rainer Waser. "Coexistence of Bipolar and Unipolar Resistive Switching Behaviors in a Pt-TiO[sub 2]-Pt Stack". In: *Electrochemical and Solid-State Letters* 10.8 (2007), G51. DOI: `10.1149/1.2742989`.

[92] H. F. Tian et al. "Resistance switching effect in LaAlO3/Nb-doped SrTiO3 heterostructure". In: *Applied Physics A: Materials Science and Processing* 102.4 (2011), pp. 939–942. DOI: `10.1007/s00339-011-6276-5`.

[93] G. M. Wolten. “Diffusionless Phase Transformations in Zirconia and Hafnia”. In: *Journal of the American Ceramic Society* 46.9 (1963), pp. 418–422. DOI: `10.1111/j.1151-2916.1963.tb11768.x`.

[94] G. Teufer. “The crystal structure of tetragonal ZrO2”. In: *Acta Crystallographica* 15.11 (1962), pp. 1187–1187. DOI: `10.1107/S0365110X62003114`.

[95] J. D. McCullough and K. N. Trueblood. “The crystal structure of baddeleyite (monoclinic ZrO2)”. In: *Acta Crystallographica* 12.7 (1959), pp. 507–511. DOI: `10.1107/S0365110X59001530`.

[96] S. Shukla and S. Seal. “Mechanisms of room temperature metastable tetragonal phase stabilisation in zirconia”. In: *International Materials Reviews* 50.1 (2005), pp. 45–64. DOI: `10.1179/174328005X14267`.

[97] Vincenzo Fiorentini and Gianluca Gulleri. “Theoretical Evaluation of Zirconia and Hafnia as Gate Oxides for Si Microelectronics”. In: *Physical Review Letters* 89.26 (Dec. 2002), p. 266101. DOI: `10.1103/PhysRevLett.89.266101`.

[98] Yew Hoong Wong and Kuan Yew Cheong. “ZrO2 thin films on Si substrate”. In: *Journal of Materials Science: Materials in Electronics* 21.10 (June 2010), pp. 980–993. DOI: `10.1007/s10854-010-0144-5`.

[99] Debashis Panda and Tseung-Yuen Tseng. “Growth, dielectric properties, and memory device applications of ZrO2 thin films”. In: *Thin Solid Films* 531 (Mar. 2013), pp. 1–20. DOI: `10.1016/j.tsf.2013.01.004`.

[100] P.Y. Kuei, J.D. Chou, C.T. Huang, H.H. Ko, and S.C. Su. “Growth and characterization of zirconium oxide thin films on silicon substrate”. In: *Journal of Crystal Growth* 314.1 (2011), pp. 81–84. DOI: `10.1016/j.jcrysgro.2010.10.162`.

[101] Dongsoo Lee et al. “Resistance switching of the nonstoichiometric zirconium oxide for nonvolatile memory applications”. In: *IEEE Electron Device Letters* 26.10 (Oct. 2005), pp. 719–721. DOI: `10.1109/LED.2005.854397`.

[102] Weihua Guan, Shibing Long, Rui Jia, and Ming Liu. “Nonvolatile resistive switching memory utilizing gold nanocrystals embedded in zirconium oxide”. In: *Applied Physics Letters* 91.6 (2007), p. 062111. DOI: `10.1063/1.2760156`.

[103] Qi Liu et al. “Resistive switching memory effect of ZrO[sub 2] films with Zr[sup +] implanted”. In: *Applied Physics Letters* 92.1 (2008), p. 012117. DOI: `10.1063/1.2832660`.

[104] Weihua Guan et al. “Resistance Switching Characteristics of Zirconium Oxide Containing Gold Nanocrystals for Nonvolatile Memory Applications”. In: *Journal of Nanoscience and Nanotechnology* 9.2 (2009-02-01T00:00:00), pp. 723–726. DOI: `doi:10.1166/jnn.2009.C011`.

[105] Chun-Chieh Lin, Yi-Peng Chang, Huei-Bo Lin, and Chu-Hsuan Lin. “Effect of non-lattice oxygen on ZrO2-based resistive switching memory”. In: *Nanoscale Research Letters* 7.1 (2012), p. 187. DOI: `10.1186/1556-276X-7-187`.

[106] Chih Yang Lin, Chung Yi Wu, Chen Yu Wu, Chun Chieh Lin, and Tseung Yuen Tseng. “Memory effect of RF sputtered ZrO2 thin films”. In: *Thin Solid Films* 516.2-4 (2007), pp. 444–448. DOI: `10.1016/j.tsf.2007.07.140`.

[107] Myung Soo Lee, Sungho Choi, Chee-Hong An, and Hyoungsub Kim. “Resistive switching characteristics of solution-deposited Gd, Dy, and Ce-doped ZrO2 films”. In: *Applied Physics Letters* 100.14 (2012), p. 143504. DOI: `10.1063/1.3700728`.

[108] Chih-Yang Lin, Chung-Yi Wu, Chen-Yu Wu, Tseung-Yuen Tseng, and Chenming Hu. “Modified resistive switching behavior of ZrO[sub 2] memory films based on the interface layer formed by using Ti top electrode”. In: *Journal of Applied Physics* 102.2007 (2007), p. 094101. DOI: `10.1063/1.2802990`.

[109] Kyung-Hyun Choi et al. “Investigation on switching behavior of ZrO2 thin film for memory device applications”. In: *Materials Science in Semiconductor Processing* 16.5 (Oct. 2013), pp. 1285–1291. DOI: `10.1016/j.mssp.2012.12.019`.

[110] Yingtao Li et al. “Resistive switching properties of Au/ZrO2/Ag structure for low-voltage nonvolatile memory applications”. In: *IEEE Electron Device Letters* 31.2 (2010), pp. 117–119. DOI: `10.1109/LED.2009.2036276`.

[111] Sheng Yu Wang et al. “Improved resistive switching properties of Ti/ZrO2/Pt memory devices for RRAM application”. In: *Microelectronic Engineering* 88.7 (2011), pp. 1628–1632. DOI: `10.1016/j.mee.2010.11.058`.

[112] Guo Yong Zhang et al. “Unipolar resistive switching in ZrO2 thin films”. In: *Japanese Journal of Applied Physics* 52.4 PART 1 (2013). DOI: `10.7567/JJAP.52.041101`.

[113] B. Sun et al. “Highly uniform resistive switching characteristics of TiN/ZrO2/Pt memory devices”. In: *Journal of Applied Physics* 105.6 (2009), p. 061630. DOI: `10.1063/1.3055414`.

Chapter 2

Instrumentation

This chapter focuses on the description of experimental techniques used to fabricate and characterise RRAM devices. Pulsed laser deposition was used to prepare thin films of several materials and with a variety of properties. Such properties were investigated by means of atomic force microscopy, scanning and transmission electron microscopy on the majority of samples prepared. A probe station, composed of sourcemeters and micropositioning probes was used to investigate the electrical behaviour of RRAM devices. A focused ion beam system was used to prepare TEM specimens, as well as to electrically connect them, prior to in-situ characterisation.

2.1 Pulsed Laser Deposition System

2.1.1 Introduction

Thin films and surface science play a fundamental role in the high-tech industries of today. Research areas that have benefited from thin film development are numerous, with microelectronics clearly one of the best and most successful examples. The demand for smaller and smaller devices with higher speeds, especially in next generation integrated circuits, requires advanced materials and new processing techniques. In this regard, the physics and technology of thin films play an important role in achieving this goal. Faraday was amongst the first to deposit thin films for scientific purposes by exploding metal wires in a container held under vacuum [114]. Numerous ways to deposit thin films have been developed and perfected since his pioneering work. Nowadays the number and variety of systems available for the deposition of thin films is remarkable, and understanding which process is best suited to each material and application is a challenge.

One of the principal challenges in solid-state physics is the discovery and application of novel materials and their incorporation in solid-state devices [115]. Although pulsed laser deposition (PLD) had already been used in the '60s and '70s, it was only in the '80s that the technique became widespread, after the discovery of superconductivity in copper oxide based ceramics [115, 116]. These compounds required multiple elements with diverse evaporative properties that had to be delivered in the correct stoichiometry in order to realise a superconducting film. Simultaneously, the material was an oxide, requiring an oxidising ambient during growth. Pulsed laser deposition has several characteristics that made it remarkably competitive in the complex oxide thin-film research arena as compared to other film growth techniques. These include the ability to transfer stoichiometry, the creation of excited oxidising species, and a simplicity in the initial setup and in the investigation of arbitrary oxide compounds. One could rapidly investigate thin-film deposition of nearly any oxide compound regardless of the complexity of the crystal chemistry [117]. The growth of thin films via PLD differs considerably from that of other deposition methods because it has discrete deposition rates and creates ions with high kinetic energies in the hyperthermal energy interval (1-10^3 eV) [118]. Sputtering is one other technique that promotes growth using a beam of atoms with energies between 10 and 100 eV, but it suffers from the fact that it also sputters surfaces other than the intended target. Conventional thermal deposition techniques suffer from being unable to accommodate two or more chemical systems on the same substrate: the growth temperature needed for one can result in the thermal decomposition of the other [115]. The ability to deposit films using high kinetic energy species with PLD under nonthermal conditions may alleviate such difficulties [115, 118]. In PLD systems a UV laser is used to ablate a solid target inside a vacuum chamber and transfer the ablated material onto a substrate, as depicted in figure 2.1. The interaction of the laser with the solid will normally yield congruent transfer of material, i.e. material will be transferred from the target to the substrate without altering the stoichiometry. Interestingly, this is not always the case, as will be described in chapters 3 and 4. Still, it is this phenomenon that makes PLD such a versatile technique: material transfer is independent of material's fundamental properties, including target melting temperature and vapour pressure.

Figure 2.1 also shows another advantage of PLD over other deposition systems: the laser used to ablate materials, and hence, be responsible for thin film growth is outside the vacuum chamber. This is useful as additional vacuum chambers can be used, to grow thin films from different materials for instance, with the same laser source [119].

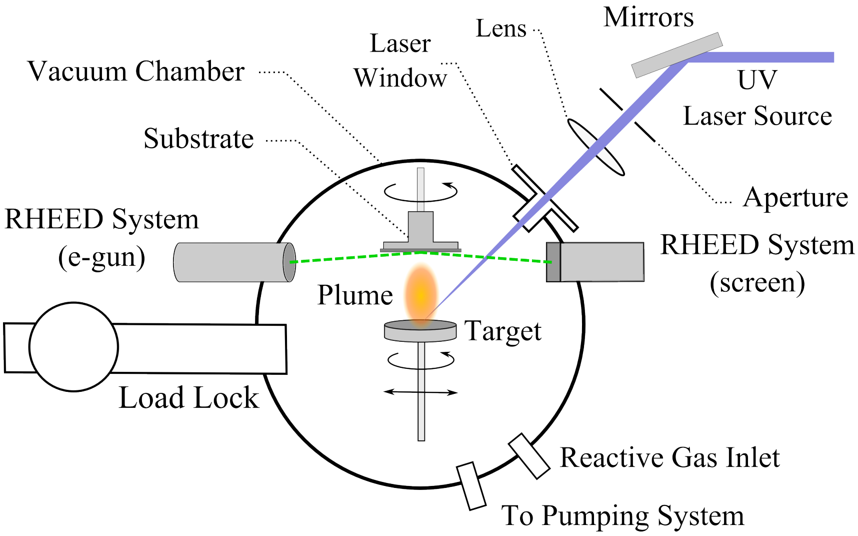

Figure 2.1: Schematic of the pulsed laser deposition system used in this work. A laser ablates a target that is rotating and rastering, transferring material to the substrate placed above the target. RHEED system is used to monitor the existence of epitaxial growth.

2.1.2 Neocera PLD System

The turn-key system used in this work is manufactured by Neocera and equipped with a pulsed 248 nm UV laser from Coherent. This laser has a pulse duration of 20 ns and a pulse frequency that can be adjusted from 1 to 20 Hz. The energy of the pulses (normally converted to fluence) can be adjusted, and where 1-2 J/cm^2 are typical values. It is important to mention that, due to space limitations, the laser optical system is set-up so that the beam is focused on the target surface, meaning the ablation is performed at maximum intensity. This is important as focusing introduces aberrations in the laser beam that changes the ablation process. Ideally, the aperture, seen in figure 2.1, should be focused as opposed to the laser beam itself. Also, it was observed that the lens clips the very edges of the laser beam profile, contributing to its non-uniformity. The system is equipped with a resistance heater capable of heating samples up to 1000 °C. The sample to target distance is 8 cm. The main chamber is evacuated with a Pfeiffer 355l/s turbomolecular pump backed by a scroll pump. The loadlock and RHEED chamber with one and two Pfeiffer 67 l/s turbo pumps, respectively, backed by membrane pumps. This system is capable of reaching base pressures of about 5 x 10^{-9} Torr a few days after being vented. A detailed vacuum diagram of the entire PLD system can be found in the Appendix. Table 2.1 summarises all the deposition conditions for the samples analysed and discussed in chapters 3−6.

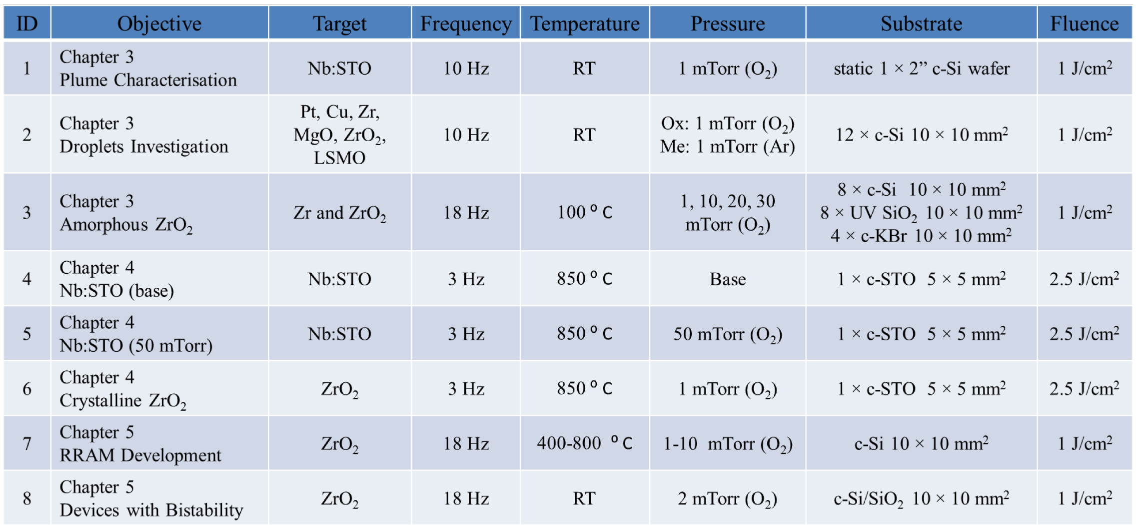

ID	Objective	Target	Frequency	Temperature	Pressure	Substrate	Fluence
1	Chapter 3 Plume Characterisation	Nb:STO	10 Hz	RT	1 mTorr (O_2)	static 1 × 2” c-Si wafer	1 J/cm^2
2	Chapter 3 Droplets Investigation	Pt, Cu, Zr, MgO, ZrO_2, LSMO	10 Hz	RT	Ox: 1 mTorr (O_2) Me: 1 mTorr (Ar)	12 × c-Si 10 × 10 mm^2	1 J/cm^2
3	Chapter 3 Amorphous ZrO_2	Zr and ZrO_2	18 Hz	100 ° C	1, 10, 20, 30 mTorr (O_2)	8 × c-Si 10 × 10 mm^2 8 × UV SiO_2 10 × 10 mm^2 4 × c-KBr 10 × 10 mm^2	1 J/cm^2
4	Chapter 4 Nb:STO (base)	Nb:STO	3 Hz	850 ° C	Base	1 × c-STO 5 × 5 mm^2	2.5 J/cm^2
5	Chapter 4 Nb:STO (50 mTorr)	Nb:STO	3 Hz	850 ° C	50 mTorr (O_2)	1 × c-STO 5 × 5 mm^2	2.5 J/cm^2
6	Chapter 4 Crystalline ZrO_2	ZrO_2	3 Hz	850 ° C	1 mTorr (O_2)	1 × c-STO 5 × 5 mm^2	2.5 J/cm^2
7	Chapter 5 RRAM Development	ZrO_2	18 Hz	400-800 ° C	1-10 mTorr (O_2)	c-Si 10 × 10 mm^2	1 J/cm^2
8	Chapter 5 Devices with Bistability	ZrO_2	18 Hz	RT	2 mTorr (O_2)	c-Si/SiO_2 10 × 10 mm^2	1 J/cm^2

Table 2.1: Deposition conditions regarding the samples analysed in this work.

2.1.3 Laser – Solid Interaction

When a pulse of UV laser light hits the target inside the vacuum chamber, the portion of light that is not reflected is absorbed. The absorbed electromagnetic energy at the target is immediately converted into electronic excitation in the form of plasmons, unbound electrons and, in the case of insulators, excitons [115]. The region of the target within the laser profile that absorbs the electromagnetic energy is termed the skin depth, δ, and is given by

$$\delta = \sqrt{\frac{2}{\omega\mu\sigma}}, \tag{2.1}$$

where ω is the angular frequency of the radiation, μ is the magnetic permeability of the target material, and, σ is its electrical conductivity [120]. After electrons absorb the incident energy, the target heats, melts and/or vaporises. The material just beneath the skin depth that heats to a specified depth, ι_T, is called the heat penetration depth and is given by

$$\iota_T = \sqrt{\frac{2k\tau_P}{\rho c}}, \tag{2.2}$$

where k is thermal conduction, τ_P is the pulse length of the laser, ρ is the material's mass density and c is the speed of light [115, 120, 121]. The vapour produced by the interaction between the laser and the target can then act in two distinctive ways. If the laser fluence is low, then the vapour will not be sufficiently dense to absorb the incident laser and will act like a transparent medium. If this is the case, the deposition rate at the sample will be marginal and there is no congruent material deposition. However, if the fluence is high enough, a dense vapour cloud (capable of absorbing the laser) is formed and will be excited until breakdown, forming a plasma, as illustrated in figure 2.2c [116, 121]. This plasma is responsible for the existence of surface processes far from thermal equilibrium that lead to congruent material deposition [115]. It should be noted that both processes (material vaporisation and plasma formation) will take place almost immediately, normally within the first 100 ps of the laser pulse [115]. As the plasma expands it cools, making it transparent to the incident laser radiation so that the target is vaporised again. It is the plasma expansion that effectively sputters the target surface and is responsible for thin film growth, as explained in detail in chapter 3, and is illustrated in figures 2.2d-f. The vapour will start absorbing the laser once it is dense enough and the plasma is renewed, i.e. a self-regulating plasma is established within the laser pulse duration [122].

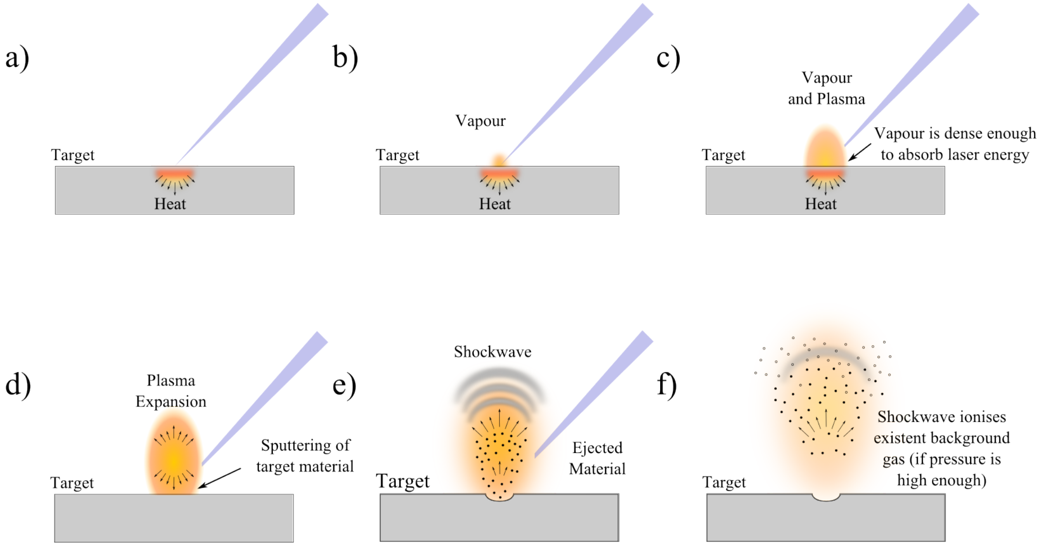

Figure 2.2: Illustration of the several steps of laser-solid interaction.

Several factors have a drastic influence on the coupling of the optical energy to the target surface such as: the laser pulse duration and energy profile, the photon absorption of the incident beam by the vaporised species and the target properties [116]. In other words, all target materials will have a different fluence threshold for congruent deposition. The way that the expanding plasma plume interacts with the background gas depends on the pressure of the gas and what elements are present in the deposition chamber, as seen in figure 2.3. Several models have been presented and there is experimental evidence for at least three modes of plume expansion in a background gas, depending on the pressure inside the chamber [122–124]. For low pressures, below 7 mTorr, the plume expands unimpeded, without interacting with the background gas. For pressures in the range of 7-150 mTorr, the plume couples with the background gas, resulting in shock-wave-like expansion dynamics at the plume front. In this regime, this shock-wave is capable of ionising part of the background gas through high energy collisions between gas molecules and ejected material. The ionised gas is highly reactive and will easily interact with the ejected target particles on their way to the substrate. However, for even higher pressures (above 150 mTorr) the stopping power of the background gas prevents interaction between the ejected material and the majority of the background gas [124].

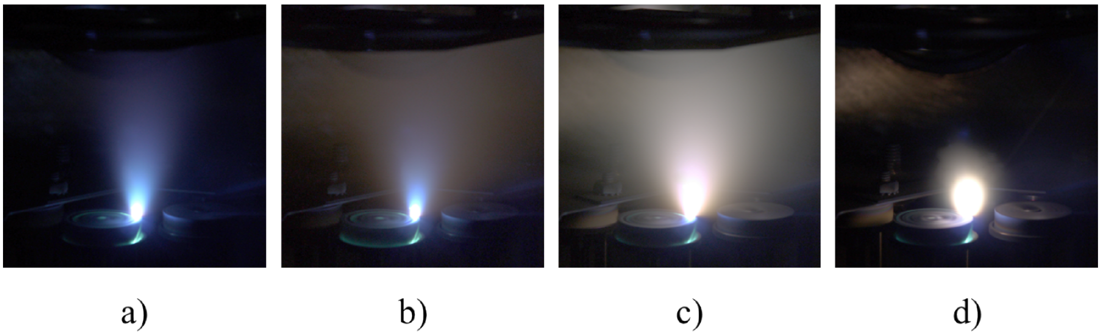

Figure 2.3: Example of laser ablation at different oxygen background pressures. a) base pressure (10^{-9} Torr), b) 5 mTorr, c) 40 mTorr and d) 200 mTorr. For a sense of scale, targets are 1 inch in diameter.

Figure 2.3 illustrates the three plume expansion modes described hereby for a ZrO_2 target in an $O_2(g)$ environment. In figures 2.3a and 2.3b there is hardly any interaction with the background gas. In figure 2.3c, the ejected species are clearly reacting with the background gas, but still reaching the substrate. This can be inferred by the loss of directionality but also by the colour of the plume, which is different and hence suggest some ionisation of the background gas. This contrasts with figure 2.3d where the very high pressure inhibits any significant plasma expansion and film growth is marginal. Films grown at such high pressures no longer benefit from high kinetic energy species, and are mostly the product of condensation of target vapour i.e. congruent deposition does not happen.

2.1.4 Reflective High Energy Electron Diffraction

Reflection high-energy electron diffraction (RHEED) is an essential tool for in-situ assessment of the deposition process [125, 126]. It exploits diffraction of electrons by surface atoms providing information about the surface crystallography and roughness. A generic RHEED setup is illustrated in figure 2.4.

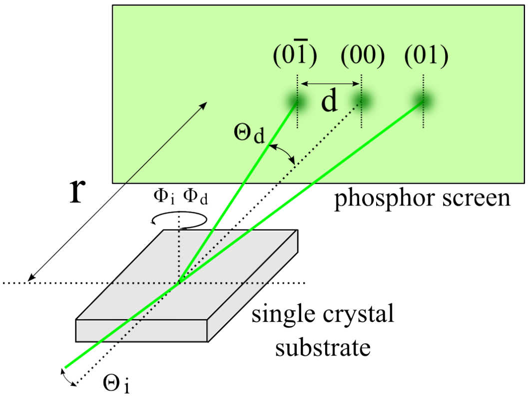

Figure 2.4: Example of RHEED setup geometry in use in the pulsed laser deposition chamber. Θ_i, (Θ_d), Φ_i and (Φ_d) are the incident and azimuthal angles of the incident (and diffracted) beam. Adapted from [125].

An electron beam (e-beam) strikes the sample surface at a grazing angle θ_i, with an energy typically of 20 t0 30 kV. The corresponding amplitude of the wavevector, $\vec{k_0}$, for these high-energy electrons can be estimated using equation 2.3 [125]:

$$E = \sqrt{\frac{\hbar^2 |\vec{k_0}|}{m^*}}, \tag{2.3}$$

where m^* is the effective mass of the electron. The angle of incidence is typically set to a few degrees ($0.1° - 5°$). At these grazing angles the penetration depth of the incident electrons is only a few atomic layers, which makes RHEED an extremely surface sensitive diffraction technique. The coherence length [127], which is the maximum distance between reflected electrons that are able to interfere, is determined by the beam convergence and the energy spread of the electrons, and is typically of the order of hundreds of nanometres. The scattered electrons are collected on a phosphorus screen to form a diffraction pattern characteristic for the crystal structure and morphology of the surface.

The diffraction pattern of the scattered electrons can be understood by the construction of the Ewald sphere. The intersection of the Ewald sphere leads to narrow streaks when a non-divergent monochromatic beam is used. Energy spread in the incident beam, detector resolution, non-elastic scattering and angular divergence of the beam cause the streaks to spread in the direction of the rods [128]. Reflection high-energy electron diffraction spots are produced when the momentum of the incident beam and that of the diffracted beam differ by a reciprocal lattice vector $\vec{G}$ [125], as given by:

$$\vec{k_S} - \vec{k_0} = \vec{G}. \tag{2.4}$$

where $\vec{k_S}$ and $\vec{k_0}$ are the wave vectors of the diffracted and incident beams. The main reason why RHEED is used during thin film growth in several deposition techniques is the observation of intensity oscillations of the specular intensity during deposition [129]. In a simplified way, the intensity oscillations can be linked to a layer-by-layer growth mechanism, as illustrated in figure 2.5. Material deposited on an initially flat surface leads to roughening and a decrease in RHEED intensity, whereas upon completion of a crystal layer the surface becomes smoother again, accompanied by a rise in RHEED intensity, i.e. periodic island nucleation, growth and coalescence.

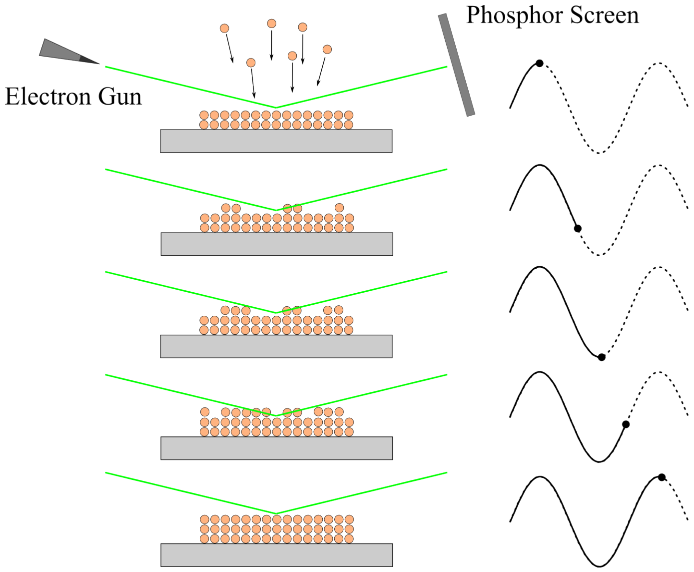

Figure 2.5: Schematic of layer by layer growth giving rise to RHEED oscillations.

Electrons are easily scattered out of the specular beam by step edges on the crystal surface since (1) the layer thickness is much larger than the wavelength of the electrons and (2) electrons have a high diffuse scattering cross-section. As a result, periodic intensity variations are expected during 2D growth, which can be used to determine the growth rate [125]. Accordingly, RHEED can be used as a perfect thickness monitor, since the oscillation period corresponds to the deposition of one unit cell, as illustrated by figure 2.5. RHEED oscillations were achieved for the epitaxial deposition of Nb:STO crystalline thin films. As such, the analysis and discussion of RHEED results is presented in chapter 4.

2.2 Atomic Force Microscope

The atomic force microscope is one of the family of scanning probe microscopes (SPM) that is widely used to image and measure properties of materials, chemicals and biological surfaces. There are two main forms of SPM: the Scanning Tunneling Microscope (STM) and Atomic Force Microscope (AFM). STM was invented by Gerd Binnig and Heinrich Rohrer [130], in the early eighties, for which they received the Nobel Prize in 1986. It operates by recording a position-dependant tunnelling current between a surface and an atomically sharp tip. However, a limitation of STM is that it can only image material surfaces that are electrically conductive. Atomic Force Microscope (AFM) was invented by Binnig and Quate in 1986 to overcome the limitations of STM [131].

2.2.1 Working Principle

The AFM consists of a cantilever with a sharp tip, also termed probe, that is scanned over the surface of the sample under analysis. When the tip and a surface are in close proximity, atomic forces between the tip and the surface lead to a deflection of the cantilever-tip assembly. The atomic force between a sample and tip are measured using a laser and a detector to monitor the cantilever motion. A three-dimensional image can finally be constructed by recording the cantilever motion in the vertical direction, z axis, as a function of sample's horizontal position [132]. With scanning, the tip is rastered on the surface of the sample, moving vertically to maintain feedback with the contour of the surface features. The basic operation procedure of a typical AFM is shown in figure 2.6.

Tthe laser beam is deflected from the cantilever, providing a difference in light intensities between the several regions of a photodetector segmented into quadrants. Feedback from the photodiode difference signal, through software control from the computer, enables the tip to maintain either a constant force or constant height above the sample [132–134]. In an AFM the probe is very sharp, typically less than 50 nm in diameter and the areas scanned by the probe are normally less than 100 μm. In practice, the heights of surface

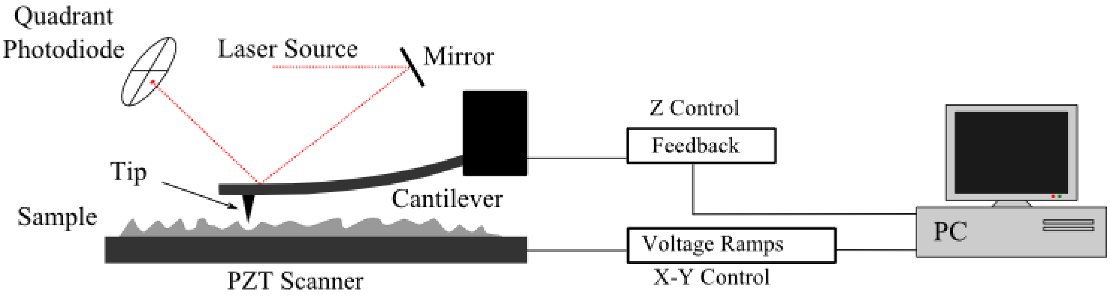

Figure 2.6: Schematic of an atomic force microscope including feedback control mechanisms.

features scanned with an AFM are less than 20 μm. Scan times can range from a fraction of a second to many 10's of minutes depending on the size of the scan and the height of the topographic features on a surface. Typically, the magnification of an AFM may be between 100 X and 100,000,000 X in the horizontal and vertical axis, respectively [135]. A AFM can be operated in three different modes: (1) non-contact mode, (2) contact mode, and (3) tapping mode. The interaction forces between the tip and sample in all of the three modes can be distinctly identified on a force-displacement curve as shown in figure 2.7.

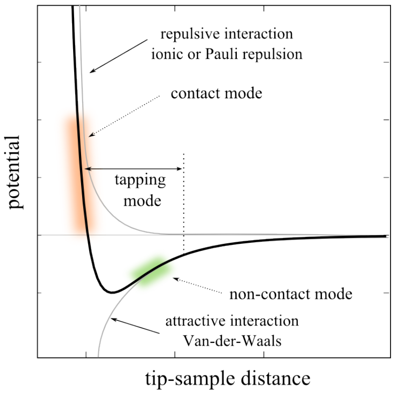

Figure 2.7: Interatomic force variation versus distance between AFM tip and sample, indicating where the main modes operate.

When the interatomic distance is quite large, weak attractive forces are generated between the tip and the sample. As the atoms are gradually brought closer to each other, the attractive forces increase until the atoms become so close that the electron clouds begin to repel each other electrostatically. This repulsive force between the atoms progressively weakens the attractive forces as the interatomic distance decreases. The interaction force becomes zero when the distance between the atoms reaches a couple of angstroms and becomes fully repulsive when the atoms are in contact, as seen in figure 2.7.

Non-Contact mode, NC-AFM

In non-contact mode, the cantilever tip “floats” about 50 to 150 Å above the sample surface to detect the attractive Van der Waals forces acting between the tip and the sample, and topographic images are constructed by scanning the tip above the surface. Since the attractive forces from the sample are substantially weaker than the forces used by contact mode, the tip must be given a small oscillation so that these small forces can be detected by measuring the change in amplitude, phase, or frequency of the oscillating cantilever [133]. In many cases, a contaminant layer is substantially thicker than the range of the van der Waals force gradient, and therefore, attempts to image the true surface with NC-AFM fail as the oscillating probe becomes trapped in the contaminant layer or “floats” beyond the effective range of the forces it attempts to measure. This is a major drawback of the NC-AFM imaging technique, which significantly degrades the resolution of the generated topographical images [133].

Contact mode, C-AFM

When in contact mode, also known as “repulsive” mode, the tip is in close contact with the sample as it scans the surface. In this case, the interaction forces between the tip and the sample are mainly repulsive in nature. A examination of the tip-surface interaction curve in figure 2.7, plotted for varying interatomic distances, reveals that the slope of the curve in the contact regime is very steep. This is because, at such close interatomic distances, the electron clouds in the atoms repel each other electrostatically. As a result, the repulsive van der Waals force dominates any other attractive force that may tend to act [133].

Tapping mode, T-AFM

The technique of tapping mode AFM (T-AFM) is a key advance in AFM technology, and in fact, all AFM measurements presented in this thesis were acquired in tapping mode. This technique allows high resolution imaging of soft samples that are difficult to examine using the contact AFM technique, like for instance, biological samples or processes that happen in solid-liquid interfaces [133, 136]. It overcomes problems such as friction and adhesion that are usually associated with conventional AFM imaging systems. Furthermore, tapping mode AFM has additional advantages over conventional contact mode operation such as greatly reduced lateral force and low sensitivity to cantilever thermal drift [137]. In tapping mode, the cantilever is oscillated at or near its natural resonant frequency using a

PZT actuator [137]. The vibrating tip is now moved close to the sample until it begins to lightly tap the surface. During scanning, the probe tip alternately touches the surface and lifts off at frequencies of about 50 to 500 kHz. Owing to the energy losses caused due to intermittent contacting of the tip with the surface, the amplitude of vibration changes according to the surface topography of the sample. During tapping mode operation, the oscillation amplitude is kept constant through a feedback loop. When the tip passes over a bump in the surface, its vibration amplitude decreases due to less vibrating space. On the other hand, when it passes over a depression, its vibration amplitude increases, as it approaches its free air amplitude [133]. This change in oscillation amplitude is detected by the optical system and fed back to the controller, which compares the measured value with the set reference value and generates an error signal [136]. This signal is used to actuate the PZT element that adjusts the tip-sample separation to maintain constant amplitude and thereby constant force on the sample. The phase difference between the driving signal of the piezo oscillating the cantilever in the T-AFM and the resulting motion of the tip is exploited in order to access additional information about the tip sample interaction. Indeed phase AFM was used in chapter 4 while mapping surface terminations in single crystal $SrTiO_3$ (STO) substrates. All AFM work presented in chapters 3 and 4 was performed on a Digital Instruments Dimension 3100.

2.3 Transmission Electron Microscope

The invention of the electron microscope is attributed to the pioneering work of Louis de Broglie, Von M. Knoll and Ernest Ruska. It was Louis de Broglie, in 1924, who first introduced the concept of wave-particle duality and that electrons could be considered as waves with short wavelengths [138]. The de Broglie wavelength (given in equation 2.5), relates the wavelength, λ, of any particle to its momentum, p, by Planck's constant, h.

$$\lambda = \frac{h}{p}. \tag{2.5}$$

The introduction of this concept paved the way for future research with the application of electrons, most notably with two independent electron diffraction experiments carried out by Davisson and Germer and Thomson and Reid in 1927 [139–141]. In fact, both groups confirmed experimentally the de Broglie wavelength relation. A few years later, in 1932, Von M. Knoll and Ernest Ruska published their pioneering paper describing the invention of the transmission electron microscope (TEM) [142, 143]. The invention was greatly motivated by the idea that an electron microscope would fundamentally have better spatial resolution than that of visible light microscopes (VLM). The optical resolution limit for any magnification system had already been described by Abbe in 1873, given by equation 2.6.

$$\rho = \frac{\lambda}{2NA}, \tag{2.6}$$

where λ is the wavelength employed, and NA is the numerical aperture; Abbe was also amongst the first to actually use the term “numerical aperture”, which is normally used to describe the acceptance cone of an objective. Abbe’s resolution limit implies that a good VLM has a maximum achievable resolution of about 300 nm, which was surpassed by Driest and Müller, in 1935, only 10 years after the first EM was built, using a TEM [144]. In 1945 (only 20 years after de Broglie’s breakthrough), the resolution of TEM was already at the order of 1.0 nm, which represents an astonishing increase in spatial resolution of more than 2 orders of magnitude over VLM, as seen in figure 2.8. Since then, the progress has been continuous, and nowadays there are many analytical and structural techniques that benefit from the particular characteristics of electron microscopy.

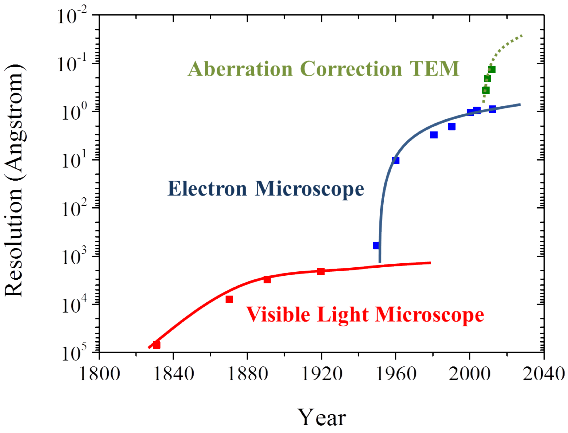

Figure 2.8: Evolution of the limits of resolution depending on the technology used. Adapted from [145]

Microscopes that use lenses, will normally have the following components: an illumination source, illumination lenses, a specimen, a magnifying and a detection system. For all the microscopy work presented in this thesis, a *FEI Tecnai 20* (T20) and a *JEOL ARM 200F*

(ARM) were used, so, the description of the several components in a TEM will be limited to those two instruments. These microscopes (and some additional hardware usually found in TEMs) will be described in detail in the following sections in an effort to elucidate the importance of electron microscopy in current research of solid state physics.

2.3.1 Electron Sources

The first component that directly influences electron microscopy in general, is the electron source or gun [139]. There are three main types of electron guns normally found in modern TEMs: the thermionic type (used in the T20), the cold field emission type (used in the ARM) and the Schottky field emission type. The physical processes that govern electron emission is different in each type and this directly affects the characteristics of the electron beam.

Thermionic emission takes place when a tungsten filament or LaB_6 crystal is heated until electrons have enough energy to overcome the work function, Φ. The physics that govern thermionic emission are given by Richardson's law [139] that relates the current density, J, to the tip temperature, T, given by equation 2.7

$$J = AT^2 e^{-\frac{\Phi}{kT}}, \tag{2.7}$$

where k is the Boltzmann's constant and A is Richardson's constant. LaB_6 crystals are preferred over a W filament due essentially to its low Φ. A schematic of a thermionic electron gun is represented in figure 2.9a.

A high voltage is applied between the anode and the cathode to extract and accelerate the electrons from the heated LaB_6 crystal. A cylindrical electrode, known as Wehnelt, is held at a different potential, typically 2-3 kV, which focuses the electrons in a crossover between the electrodes.

In a cold FEG the electron emission takes place due to the high electric field applied to a sharp tip (usually made of Tungsten) and another electrode placed nearby. The sharp tip locally enhances the electric field (given by equation 2.8), to the point at which electrons tunnel out [139].

$$E = \frac{V}{r}, \tag{2.8}$$

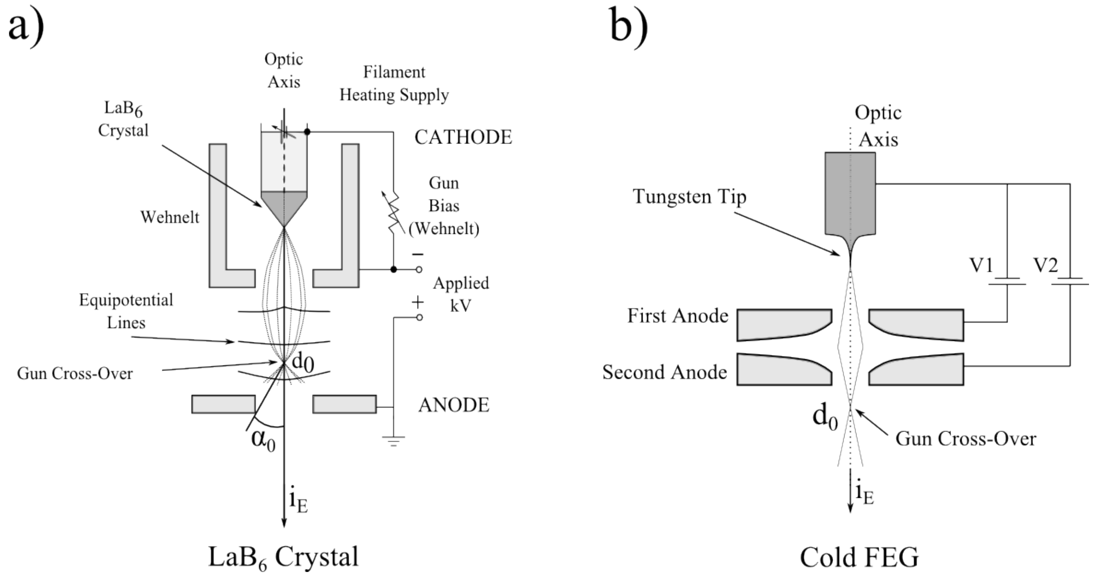

Figure 2.9: Schematic diagrams of a) a thermionic and b) a cold FEG electron emission guns. Adapted from [139]

where E, represents the electric field, V, the applied voltage and r, the tip radius. The current density, J, of field emission can be estimated from the Fowler-Nordheim formula, given in equation 2.9 [146]

$$J = aE^2 e^{\frac{-B\Phi^{3/2}}{E}}, \tag{2.9}$$

where E is the electric field, Φ is the work function, B is a constant and α is a material constant. A schematic of a cold FEG is represented in figure 2.9b. The first anode will extract the electrons from the sharp tip, and the second electrode accelerates the electrons to the selected potential. The use of two anodes enables the fine tuning of the gun cross-over which in turn reduces the beam diameter, d_0, increasing spatial resolution. Another benefit of the cold FEG is the lower energy spread (ΔE) of the emitted electrons when compared to thermionic sources, especially useful for analytical work. In fact, the main characteristics of such an electron beam are its diameter, d_0, emission current, i_e, and the convergence semi-angle, α_0 [139]. Brightness is the current density per unit solid angle of the source, and is one of the most important parameter in an electron beam. The brightness of any electron beam in a TEM is give by the following expression (equation 2.10)

$$\beta = \frac{i_C}{\pi(\frac{d_0}{2})^2\pi(\alpha_0)^2} = \frac{4i_c}{(\pi d_0\alpha_0)^2}, \tag{2.10}$$

where $i_C/\pi(d_0/2)^2$ is the current per unit area, and $i_C/\pi(\alpha_0)^2$ is the solid angle of the source [139]. As mentioned before, the momentum of the electrons in the beam will determine their wavelength. Practically, the wavelength of the electrons in a beam will be governed by the potential at which the microscope is operating. From the de Broglie relation (equation 2.5 on page 52) the wavelength (in angstroms) can be expressed as in equation 2.11

$$\lambda(\text{Å}) = \frac{h}{p} = \frac{h}{\sqrt{2m_0eV}} \approx \frac{12.27}{\sqrt{V}}. \tag{2.11}$$

Because TEM generally use electrons which move faster than half the speed of light, relativistic effects must be taken into consideration, and so the corrected wavelength is

$$\lambda(\text{Å}) = \frac{h}{p} = \frac{h}{\sqrt{2m_0eV}(1+\frac{eV}{2m_0c^2})} \approx \frac{12.27}{\sqrt{V(1+0.978\times10^{-6})}}. \tag{2.12}$$

For the majority of the TEM work presented in this thesis, both the ARM and the T20 were operating at 200 kV, which translates to an electron wavelength of 2.51 pm. Table 2.2 summarised the differences in the main characteristics of electron beams produced by different sources.

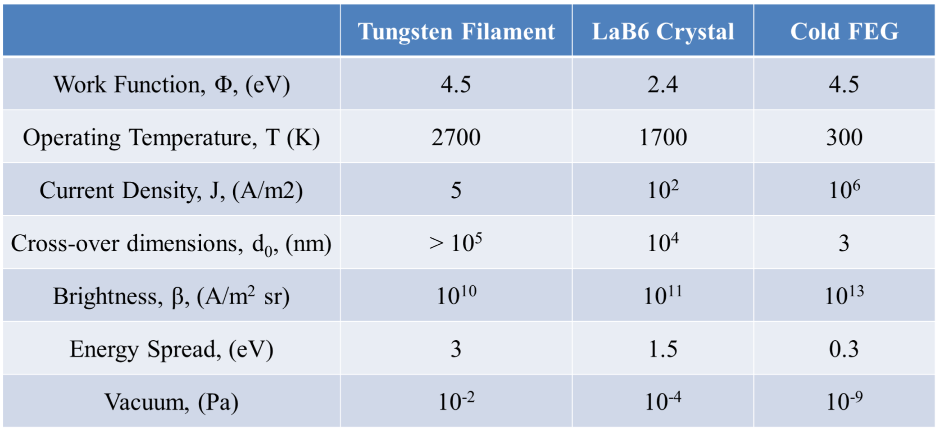

	Tungsten Filament	LaB6 Crystal	Cold FEG
Work Function, Φ, (eV)	4.5	2.4	4.5
Operating Temperature, T (K)	2700	1700	300
Current Density, J, (A/m2)	5	10^2	10^6
Cross-over dimensions, d_0, (nm)	$> 10^5$	10^4	3
Brightness, β, (A/m^2 sr)	10^{10}	10^{11}	10^{13}
Energy Spread, (eV)	3	1.5	0.3
Vacuum, (Pa)	10^{-2}	10^{-4}	10^{-9}

Table 2.2: Comparison between different types of electrons sources in different gun assemblies. Adapted from [139].

From table 2.2 it is clear how the CFEG gathers the best set of electron beam characteristics of all sources: (1) it has the smallest gun cross-over diameter, which translates into having the smallest true source object in a TEM, improving spatial resolution; (2) it has the highest brightness, meaning images and spectroscopic work can be achieved with shorter exposure times, avoiding sample drift and other temporal instabilities; (3) the smallest energy spread will result in spectroscopy with much better resolution, enabling for instance, the study of fine structure in EELS, as will be explained in the next section and reported in chapter 6.

2.3.2 Electron Optics

Because all electron sources generally produce a diverging beam of electrons, this must be focused onto the specimen. Focusing any electron beam not only increases the intensity but also makes the probe smaller (*probe* is used when mentioning a focused electron beam). Electrons are charged particles, hence influenced by electromagnetic fields. As such, lenses in an TEM utilise magnetic and electrostatic fields to direct the electron beams as desired. This is achieved because when an electron with charge, q, enters a magnetic field with strength, $\vec{B}$, and an electric field, $\vec{E}$, it experiences a force termed the Lorentz force, $\vec{F}$. The Lorentz force can be calculated using

$$\vec{F} = -e(\vec{E} + v \times \vec{B}), \tag{2.13}$$

$$F = evBsin(\theta) = evB = \frac{mv^2}{r}. \tag{2.14}$$

This results in electrons having helical trajectories when passing through a magnetic lens. The radius, r, of the helical path can be inferred by equation 2.14, and θ is indicated in figure 2.10b . Figure 2.10, illustrates a generic electron lens as well as the electron helical path caused by the Lorentz force.

In figure 2.10a the copper coils generate the magnetic field, that acts on the electrons through the soft iron polepieces. The further away from the optic axis, the bigger the magnitude of the Lorentz force acting on the electrons. Figure 2.10b illustrates the helical electron trajectories as well as the relative position of the vectors that govern the Lorentz force. Note that only electrons with some velocity component v_1 will experience the Lorentz force i.e. electrons that only have a velocity component v_2 will not experience any change

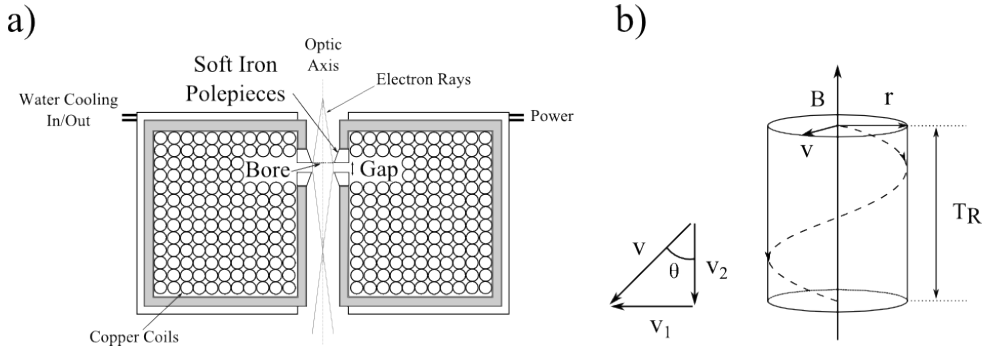

Figure 2.10: Schematic of generic electron lens. Adapted from [139]

in their trajectories. Electron optics suffer from aberrations just like their visible light counterparts. Aberrations in electron lenses are, however, much worse and it is one of the main factors limiting the resolution of TEMs. Correcting for magnetic lens aberrations is possible thanks to the pioneering work of Scherzer in 1936 [145, 147, 148]. Aberrations can be either spherical or chromatic, as illustrated in figure 2.11.

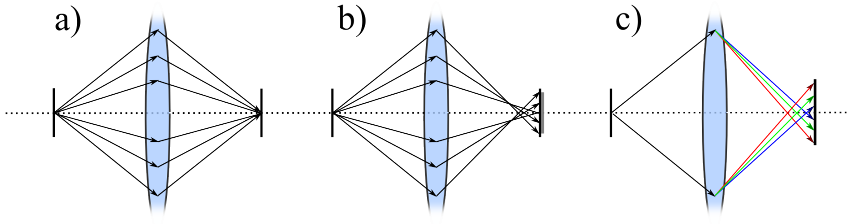

Figure 2.11: Example of lens aberrations a) "perfect" lens (no aberrations), b) spherical and b) chromatic. Adapted from [145]

Spherical aberrations arise from a radial dependence of the effective focal length: the further off axis an electron moves through the lens, the more strongly it is focused, as depicted in figure 2.11b [139]. Chromatic aberrations are caused by lenses focusing with different strengths as function of the electron energies, as illustrated in figure 2.11c. This happens because the electron beam in TEMs is not completely monochromatic i.e. the beam has an energy spread, even with cold FEGs and monochromators. Aberrations in magnetic lenses cannot be eliminated by careful and controlled lens design and production, as happens with visible light lenses [149, 150]. In practical terms, the aberrations in magnetic lenses are so large that without any method for correction, the achieved resolution is some 50-100 times larger than the wavelength of the electrons in the TEM beam [148, 151]. The aberrations introduced by magnetic lenses in a TEM took almost 40 years to correct. Advances in this particular field have only become possible due to the advancement in electronic technology and in computer-assisted alignment of correctors consisting of many elements [149]. The best way to correct for aberrations is to accurately and extensively measure which types of aberrations are involved. Such aberrations have to be corrected by the user through quadrupole, sextupole and octopole magnetic lenses that effectively produce a “symmetric” effect, and hence cancel the aberrations in the original (pre corrector) electron beam. Quadrupole-octopole correctors are necessary to compensate for both the chromatic and the spherical aberrations, while a hexapole corrector suffices to eliminate the spherical aberration which is the dominant resolution-limiting aberration at accelerating voltages larger than about 100 kV [150].

2.3.3 Electron-Matter Interactions

The interaction between fast electrons and matter gives rise to many useful electronic excitation processes, illustrated in figure 2.12. In transmission electron microscopy one makes use of the transmitted portion of the incident electron beam, whereas scanning electron microscopy (SEM), described in the next section, uses the backscattered (BSE) and secondary electron (SE) contributions. The majority of the signals analysed in a TEM are either the elastic or inelastic portion of the transmitted fast electron beam.

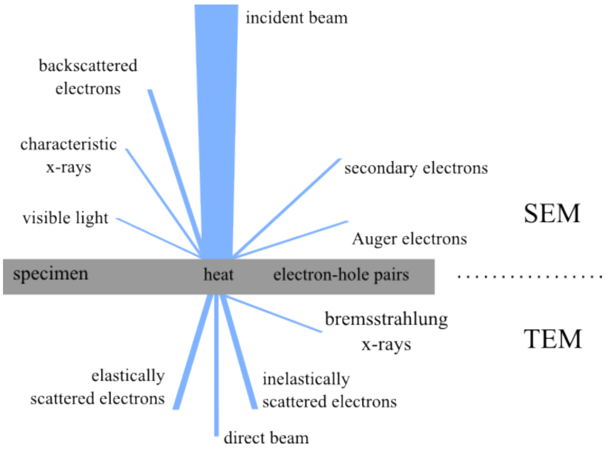

Figure 2.12: Schematic diagram showing interactions of an electron beam with matter (a thin TEM specimen).

Elastic scattering is caused by the interaction of incident electrons with the electrostatic field of atomic nuclei [152]. This mechanism will mostly contribute to the formation of diffraction patterns or images where the contrast arises from diffraction effects. In simplistic terms, we can say that elastic scattering reveals information about the structure of the sample [153]. Inelastic scattering is caused by the electrostatic interaction between the incident and atomic electrons, and can take different forms [154]. For instance, in the case of insulators or semiconductors (like metal-oxides characterised herein) the excitation of electrons from the valence to the conduction band, as depicted in figure 2.13b, gives rise to a unique chemical fingerprint [154].

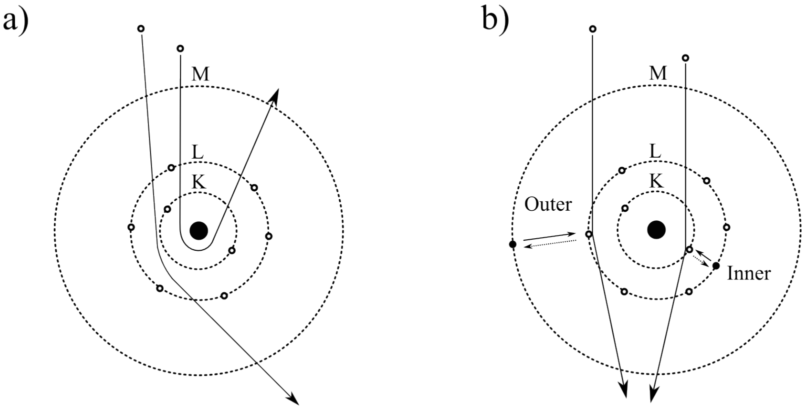

Figure 2.13: Particle view of electron scattering. a) Elastic scattering is caused by Coulomb attraction by the nucleus. b) Inelastic scattering results from Coulomb repulsion by inner or outer-shell electrons. Adapted from [152].

This unique fingerprint arises because all elements have characteristic energy levels (ionisation/excitation), which can be inferred from changes to the energy of incident electrons. Therefore, inelastically scattered electrons will mostly contribute to elemental or compositional analytical techniques, namely energy filtered imaging, EFTEM, or electron energy loss spectroscopy, EELS.

2.3.4 Magnetic Prism and Energy Loss Spectrometer

In order to measure the electron energy loss due to interaction with the specimen, a spectrometer is required. The key component in an electron spectrometer is the magnetic prism, responsible for dispersing electrons with different energies. This is usually achieved by applying a constant magnetic field perpendicular to the electron trajectory, as depicted in figure 2.14. Electrons that lose no energy will be bent 90°, whereas electrons that scattered inelastically will be dispersed as a function of their energy loss, similarly to what happens to visible light going through a prism. An isolated drift tube inside the magnetic prism is used to change the speed of all the electrons in the beam, with the application of a voltage. By changing the kinetic energy of the electrons travelling through the magnet it is possible to shift the energy-loss spectra, and therefore analyse different electronic transitions and energy loss regions.

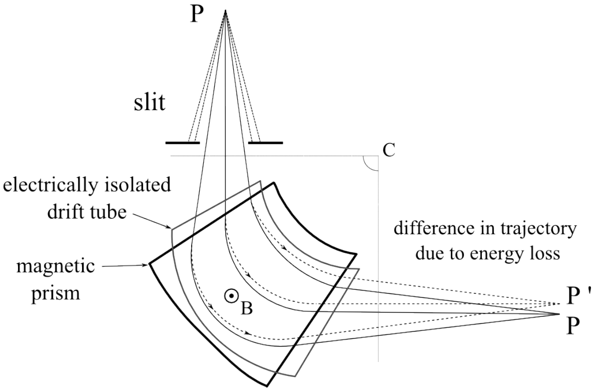

Figure 2.14: Magnetic prism that disperses electrons with different energies. Differences in the energy loss are attributed to specific elements or bonding states. Electrons that lost energy will be dispersed and focused on P' instead of P. Adapted from [154].

Because the prism also focuses the electrons (with imperfect magnetic lenses), it introduces second order aberrations [154], which is why the majority of the spectrometers are equipped with an aberration corrector. In addition, magnification of the dispersion is needed, in order to achieve 1 eV or less in energy resolution [152]. To avoid undesired rotation effects while magnifying, a quadrupole lens assembly is often used [154]. After the corrector, an energy loss spectrum can be recorded, which nowadays is usually done with a charge-coupled device, or CCD. A more detailed analysis is provided in the EELS section.

2.3.5 Image formation in TEM

Image formation in TEM follows two main modes: diffraction or imaging. These two primary modes, central to TEM operation, mean that the projection system is working in a complimentary way. This should not be confused with the two types of illumination on the specimen: broad "parallel" beam or focused "probe" [139]. Conventional TEM (CTEM) implies that the microscope has parallel illumination, whereas a focused probe often means the microscope is in scanning (STEM) mode. This results in two illumination and two projector main configurations, as illustrated in figure 2.15. The majority of the materials characterisation was done on the ARM. As such, the detailed description of the microscope column is limited to the JEOL ARM 200F (which is very similar to the T20 in CTEM mode). The lenses in the TEM can be grouped into illumination, imaging and magnification systems, as depicted in the inset of figure 2.15.

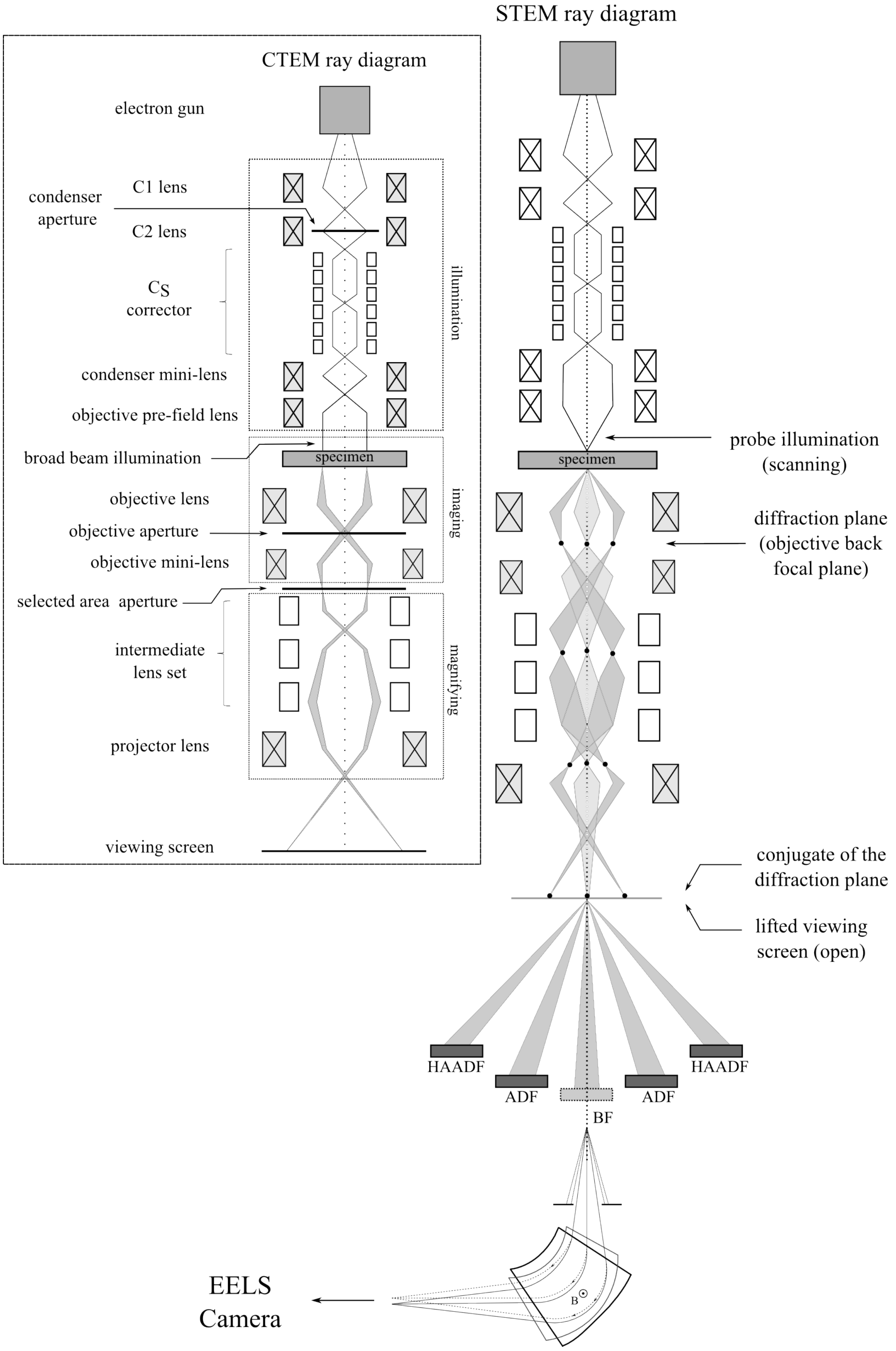

Figure 2.15: Schematic of the ray diagram of the ARM 200F in STEM mode, with inset of CTEM and main system components. Note that apertures are only indicated in CTEM mode (inset).

The first lens is usually the C1 lens, which provides a demagnified image of the electron gun. The demagnified image is the effective point object of the source, and its dimensions are given by the gun crossover diameter and convergence angle, as mentioned in page 55. The C2 lens is one of the most important lens in the whole microscope as it controls the convergence angle of the electron beam on the specimen. A practical implication is that a change in intensity of the C2 lens changes the diameter of the electron beam on the viewing screen. These two lenses (C1 and C2) make up the condenser lens assembly as they change the characteristics of the illumination source, namely the size and convergence angle of the beam incident on the specimen. Immediately after the C2 lens there is the condenser aperture. The aperture restrains the electron beam's convergence angle (α_0) increasing its coherency, at the expense of the brightness (see figure 2.9 in page 55). After the condenser lenses, the ARM is equipped with six aberration correcting multipole lenses. Following the condenser and aberration corrector multipole lenses, there is the objective lens assembly. The objective lens is critical in TEMs because it is in the middle of the objective lens that the specimen is located. It is the objective lenses that limit the overall achievable resolution of the entire microscope. In CTEM, it is also the first lens of the magnification system, which is formed by: objective (imaging), intermediate and projector lenses (magnifying), and the objective and selected area apertures, illustrated in figure 2.15. In STEM it is the scan size of the probe that determines the magnification, and not the imaging and the projector lenses [139]. Also, in STEM, the microscope is operated in diffraction mode, figure 2.15. Diffraction work in CTEM is also carried out with the imaging and projector assemblies in diffraction mode, but broad beam illumination is usually used.

CTEM bright and dark field

In CTEM the illumination system is providing broad beam illumination on the specimen. With this type of illumination it is possible to either image the sample or perform electron diffraction (see figure 2.15). To accomplish this, the intermediate lens strength is different when the back focal plane (BFP) or the image plane are in focus. The projection system will then project either the BFP or the image plane onto the viewing screen. In addition, it is possible to create an image of the specimen by selecting beam scattered through specific angular ranges, creating "bright field" or "dark field" images. Figure 2.16 illustrates how this can be achieved. In the first case, depicted in figure 2.16a, only the bright spot of the diffraction pattern is allowed through the objective aperture, resulting in a bright field image (assuming the image plane is focused by the intermediate lens).

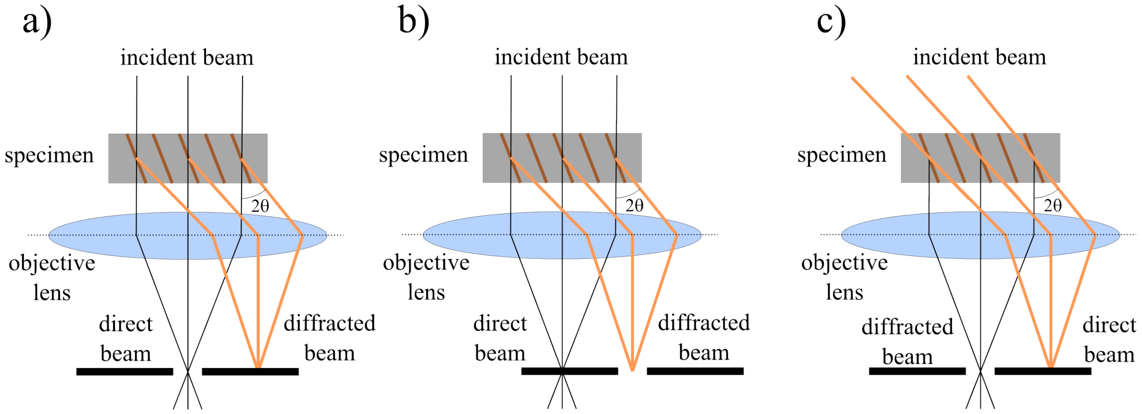

Figure 2.16: Illustration of aperture position and tilt of the incident electron beam to use the microscope in a) bright, b) dark and c) centred dark field. Adapted from [139].

If, on the other hand, we allow one of the diffraction spots through the aperture, a dark field image is obtained, as seen in figure 2.16b. This is interesting because it makes possible the imaging of crystals with a specific crystallographic orientation. A centred dark field image is obtained when the incident beam is tilted, which gives rise to a diffracted beam parallel to the optic axis, figure 2.16c. This technique is preferential mainly because it avoids the use of the outer regions of the objective magnetic lens, which is more prone to aberrations. Instead, the centre of the objective lens is used, which should originate a better quality image when compared to the previous case.

STEM annular dark field and HAADF

In STEM mode, the illumination system is configured in a way such that it produces a focused spot on the sample , forming a probe (as shown in figure 2.15). This probe is scanned over the specimen, and the transmitted electrons will be collected using annular detectors. The detector system surrounds the beam and is normally composed of three independent solid state detectors that have different collection angles (seen in the bottom part of figure 2.15). The projection system magnifies the BFP so that a diffraction pattern is obtained. In STEM we only use the central disc, which contains the non-scattered and inelastically scattered electrons, to image and to do analytical work. This is the reason why in STEM the source of contrast is mostly the atomic number of the elements that form the sample. The detector in the centre (aligned with the beam) is used for bright field images, the annular dark field is used to image the electrons scattered at lower angles, whereas the high angle annular dark field (HAADF) is used for higher scattering angles.

For STEM-EELS, however, the BF detector is removed to allow the beam to enter the spectrometer. This means that when acquiring EELS data, only the ADF and/or HAADF detectors are used.

2.3.6 Electron Energy Loss Spectroscopy (EELS)

Spectroscopy as a function of electron energy loss is one of the most important analytical/quantitative characterisation techniques in a TEM. Basically, there are two slightly different ways to make good use of the inelastically scattered electrons: electron energy loss spectroscopy, EELS, and energy filtered TEM, EFTEM. In EELS the inelastically scattered electrons are dispersed in energy into a spectrum, which can be interpreted, quantified and used to form images. Normally EELS spectra can be divided into two regions, low-loss and high-loss, at an energy of about 50 $\sim$ 100 eV. The reason for this division has to do with the enormous intensity difference between the two regions. In simple terms, the low-loss region contains electronic information about the more weakly bound conduction and valence band electrons. On the other hand, the high-loss region primarily contains elemental information about the more tightly bound, core-shell electrons, and about the bonding and atomic distribution [139]. It is important to mention that in EELS it is *preferred* that energy loss happens in a single scattering event. In other words, single scattering means that each electron that goes through the sample undergoes, at most, one scattering event. The reason for this simplification has to do with the complexity involved in interpreting *plural* (a few) and *multiple* (many) scattering events. In practical terms, the signal to background ratio diminishes with the number of scattering events, which should be avoided. Sample thickness and the accelerating voltage are the two parameters that mostly govern scattering, and this is the reason that, for STEM EELS, samples should as thin as possible, typically less than 75 nm. If the specimen is relatively thick, plural scattering increases the background intensity, complicating its fitting and extraction by reducing the signal to background ratio. This is more of a problem for moderate energy losses (up to a few hundred eV), where the background slope changes on the scale of the plasmon energy, whereas, at higher losses, the background slope changes more slowly and is little affected by plural scattering [155]. A typical low-loss EELS spectrum is represented in figure 2.17.

In terms of electrons detected, the biggest contribution arises from electrons that either scattered elastically, did not scatter at all, or that experienced energy losses that are below what can be resolved by the spectrometer. This results in a very intense peak, termed the

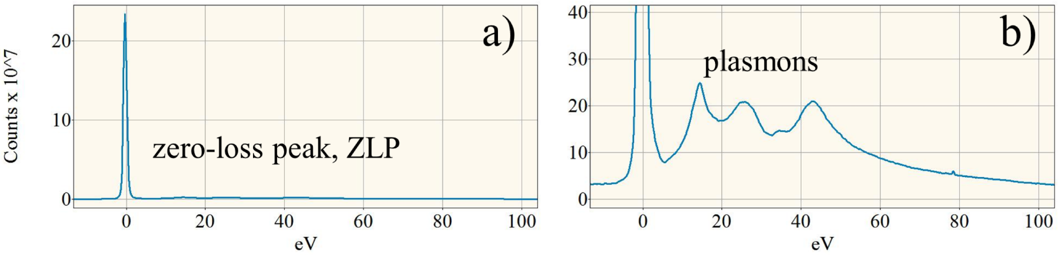

Figure 2.17: Example of low loss spectra obtained using the EELS spectrometer in the ARM. a) zero loss peak, ZLP, and b) plasmon region after the ZLP. The high loss region starts at approximately 50 eV energy loss.

zero loss peak, ZLP, illustrated in figure 2.17a. Immediately after the ZLP and with much lower intensities, there is the plasmon region, illustrated in figure 2.17b. A transmitted electron will produce (in its wake) an oscillation of the electron density with angular frequency given by

$$\omega_p = (n_e^2/\epsilon_0 m), \tag{2.15}$$

where n_e is the density of atomic electrons (with effective mass, m) that are electrostatically coupled within the solid [154]. The plasmon wake will produce a backwards force (in relation to the incident electrons) and cause electron energy loss [154] according to

$$E_p = (h/2\pi)\omega_p = (he^2/w\pi\epsilon_0)(n_e/m). \tag{2.16}$$

In other words, plasmons can provide insight on the dielectric response of the specimen to high-energy electrons [139]. Plasmonic losses are usually centred around E_p and are in the range of 3 - 30 eV for most materials. Even if the plasmonic signature is not element specific, stoichiometry and local composition can still be inferred by measuring the plasmon energy shifts and comparing them to reference spectra from samples with known composition. Also, transitions from oxygen s and p states to transition metals s, p and d states, provide valuable information regarding the electronic properties of the sample. A detailed discussion regarding low loss spectra is provided in chapter 6, while analysing PCMO based RRAM devices. For higher energy losses, the spectrum is composed of smaller features that spread from approximately 100 eV to above 2500 eV. These features represent ionisation losses, and happen when an inner-shell electron is excited to an outer-shell.

These ionisation losses are vital in EELS because such processes are characteristic of the atoms involved, providing direct information about their chemistry, oxidation state and possibly structure. The overall intensity of these features is much lower than the ZPL, which until very recently, represented a big challenge to record simultaneously. An example of a high loss (also termed *core loss*) is illustrated in figure 2.18, showing the zirconium, titanium and oxygen characteristic features.

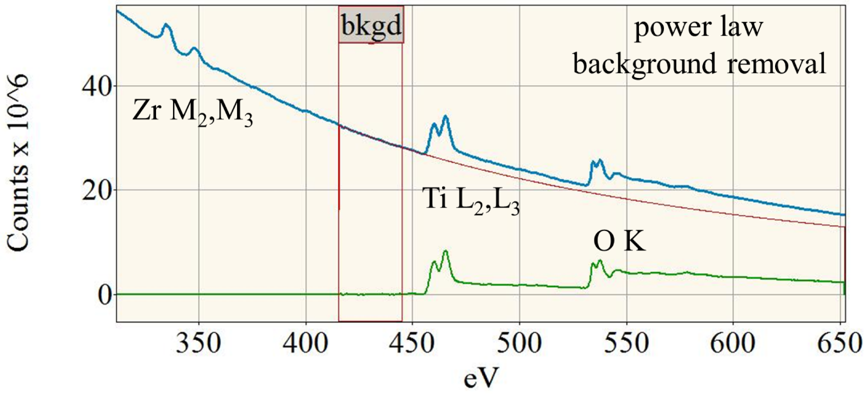

Figure 2.18: Example of an EELS high loss spectrum illustrating the zirconium, titanium and oxygen edges. Removal of the power-law background, showing the edges in detail.

These high energy loss features are caused by the excitation of inner electrons, which have known binding energies, hence making it possible identify and distinguish elements. In addition, quantification is possible by measuring and integrating the edge intensity above the background. Figure 2.18 illustrates the background subtraction for the titanium and oxygen edges. The background intensity and shape arises mostly from the plasmon contribution, as mentioned in the previous section. One advantage of high loss EELS is the possibility to determine in absolute terms, and without any standard sample, the stoichiometry of a given specimen.

In EFTEM a slit is used to filter electrons with a given energy, and an image is formed only with the contribution of those electrons. More specifically, a total of three images is acquired: two before, and a third after a certain edge. An energy filtered image is obtained by comparing the three images obtained i.e. the first two images are representative of the background, whereas the third is composed only of electrons that had the energy loss event (represented by the edge). EFTEM will give rise to images that show the spatial distribution of a particular element, but little can be known about an element's bonding states for instance. Such type of images are presented while characterising ZrO_2 based

RRAM devices in chapter 5. For all the characterisation presented in this work, EELS was performed on a Gatan Quantum 965 spectrometer.

2.4 Scanning Electron Microscope and Focused Ion Beam

A typical scanning electron microscope (SEM) has a similar electron optical configuration to the upper column of a TEM, but where images are formed using the BSE and SE electron contributions, as depicted in figure 2.12 on page 59. An electron beam, with a lower accelerating voltages, typically 5−10 kV, is scanned over the sample to generate BSE and SE signals. The SEM was used to image the PLD targets after ablation and to investigate the existence of droplets on the surface of thin films deposited by PLD. In this work, SEM analysis and FIB nanofabrication were performed on a dual beam FEI Nova NanoLab.

The focused ion beam (FIB) technique was mainly developed during the late '70s and the first commercial instruments were introduced in the early '90s [156]. Modern FIB systems are widely available in solid-state physics research and processing environments, as well as in failure analysis and chip-design centres. The technology enables localised milling and deposition of conductors and insulators with high precision, hence its success in device modification, mask repair, process control and failure analysis [156]. Additionally the FIB tool has been used for the preparation of transmission electron microscopy (TEM) specimens from a wide range of materials including semiconductors, metals, ceramics, polymers, biological materials, and tissues [157, 158].

The structure of the column is similar to that of a scanning electron microscope, the major difference being the use of a gallium ion (Ga^+) beam instead of an electron beam. A vacuum of about 1 x 10^{-4} Pa is maintained inside the column. The ion beam is generated from a liquid-metal ion source (LMIS) by the application of a strong electric field. This electric field causes the emission of positively charged ions from a liquid gallium cone, which is formed on the tip of a tungsten needle. A typical extraction voltage is 7000 V, and a typical extraction current, under normal operating conditions, is 2 μA [156].

When energetic ions hit the surface of a solid sample, the most important physical effects on the substrate are: sputtering of neutral and ionised substrate atoms (which enables substrate milling), secondary electron emission (which enables imaging), displacement of atoms in the specimen (causing beam induced damage) and heating. Chemical interactions include the breaking of chemical bonds, thereby dissociating molecules (which enables material deposition) [156]. Figure 2.19 illustrates the three main modes described so far.

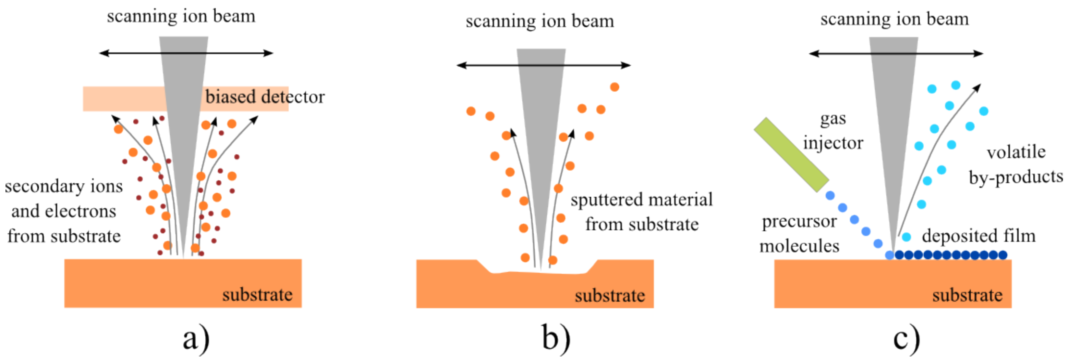

Figure 2.19: Schematic illustrating the working principle of the FIB when a) imaging b) milling and c) depositing. Adapted from [156].

As illustrated in figure 2.19a, during FIB imaging the finely focused ion beam is raster scanned over a substrate, and secondary particles (neutral atoms, ions and electrons) are generated. As they leave the sample, the electrons or ions are collected on a biased detector (a microchannel plate detector, MCP). The detector bias is positive or negative, respectively, for collecting secondary electrons or secondary ions. It should be mentioned that imaging with FIB inevitably induces some damage to the sample. Most of the Ga^+ ions that arrive at the sample surface enter the sample, and thus, ion implantation occurs. The depth of this implanted region is related to the ion energy and the angle of incidence [156].

The removal of sample material is achieved using a high ion current beam. The result is a physical sputtering of sample material, as illustrated schematically in figure 2.19b. By scanning the beam over the substrate, an arbitrary shape can be etched [156].

FIB enables the localised maskless deposition of both metal and insulator materials. The metals that can be deposited on commercially available machines are platinum (Pt) and tungsten (W). In the case of W, an organometallic precursor gas is $W(CO)_6$. The deposited insulator material is SiO_2, where 1, 3, 5, 7- tetramethylcyclotetrasiloxane (TMCTS) and oxygen, are typical precursors. The deposition process is illustrated in figure 2.19c; the precursor gases are sprayed on the surface by a fine needle (injector), where they adsorb. In a second step, the incident ion beam decomposes the adsorbed precursor gases. Then the volatile reaction products desorb from the surface and are removed through the vacuum system while the desired reaction products (W or SiO_2) remain fixed on the surface as a thin film[156].

2.4.1 Preparation of in-situ RRAM devices

Preparation of RRAM devices that consist on TEM specimens was attempted, with the objective of performing in-situ STEM EELS analysis during device operation. The first stage in such preparation is to mount a TEM lamella onto a TEM membrane. Two different experimental approaches were followed: the first relies on ex-situ manipulation of the lamella, with a thinned glass needle, when placing it over the SiN membrane window. The second approach, makes use of the FIB to place the lamella onto the membrane in-situ. Both approaches have advantages and disadvantages, as explained next.

Starting with the ex-situ manipulation approach, figure 2.20a is a SEM image illustrating four gold electrodes with a wire bonded to each one. The use of four electrodes is advantageous as up to three lamellae can be electrically connected in a single TEM membrane. Wire bonding was used to connect the gold pads to either a chip carrier or to the TEM rod.

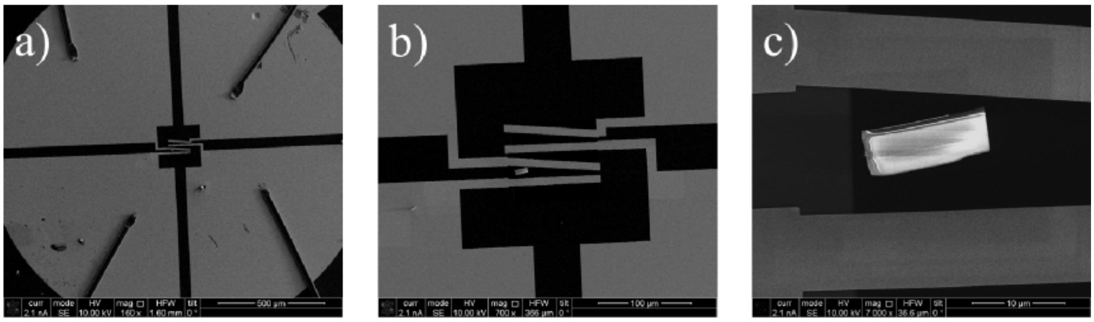

Figure 2.20: TEM specimen placed on a TEM membrane window prior to being electrically connected with the FIB. a) low magnification view, showing the wire bonding done on the gold pads b) detail of the gold pad extremities where the lamella will be bonded to, and c) higher magnification view of the TEM lamella prior to FIB bonding.

Figure 2.20b illustrates the gold electrodes patterned on the SiN window, and a lamella between the third and fourth electrode lines. Additionally, lamellae can be place between the first and second or between the second and third gold electrodes, for convenience. Figure 2.20c shows a lamella that has no been thinned to electron transparency and without being electrically connected to the gold electrodes. The advantage of this approach is linked to this last point: using the FIB to electrically connect the lamella to the gold electrode over the SiN window does not create a short-circuit because there is no underlying Si substrate under the window. On the other hand, the existence of the thin SiN window will surely influence the EELS measurements, by increasing the overall thickness of the sample and adding Si and N EELS edges to an already complicated EELS spectra. Another disadvantage of this experimental approach is the very challenging step while placing the lamellae on the correct place with the ex-situ manipulator. Not only does this make precise lamellae placement very challenging, but it also adds great uncertainty as several lamellae are "lost" or damaged in the transfer process.

In fact, a second approach was developed mainly to overcome this difficulty. However, the use of the FIB to precisely place the lamellae requires the TEM membranes to be cut in half, the reason for this being the internal geometry of the FIB itself. Figure 2.21a shows the cut membrane in cross section, illustrating where and how the lamella is placed in-situ using the FIB. The red dashed circle highlights the Pt deposition made with the FIB and responsible for keeping the lamellae in the correct place. The dashed lines highlight the thicker SiN film required so that the FIB Pt deposition process does not lead to short-circuits. The lamella and TEM membrane are seen in top view in figure 2.21b, where the device layers are also visible.

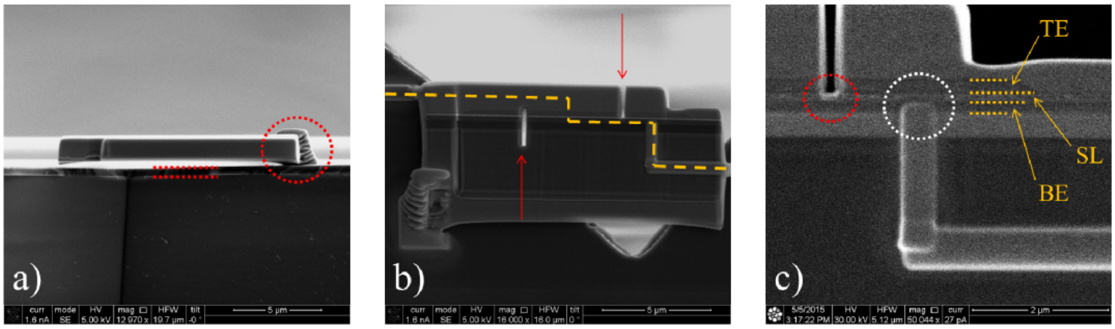

Figure 2.21: Alternative configuration: lamella is placed on a corner of a TEM membrane window, where EELS will not be influenced by the SiN. a) cross section view b) top view, highlighting the current path and c) higher magnification view of one of the FIB connections, illustrating how small the tolerances are. TE is top electrode, BE is bottom electrode and SL is the switching layer.

Note how the lamella is placed on the corner of the SiN window (removed while cutting the membrane), allowing for STEM EELS measurements to be performed without the influence of SiN. The two red arrows in figure 2.21b illustrate where two cuts were done to force the switching to occur in a specific region, indicating where the STEM EELS analysis should be performed. The current path is highlighted with the yellow dashed lines, from the top to the bottom electrode connections. A detailed view of the electrical connection to the bottom electrode and one of the cuts mentioned before, are seen in figure 2.21c. This figure is illustrative of how small the tolerances are when performing electrical connections to TEM lamella, and why the FIB is completely necessary. The red dashed circle illustrates one of the cuts, where the top electrode and active layer are interrupted, but not the bottom electrode. Analogously, the bottom electrode is electrically connected by FIB deposited Pt, but it is essential that the active layer and top contacts are not (white dashed circle).

2.5 Probe Station and In-Situ

A probe station was used to perform electrical characterisation of RRAM devices. It uses two Keithley sourcemeters, one for the electrical measurements and the other for the temperature control. Temperature control is achieved using a Peltier junction and temperature is measured using thermocouples. Electrodes on RRAM devices are accessed using tungsten probes mounted on micromanipulators. Also, the apparatus is enclosed in a glove box so oxygen can be purged, not affecting the devices while cycling. Finally, electrical measurements and the temperature control are performed using a computer running LabVIEW, which was developed specifically to perform RRAM-type characterisation. Figure 2.22 illustrates a the probe station performing measurements.

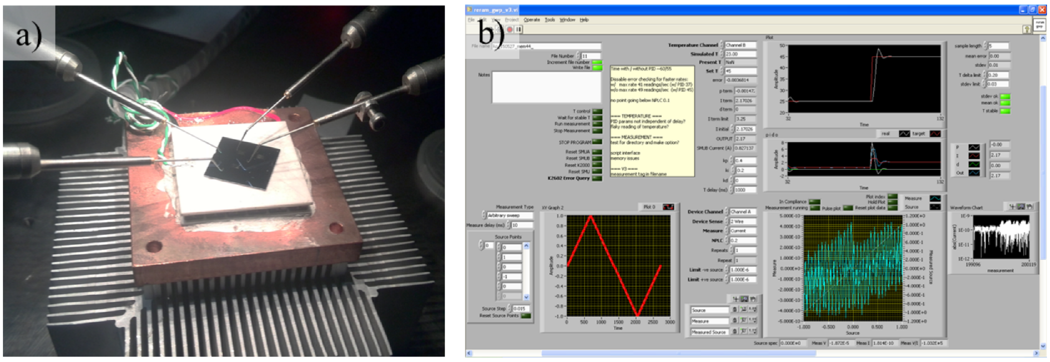

File Number: 11
Temperature Channel: Channel B
Simulated T: 23.00
Present T: NaN
Set T: 45
error: -0.0036814
p-term: -0.00147
I term: 2.17026
d term: 0
I term limit: 3.25
I initial: 2.17026
OUTPUT: 2.17
SMUB Current (A): 0.827137
kp: 0.4
ki: 0.2
kd: 0
T delay (ms): 1000
sample length: 5
mean error: 0.00
stdev: 0.01
T delta limit: 0.20
stdev limit: 0.03
P: -0.00
I: 2.17
d: 0.00
Out: 2.17
Measurement Type: Arbitrary sweep
Measure delay (ms): 10
Source Points: 0, 1, 0, -1, 0
Source Step: 0.015
Device Channel: Channel A
Device Sense: 2 Wire
Measure: Current
NPLC: 0.2
Repeats: 1
Repeat: 1
Limit -ve source: 1.000E-6
Limit +ve source: 1.000E-6
Source spec: 0.000E+0
Meas V: -1.872E-5
Meas I: 1.814E-10
Meas V/I: -1.032E+5

Time with / without PID ~60/55

Dissable error checking for faster rates:
w/ max rate 41 readings/sec (w/ PID 37)
w/o max rate 49 readings/sec (w/ PID 45)

no point going below NPLC 0.1

=== TEMPERATURE ===
PID params not independent of delay?
flaky reading of temperature?

=== MEASUREMENT ===
test for directory and make option?

script interface
memory issues

=== V3 ===
measurement tag in filename

Figure 2.22: a) Sample on the Peltier stage used for heating and cooling of the substrates under electrical testing, and b) LabVIEW interface where all parameters are configured, namely the current compliance for both polarities.

One specific advantage of using a dedicated LabVIEW interface to perform RRAM measurements is its ability to use different current limits (or compliances) for different voltage polarities. This ability is exceptionally important in RRAM devices as for bipolar devices (which covers all devices characterised in this thesis) it is essential to have a compliance during SET but not when performing RESET.

2.6 Experimental Procedures

In addition to the PLD, for the deposition of the metal electrodes, a Plassys e-beam evaporator and a Plassys sputtering systems were used within James Watt Nanofabrication Centre (JWNC). Typically, such electrodes comprise a 5 nm gold adhesion layers followed by 80 nm of titanium. One advantage regarding the use of Plassys IV e-beam evaporator is the purity of the deposited layers, which in this particular case means the titanium is not marginally oxidised, which contrast with films deposited using the sputtering system. Another advantage of the Plassys IV is the fine control over film thickness, made possible with a quartz crystal microbalance. The fine control over thickness made the preparation of planar bottom electrodes possible, as explained on chapter 5 when describing figure 5.7 on page 134. Photolithography, also performed at JWNC, was done using a photoresist primer, before spinning the S1818 photoresist used for all devices. Spinning of the photoresist primer was performed for 20 seconds at 2000 rpm, followed by 30 seconds at 4000 rpm for the S1818. The undercut (which was only used in the crossbar architecture) was achieved by spinning a first layer of LOR e-beam resist before the S1818 photoresist. Soft baking was done for 120 seconds at 115 °C in air. For all patterning done throughout the thesis, no hard baking was used. Alignment and exposure were always performed on the SUSS MicroTec MA6 (also in JWNC), under "hard contact" mode and with an exposure duration of 5.5 seconds. Development of the photoresist was performed with the Microposit developer at room temperature and for 75 seconds, with a dilution of 1:1 (vol/vol). Optical microscopy was always employed to verify if the photolithography steps were successful. After exposure and development, samples were mildly "ashed" in an oxygen containing plasma (2 minutes at 40 W) to remove any photoresist residue possibly left behind. Dry etching was performed on a RIE 80 Plus system, using CHF_3 with a flow of 30 sccm, a pressure of 30 mTorr, at room temperature and for 5 minutes. Device patterning was always achieved by means of lift-off in acetone and without sonication. Thermally oxidised n-type silicon wafers (SiO_2 300 nm) were used as substrates for amorphous and poly-crystalline RRAM devices to avoid short-circuits due to the very thin (5 nm) native oxide on common ones. All targets are from PI-KEM and have a purity of 99.99%. Nb:STO target has a Nb doping of 10%.

Bibliography

[114] Milton Ohring. *The Materials Science of Thin Films.* 1992.

[115] P. Willmott and J. Huber. "Pulsed laser vaporization and deposition". In: *Reviews of Modern Physics* 72.1 (Jan. 2000), pp. 315–328. DOI: `10.1103/RevModPhys.72.315`.

[116] C. Belouet. "Thin film growth by the pulsed laser assisted deposition technique". In: *Applied Surface Science* 96-98 (Apr. 1996), pp. 630–642. DOI: `10.1016/0169-4332(95)00535-8`.

[117] "Pulsed Laser Deposition of Complex Materials: Progress Toward Applications". In: *Pulsed Laser Deposition of Thin Films.* John Wiley & Sons, Inc., 2006, pp. 1–31. DOI: `10.1002/9780470052129.ch1`.

[118] M. R. Rashidian Vaziri, F. Hajiesmaeilbaigi, and M. H. Maleki. "Monte Carlo simulation of the subsurface growth mode during pulsed laser deposition". In: *Journal of Applied Physics* 110.4 (2011), p. 043304. DOI: `10.1063/1.3624768`.

[119] "http://www.surface-tec.com/workstation.php". In:

[120] Peter Schaaf. "Laser nitriding of metals". In: *Progress in Materials Science* 47.1 (Jan. 2002), pp. 1–161. DOI: `10.1016/S0079-6425(00)00003-7`.

[121] S Amoruso, R Bruzzese, N Spinelli, and R Velotta. "Characterization of laser-ablation plasmas". In: *Journal of Physics B: Atomic, Molecular and Optical Physics* 32.14 (1999), R131.

[122] W Svendsen, O Ellegaard, and J Schou. "Laser ablation deposition measurements from silver and nickel". In: *Applied Physics A* 255 (1996), pp. 247–255.

[123] S. Amoruso, a. Sambri, and X. Wang. "Plume expansion dynamics during laser ablation of manganates in oxygen atmosphere". In: *Applied Surface Science* 253.19 (July 2007), pp. 7696–7701. DOI: `10.1016/j.apsusc.2007.02.041`.

[124] X.Y Chen, Z.C Wu, B Yang, X.Y Lei, and Z.G Liu. “Four regions of the propagation of the plume formed in pulsed laser deposition by optical-wavelength-sensitive CCD photography”. In: *Thin Solid Films* 375.1-2 (Oct. 2000), pp. 233–237. DOI: `10.1016/S0040-6090(00)01260-8`.

[125] “In Situ Diagnostics by High-Pressure RHEED During PLD”. In: *Pulsed Laser Deposition of Thin Films*. John Wiley & Sons, Inc., 2006, pp. 85–97. DOI: `10.1002/9780470052129.ch4`.

[126] Michio Naito, Hideki Yamamoto, and Hisashi Sato. *Reflection high-energy electron diffraction and atomic force microscopy studies on homoepitaxial growth of SrTiO3(001)*. 1998. DOI: `10.1016/S0921-4534(98)00338-4`.

[127] Z. Zhang and Max G. Lagally. *Atomistic Processes in the Early Stages of Thin-Film Growth*. 1997. DOI: `10.1126/science.276.5311.377`.

[128] Dave H.a Blank, Guus J.H.M Rijnders, Gertjan Koster, and Horst Rogalla. “In-situ monitoring by reflective high energy electron diffraction during pulsed laser deposition”. In: *Applied Surface Science* 138-139 (1999), pp. 17–23. DOI: `10.1016/S0169-4332(98)00470-X`.

[129] J.H. Neave, B.A. Joyce, P.J. Dobson, and N. Norton. “Dynamics of film growth of GaAs by MBE from Rheed observations”. English. In: *Applied Physics A* 31.1 (1983), pp. 1–8. DOI: `10.1007/BF00617180`.

[130] G. Binnig, H. Rohrer, Ch. Gerber, and E. Weibel. “Surface Studies by Scanning Tunneling Microscopy”. In: *Phys. Rev. Lett.* 49 (1 July 1982), pp. 57–61. DOI: `10.1103/PhysRevLett.49.57`.

[131] G. Binnig, C. F. Quate, and Ch. Gerber. “Atomic Force Microscope”. In: *Phys. Rev. Lett.* 56 (9 Mar. 1986), pp. 930–933. DOI: `10.1103/PhysRevLett.56.930`.

[132] R. N. Jagtap and a. H. Ambre. “Overview literature on atomic force microscopy (AFM): Basics and its important applications for polymer characterization”. In: *Indian Journal of Engineering and Materials Sciences* 13.4 (2006), pp. 368–384.

[133] Nader Jalili and Karthik Laxminarayana. “A review of atomic force microscopy imaging systems: Application to molecular metrology and biological sciences”. In: *Mechatronics* 14.8 (2004), pp. 907–945. DOI: `10.1016/j.mechatronics.2004.04.005`.

[134] "Force measurements with the atomic force microscope: Technique, interpretation and applications". In: *Surface Science Reports* 59.1-6 (2005), pp. 1–152. DOI: `10.1016/j.surfrep.2005.08.003`.

[135] Peter Jonathan Eaton, Peter Eaton, and Paul West. *Atomic force microscopy.* Oxford University Press, 2010.

[136] P. K. Hansma et al. "Tapping mode atomic force microscopy in liquids". In: *Applied Physics Letters* 64.13 (1994), pp. 1738–1740. DOI: `10.1063/1.111795`.

[137] Younkoo Jeong, G. R. Jayanth, Sissy M. Jhiang, and Chia-Hsiang Menq. "Direct tip-sample interaction force control for the dynamic mode atomic force microscopy". In: *Applied Physics Letters* 88.20 (2006), p. 204102. DOI: `10.1063/1.2203958`.

[138] L. de Broglie. "La nouvelle dynamique des quanta." In: *Annalen der Physik* 3.3 (1925), pp. 22–128.

[139] David B. Williams and C. Barry Carter. *Transmission Electron Microscopy - A Textbook for Materials Science.* 2009th ed. Springer.

[140] C. Davisson and L. H. Germer. "Diffraction of Electrons by a Crystal of Nickel". In: *Phys. Rev.* 30 (6 Dec. 1927), pp. 705–740. DOI: `10.1103/PhysRev.30.705`.

[141] C.J. Davisson and L.H. Germer. "PHYSICS: Davisson and Germer". In: *Proceedings of National Academy of Sciences* 14 (1928), pp. 317–322.

[142] Von M. Knoll, E. Ruska. "Beitrag zur geometrischem Elektronenoptik. I". In: *Annalen der Physik* 12.5 (1932).

[143] Ernst Ruska. "The Development of the Electron Microscope and of Electron Microscopy". In: *Bioscience Reports* 7.8 (1987).

[144] E. Driest and H.O. Müller. "Elektronenmikroskopische Aufnahmen." In: *Wiss. Mikroskopie* 52.3 (1935), pp. 53–57.

[145] S J Pennycook and A I Kirkland. "Materials Advances through Aberration- Corrected Electron". In: *MRS Bulletin* 31.January (2006), pp. 36–43.

[146] A V Crewe, D N Eggenberger, J Wall, and L M Welter. "Electron Gun Using a Field Emission Source". In: *Review of Scientific Instruments* 576.39 (1968). DOI: `10.1063/1.1683435`.

[147] O. Scherzer. "Über einige Fehler von Elektronenlinsen". German. In: *Zeitschrift für Physik* 101.9-10 (1936), pp. 593–603. DOI: `10.1007/BF01349606`.

[148] Peter W Hawkes. “The long road to spherical aberration correction”. In: *Biology of the Cell* 93 (2001), pp. 432–439.

[149] Harald Rose. “Outline of an ultracorrector compensating for all primary chromatic and geometrical aberrations of charged-particle lenses”. In: *Nuclear Instruments and Methods in Physics Research Section A* 519 (2004), pp. 12–27. DOI: `10.1016/j.nima.2003.11.115`.

[150] Harald Rose. “Prospects for aberration-free electron microscopy”. In: *Ultramicroscopy* 103 (2005), pp. 1–6. DOI: `10.1016/j.ultramic.2004.11.017`.

[151] P D Nellist and S J Pennycook. “Subangstrom Resolution by Underfocused Incoherent Transmission Electron Microscopy”. In: *Physical Review Letters* 81.19 (1998), pp. 4156–4159.

[152] Ray Egerton. *Electron energy-loss spectroscopy in the electron microscope*. 3rd Edition. Springer Science & Business Media, 2011.

[153] “Electron Energy Loss Spectrometry and Energy Dispersive X-ray Analysis”. In: *Aberration-Corrected Analytical Transmission Electron Microscopy*. John Wiley and Sons, Ltd, 2011, pp. 163–210. DOI: `10.1002/9781119978848.ch7`.

[154] R F Egerton and M Malac. “EELS in the TEM”. In: *Journal of Electron Spectroscopy and Related Phenomena* 143 (2005), pp. 43–50. DOI: `10.1016/j.elspec.2003.12.009`.

[155] Joanna Bobynko, Ian MacLaren, and Alan J Craven. “Spectrum imaging of complex nanostructures using DualEELS: I. digital extraction replicas”. In: *Ultramicroscopy* 149 (Nov. 2015), pp. 9–20. DOI: `10.1016/j.ultramic.2014.10.014`.

[156] Steve Reyntjens and Robert Puers. “A review of focused ion beam applications in microsystem technology”. In: *Journal of Micromechanics and Microengineering* 11.4 (2001), pp. 287–300. DOI: `10.1088/0960-1317/11/4/301`.

[157] L. a. Giannuzzi and F. a. Stevie. “A review of focused ion beam milling techniques for TEM specimen preparation”. In: *Micron* 30 (1999), pp. 197–204. DOI: `10.1016/S0968-4328(99)00005-0`.

[158] Thoru Ishitani and Hideki Tsuboi. “Transmission electron microscope sample preparation using a focused ion beam”. In: *Journal of Electron Microscopy* 326 (1994), pp. 322–326.

Chapter 3

Deposition of Amorphous Zirconia Thin Film via PLD

This chapter will start with a brief characterisation of the PLD system, which was commissioned during the course of this research, as well as cover aspects related to the deposition of amorphous zirconia thin films. Specifically, the link between PLD parameters during growth and the morphological, structural and electrical properties is discussed and presented. The objective is to understand which experimental conditions in the PLD give rise to films with adequate properties. Ultimately, such films were integrated into the zirconia based RRAM devices that will be presented in chapters 5

3.1 Introduction

Resistive switching has been observed in a wide variety of materials, ranging from single crystal perovskites, like Fe:STO and PCMO, to poly-crystalline binary oxides like TiO_2, HfO_2 and ZrO_2. However, in chapter 1 it was discussed how the resistive switching phenomena typically do not originate from the material itself but rather from the distribution and density of defects. Thus, control of the concentration of oxygen vacancies and structure, for instance, is of critical importance when designing RRAM devices, and is the main motivation for the work presented in this chapter. The impact of structural inhomogeneities, such as those introduced by defects in crystalline systems, described in chapter 4, are also under debate [4, 159–161]. For example, grain boundaries in polycrystalline insulators are linked to higher on/off ratios and greater ease of switching because they act as fast migration paths. However, material granularity will limit scalability since devices of comparable size to the grains themselves will exhibit greater performance variability [161–163]. For this reason, fully amorphous switching layers may be better RRAM candidates because they offer structural homogeneity and do not require high temperature processing or the epitaxially-matched substrates that are needed for single crystal materials. Indeed, recent reports suggest that amorphous RRAM devices can offer an enhanced reproducibility and better long term stability when compared to polycrystalline based devices [163]. In addition, depositions are done at room temperature, thereby retaining compatibility with a number of potential substrates and processing techniques, a particular advantage of amorphous RRAM devices that are required to be CMOS compatible.

3.1.1 Droplet Formation in PLD

Pulsed Laser Deposition suffers from the formation of macroscopic particulates that are normally termed “droplets”. This phenomenon is often regarded as one of PLD’s biggest drawbacks [164–168] and is perhaps the greatest obstacle to the use of PLD in commercial applications [115, 165]. Many techniques have been developed to reduce or eliminate droplet formation, for example: circular motion of an aperture inside the chamber [166]; off-axis deposition [167–169]; fine polishing targets to reduce surface roughening due to ablation [170–173]; supersonic gas-jet deflection [174]; and laser focusing/defocusing [175]. There are several mechanisms by which material can be removed from the surface of a target during laser ablation, as explained in chapter 2 when describing laser-solid interaction (on page 44). “Thermal” or “photothermal” sputtering normally refers to the process where light energy is converted to vibrational energy before bond breaking [176]. This process is clearly distinct from a “photochemical” or “electronic” process in which laser induced electronic excitations lead directly to bond breaking before any electronic to vibrational transfer of energy has occurred [176]. Both thermal and electronic processes remove atomic-size material from the target [176]. Processes described as “hydrodynamical” and “exfoliation” are two alternative methods easily identified in the literature. These methods are responsible for the introduction of bulk material (particulates or droplets) into the ablation plume [176]. Subsurface boiling and recoil ejection are two examples of hydrodynamical processes. Subsurface boiling will take place in materials with high thermal conductivities and low melting temperatures. In these materials, the time needed to convert laser energy into heat and transfer it into the bulk is shorter than the time needed to evaporate the surface layer (skin depth) [115]. When the transient melt below the skin depth is subjected to the recoil pressure (that can reach 10^4 N) of the expanding plume, droplets can be ejected as the melt is literally squeezed out of the solid bulk [115], as illustrated in figure 3.1.

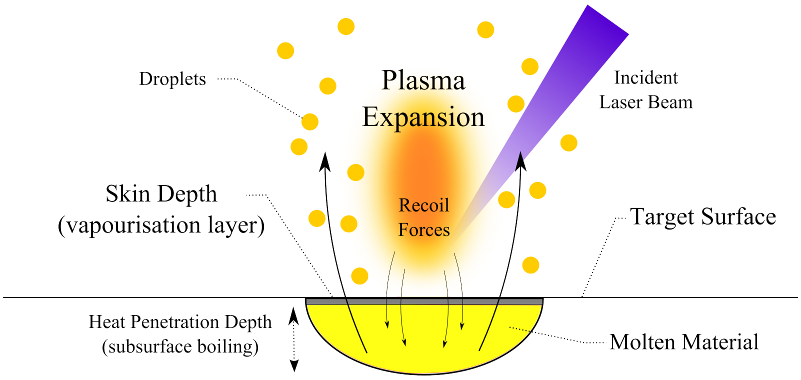

Figure 3.1: Laser-solid interaction showing the skin depth, the heat penetration depth and the molten material. As the plasma expands, recoil forces will squeeze the melted material, ejecting it from the target as micron-sized droplets.

Subsurface boiling is the main source of droplets, especially when metallic targets are used. In comparison with oxides, metals will generally have lower melting points and high thermal and electric conduction, which is not desirable because good thermal conduction facilitates the melting of material. Another difficulty with metallic targets is their inherent optical reflectivity to incident radiation. This causes less energy to be absorbed which leads to heating of the materials instead of its vaporisation.

Exfoliation describes particulate ejection due to an increased surface roughening caused by repeated melt-freeze cycles of the irradiated target material. Macroscopic outgrowths, sketched in figure 3.2, eventually become necked off and thermally decouple from the bulk, breaking away as macroscopic particulates, which are normally a few micrometres in length. [115]. Exfoliation is a morphological process that can be greatly reduced by regularly treating the target surface before deposition [115, 170–173]. Normal target surface treatments typically involved fine grinding and polishing, followed by mild laser ablation to remove contaminants from the surface.

The dimensions and morphology of macroscopic particulates ejected from the target by hydrodynamical and exfoliation methods are different, making it possible to identify and classify them using image processing techniques, as will be shown in the next section. Droplets limit the use of PLD systems in the preparation of many types of devices, as the macroscopic size of droplets can be orders of magnitude larger than film thickness. For devices with several layers, the existence of microscopic droplets in the first layer could hinder fabrication altogether, as it could lead to short-circuits forming in devices. Efforts

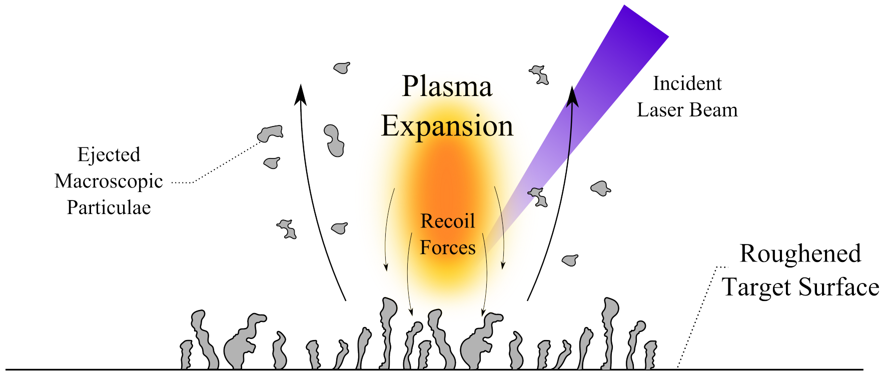

Figure 3.2: Laser-solid interaction showing a roughened target surface. With the repeated melt-freeze cycles these structures can detach from the target surface and produce particulates that can be deposited onto the substrate surface.

were made to minimise this issue by the use of a collimating aperture in the laser path, as depicted in figure 2.1). It is suggested that a faster and more homogeneous ablation reduces the volume of the transient melt just beneath the skin depth [177]. If less material is molten, less material is squeezed once the plasma expands and hence fewer droplets are formed during ablation. In figure 3.3 the two types of macroscopic particulates described hereby are clearly visible. The rounded particles are droplets created from melted target material, whereas the bigger and irregular ones arise from exfoliation of the target surface.

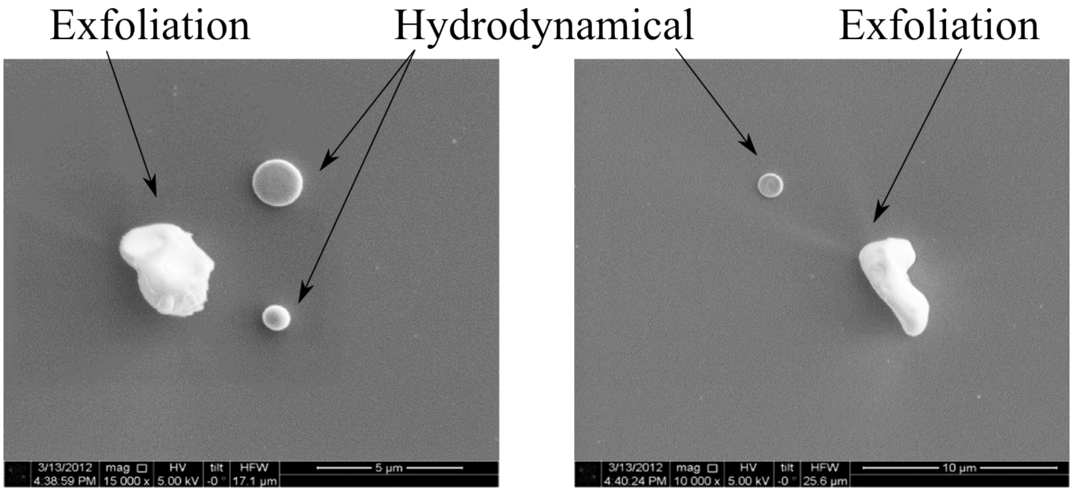

Figure 3.3: SEM images of macroscopic ejected material on the surface of ZrO_2 obtained via PLD.

In addition to particles ejected from the ablation targets, one can also observe nanoparticles that form in the gas phase when the background pressure is sufficiently high for heterogeneous particle nucleation. These particles, with diameters ranging from 10 to 50 nm approximately, can become embedded in a depositing film.

3.1.2 Thin Film Growth

The application of thin films in multilayer electronic devices, requires smooth film surfaces and interfaces. An understanding of the different mechanisms affecting the growth mode is, therefore, necessary to control the surface morphology during thin-film deposition [178]. Growth of thin films from atoms deposited from the gas phase is intrinsically a non-equilibrium phenomenon governed by a competition between kinetics and thermodynamics. Precise control of the growth and thus of the properties of deposited films becomes possible only after an understanding of this competition is achieved [127]. Tthis chapter will focus on the deposition of amorphous zirconia thin films, hence a thermodynamical description of mechanisms is followed. In contrast, chapter 4 deals with epitaxial growth of thin films, where kinetics are also required to explain growth mechanisms.

During the very first stages of film formation in a deposition process, adsorbed atoms or molecules known as adatoms condense on the substrate [114]. As the deposition process continues, a uniform distribution of small yet highly mobile aggregates of material is observed. In the next stage of thin film growth the islands will coalesce, diminishing the voids between them. Eventually a critical thickness will be reached where all the voids will be eliminated and the film is continuous. Structural order is normally preserved on islands and interfaces between random coalesced and initially disoriented particles [114, 179]. The processes of nucleation and coalescence take place during the initial stages of the deposition, usually during the first 20 nm of film thickness. There are five different modes of thin film growth that are commonly distinguishable, as sketched in figure 3.4 [121, 180].

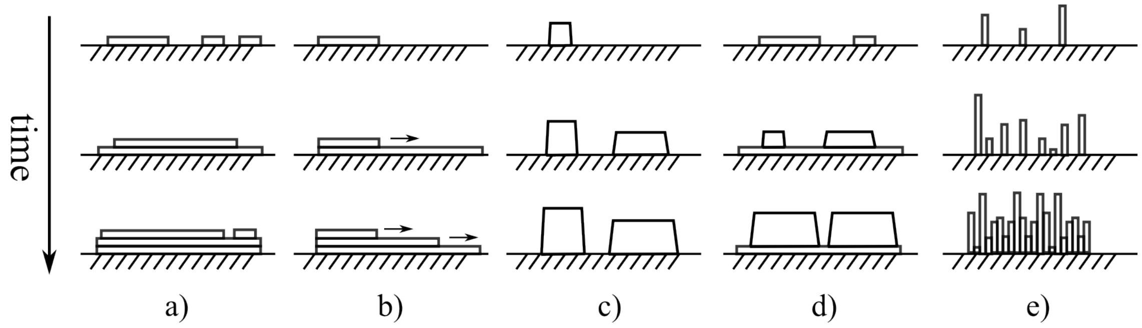

Figure 3.4: The fives modes of crystal growth, re-drawn from reference [180]; a) layer-by-layer (Frank-van der Merwe), b) step-flow, c) island growth (or Volmer-Weber), d) layer-by-layer with island growth (Stranski-Krastanov) and e) columnar growth.

There are many experimental parameters that influence the type of growth observed for one given material, including substrate temperature and pressure, for example. However, the material to be deposited plays the most important role. For a comprehensive analysis of what parameters exactly govern the growth mode in thin films the free-energy is normally considered [114]:

$$\Delta G = a_3 r^3 \Delta G_v + a_1 r^2 \gamma_{vf} + a_2 r^2 \gamma_{fs} - a_2 r^2 \gamma_{sv}. \tag{3.1}$$

The term ΔG is the Gibbs free-energy per unit volume, Which drives the condensation reaction. The term γ refers to several interfacial tensions and the subscripts f, s and v represent film, substrate and vapour respectively. ΔG_v corresponds to the change in chemical free energy per unit volume, which in this case is negative, meaning that the condensation process results in a reduction of energy. The constants a_1, a_2 and a_3 are geometric considerations regarding the change of the shape of nuclei on the substrate, where a_0 is the shape of a single adatom, according to figure 3.5 [114]. Consideration of the mechanical equilibrium among the interfacial tensions yields Young's equation [114]:

$$\gamma = \gamma_{fs} + \gamma_{vf} cos(\theta). \tag{3.2}$$

If equation 3.2 holds, then the contact angle, θ, depends only on the surface properties of the involved materials. Figure 3.5 illustrates an aggregate on the substrate surface and shows some of the geometric concepts described above. The way this aggregate will evolve depends on the contact angle and on the interfacial tensions.

From the five growth modes mentioned before (figure 3.5), three growth modes can be distinguished based on Young's equation (3.2). If $\theta > 0$, island growth (Volmer-Weber) is the dominant process and:

$$\gamma_{sv} < \gamma_{fs} + \gamma_{vf}. \tag{3.3}$$

If the deposit completely "wets" the substrate surface and $\theta = 0$, layer by layer (Frank van-der Merwe) dominates and,

$$\gamma_{sv} = \gamma_{fs} + \gamma_{vf}. \tag{3.4}$$

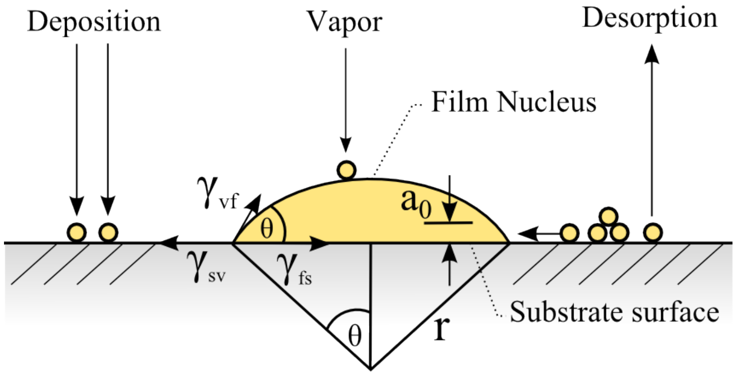

Figure 3.5: Representation of a cluster illustrating basic atomistic processes on the substrate surface during vapour deposition (adapted from [114]). All the interfacial tensions are represented (γ_{sv}, γ_{fs} and γ_{vf}) as well as the contact angle, θ, responsible for the growth mode.

This condition is a particular case for systems where the substrate and film lattice match perfectly, normally termed auto or homoepitaxy. However, if the strain energy per unit area of film overgrowth is large with respect to γ_{vf}, nuclei will form above the layers, resulting in layer-by-layer with island growth (Stranksi-Krastanov), where:

$$\gamma_{sv} > \gamma_{fs} + \gamma_{vf} \tag{3.5}$$

As the film growths thicker, and further away from the early film formation, the deposition variables or parameters take over and become responsible for the physical properties that thin films exhibits. From all the experimental parameters available in a deposition system the consensus is that the substrate temperature (T) and the particle energy have the greatest influence when it comes to influencing film structure [181].

Both parameters influence the structure by directly changing the mobility of adatoms on the substrate surface. Figure 3.6 illustrates how these parameters influence the structure of grown films. Different adatom mobility on the surface will result in films with different morphologies. The increase in substrate temperature will give rise to denser films comprising bigger grains while the use of lower temperatures produces columnar films with increased porosity. The adatom energy, however, can be influenced by indirect experimental parameters that might not be so evident. In the case of PLD in particular, the pressure and the laser energy are two parameters that directly influence the energy of particles

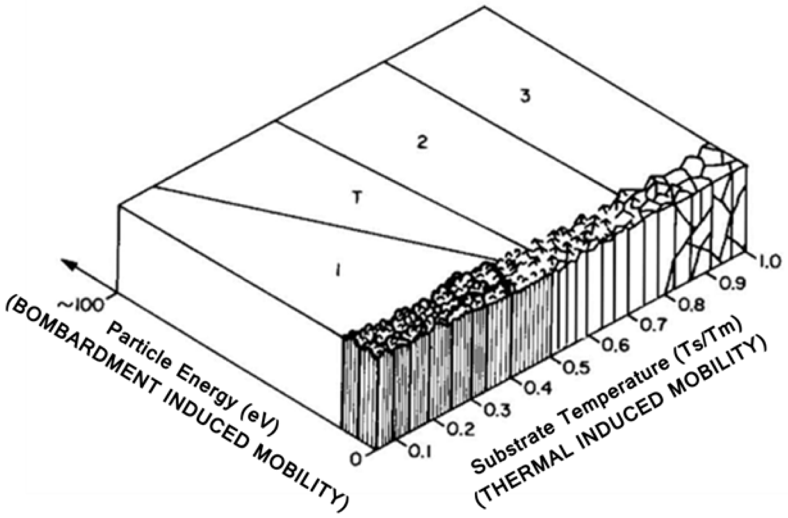

Figure 3.6: Structure Zone Model (SZM) correlating substrate temperature with particle energy or thermodynamics with kinetics (adapted from [181]). Ts/Tm is the ratio of the substrate temperature with the melting temperature of the material to be deposited.

arriving at the substrate's surface. The depositions described in this chapter were all of the type Stransky-Krastanov, i.e. three dimension growth, where all films were grown without any lattice match with the substrate. In chapter 4, description of the requirements and challenges with homo and hetero-epitaxy will be presented and discussed.

3.2 Results

This section will start by presenting a characterisation regarding the homogeneity of the PLD deposition system. In addition, droplet formation in PLD is investigated and discussion about how this was mitigated, is given. Finally, amorphous deposition of zirconia thin films are presented, linking properties with grow conditions in the PLD. Deposition conditions for the samples characterised in this chapter were summarised in table 2.1 (presented on chapter 2 on page 44). TEM analysis was performed at 80 kV to minimise beam induced damage on the amorphous ZrO_2 films.

3.2.1 PLD System Characterisation

Starting with the characterisation of the thickness homogeneity of our PLD system, an entire 2 inch c-Si wafer was used to deposit Nb:STO, which was chosen mainly due to the high growth rates associated with oxides, when compared to with metals. Figure 3.7

illustrates the results obtained.

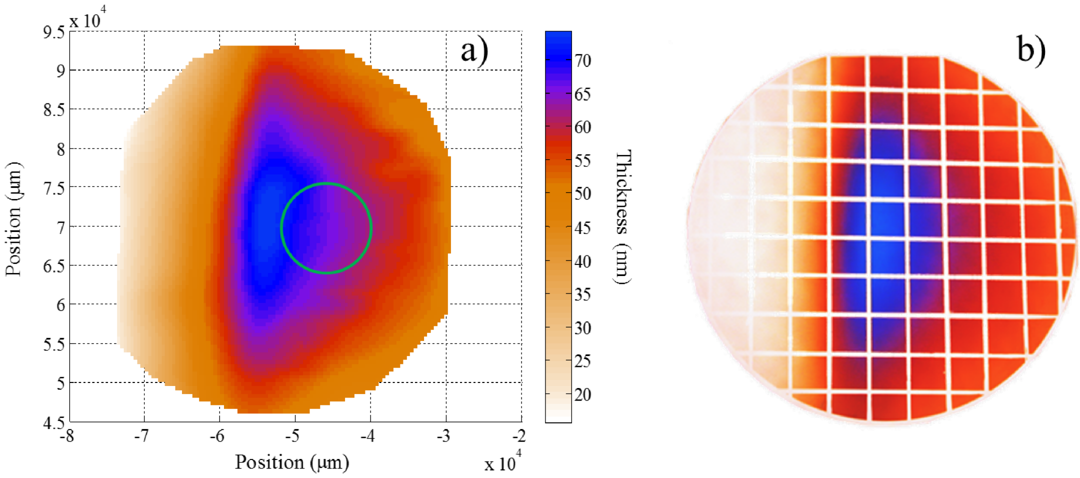

Figure 3.7: Thickness profile a) Matlab interpolation and b) photograph of the wafer after deposition and lift-off. Blue regions are caused by a thicker film and its elongated shape is probably related to the laser beam incidence angle. The white lines in b) were caused by the post-deposition lift-off used to create the steps where the thickness was measured by AFM. Deposition was performed at 1 mTorr (O_2) and with 20000 shots at a frequency of 18 Hz and with a fluence of 1.5 J/cm^2. Details about the Matlab code that interpolates the thicknesses can be found in Appendix. Scale is the same on both images.

The colours on the substrate are directly correlated to thickness, and where blue represents the thicker region. The loss of horizontal symmetry is thought to happen because of an electrostatic grounding effect between the plasma plume and a metallic protection plate near the target, inside the PLD chamber. The highlighted green circle, in figure 3.7a, represents the optimum substrate position. The diameter of the highlighted area is to 14 mm, so that the homogeneity of a rotating 10 x 10 mm^2 Si chip could be determined. Although it seems to be relatively inhomogeneous, results shown on figure 3.7 was obtained for a static substrate. If the substrate is rotated at a constant speed for the entire deposition length, homogeneity is greatly increased. The Matlab code was used to study the achievable homogeneity on a 10 x 10 mm^2 c-Si chip under constant rotation. Calculations were carried out in the entire wafer surface and with different substrate sizes so that the best position could be determined. With substrates in the optimum position, and rotating, thickness homogeneity for a 10 x 10 mm^2 substrate is virtually 100%. Details on the experimental conditions and data processing regarding the plume characterisation can be found in section 8.1.1 of the Appendix.

As discussed in the introduction to this chapter, a major drawback normally associated with PLD is the formation of macroscopic particulates on the thin film surface that can prevent the use of PLD for RRAM device fabrication. To minimise the formation of macroscopic particulates (1) an aperture was introduced in the laser path (as depicted in figure 2.1 on page 43) and (2) the area of the target that is ablated was minimised. The lower flux tails in the laser profile without the aperture are not energetic enough to evaporate the target material, thus increasing the area of melted material that contributes to particulate ejection from splashing [164, 165]. Figure 3.8 illustrates the effect the aperture has on the laser beam profile.

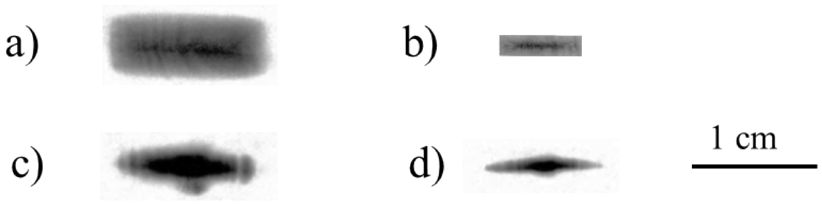

Figure 3.8: Laser beam profile: a) before the aperture b) after the aperture before focusing. Laser beam profile at the target surface: c) without the aperture d) with the aperture.

The lower flux tails on figure 3.8a are removed with the aperture, as illustrated by figure 3.8b. Moreover, the aberrations introduced by the focusing lens are clearly seen in both figures 3.8c and 3.8d. Several depositions were made to study of how the introduction of the laser aperture changed the density of droplets on the surface of the deposited thin films using several target materials. It is known that the nature of the target material (oxide, metal, insulator or conductor) can greatly influence the density of droplets [182]. For this reason thin films of copper, platinum, zirconium, zirconium oxide, magnesium oxide and $LaSrMnO_3$ (LSMO) were deposited with and without the aperture. It is expected that the oxide targets will yield thin films with a lower density of droplets than that of films obtained with the metallic targets (as discussed on page 80) [182]. The use of the aperture influences not only the density of droplets but also the growth rate of all thin films, which is consistent with the decrease in photon fluence (approximately 60%), and the reason why all thicknesses were normalised to 10 nm. The growth rates for different materials should not be directly compared as the deposition conditions, namely pressure and number of shots varied between materials. However, for the same material (with and without the aperture) the experimental conditions were absolutely the same. Table 3.1 summarises the thicknesses obtain with and without the aperture.

The thickness ratio between films obtained with and without the aperture range from 10 to 2.2 for Pt and LSMO respectively, which seems to indicate a clear difference in the

Material	Thickness (with aperture, nm)	Thickness (without aperture, nm)
Pt	4	40
Cu	4	15
Zr	26	70
ZrO_2	27	70
MgO	10	46
LSMO	80	180

Table 3.1: Thicknesses obtained for all materials, with and without the aperture on the laser path.

fluence threshold of these materials. Typically during deposition, the targets are moved continuously using a raster and a rotation movement in order to induce a homogeneous erosion on the target surface. The reduction of the ablated area was achieved by maintaining the target rotation but removing the raster movement. By doing so, the ablation does not happen on the entire target surface, but rather on a ring. The reduction of the ablation area benefits, not only the initial cleaning stage, but also how fast a steady state is achieved with laser ablation. After a few thousand shots a ring becomes visible on the target surface where the ablation takes place, as seen in figure 3.9a.

The target surface was analysed in more detail to understand how achieving a steady state and the introduction of the aperture, benefits the deposition of thin films without macroscopic particulates. Figure 3.9b–d illustrates the differences on the target surface when analysed with the SEM. The two higher magnification images in figures 3.9c and 3.9d illustrate just how different the ablation process can be. The centre of the ablation ring is where the laser flux is higher and therefore this is the region where the sputtering takes place. The sputtering is responsible for smoothing of the surface as the plasma expansion forces involved will be enough to gradually remove surface features presented in figure 3.9c. The outer regions of the ablation ring undergo frequent melt-freeze cycles that enhance the growth of structures presented in figure 3.9c that, due to the lack of sputtering, will remain on the target surface. It was observed that reducing the beam profile by cutting the lower flux tails the particulate density decreased significantly. An interesting observation is that the ablation path on the target surface is about 800 μm wide which is much smaller than the beam profile itself, which is approximately 0.8 cm, as depicted in figure 3.9a. This means that even with the use of an aperture the focused laser beam profile at the target surface is far from uniform and only the middle area receives sufficient flux to vaporise zirconium. Scanning electron microscopy was used to determine of density of droplets

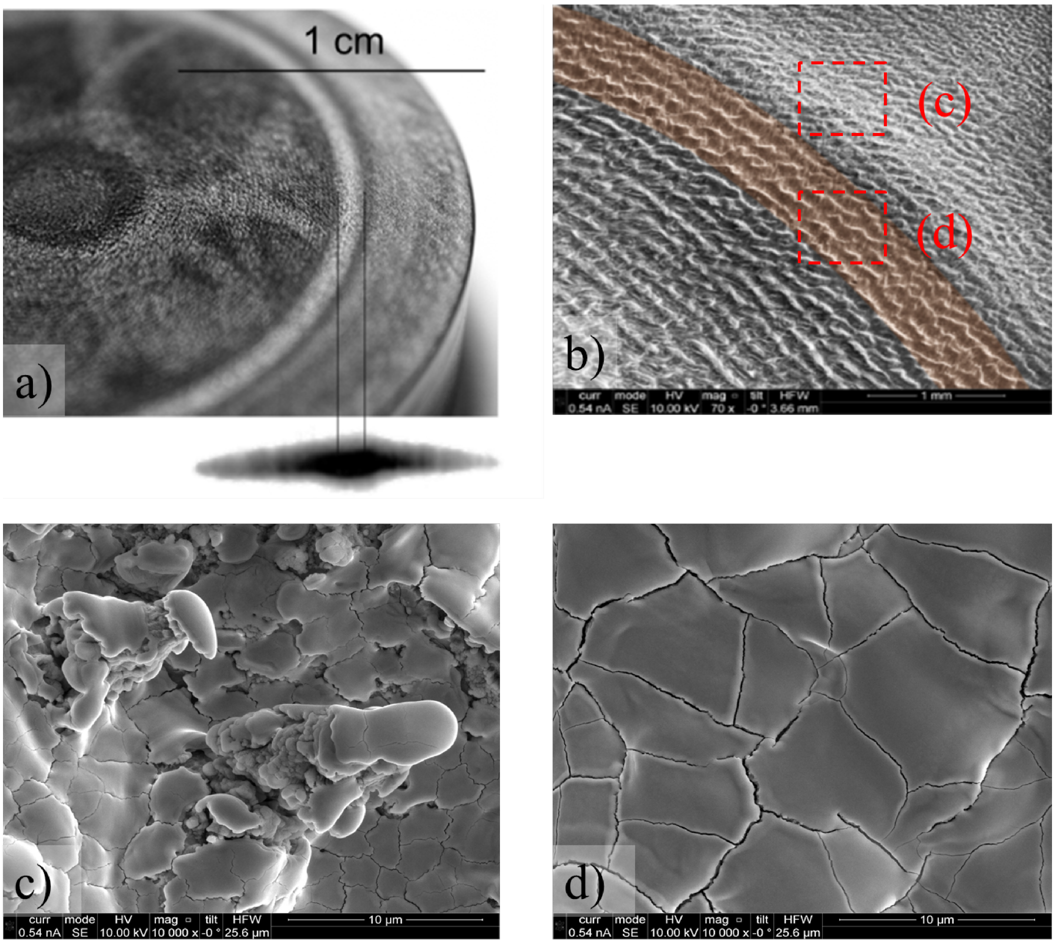

Figure 3.9: a) Photograph of the 1 inch Zr PLD target with the ablation ring. The laser beam profile is shown for a sense of scale (under the photograph in a). b) SEM image of the Zr target surface. The highlighted region represents the ablation path. c) Region adjacent to the ablation ring where exfoliation features are visible and d) smooth region in the middle of the ablation ring where the sputtering takes place.

obtained for each target material. Figures 3.10a and 3.10b were obtained with the SEM and illustrate the effect the aperture had on the density of droplets on metallic Pt films. Figures 3.11a and 3.11b were obtained with the SEM on LSMO thin films deposited with the PLD. Note how the density of particulates is lower when compared with Pt films. As an example only the SEM images of Pt and LSMO thin films are shown. The results obtained for other materials show exactly the same result: (1) there is a great reduction in droplets when the aperture is used, and (2) oxide targets yield thin films with a lower droplet density.

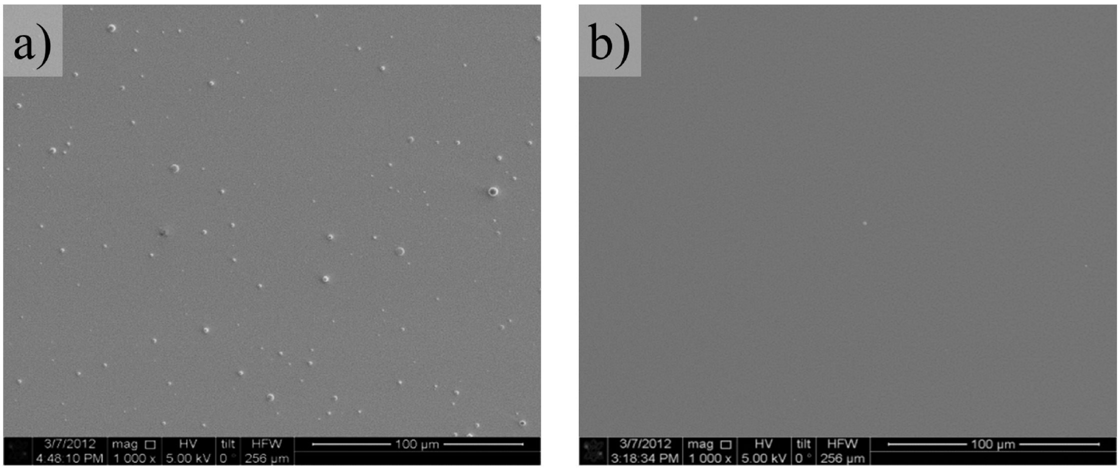

Figure 3.10: Platinum thin films deposited (a) without the aperture and (b) with aperture in 1 mTorr argon and at room temperature. Note how there are almost no visible droplets on (b).

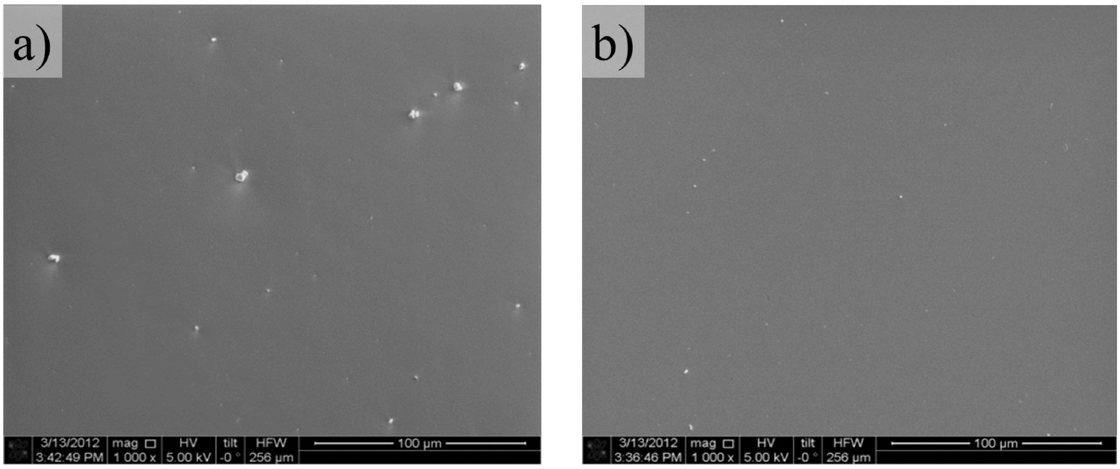

Figure 3.11: LSMO thin films (a) without the aperture and (b) with aperture in 1 mTorr oxygen and at room temperature. Note how there are almost no visible droplets on (b).

There is a striking observation one can make about figures 3.10 and 3.11: a different shape of particulates is obtained whether a metal or an oxide target is used. This illustrates the two very different types of macroscopic ejected material mentioned in the introductory chapter: (1) droplets originated by "hydrodynamical" processes, and (2) particulates from the necked off and roughened targets typical of "exfoliation", as illustrated on figure 3.3 on page 81. By ablating targets with an aperture and by achieving a smooth target surface, particulate free films were obtained using a PLD system, as illustrated by figures 3.10b and 3.11b.

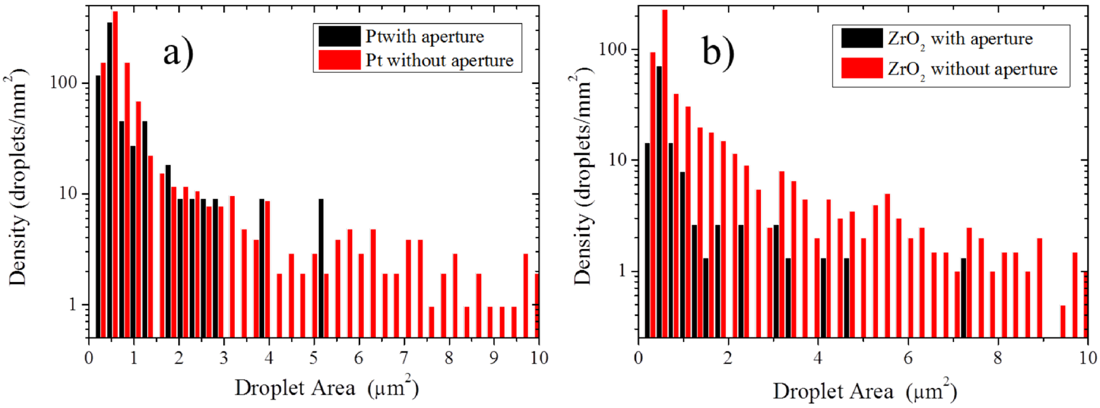

Figure 3.12: Density as a function of droplet size for a) platinum and b) ZrO_2 films deposited with and without the aperture. In both materials the use of the laser aperture is clearly beneficial.

Figure 3.12 presents a quantified comparison between films deposited with and without the laser aperture. Note how, for both materials, the bigger sized particulates were almost eliminated. The outcome of such improvement is a much better RRAM device yield, as the possibility of short-circuits being created due to macroscopic particulates is greatly reduced. Additional information and details on how the droplet density was determined can be found in section 8.1.3 in the Appendix.

3.2.2 Deposition of amorphous ZrO_2

This section will present a study performed to understand how to grow amorphous zirconia thin films with good properties for integration in RRAM devices. Properties like surface roughness, structural order, oxidation level and electrical conductivity, for instance, dictate how RRAM devices behave [183, 184]. It is, therefore, essential to systematically characterise amorphous zirconia films, as a function of the experimental parameter space in Glasgow's PLD. Zirconia samples were prepared at different oxygen pressures (1, 10, 20, and 30 mTorr) and characterised morphologically, structurally, chemically and optically. Figure 3.13 was obtained when films deposited at 1 and 30 mTorr were analysed with the AFM in topography mode.

It is clear from figure 3.13 that films grown at different pressures have different surface morphologies. Films deposited 1 mTorr (3.13a) are much smoother and without any particular geometric features, whereas films deposited at 30 mTorr (3.13b) are clearly

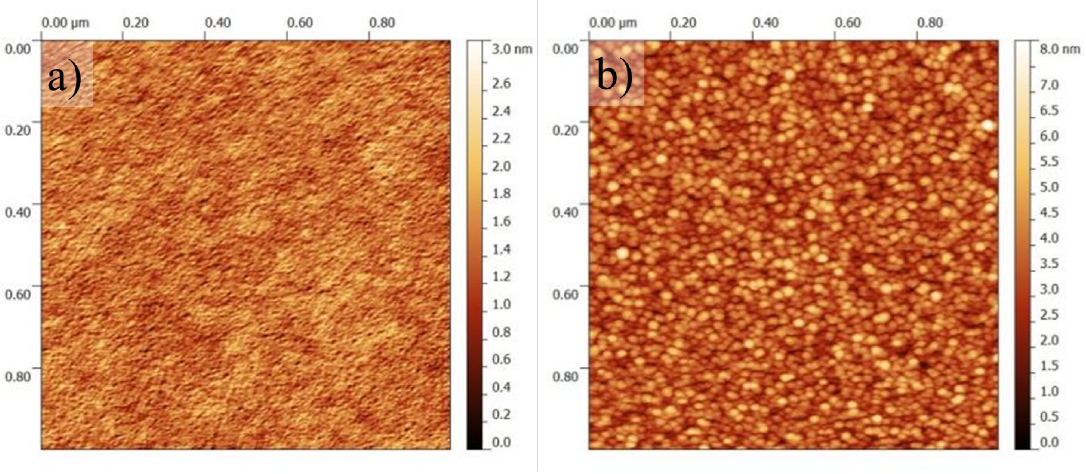

Figure 3.13: AFM images of zirconia films, 30 nm thick, grown using a ZrO_2 target at a) 1 mTorr and b) 30 mTorr of O_2. Note the different vertical scale bar for both images: 3 and 8 nm respectively. Both scans are 2 x 2 μm^2

composed of rounded grains. Figure 3.14 illustrates a typical line profile (peak-to-peak roughness) obtained on each of the AFM images above. This line profile is useful because it gives a clear indication of how thin zirconia layers can be, before surface roughness starts dominating film properties. The difference in morphology also suggests that film density is affected by the pressure, which is in agreement with the literature [183]. This is interesting, because such changes will, in turn, influence how the material behaves, for instance, under applied bias [183].

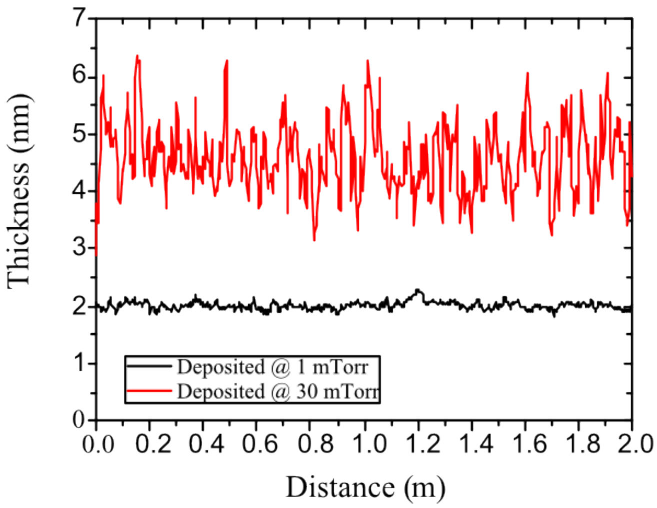

Figure 3.14: AFM images of ZrO_2 films deposited at RT and with an oxygen pressure of (a) 1 mTorr and (b) 30 mTorr. Profiles offsetted for clarity.

In other words, choosing the oxygen pressure best suited for the preparation of RRAM devices is vital, as it influences not only material fundamental properties, but also fabrication. The increase in roughness observed for films deposited at higher pressures is thought to be attributed to both shadowing and lower surface diffusion, as explained on page 85. Shadowing is evident because the substrate holder used leaves a particular shape on the sample which is equivalent to the use of a shadow mask. It was observed that the sharpness of the edge changes from a very sharp to a diffuse line with increasing background pressure, indicating that there is a loss of directionality in the ablated species. For the pressure range used here, 1 to 30 mTorr, the mean free path of the ablated species changes from 50 cm to 1.5 cm respectively which can help explain the difference in the surface morphology observed in figures 3.13 and 3.14. In addition, a loss in directionality also indicates collisions between ablated species and the background gas, that will enhance thermalisation of species which further increases surface roughness by lowering the diffusion length at the surface. One of the most common statistical parameter to describe the surface roughness of a thin film is the roughness coefficient (α) derived from the height-to-height correlation function [185]. Another important parameter that can be derived from this function is the lateral correlation length, (ξ), which can be interpreted as the characteristic feature size on the surface, for example nanoparticles or grains. Figure 3.15 presents the obtained surface roughness and characteristic feature size for both batches of samples.

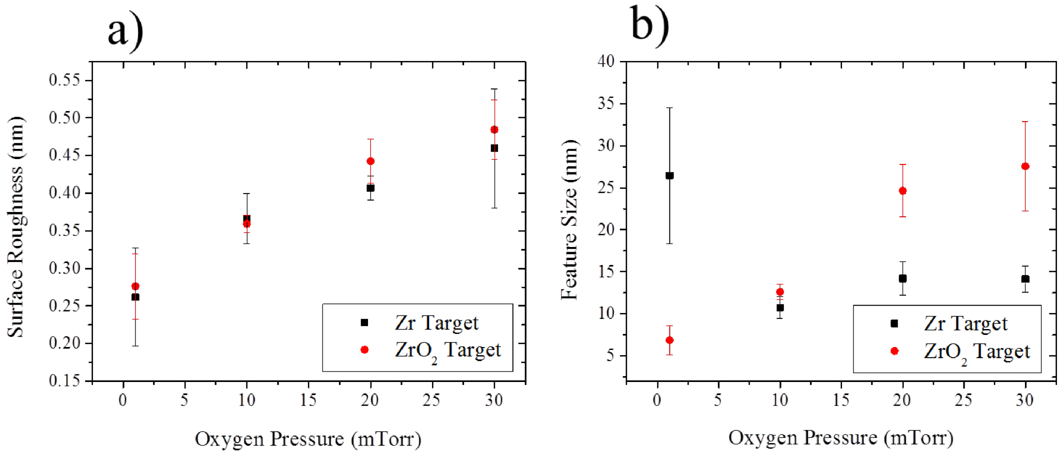

Figure 3.15: a) Roughness of ZrO_2 obtained by ablating a Zr and a ZrO_2 target and b) characteristic feature size of ZrO_2 obtained by ablating a Zr and a ZrO_2 target at different oxygen pressures. All films are 30 nm thick. AFM images used for the morphology analysis were all 1 × 1 and 2 × 2 μm^2 scans.

The increase in surface roughness with increasing oxygen background pressure is also clearly observed for films obtained with the Zr target, as illustrated in figure 3.15. It is likely that this increase is due to the two mechanisms mentioned above: shadowing and lower diffusion length at the sample surface, both due the existence or absence of collisions between the ablated species and the background gas molecules. According to figure 3.15a the roughness of ZrO_2 films obtained by ablating a Zr and a ZrO_2 target is low and similar between samples, ranging from 0.27 to almost 0.5 nm. Although there is an increase in surface roughness, it is well within the typical requirements for device use. Figure 3.15b shows how the feature size evolves with increasing oxygen pressure during film growth. It is possible that the first data point for films grown using the Zr target is misinterpreted given that the lack of morphological features makes their size determination difficult. The feature sizes range from 7 nm to 27 nm, when deposited at 1 mTorr and 30 mTorr respectively, by ablating the ZrO_2 target, correlating well with figure 3.15b.

Transmission electron microscopy was performed on samples deposited with both targets at 1 and 10 mTorr oxygen pressure, and results are presented next. Such depositions were performed on 10 × 10 mm^2 KBr substrates, dissolved in deionised water and the films transferred to a copper grid. No plasma cleaning was performed in these samples, to avoid surface oxidation of the ZrO_2 films. Figure 3.16 shows the background subtracted EELS measurements of oxygen K edge and of the low loss region, conducted on films deposited with both targets, at 1 and 10 mTorr.

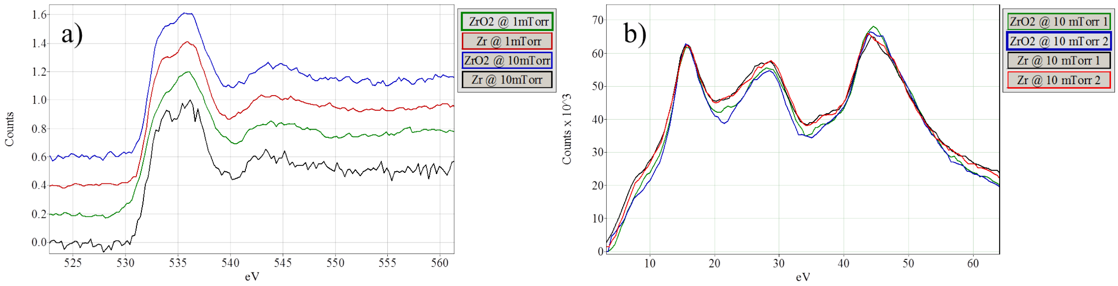

Figure 3.16: EELS measurements on ZrO_2 deposited at 1 and 10 mTorr using the Zr and ZrO_2 targets. a) Oxygen K edge and b) low-loss region comparing films deposited with Zr and ZrO_2 targets, both at 10 mTorr. Numbers 1 and 2 indicate that spectra was obtained on different measurements and in different regions on the samples. Spectra were scaled vertically by matching the intensities on the first feature.

These samples were chosen because 1 and 10 mTorr gave the biggest difference in the roughness analysis. Figure 3.16a shows the oxygen K edge for samples deposited at 1 and 10 mTorr. Surprisingly, all the spectra appear to be very similar, without subtle differences normally attributed to differences in the oxidation states. In this plot, the biggest difference is expected to be between samples deposited with the Zr target at 1 mTorr and those using the ZrO_2 target at 10 mTorr, which are represented by the red and blue lines, respectively. Nevertheless, both profiles match perfectly, indicating no difference in the oxygen K edge for films deposited at 1 and 10 mTorr with Zr and ZrO_2 targets, respectively. The Zr M edge showed exactly the same result and because of this its not shown. However, some differences are found for the low-loss region, in the spectra obtained for films deposited with Zr and ZrO_2 at 10 mTorr. There is very good agreement on the position of the main features, but subtle differences around 22 and 37 eV. Interestingly, this variation has been linked to different structures, namely cubic and tetragonal phases, in cation stabilised zirconia [186, 187]. Alternatively, such differences were suggested to be linked to different collective excitations between the valence and conduction bands of transition metals [186]. A more detailed analysis covering low-loss EELS in stabilised zirconia is presented in chapter 6, when presenting the characterisation performed on devices from collaborators from Jülich. Results presented here suggest that all films analysed have very similar stoichiometries. Furthermore, the determination of the absolute stoichiometry was impossible to calculate without performing measurements on reference samples with a variety of known compositions. Hence, for all measurements, and for practical purposes, zirconia films deposited at 1 and 10 mTorr, and with Zr and ZrO_2 have the same oxidation level. Interestingly, this can suggest two things: first, the minimum oxygen pressure used here is high enough to promote complete zirconia oxidation, and second, oxidation is not taking place during laser ablation but rather at the film surface. It is important to note that the results presented herein are a summary of the extensive number of datasets analysed. Figure 3.17 shows what films look like in CTEM with a magnification of 40 kx.

The first observation is that films deposited at the same pressure have the same characteristic features, in other words, images look similar for films deposited at the same background pressure. It is clear that films deposited at 1 mTorr, shown in figures 3.17a and 3.17b, have significantly larger features when compared to those present in films deposited at 10 mTorr, shown in figures 3.17c and 3.17d. It is also clear that films deposited by ablating the ZrO_2 target, seen in figures 3.17b and 3.17d, have a higher density of features in comparison with the films deposited with the Zr target, seen in figures 3.17a and 3.17c). Interestingly, bright field images also suggest that the distribution of nanocrystallites is homogeneous, suggesting that this is due to nucleation while film is growing. It is evident that the use of different oxygen pressures induces greater changes on the film's properties than those caused by the use of metal or metal-oxide target, which was unexpected. The TEM bright field

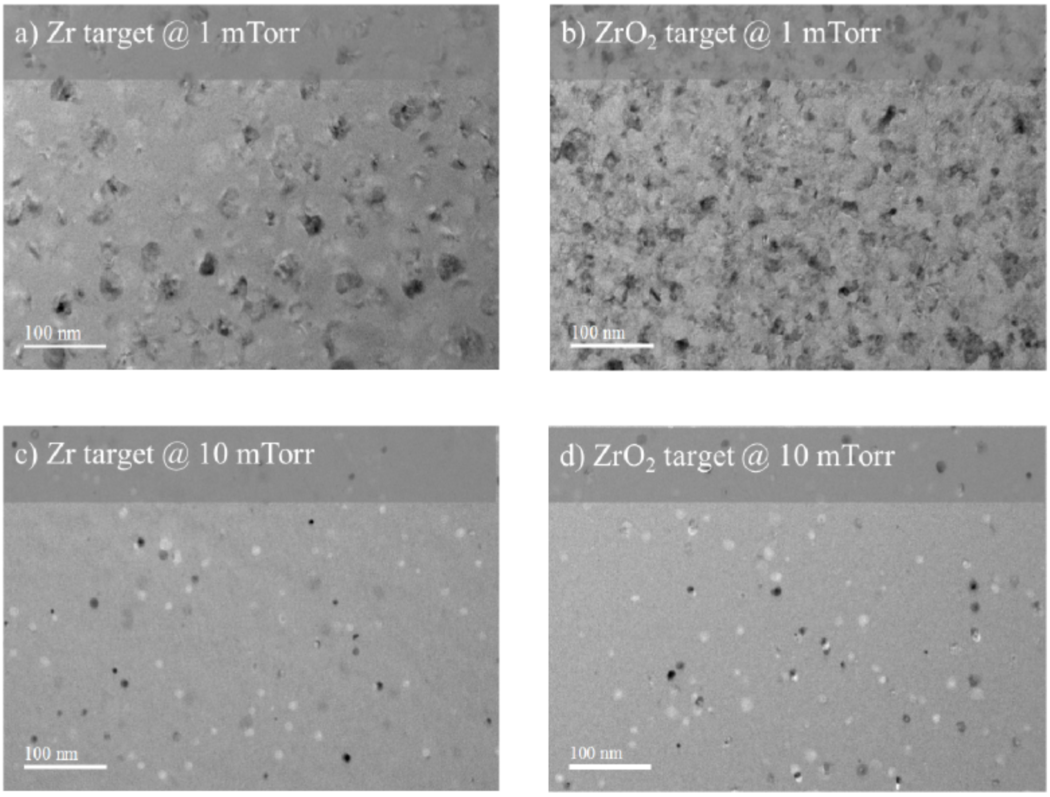

Figure 3.17: Bright field CTEM image of the ZrO_2 films imaged at 40kx.

images obtained from films deposited at 1 mTorr are consistent with the literature [183], especially the shape and density of crystallites. Alternatively, nanocrystallites can also be explained by heterogeneous particle nucleation in the gas phase, when the background pressure during laser ablation is sufficiently high, becoming embedded in a depositing film [178, 188]. Heterogeneous particle nucleation would explain why spherical nanoparticles are only seen on films deposited at higher pressures. In order to understand what the features are higher magnification imaging was performed on the same samples. Figure 3.18 presents ZrO_2 films deposited using the Zr target at 1 and 10 mTorr.

The first striking observation has to do with the amorphous characteristic of the films. It is clear from figure 3.18 that the features seen in the lower magnification images are nanocrystallites dispersed in an amorphous matrix. According to figure 3.18 the deposition background pressure influences the density and size of the crystallites, which changes from 30 to 10 nm for 1 and 10 mTorr respectively. The inset of both images shows higher magnification images where the lattice fringes are clearly seen: for both films, fringes are consistent with cubic ZrO_2 with d_{100} = 5.04 Å and d_{111} = 2.95 Å [189, 190]. Figure 3.19 shows electron diffraction patterns obtained for the samples imaged and presented

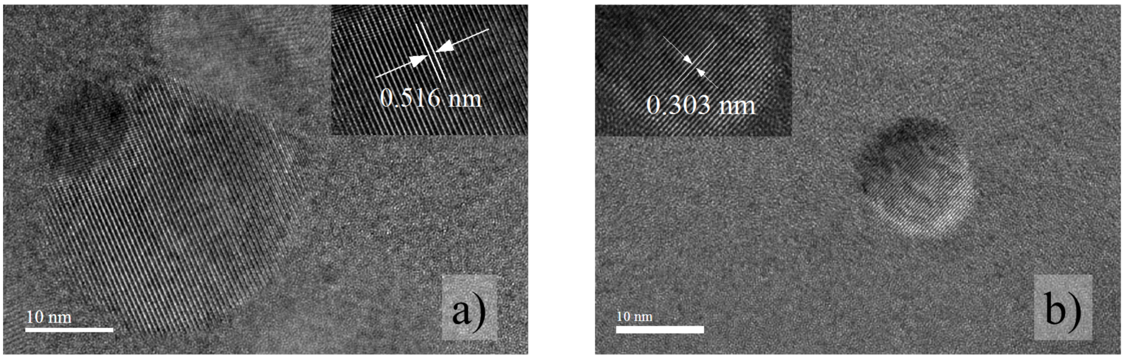

Figure 3.18: Bright field HRTEM image of the ZrO_2 films imaged at 400kx. Films were deposited using the Zr target at a) 1 mTorr and b) 10 mTorr.

before. They show that films deposited at 1 mTorr are textured which contrasts with the non-textured films obtained at 10 mTorr. At this point it is important to remember that planar view and diffraction figures were obtained with films deposited onto single crystal KBr substrates. The diffraction patterns, figures 3.19a and 3.19b strongly suggest that there is some structural order induced from the sc-KBr substrate, indicated by the four fold symmetry. This phenomenon is very unlikely to occur when depositing onto amorphous layers, suggesting not only a lower density of nanocrystallites in such films, but also a lack of crystalographic alignment. Still, the diffractograms reveal that the main part of the intensity is allocated to diffuse rings, although they are interspersed with a small number of singular spots. These observations corroborates the film is predominantly amorphous, but a few small crystallites [191] with dimensions of 10 to 30 nm are present, as mentioned above. It is also observed that films deposited with the ZrO_2 target seem to have a bigger nanocrystallite density when deposited at the same pressure, as shown by the existence of more interspersed spots (note that the higher density of nanocrystallites is also seen in figure 3.17).

It is known that pulsed laser deposition generates high energy ions that will promote surface mobility giving rise to smooth and compact films [115], as discussed in chapter 2 while describing pulsed laser deposition technique. When compared to other PVD or CVD deposition techniques, PLD makes use of ionic species with the highest kinetic energy which is useful because it enables the preparation of films with higher crystallinity [116, 118] possibly at lower substrate temperatures. It is likely that the increase in pressure (from 1 to 10 mTorr) is responsible for an increase in the amorphous-to-crystalline ratio because collisions with the background gas particles quench the ablated species. Lower

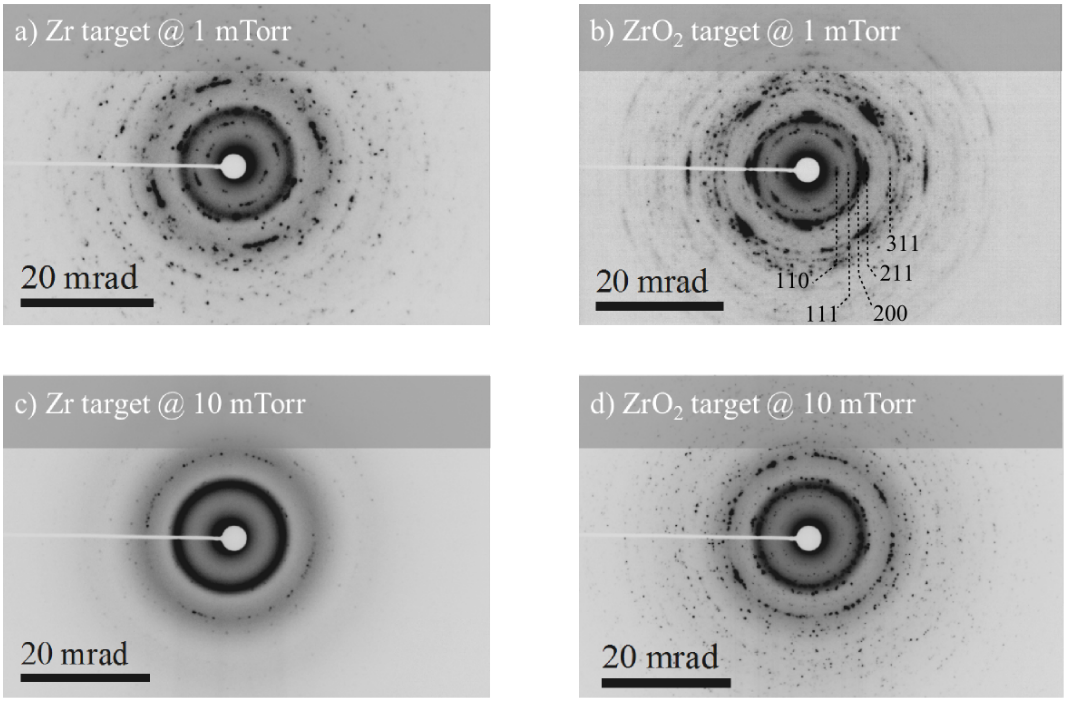

Figure 3.19: Diffraction patterns of the ZrO_2 films obtained for 1 and 10 mTorr deposited with Zr and ZrO_2 targets.

energy species will have lower mobility once on the substrate giving rise to amorphous materials, as covered in the introduction on page 85. Crystallisation will also be induced by high energy ions occasionally hitting the amorphous film during deposition. In addition, oxide targets will give rise to more energetic ablation judging by the finer lines in the diffraction images of figure 3.19. Finally, the optical properties of the target, namely its reflectivity, will influence how the ablation process takes place. Hence, it is possible that the higher absorption of the ZrO_2 target promotes more energetic plasma expansion, that leads to ejection species with higher energies, yielding more crystalline films.

Optical analysis that comprises transmittance and band gap determination was made in order to compare how the oxygen pressure during growth influences the structural and optoelectronic properties of the films. Figure 3.20 shows transmittance curves for zirconia films obtained by ablating ZrO_2 and Zr targets respectively. The general trend for both plots is an increased transmittance for films deposited at higher oxygen pressures, regardless of which target was used. This agrees with literature for ZrO_2 and is a normal trend in a significant number of binary metal oxides [192–195].

The trend for samples obtained with the ablation of Zr is similar for all pressures, which is what happens for ZrO_2 albeit with a different trend. Moreover, it appears that the samples deposited at 1 and 10 mTorr are optically very similar, even when films are deposited by

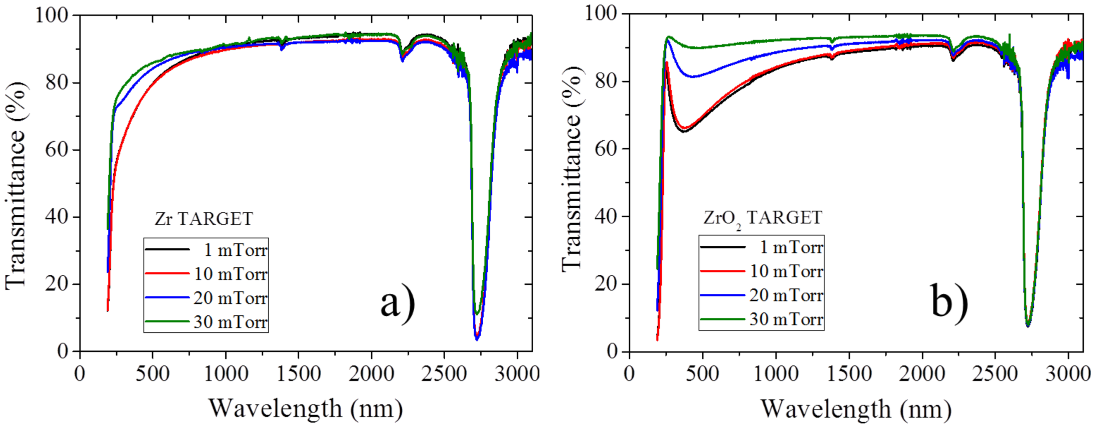

Figure 3.20: Total optical transmittance for ZrO_2 films prepared by ablating a) ZrO_2 and b) Zr target at different oxygen pressures. All films are 30 nm thick.

ablating different target materials. This corroborates the hypothesis that the minimum oxygen pressure used hereby is enough to fully oxidise zirconium. The behaviour of samples deposited at 20 and 30 mTorr is different, in both batches, and it follows the expectation that zirconia films should become more transparent with increasing oxygen pressure during growth [195, 196]. Zirconia is an insulator with a direct optical band gap that ranges from 4.2 to 7.1 eV depending on the crystalline phase and the determination method [194, 196–198]. Cubic zirconia has the lowest band gap and monoclinic has the highest [194, 199]. The fundamental optical absorption, which corresponds to electron transition from the valence band to conduction band, can be used to determine the nature and value of the optical band gap. The relation between the absorption coefficients (α) and the incident photon energy ($h\nu$) can be written as $(\alpha h\nu)^{1/n} = A(h\nu - Eg)$ in what is known as a Tauc plot and where A is a constant, Eg is the band gap of the material and exponent n depends on the type of transition. For direct allowed, $n = 1/2$, for indirect allowed transition, $n = 2$, and for direct forbidden, $n = 3/2$ [200]. Figure 3.21 shows Tauc plots for direct and indirect interband transitions, for films obtained with both targets.

Direct band gap values determined for all samples are in very good agreement with the literature, depending on the crystalline phase and determination method [194, 197]. Films deposited with higher oxygen pressure have a marginally higher band-gap, changing from 5.45 to 5.87 eV and 5.80 to 5.90 eV for films obtained with Zr and ZrO_2 targets respectively. More importantly, the onset of the transition is more abrupt in films deposited with the ZrO_2 which suggest that such films have band gaps with less traps. This is of importance as RRAM device behaviour as traps are a known source of resistive switching, as covered

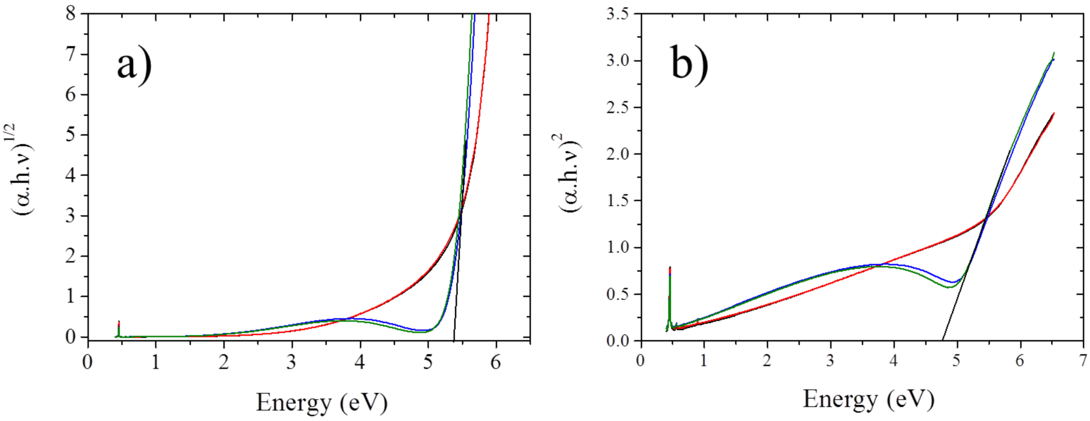

Figure 3.21: Tauc plot for zirconia films obtained by ablating Zr (black and red) and ZrO_2 (blue and green). a) direct and b) indirect band-gap. Absorption profiles are presented for samples deposited at 1 and 10 mTorr, for the sake of clarity.

in chapter 1 when describing space charge limited conduction, SCLC. Furthermore, an indirect band gap seems to exist as one can see by the linear fit, shown in figure 3.21b. This is surprising as zirconia is direct band gap material. Dash et al., among others, have suggested that the electronic excitation that resembles an indirect band gap, can be attributed to extrinsic absorption or to oxygen vacancy centres in the gap [201, 202]. Transitions attributed to “indirect band-gaps” have a lower values, ranging from 4.6 for films deposited with the Zr target, to 4.9 eV for ZrO_2, which agree with reported values [195, 201, 202]. Finally, some losses are not related to fundamental electronic absorption, but originate from scattering, mainly at grain boundaries, whose density is dependant on deposition conditions, as illustrated with the CTEM images on figures 3.17a, 3.17b and 3.18a.

3.3 Conclusion

Characterisation of the PLD ablation plume made possible the deposition of thin films with very good thickness homogeneity across a wide range of substrate sizes. The Matlab code developed for calculating the optimal substrate position gave very accurate thickness predictions that were matched by experimental results. Droplet free films were achieved by modifying the deposition procedure in two ways: first by adding an aperture to the laser path, and second by reducing the ablation area on the targets. The laser aperture reduces the beam's cross section, eliminating the lower flux tails and promoting homogeneous vaporisation of the target surface. By reducing the ablation area, it is possible to achieve a smoother target surface, greatly reducing the possibility of exfoliation which further helps in reducing macroscopic particulate formation.

Amorphous zirconia thin films were deposited at several oxygen pressures and with different targets (Zr and ZrO_2) to understand of this can affect their properties. When it comes to surface roughness, it was shown that films deposited at higher pressures, 30 mTorr, are rougher than films deposited at lower pressures, 1 mTorr. This is attributed to (1) a lower surface diffusion during film growth and (2) to shadowing, where it is the loss of directionality of the ablated species that increases roughness. Surface roughness is important because RRAM devices use insulator layers with increasingly lower thicknesses, sometimes of the same order of magnitude as surface roughness. One good example is the YSZ/PCMO RRAM devices presented in chapter 6, where the YSZ has a total thickness of 3 nm, which is lower than the peak-to-peak roughness profile shown in figure 3.14. Structural order is also affected by different growth conditions. The first interesting observation is that films grown with a metallic or oxide target seem to have less of an influence in film properties than when compared to films deposited at different pressures. Films deposited at 1 mTorr have significantly bigger crystallites than films deposited at 10 mTorr, for both targets. Diffraction results suggest that the use of single crystal substrates plays a role in film growth, as indicated by the symmetry in diffraction patterns. Hence, this effect is not expected to play a significant role in the RS behaviour of amorphous based devices. EELS analysis was performed extensively on zirconia films grown at all pressures, but differences are subtle and ambiguous. This is the reason for not focusing much on EELS results obtained for zirconia TEM specimens. However, EELS results indicate that films grown at 1 mTorr are already oxidised to ZrO_2, which indicates that oxidation is mostly happening at the surface of the film during growth. It likely possible that changes on the oxidation level of zirconia take place at oxygen pressures lower than 1 mTorr, the minimum employed here. This is corroborated by UV-VIS analysis where there is almost no variation in the value of the direct band gap. However, the trend of the Tauc plot suggests that films deposited with the ZrO_2 target may have lower trap densities within the energy gap. Additionally, the existence of an "indirect band-gap" for zirconia is linked to the existence of extrinsic absorption, by doping or impurities, or to oxygen vacancy centres in the gap.

In chapter 5 and 6, electrical characterisation of of RRAM devices based on amorphous and crystalline zirconia will be presented. In both cases, films were grown with an oxygen pressure of 2 mTorr, because they yield devices with better performance figures. Interestingly, films grown at a pressure higher than 10 mTorr give rise to devices which are too insulating and, even though RS is always observed, it is much less reproducible. Interestingly, with the results presented in this chapter, the increase in resistance should be related to the existence of less crystallites and not differences in stoichiometry.

Bibliography

[4] Shimeng Yu, Byoungil Lee, and H S Philip Wong. *Functional Metal Oxide Nanostructures.* Ed. by Junqiao Wu, Jinbo Cao, Wei-Qiang Han, Anderson Janotti, and Ho-Cheol Kim. Vol. 149. Springer Series in Materials Science. New York, NY: Springer New York, 2012, pp. 303–335. DOI: `10.1007/978-1-4419-9931-3`.

[114] Milton Ohring. *The Materials Science of Thin Films.* 1992.

[115] P. Willmott and J. Huber. “Pulsed laser vaporization and deposition”. In: *Reviews of Modern Physics* 72.1 (Jan. 2000), pp. 315–328. DOI: `10.1103/RevModPhys.72.315`.

[116] C. Belouet. “Thin film growth by the pulsed laser assisted deposition technique”. In: *Applied Surface Science* 96-98 (Apr. 1996), pp. 630–642. DOI: `10.1016/0169-4332(95)00535-8`.

[118] M. R. Rashidian Vaziri, F. Hajiesmaeilbaigi, and M. H. Maleki. “Monte Carlo simulation of the subsurface growth mode during pulsed laser deposition”. In: *Journal of Applied Physics* 110.4 (2011), p. 043304. DOI: `10.1063/1.3624768`.

[121] S Amoruso, R Bruzzese, N Spinelli, and R Velotta. “Characterization of laser-ablation plasmas”. In: *Journal of Physics B: Atomic, Molecular and Optical Physics* 32.14 (1999), R131.

[127] Z. Zhang and Max G. Lagally. *Atomistic Processes in the Early Stages of Thin-Film Growth.* 1997. DOI: `10.1126/science.276.5311.377`.

[159] Feng Miao et al. “Anatomy of a nanoscale conduction channel reveals the mechanism of a high-performance memristor.” In: *Advanced materials (Deerfield Beach, Fla.)* 23.47 (Dec. 2011), pp. 5633–40. DOI: `10.1002/adma.201103379`.

[160] Zhaoliang Liao et al. “Electrode engineering for improving resistive switching performance in single crystalline CeO2 thin films”. In: *Solid-State Electronics* 72 (June 2012), pp. 4–7. DOI: `10.1016/j.sse.2011.10.001`.

[161] H. Mähne et al. “Filamentary resistive switching in amorphous and polycrystalline Nb2O5 thin films”. In: *Solid-State Electronics* 72 (June 2012), pp. 73–77. DOI: `10.1016/j.sse.2012.01.005`.

[162] Youn Hee Kang et al. “Observation of conductive filaments in a resistive switching nonvolatile memory device based on amorphous InGaZnO thin films”. In: *Materials Chemistry and Physics* 138.2-3 (Mar. 2013), pp. 623–627. DOI: `10.1016/j.matchemphys.2012.12.029`.

[163] B. Govoreanu et al. “10 x 10 nm2 Hf/HfOx crossbar resistive RAM with excellent performance, reliability and low-energy operation”. In: *Electron Devices Meeting (IEDM), 2011 IEEE International.* Dec. 2011, pp. 31.6.1–31.6.4. DOI: `10.1109/IEDM.2011.6131652`.

[164] Michael Störmer and Hans-Ulrich Krebs. “Structure of laser deposited metallic alloys”. In: *Journal of Applied Physics* 78.12 (1995), p. 7080. DOI: `10.1063/1.360414`.

[165] L. Cultrera, M. Zeifman, and a. Perrone. “Investigation of liquid droplets, plume deflection, and a columnar structure in laser ablation of silicon”. In: *Physical Review B* 73.7 (Feb. 2006), p. 075304. DOI: `10.1103/PhysRevB.73.075304`.

[166] N Cherief, D Givord, and A Lienard. “Laser ablation deposition and magnetic characterization of metallic thin films based on rare earth and transition metals”. In: *Journal of magnetism . . .* 121 (1993), pp. 94–101.

[167] S Fähler, M Störmer, and HU Krebs. “Origin and avoidance of droplets during laser ablation of metals”. In: *Applied surface science* (1997), pp. 433–436.

[168] R. E. Leuchtner, J. S. Horwitz, and D. B. Chrisey. “Particulate distributions in Pt films prepared by pulsed laser deposition”. In: *Journal of Applied Physics* 83.10 (1998), p. 5477. DOI: `10.1063/1.367405`.

[169] E Agostinelli, S Kaciulis, and M Vittori-Antisari. “Great reduction of particulates in pulsed laser deposition of Ag–Co films by using a shaded off-axis geometry”. In: *Applied Surface Science* 156.1-4 (Feb. 2000), pp. 143–148. DOI: `10.1016/S0169-4332(99)00490-0`.

[170] E. Van De Riet, C. J. C. M. Nillesen, and J. Dieleman. “Reduction of droplet emission and target roughening in laser ablation and deposition of metals”. In: *Journal of Applied Physics* 74.3 (1993), p. 2008. DOI: `10.1063/1.354763`.

[171] Seong Shan Yap, Alesya Viktorovna Salomatova, Cécile Ladam, Øystein Dahl, and Turid Worren Reenaas. “Pulsed laser ablation and deposition of silicon”. In: *Applied Physics A* 101.4 (July 2010), pp. 765–770. DOI: `10.1007/s00339-010-5934-3`.

[172] H. L. Spindler, R. M. Gilgenbach, and J. S. Lash. “Effects of laser-ablation target damage on particulate production investigated by laser scattering with deposited thin film and target analysis”. In: *Applied Physics Letters* 68.23 (1996), p. 3245. DOI: `10.1063/1.116562`.

[173] Jyrki Lappalainen, Johannes Frantti, and Vilho Lantto. “Surface Structure and Particulate Generation in”. In: *Journal of the American Ceramic Society* 96 (1999), pp. 889–896. DOI: `10.1111/j.1151-2916.1999.tb01850.x`.

[174] Peter K. Schenck, Mark D. Vaudin, David W. Bonnell, John W. Hastie, and Albert J. Paul. “Particulate reduction in the pulsed laser deposition of barium titanate thin films”. In: *Applied Surface Science* 127-129 (May 1998), pp. 655–661. DOI: `10.1016/S0169-4332(97)00721-6`.

[175] J. Brandenburg et al. “Pulsed laser deposition of metals: consequences of the energy distribution within the laser spot on film growth”. In: *Applied Physics A* 79.4-6 (July 2004), pp. 1005–1007. DOI: `10.1007/s00339-004-2615-0`.

[176] Ted D. Bennett, Costas P. Grigoropoulos, and Douglas J. Krajnovich. “Near-threshold laser sputtering of gold”. In: *Journal of Applied Physics* 77.2 (1995), p. 849. DOI: `10.1063/1.359010`.

[177] “Ultrafast Laser Ablation and Film Deposition”. In: *Pulsed Laser Deposition of Thin Films.* John Wiley & Sons, Inc., 2006, pp. 99–129. DOI: `10.1002/9780470052129.ch5`.

[178] “Growth Kinetics During Pulsed Laser Deposition”. In: *Pulsed Laser Deposition of Thin Films.* John Wiley & Sons, Inc., 2006, pp. 177–190. DOI: `10.1002/9780470052129.ch8`.

[179] J.F.M. Cillessen, R.M. Wolf, and D.M. de Leeuw. “Pulsed laser deposition of heteroepitaxial thin Pt films on MgO(100)”. In: *Thin Solid Films* 226.1 (Apr. 1993), pp. 53–58. DOI: `10.1016/0040-6090(93)90205-4`.

[180] M.A. Herman, W. Richter, and H. Sitter. *Epitaxy: Physical Principles and Technical Implementation.* Springer Series in Materials Science. Springer Berlin Heidelberg, 2010.

[181] R Messier, AP Giri, and RA Roy. "Revised structure zone model for thin film physical structure". In: *... of Vacuum Science & Technology A* 16802.June (1984), pp. 500–503.

[182] "Pulsed Laser Deposition of Metals". In: *Pulsed Laser Deposition of Thin Films.* John Wiley & Sons, Inc., 2006, pp. 363–382. DOI: 10.1002/9780470052129.ch16.

[183] G. Balakrishnan, K. Thanigaiarul, P. Sudhakara, and Jung Il Song. "Microstructural and optical properties of nanocrystalline undoped zirconia thin films prepared by pulsed laser deposition". In: *Applied Physics A* 110.2 (Sept. 2012), pp. 427–432. DOI: 10.1007/s00339-012-7232-8.

[184] Aditya Sharma et al. "Monoclinic to tetragonal phase transition in ZrO2 thin films under swift heavy ion irradiation: Structural and electronic structure study". In: *Chemical Physics Letters* 592 (Jan. 2014), pp. 85–89. DOI: 10.1016/j.cplett.2013.12.012.

[185] R. Álvarez et al. "Morphological evolution of pulsed laser deposited ZrO[sub 2] thin films". In: *Journal of Applied Physics* 107.5 (2010), p. 054311. DOI: 10.1063/1.3318604.

[186] Dw McComb. "Bonding and electronic structure in zirconia pseudopolymorphs investigated by electron energy-loss spectroscopy." In: *Physical review. B, Condensed matter* 54.10 (Sept. 1996), pp. 7094–7102.

[187] S Ostanin et al. "Effect of relaxation on the oxygen K -edge electron energy-loss near-edge structure in yttria-stabilized zirconia". In: *Physical Review B* 62.22 (2000), pp. 728–735. DOI: 10.1103/PhysRevB.62.14728.

[188] D. P. Norton, C. Park, J. D. Budai, S. J. Pennycook, and C. Prouteau. "Plume-induced stress in pulsed-laser deposited CeO2 films". In: *Applied Physics Letters* 74.15 (1999), p. 2134. DOI: 10.1063/1.123780.

[189] S. K. Peneva, S. Gutzov, K. D. Djuneva, G. Atanasov, and Ts Marinova. "Metastable ZrO2 crystal structures in electron beam evaporated thin films". In: *Zeitschrift fur Kristallographie* 215.2 (2000), pp. 88–95. DOI: 10.1524/zkri.2000.215.2.88.

[190] R.a. Ploc. "The lattice parameter of cubic ZrO2 formed on zirconium". In: *Journal of Nuclear Materials* 99.1 (1981), pp. 124–128. DOI: 10.1016/0022-3115(81)90146-X.

[191] Sebastian Heiroth et al. “Crystallisation and grain growth characteristics of yttria-stabilized zirconia thin films grown by pulsed laser deposition”. In: *Solid State Ionics* 191.1 (2011), pp. 12–23. DOI: `10.1016/j.ssi.2011.04.002`.

[192] a De and S Ray. “A study of the structural and electronic properties of magnetron sputtered tin oxide films”. In: *Journal of Physics D: Applied Physics* 24.5 (May 1991), pp. 719–726. DOI: `10.1088/0022-3727/24/5/014`.

[193] M.F. Al-Kuhaili and S.M.a. Durrani. “Effect of annealing on pulsed laser deposited zirconium oxide thin films”. In: *Journal of Alloys and Compounds* 509.39 (Sept. 2011), pp. 9536–9541. DOI: `10.1016/j.jallcom.2011.07.062`.

[194] G. Balakrishnan et al. “Influence of oxygen partial pressure on the properties of pulsed laser deposited nanocrystalline zirconia thin films”. In: *Applied Surface Science* 257.20 (Aug. 2011), pp. 8506–8510. DOI: `10.1016/j.apsusc.2011.05.003`.

[195] S. Heiroth, R. Ghisleni, T. Lippert, J. Michler, and A. Wokaun. “Optical and mechanical properties of amorphous and crystalline yttria-stabilized zirconia thin films prepared by pulsed laser deposition”. In: *Acta Materialia* 59.6 (2011), pp. 2330–2340. DOI: `http://dx.doi.org/10.1016/j.actamat.2010.12.029`.

[196] Meltem Asiltürk, Esin Burunkaya, Funda Say, and Nadir Kiraz. “Structural and optical properties of thin fi lms prepared from surface modified ZrO2”. In: *Journal of Non-Crystalline Solids* 357 (2011), pp. 206–210. DOI: `10.1016/j.jnoncrysol.2010.09.034`.

[197] Francoise Hanus and Lucien D. Laude. “Pulsed laser deposition of polycrystalline zirconia thin films”. In: (May 1998). Ed. by Vladimir I. Pustovoy, pp. 17–21. DOI: `10.1117/12.308617`.

[198] M Filipescu, N Scarisoreanu, V Craciun, B Mitu, and A Purice. “High-k dielectric oxides obtained by PLD as solution for gates dielectric in MOS devices”. In: *Applied Surface Science* 253 (2007), pp. 8184–8191. DOI: `10.1016/j.apsusc.2007.02.166`.

[199] Latha Kumari et al. “Synthesis, microstructure and optical characterization of zirconium oxide nanostructures”. In: *Ceramics International* 35.6 (Aug. 2009), pp. 2401–2408. DOI: `10.1016/j.ceramint.2009.02.007`.

[200] a.N. Banerjee, S. Kundoo, and K.K. Chattopadhyay. “Synthesis and characterization of p-type transparent conducting CuAlO2 thin film by DC sputtering”. In: *Thin Solid Films* 440.1-2 (Sept. 2003), pp. 5–10. DOI: `10.1016/S0040-6090(03)00817-4`.

[201] L. Dash, Nathalie Vast, Philippe Baranek, Marie-Claude Cheynet, and Lucia Reining. “Electronic structure and electron energy-loss spectroscopy of ZrO2 zirconia”. In: *Physical Review B* 70.24 (Dec. 2004), p. 245116. DOI: `10.1103/PhysRevB.70.245116`.

[202] Paul Erhart, Andreas Klein, Russell G. Egdell, and Karsten Albe. “Band structure of indium oxide: Indirect versus direct band gap”. In: *Physical Review B - Condensed Matter and Materials Physics* 75.15 (2007), pp. 1–4. DOI: `10.1103/PhysRevB.75.153205`.

Chapter 4

Optimisation of Epitaxial Thin Film deposition via PLD

This chapter focuses on the deposition of crystalline and conductive perovskites oxides for use as electrodes. It builds on the results of the last chapter but will focus on optimised deposition of epitaxial films, which typically requires finer kinetic control over the deposition process. It is shown that the preparation of single crystal substrates is key to subsequent epitaxial deposition of electrodes with the required electrical, structural and morphological properties. The optimisation of the deposition parameters is described using a correlation with RHEED measurements. Resistive switching devices prepared with the techniques described in this chapter will be characterised electrically and by STEM EELS in chapter 6.

4.1 Introduction

The deposition of epitaxial thin films is experimentally more demanding than the deposition of amorphous or polycrystalline materials. The reason for this has to do with a number of constraints, including the need to have matched lattices and, ideally, similar thermal expansion coefficients between the film and the substrate. In the previous chapter, thermodynamics was used to describe amorphous thin film growth, and the resulting film morphology is commonly rationalised by considerations of the surface and interfacial energies of film and substrate. For the description of epitaxial films, on the other hand, kinetic considerations are also important. In many vapour-phase deposition techniques, for example PLD, the growing film is usually not in thermodynamic equilibrium. In fact, the deposition can be regarded as instantaneous for every laser pulse in PLD, followed by a period of time where the adatoms rearrange on the surface by migration and subsequent incorporation through nucleation and growth. This rearrangement process can also be considered as an annealing process, but the kinetic energy available to adatoms derives from the ablation process, and can greatly exceed typical thermal energies determined by the substrate temperature. As a result, the two basic processes, random deposition then growth through rearrangement are separated in time, which is unique to PLD [178]. However, because of kinetic limitations to surface diffusion, the deposited material may not rearrange itself to minimise the surface energy. For example, a high supersaturation of the vapour leads to a large nucleation rate, and in this case, kinetic effects will lead to the occurrence of different growth modes [178]. In the case of homoepitaxy, where the substrate and film are the same material, there is no difference in thermal expansion coefficients or lattice mismatch, thus, the crystalline structure of the substrate is extended into the growing film [178]. If this is the case, only two-dimensional (2D) growth modes are expected, on the basis of the thermodynamic arguments set out in figure 3.4 (page 82). However, the behaviour of deposited species is determined by a number of kinetic parameters, including a surface diffusion coefficient (D_s) of the adatoms along each crystallographic direction, the sticking probability of an adatom arriving at the edge of a terrace, and the additional energy barrier (E_s) for adatoms to descend the edge to a lower terrace. The diffusion coefficient is the most important as it determines the average distance an atom can travel on an atomically flat surface before being trapped [178]. This distance is the surface diffusion length l_D and can be defined by:

$$l_D = \sqrt{D_s \tau} \tag{4.1}$$

where τ is the amount of time an adatom spends at a surface before re-evaporation. The surface diffusion coefficient D_s can be expressed as:

$$D_s = \upsilon a^2 exp(\frac{-E_A}{kT}) \tag{4.2}$$

where E_A is the activation energy for diffusion, υ the attempt frequency and a is the characteristic jump distance [178]. To understand the possible 2D growth modes on both singular and vicinal substrates, two diffusion processes have to be considered. First, the diffusion of atoms on a terrace ("intralayer" mass transport) and second, the diffusion of an atom to a lower/upper terrace ("interlayer" mass transport). Intralayer mass transport will lead to step-flow growth as l_D is larger than the average terrace width. In other words, surface diffusion is high enough to enable adatoms to reach the edges of the steps where they coalesce (and not anywhere else on the surface). In contrast, when intralayer mass transport is not fast enough, preventing adatoms reaching the steps, layer-by-layer growth is observed. In this case, nuclei will be formed until a saturation density is reached and, at this point, islands will start to form from the middle of the terraces.

Growth of atomically sharp oxide heterostructures is essential to fabricating high performance RRAM devices based on homogeneous or interfacial resistive switching. Such devices consist of heteroepitaxial interfaces between metal oxides, typically with perovskite structure (with composition ABO_3), and the performance (and essentially reproducibility) often depends on the quality of the interface [26, 27]. If the surface structure is simply the unreconstructed termination of the bulk crystallography, then a perovskite (100) surface has two possible terminations, AO and BO_2, since the crystal consists of an alternating stack of these two planes. Thus, if the terminating layer is not uniquely defined, two types of interfaces can form, degrading interfacial properties due to chemical and electronic uncertainty on a unit-cell scale [203, 204]. An ideal surface should have only one of the two terminations with a regular step structure. Figures 4.1a and 4.1b illustrates the unit cell of STO and atomic planes composed of SrO and TiO_2 alternately.

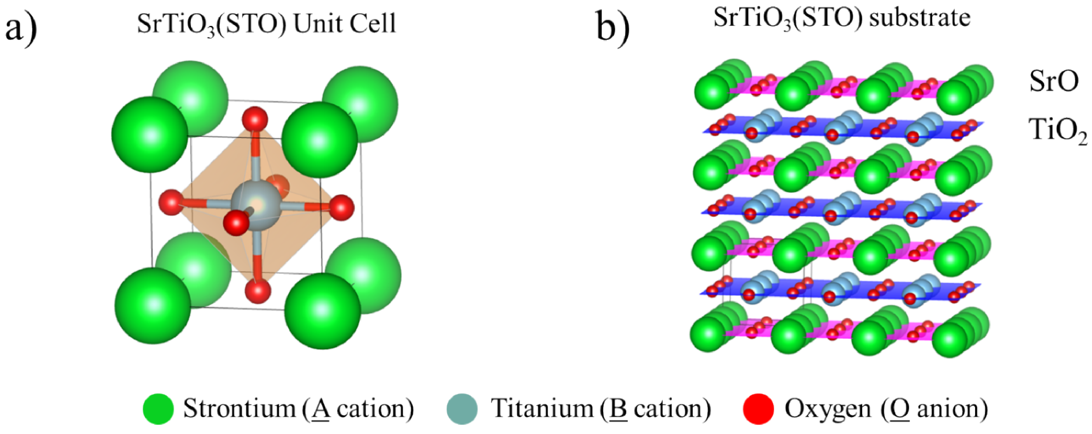

Figure 4.1: Schematic of $SrTiO_3$ a) unit cell and b) atomic planes alternating between SrO (pink) and TiO_2 (blue).

The cubic form of STO is referred to as an ideal perovskite and has a unit-cell edge length of approximately 3.9 Å [205]. In such cubic structure the A cations are located at the corners, O atoms are on the faces and the B cation is in the centre of the unit cell, as seen in figure 4.1. A tolerance factor, t, was defined by Goldschmidt in 1926 [206], to describe the stability limits of the perovskite structure, according to

$$t = (R_A + R_O)/2^{1/2}(R_B + R_O), \tag{4.3}$$

where R_A, R_B, and R_O are the ionic radii of A and B cations and oxygen. Perovskites are stable within the range of $0.75 < t < 1.0$ with t normally between 0.8 and 0.9, meaning that its structure possesses a high degree of compositional flexibility, which allows the accommodation of a wide variety of A and B cations. Because of this, perovskites exhibit many interesting conducting and chemical properties, including catalytic activity, but most important for RRAM properties, oxygen transport capability [205]. In fact, this is one of the reasons for using $PrCaMnO_3$ (PCMO) in the RRAM devices characterised in chapter 6. Interestingly, a different oxygen pressure during film growth induces changes that range from differences in the structure, as explained in chapter 6 regarding stabilised zirconia, to different oxidation states, which are known to influence RRAM device behaviour. For the devices presented in chapter 6, an epitaxial conductive oxide was required to form the bottom electrode, hence, Nb:STO thin films deposited at different oxygen pressures are characterised and an explanation of how such variation influences RRAM devices is presented. In order to do this, strontium titanate substrates were used because they have no lattice mismatch with Nb:STO and only a very small (0.6%) mismatch with pseudocubic $SrRuO_3$ (which is another electrode candidate material) and are chemically stable at high temperatures [207]. This not only enables the deposition of more complex RS layers, like PCMO and $LaSrMnO_3$ (LSMO), but also allows for the deposition of ZrO_2 at very high temperatures (≈ 750 °C) where a metallic electrode would not be suited because it would (1) thermally decompose or (2) oxidise and become insulating. The next section will start by presenting a summarised characterisation of STO substrates, explaining how to obtain adequate surface properties for the epitaxial deposition of crystalline and conductive perovskite oxides.

4.2 Results

The results presented in the next section summarise progress towards optimised single crystal substrate preparation and epitaxial growth. Although a body of literature exists, it was found that both tasks are experimentally challenging, hence, many substrate preparation recipes were tested and PLD experimental parameters studied. The subsequent deposition of Nb:STO films is the main focus here, although the optimised substrate prep was also used for growth of $SrRuO_3$ (SRO), $LaSrTiO_3$ (LSTO) and $LaSrMnO_3$ (LSMO) in other projects, not reported here.

4.2.1 Preparation of $SrTiO_3$ (STO) substrates

Many studies describe STO surface treatments steps aimed at achieving atomically flat and single terminated surfaces, where high temperature annealing and acidic etching are often employed [128, 203, 204, 208–211]. High temperature anneals will restructure the surface as well as burn off organic contaminants. Acidic etching has been used to dissolve one of the terminations preferentially, giving rise to single terminated substrates. Alternatively, it has been shown that water etching can also be employed to obtain single terminated surfaces [212–214], the reason for this being the ionic nature of the SrO bond as opposed to the covalent in TiO_2, and the formation of SrO hydroxyl species [212, 215]. The advantage of water etching is (1) the non-toxicity of the process and (2) increase in reproducibility because water will only etch SrO [212]. As such, all substrates prepared within the scope of this work were etched with water. The AFM height images in figure 4.2 show (a) the surface of an as-received substrate and (b) the surface after annealing.

The as-received substrates, seen in figure 4.2a, show evidence of atomic steps, but these are very irregular and often show the effects of polishing, typically identified by scratches and steps with many unit cells in height (shown in the inset figure). Additionally, as-received substrates will regularly have small particulates that will affect epitaxial growth. There is general agreement in the literature that annealing in the range of 800-1000 °C gives the best results in terms of reproducibility of the surfaces obtained [204, 209, 212]. Furthermore, annealing at temperatures greater than 1300 °C seems to facilitate the migration of SrO to the surface [203, 210], which in our case is undesirable. However, we found that annealing at 1000 °C, even for longer periods of time, consistently gave unreproducible results where atomic steps were not seen regularly, contrasting with literature explicitly. In contrast, annealing the substrates for 2 hours at 1250 °C in the presence of oxygen,

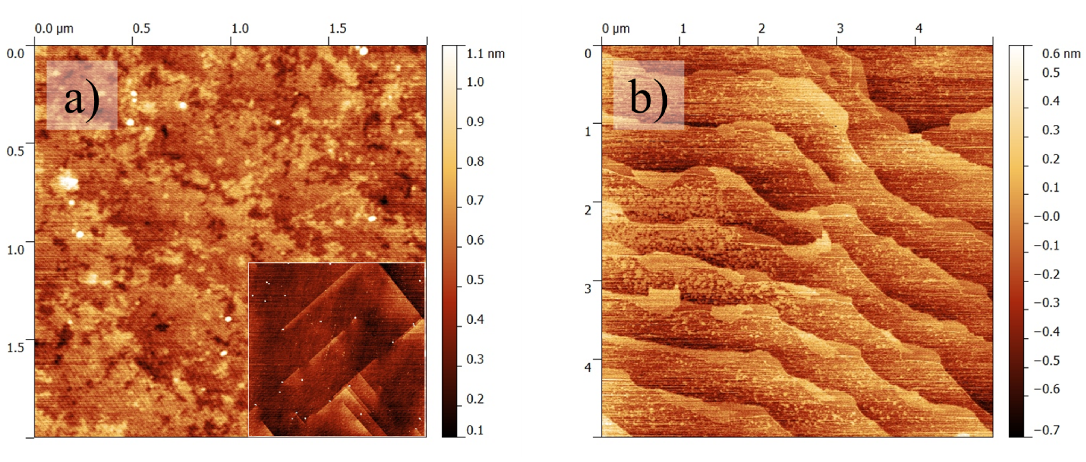

Figure 4.2: AFM images of the surface of $SrTiO_3$ substrates a) 2x2 μm^2 as received (inset 20x20 μm^2) b) 5x5 μm^2 after 2 hour anneal at 1250 °C in air.

a much smoother surface is obtained, with well defined atomic steps as can be seen in figure 4.2b. However, the surface is covered with small features that appear to be half-unit cell in height, suggesting a double terminated surface where TiO_2 and SrO coexist, as depicted by the yellow regions in figure 4.2b. By performing a short (30 second) water etch, surface smoothness improved significantly, and a reduction in the density of half-unit cell features is visible (figure 4.3a). At this point, additional water etches only turn the surface rougher and eventually another high temperature anneal is necessary. AFM phase imaging was used to try and understand what causes such features, what are they and how to avoid them. The phase imaging is sensitive to material surface properties such as elasticity and viscoelasticity on a nanometre scale, and can possible distinguish between TiO_2 and SrO terminated surfaces because of different damping conditions on tapping frequency, induced by different termination chemistry [210, 216–218]. Figure 4.3 shows height and phase images, of the same substrate, acquired during the same AFM scan. Interestingly, in the phase image of figure 4.3b, two distinct and alternate regions can easily be seen. This observation strongly suggests that two terminations, TiO_2 and SrO, are present in the surface. Additionally, by combining the height and phase images, shown in figure 4.3c, it appears that the terraces seen in the topography of figure 4.3a have both terminations. Regions close to the step appear yellow in figure 4.3b, whilst regions further away from the step edge, appear red and have a different termination. Figure 4.4 shows a smaller region on the same substrate surface, and where the height and phase images are presented together with a line profile (shown on figure 4.4c). The most interesting observation is related to the height differences given by the line profile, which for all

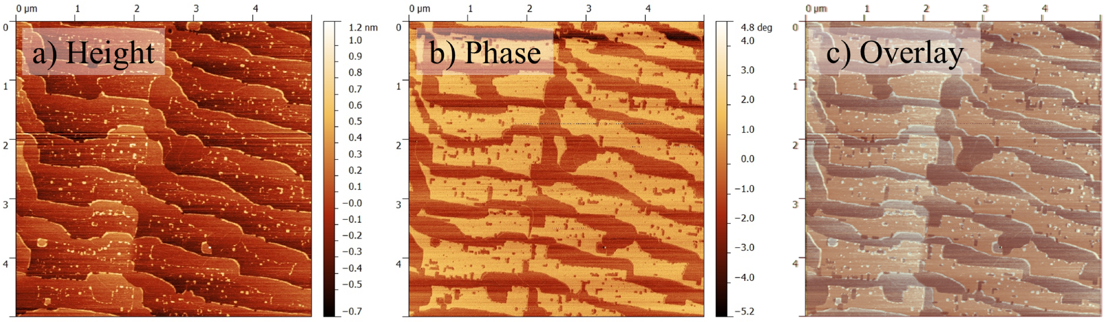

Figure 4.3: AFM images of the $SrTiO_3$ substrate shown in figure 4.2 after water etching, a) height and b) phase images c) overlay of height and phase images.

plateaus and small features match a half-unit cell of STO, approximately 2 Å (as given by the horizontal dashed lines).

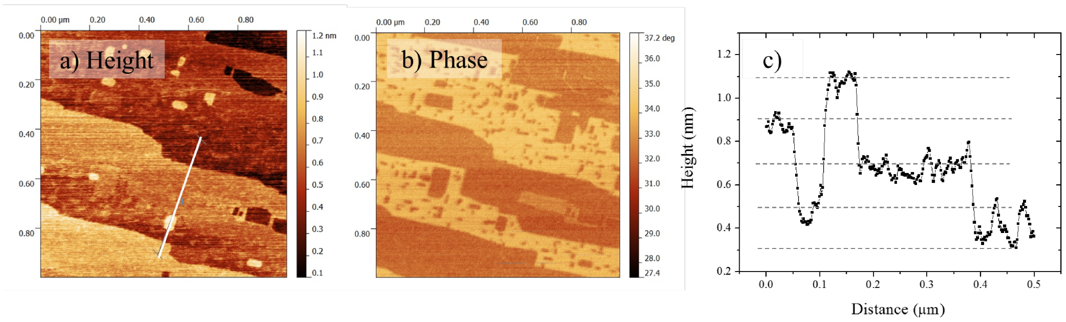

Figure 4.4: AFM images of the $SrTiO_3$ substrate shown in figure 4.2c in a) height and b) phase image. c) Line profile obtained from the indicated region in a), showing that the two terminations have height difference of half-unit cell, ≈ 0.2 Å.

Another interesting observation is linked to the geometry of the features, with a predominance of 90° angles, in the height image that appear to match the yellow regions on the phase image, as seen in figures 4.3a and 4.3b. Similar work on STO substrates found in literature, suggests that geometrical features on both height and phase images is a signature of SrO at the surface [208, 210–212]. This analysis proves that both surface terminations are present, and therefore, the annealing step and water etch are not giving rise to atomically flat single terminated surfaces. To overcome this, the annealing temperature was lowered to 1150 °C, the anneal time was reduced to 1 hour (instead of 2) and no wet etching was performed. In fact, the reproducibility when preparing STO substrates increased significantly when wet etchings were abandoned. Figure 4.5 illustrates the best results regarding STO substrate preparation. Figures 4.5a and 4.5d, show that single terminated and flat terraces were obtained with only unit cell step heights. However, in figure 4.5b, a darker region in the vicinity of the steps is visible, and this region matches the very subtle dip seen in the line profile of figure 4.5d. This subtle dip, less than 0.5 Å, is not believed to be due to the existence of a second termination of SrO or TiO_2, but rather to SrO hydroxyl groups on the surface layers. The phase image (figure 4.5c) shows very little contrast and is completely different from those in figures 4.3b and 4.4b, which corroborates to some extent the existence of just one termination. Furthermore, features with a predominance of 90° angles are not observed, which is in accordance with a TiO_2 terminated surface.

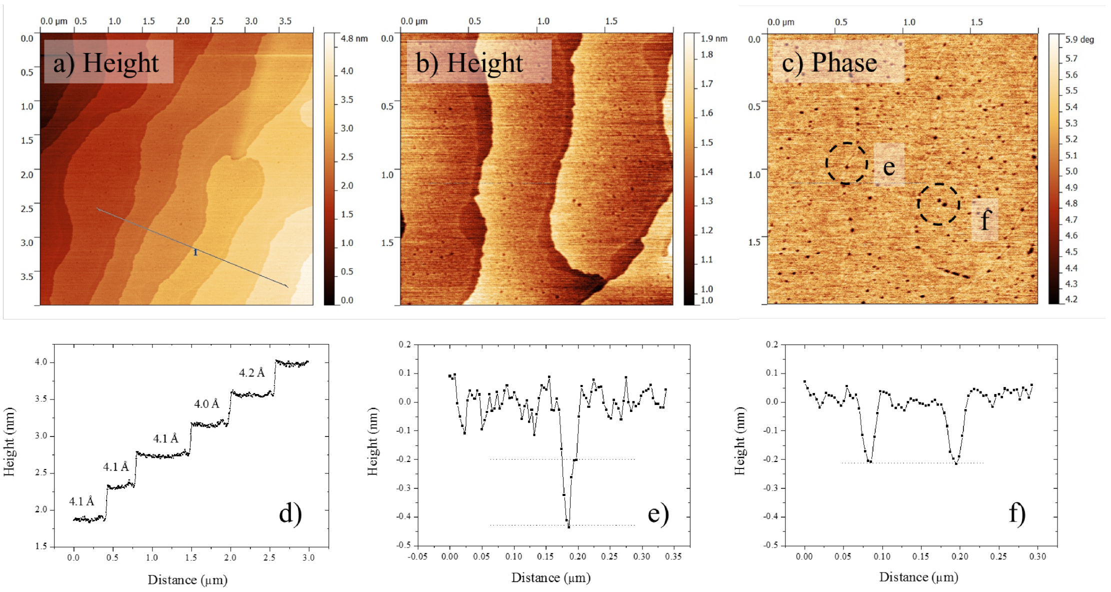

Figure 4.5: AFM scans of $SrTiO_3$ substrate a) 4x4 μm^2 height image after 1 hour air annealing at 1150 °C and levelled on one terrace, b) higher magnification height and c) phase images, d) atomic steps measured over indicated line in a). e) and f) profiles of pits indicated in c).

The phase image (figure 4.5c) also shows the existence of small pits, which are seen as dark circular spots with different sizes. The depth of such pits is given by the two profile plots in figures 4.5e and 4.5f, taken from the regions indicated in the phase image. Analysis of the height image, shows that pits are half-unit or unit cell deep, and although all were not measured, the maximum depth measured was one unit cell, approximately 4 Å. Even with the increase in reproducibility due to the single annealing step, it should be noted that the process of preparing atomically flat surfaces is very challenging and there is substantial variation between substrates, even if the preparation protocol is exactly the same. This is especially the case when comparing STO single crystal substrates from two different suppliers. Figure 4.6 illustrates the difference between STO substrates from Crystec (a) and SurfaceNet (c), that were submitted to the same annealing step, of 1 hour at 1150 °C.

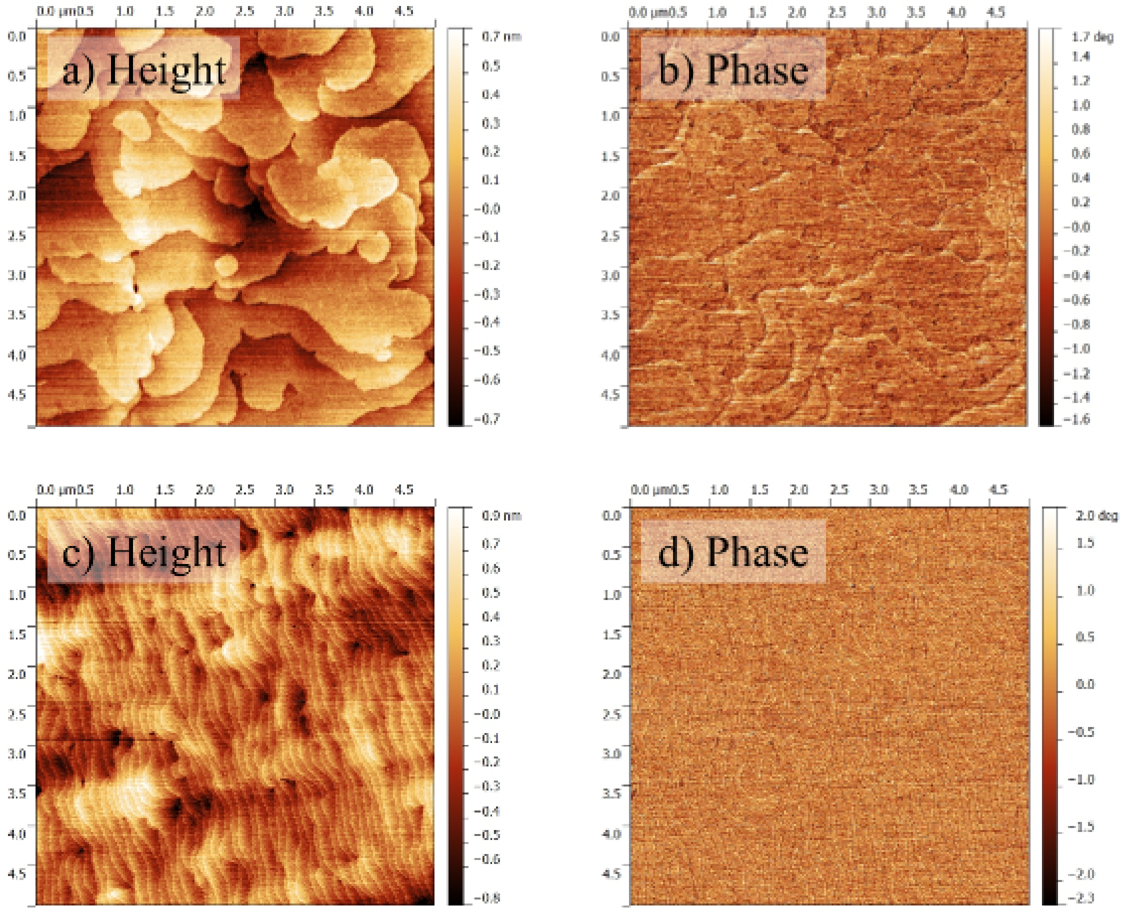

Figure 4.6: AFM scans of $SrTiO_3$ substrate a) Crystec 5x5 μm^2 height image after 1 hour air annealing at 1150 °C b) corresponding 5x5 μm^2 phase image c) SurfaceNet 5x5 μm^2 height image, d) corresponding 5x5 μm^2 phase image.

The comparison between figures 4.6a and 4.6c is very interesting because differences between both substrates are surprisingly clear. The main difference has to do with the shape of the terraces: in figure 4.6a terraces are almost circularly shaped and do not appear to be parallel, contrasting with the narrow and parallel ones seen in figure 4.6c. Moreover, the dimensions of the terraces are completely different, being much bigger for the surface illustrated in figure 4.6a. In fact, some terraces span for a few micrometres, which is surprising and difficult to find in the literature. Such differences are attributed to different miscut angles. The miscut angle of a STO substrate influences the etching kinetics, and is responsible for the different surface features, observed in figures 4.6a and 4.6c [219]. Perhaps, more importantly, both substrates surface show very little contrast in phase imaging which is promising, from the point of view of epitaxial depositions. For the two cases presented next, substrates were always prepared by performing one annealing step and were both from the same manufacturer. SurfaceNet substrates were chosen, but not because of better surface properties: rather, such substrates gave more consistent results when compared to substrates from Crystec.

4.2.2 Deposition of Nb:SrTiO$_3$ electrodes

The best results regarding the deposition of epitaxial Nb:STO thin films, 80 nm thick, to be used as electrodes in crystalline RRAM devices is presented next. Growth parameters used for films characterised and presented hereby are presented in table 2.1 with IDs 4-6 on page 44. Two different deposition conditions will be compared, where the difference is the oxygen pressure during deposition. In the first case, the deposition took place at base pressure (which is approximately 10^{-7} mTorr), whereas for the second case 50 mTorr (O_2) was used. During film growth, different pressures will influence the energy adatoms have upon reaching the substrate, and can have dramatic effects on film structure, as explained in chapters 2 and 3 [178]. Figure 4.7a shows RHEED oscillations obtained during the initial stages of deposition (represented by the red dashed ellipse), where 10 layers were grown, and the inset of figure 4.7a shows RHEED intensity for the entire deposition.

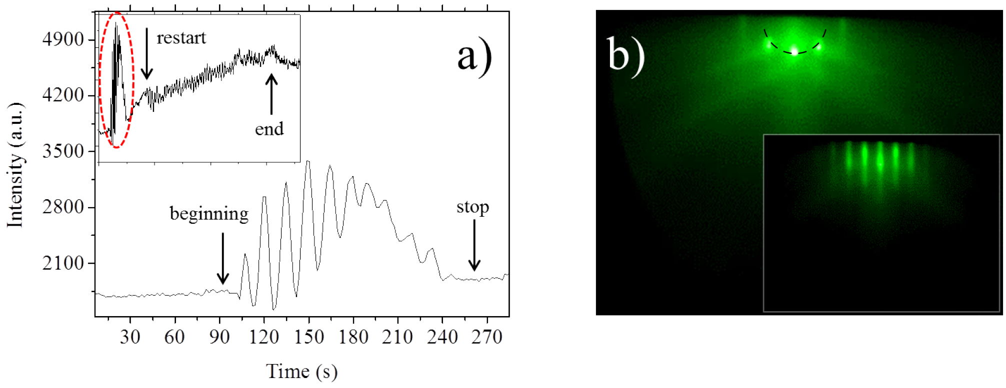

Figure 4.7: a) RHEED intensity profile during the initial stages of deposition using the main (central) specular spot, with the trend for the entire deposition in the inset figure. b) RHEED diffraction pattern showing spots on the Laue circle of the substrate prior to deposition, and inset showing RHEED pattern of grown Nb:STO film deposited at base pressure.

The increase in intensity at the beginning of the deposition is attributed to a reduction of the step density on the substrate due to the diffusion of deposited material. However, RHEED oscillations started with high amplitude, but quickly seem to fade away, indicating that the initial 2D growth was changing to 3D growth. At this point, deposition was stopped and the thin film was allowed to relax and crystallise, indicted by the "stop" arrow in figure 4.7a. The deposition was resumed approximately 5 minutes later, and smaller intensity oscillations were seen almost until the end of the deposition (indicated by the arrow). From this point on, no oscillations were observed and the intensity dropped significantly. Figures 4.7b and 4.7c show the RHEED diffraction patterns of the substrate and of the fully grown Nb:STO film, respectively. Interestingly, both diffraction patterns suggest a flat surface, where the signature of 3D features is not seen. However, figure 4.7c is characteristic of a surface where many 2D islands grew side by side, as illustrated with the existence of rods or streaks [220], as opposed to spots in the initial pattern. In fact, the loss of RHEED oscillations on the last third of the deposition process corroborates such hypothesis. Also, the existence of rods was attributed to diffraction of 3D features on the surface of cubic perovskite oxide substrates [221]. A comment on the existence of oscillations when the deposition takes place at base pressure, and hence without oxygen, is required as correct stoichiometry is a necessity in 2D growth. Chen et al. suggested that it is the underlying STO substrate that supplies the required oxygen, and therefore, films growth under stoichiometric conditions [222]. In figure 4.8 similar images are shown, for a film grown with an oxygen pressure of 50 mTorr.

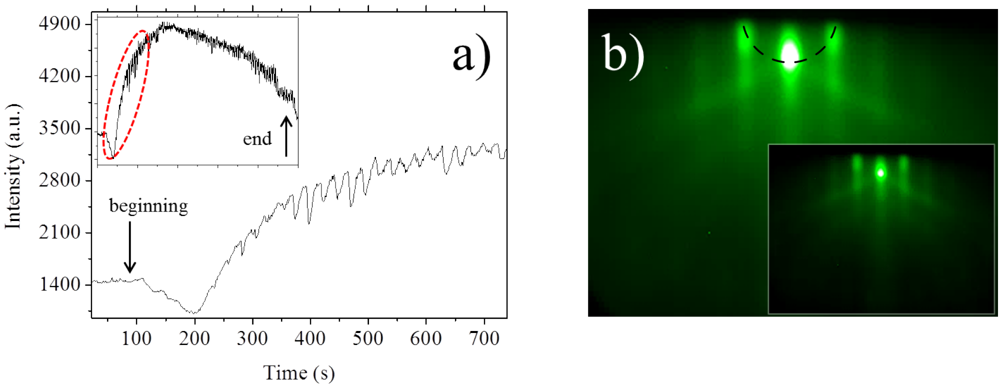

Figure 4.8: a) RHEED intensity profile during the initial stages of deposition, using the main (central) specular spot, with the trend for the entire deposition in the inset figure. b) RHEED diffraction pattern showing spots on the Laue circle of the substrate prior to deposition and inset showing the RHEED pattern of the grown Nb:STO film deposited with a pressure of 50 mTorr (O_2 also showing spots on the Laue circle).

Interestingly, RHEED oscillations were not seen at the beginning of the deposition, as seen for the previous case. Instead, oscillations start after approximately 200 seconds. This behaviour is the same as reported for epitaxial growth where substrate temperature is not high enough [223]. This can be interpreted by the effect of increased oxygen pressure during growth, responsible for lowering the surface diffusion, as explained in chapters 2 and 3. Also, the shape of the oscillations is clearly different from the ones in figure 4.7b. The inset of figure 4.8a illustrates the RHEED oscillations for the entire deposition, which in this case, last for the entire deposition possibly indicating the onset of step flow growth. In fact, the intensity of the main spot in the RHEED pattern increased intensity and remained higher than the initial intensity of the substrate. Also, both RHEED diffraction patterns (figures 4.8b and 4.8c) show very little difference which suggests that the film morphology is the same as the underlying substrate.

Differences between two thin film growth RHEED oscillations can be explained by the use of different oxygen pressures. At base pressure, adatoms will arrive at the substrate surface with much higher energy than those at 50 mTorr (O_2). The higher energy means that surface diffusion is enhanced, which can explain the initial higher amplitude oscillations seen in figure 4.7a. However, the increase in energy of the particles arriving at the substrate is known to induce compressive stress that changes film properties because of lattice distortions [188]. In contrast, films deposited with a pressure of 50 mTorr (O_2) do not suffer from compressive stress, which can explain why oscillations were seen throughout the deposition [178, 188]. Nevertheless, substrate induced effects cannot be neglected, and it is possible that small differences in growth should be attributed to subtle differences on the substrate surface.

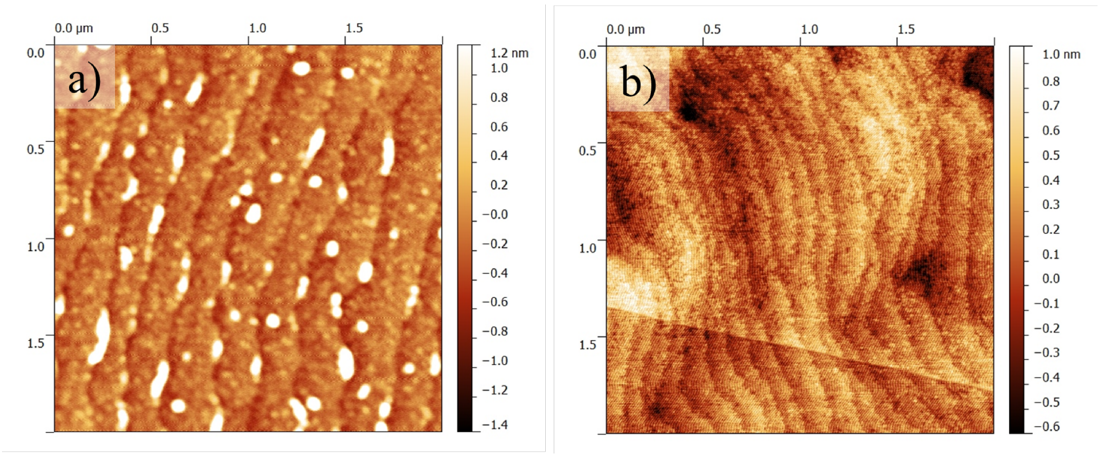

Figure 4.9: AFM images of Nb:$SrTiO_3$ films deposited at a) base pressure and b) 50 mTorr (O_2).

Figure 4.9 illustrates the surface of both Nb:STO by AFM. The first observation is the existence of atomic steps on both films which indicates that films are epitaxial. However, the film deposited at base pressure, shown in figure 4.9a, has additional protrusions, found preferentially at the step edge. Such features are approximately 2 nm in height, and seem to be elongated in the direction of the steps. In contrast, the surface of Nb:STO deposited at a pressure of 50 mTorr shows no particulates whatsoever. It is unclear what causes the enhanced nucleation at the step edges for the film deposited at base pressure, and alternatively, it is possible that such effect arises from a substrate surface characteristic. The link between these two morphologies and the kinetic parameters that govern film growth is somewhat unclear. However, both films are very flat and with clear atomic steps, which is a very satisfactory result given the thickness of the electrode, which for both cases, is approximately 80 nm.

4.2.3 Characterisation of Ti/ZrO_2/Nb:$SrTiO_3$ stack

Interestingly, almost all the Nb:STO thin films deposited are conductive, with resistivities values in the range of 10^{-4} Ω.cm, measured via the Van der Pauw technique (specific information regarding the electrical characterisation using the Van der Pauw technique can be found in section 8.3 in the Appendix). As a matter of fact, experimental parameters like oxygen pressure and substrate temperature do not seem to substantially affect the film's electrical properties, explained by conductivity arising from Nb doping and not due to oxygen vacancies. However, it should be mentioned that the results presented here are a summary of a bigger dataset, where the conductivity of the material was very often good. This is interesting, as it contrasts with challenges during the preparation of electrodes using binary metal oxides. Because of this, attention turned to the other layers that form the RRAM devices, as seen in the CTEM images in figures 4.10a and 4.10b.

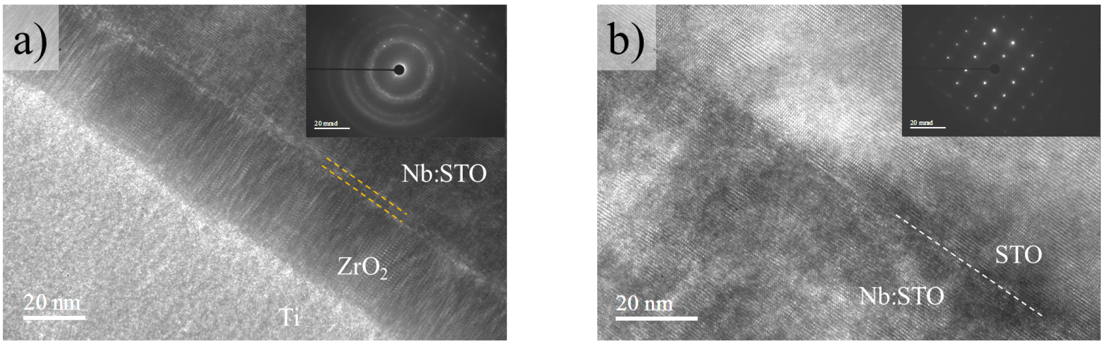

Figure 4.10: CTEM images of a) Ti/ZrO_2/Nb:STO layers and b) higher magnification of the Nb:STO/STO interface.

Figure 4.10 shows cross-sections through a Ti/ZrO_2/Nb:STO/STO stack, with the STO substrate on the top. For this RRAM device, the Nb:STO layer was deposited at base pressure, similarly to what was previously described. In figure 4.10a, three layers can be seen: Ti, ZrO_2 and Nb:STO. All layers have very different structures ranging from polycrystalline Ti to highly crystalline Nb:STO layer. More importantly for RRAM behaviour, it appears that ZrO_2 is polycrystalline, with very pronounced columnar structure. This columnar structure is of great importance because grain boundaries act like preferential migration paths for oxygen, which is a mechanism that explains RS, as covered in chapter 1. The fact these are aligned (parallel) may suggest that oxygen migration can happen from the Nb:STO to the Ti electrode. In other words, the formation of conduction filaments along the parallel grain boundaries could be facilitated by the polycrystalline structure, which is interesting. Nevertheless, devices fabricated with the processes described in this section are analysed in chapter 6, and the RS behaviour does not agree with the "classic" concept of conductive filament formation. Furthermore, there is a thin interfacial region at the ZrO_2/Nb:STO interface, that is observed on the entire TEM specimen and highlighted in figure 4.10a. In figure 4.10b a higher magnification of the Nb:STO/STO interface is seen, illustrating not only a very crystalline Nb:STO layer, but also no clear evidence of dislocations, which is important as structural defects may act like fast diffusion paths. The investigation of dislocations was performed by using Fourier analysis on several CTEM images with high magnification.

In summary, the fabrication of crystalline layers can dictate RRAM device behaviour. This happens, because oxygen pressure, substrate temperature and target contamination, for instance, can give rise to "new" interfacial layers unintentionally. Crystalline RRAM devices characterised in chapter 6 have Nb:STO bottom electrodes deposited with an oxygen pressure of 50 mTorr, which creates very different interfaces (see figure 6.6 on page 163), and gives rise to much more durable RRAM devices.

4.3 Conclusion

Epitaxial deposition of conductive Nb:STO thin films to be used as bottom electrodes in RRAM devices was achieved. In order to do this, the preparation of atomically flat STO substrates with only one termination was optimised. Best results were achieved for anneals at 1150 °C for 1 hour in the presence of oxygen, which is slightly higher than temperatures reported in the literature. Several deionised water etching recipes were tested, but best results were obtained without any etching step. The main advantage is the increase in reproducibility when only one annealing step is used.

Additionally, a comparison between Nb:STO deposited at base pressure and with an oxygen pressure of 50 mTorr was performed. AFM and RHEED analysis suggests that films deposited at 50 mTorr are smoother and layer-by-layer growth is observed for the entire deposition. The reasons behind such result are difficult to identify clearly, but it is suggested that lattice distortions may arise from compressive stress during growth when its performed at base pressure.

More importantly, it was shown how different experimental conditions during thin film growth by PLD can, more than anything, substantially change the interfaces between the electrodes and the resistive switching layer. Changes in the interfaces, or the addition of interfacial thin layers, can dramatically change how RRAM devices operate. This is especially true for the sample deposited at base pressure, where the ZrO_2/Nb:STO is not only oxidised but also contains a thin TiO_x layer. Accidental oxidation can change an interface from ohmic to Schottky, for instance, influencing device behaviour. Interestingly, a very similar effect is reported for devices prepared by collaborators from Jülich, which is going to be presented in chapter 6. In summary, attention must be given to the formation of interfacial effects during the deposition of crystalline perovskite conductive oxides as these effects may govern RS mechanisms. In the case of PLD, results indicate that the oxygen pressure used for the growth of Nb:STO and ZrO_2 layers greatly influences device behaviour. In other words, because ZrO_2 is deposited at 2 mTorr (O_2), depositing the Nb:STO layer at base pressure or 50 mTorr (O_2) gives rise to rectifying or ohmic interfaces, respectively. A direct comparison between such epitaxial heterostructures is presented in chapter 6, when analysing Ti/ZrO_2/Nb:STO RRAM devices.

Bibliography

[26] Rainer Waser and Masakazu Aono. "Nanoionics-based resistive switching memories." In: *Nature materials* 6.11 (Nov. 2007), pp. 833–40. DOI: `10.1038/nmat2023`.

[27] Rainer Waser, Regina Dittmann, Georgi Staikov, and Kristof Szot. "Redox-Based Resistive Switching Memories - Nanoionic Mechanisms, Prospects, and Challenges". In: *Advanced Materials* 21.25-26 (July 2009), pp. 2632–2663. DOI: `10.1002/adma.200900375`.

[128] Dave H.a Blank, Guus J.H.M Rijnders, Gertjan Koster, and Horst Rogalla. "In-situ monitoring by reflective high energy electron diffraction during pulsed laser deposition". In: *Applied Surface Science* 138-139 (1999), pp. 17–23. DOI: `10.1016/S0169-4332(98)00470-X`.

[178] "Growth Kinetics During Pulsed Laser Deposition". In: *Pulsed Laser Deposition of Thin Films*. John Wiley & Sons, Inc., 2006, pp. 177–190. DOI: `10.1002/9780470052129.ch8`.

[188] D. P. Norton, C. Park, J. D. Budai, S. J. Pennycook, and C. Prouteau. "Plume-induced stress in pulsed-laser deposited CeO2 films". In: *Applied Physics Letters* 74.15 (1999), p. 2134. DOI: `10.1063/1.123780`.

[203] T. Ohnishi et al. "Preparation of thermally stable TiO2-terminated SrTiO 3(100) substrate surfaces". In: *Applied Physics Letters* 85.2 (2004), pp. 272–274. DOI: `10.1063/1.1771461`.

[204] Gertjan Koster, Boike L. Kropman, Guus J.H.M. Rijnders, Dave H.a. Blank, and Horst Rogalla. "Influence of the surface treatment on the homoepitaxial growth of SrTiO3". In: *Materials Science and Engineering: B* 56.2-3 (1998), pp. 209–212. DOI: `10.1016/S0921-5107(98)00238-4`.

[205] Macarena J. Montenegro and Thomas Lippert. “Films for Electrochemical Applications”. In: *Pulsed Laser Deposition of Thin Films*. John Wiley & Sons, Inc., 2006, pp. 563–584. DOI: `10.1002/9780470052129.ch22`.

[206] Clive D. Chandler, Christophe Roger, and Mark J. Hampden-Smith. “Chemical Aspects of Solution Routes to Perovskite-Phase Mixed-Metal Oxides from Metal-Organic Precursors”. In: *Chemical Reviews* 93.3 (1993), pp. 1205–1241.

[207] Gertjan Koster et al. “Structure, physical properties, and applications of SrRuO_{3} thin films”. In: *Reviews of Modern Physics* 84.1 (Mar. 2012), pp. 253–298. DOI: `10.1103/RevModPhys.84.253`.

[208] Gertjan Koster, Guus Rijnders, Dave H.a. Blank, and Horst Rogalla. “Surface morphology determined by (001) single-crystal SrTiO3 termination”. In: *Physica C: Superconductivity* 339.4 (2000), pp. 215–230. DOI: `10.1016/S0921-4534(00)00363-4`.

[209] M. Kawasaki et al. “Atomic control of SrTiO3 surface for perfect epitaxy of perovskite oxides”. In: *Applied Surface Science* 107 (1996), pp. 102–106. DOI: `10.1016/S0169-4332(96)00512-0`.

[210] R. Bachelet, F. Sánchez, F. J. Palomares, C. Ocal, and J. Fontcuberta. “Atomically flat SrO-terminated SrTiO[sub 3](001) substrate”. In: *Applied Physics Letters* 95.14 (2009), p. 141915. DOI: `10.1063/1.3240869`.

[211] R. Gunnarsson, a. S. Kalabukhov, and D. Winkler. “Evaluation of recipes for obtaining single terminated perovskite oxide substrates”. In: *Surface Science* 603.1 (2009), pp. 151–157. DOI: `10.1016/j.susc.2008.10.045`.

[212] J G Connell, B J Isaac, G. B. Ekanayake, D R Strachan, and S S a Seo. “Preparation of atomically flat SrTiO3 surfaces using a deionized-water leaching and thermal annealing procedure”. In: *Applied Physics Letters* 101.25 (2012), pp. 1–8. DOI: `10.1063/1.4773052`. arXiv: `1210.1860`.

[213] J. E. Boschker and T. Tybell. “Qualitative determination of surface roughness by in situ reflection high energy electron diffraction”. In: *Applied Physics Letters* 100.15 (2012), pp. 21–25. DOI: `10.1063/1.3701610`.

[214] S. a. Chambers, T. C. Droubay, C. Capan, and G. Y. Sun. “Unintentional F doping of SrTiO 3(001) etched in HF acid-structure and electronic properties”. In: *Surface*

Science 606.3-4 (2012), pp. 554–558. DOI: `10.1016/j.susc.2011.11.029`. arXiv: `1110.4061`.

[215] Joseph H. Ngai et al. “Achieving A-Site Termination on La0.18Sr0.82Al0.59Ta0.41O3 Substrates”. In: *Advanced Materials* 22.26-27 (2010), pp. 2945–2948. DOI: `10.1002/adma.200904328`.

[216] S.N. Magonov, V. Elings, and M.-H. Whangbo. *Phase imaging and stiffness in tapping-mode atomic force microscopy.* 1997. DOI: `10.1016/S0039-6028(96)01591-9`.

[217] I. Schmitz, M. Schreiner, G. Friedbacher, and M. Grasserbauer. “Phase imaging as an extension to tapping mode AFM for the identification of material properties on humidity-sensitive surfaces”. In: *Applied Surface Science* 115.2 (1997), pp. 190–198. DOI: `10.1016/S0169-4332(97)80204-8`.

[218] Lugen Wang. “The role of damping in phase imaging in tapping mode atomic force microscopy”. In: *Surface Science* 429.1-3 (June 1999), pp. 178–185. DOI: `10.1016/S0039-6028(99)00368-4`.

[219] Q Gan, R a Rao, and C B Eom. “Control of the growth and domain structure of epitaxial SrRuO 3 thin films”. In: *Applied Physics Letters* 70.15 (1997), p. 1962. DOI: `dx.doi.org/10.1063/1.118792`.

[220] G. Koster. *Reflection high-energy electron diffraction (RHEED) for in situ characterization of thin film growth.* 2011, pp. 3–29. DOI: `10.1533/9780857094957.1.3`.

[221] C Xu et al. “Impact of the interplay between nonstoichiometry and kinetic energy of the plume species on the growth mode of SrTiO 3 thin films”. In: *Journal of Physics D: Applied Physics* 47.3 (Jan. 2014), p. 034009. DOI: `10.1088/0022-3727/47/3/034009`.

[222] Fan Chen et al. “Surface segregation of bulk oxygen on oxidation of epitaxially grown Nb-doped SrTiO[sub 3] on SrTiO[sub 3](001)”. In: *Applied Physics Letters* 80.16 (2002), p. 2889. DOI: `10.1063/1.1473694`.

[223] J Y Lee, J Y Juang, K H Wu, T M Uen, and Y S Gou. “Temperature dependence of RHEED oscillation in homoepitaxial growth of SrTiO3(100) films on stepped substrates”. In: *Surface Science* 449.1-3 (2000), pp. 235–242. DOI: `10.1016/S0039-6028(00)00039-X`.

Chapter 5

Fabrication and Characterisation of Amorphous ZrO_2 based RRAM Devices

This chapter will focus on the fabrication of RRAM devices based on amorphous ZrO_2. Previous chapters focused on the optimisation of the deposition parameters of zirconium oxide with adequate properties, so that it could be integrated into RRAM devices. Here, the fabrication and characterisation of devices will be described in detail, and it will be demonstrated why it is essential to develop such protocols. The objective is to perfect the preparation of devices, so that the non-volatile behaviour is mostly attributed to resistive switching, and is not due to any fabrication imperfection or measurement related issue. This is of critical importance in the quest to understanding the underlying mechanisms in resistive switching.

5.1 Introduction

So far, the discussion has focused on the RS mechanisms and on the growth of thin films by PLD. In this chapter, electrical characterisation of amorphous RRAM devices is going to be presented. The devices characterised in this chapter comprise the amorphous zirconia films that were grown and characterised in chapter 3. However, before electrical characterisation is presented, a description of fabrication and device development is given. Hence, this chapter is divided into two sections: the first part covers the development of RRAM devices, focusing on the main challenges faced regarding fabrication. The second part is an in-depth study of the resistive switching mechanisms of optimised amorphous devices.

Starting with the development and fabrication, it should be noted that results presented herein are a summary of a much broader set of experiments. Platinum, copper, aluminium and titanium were tested as electrode materials, and although resistive switching was observed with all the above electrode materials, the most reproducible result was clearly seen in devices with a bottom Ti electrode. For this reason, all ZrO_2 based RRAM device characterisation presented in this chapter was performed on asymmetric devices with one Ti and one Pt electrode. As a consequence, RS mechanisms characterised in the next section are interpreted as being valence change memories (VCM). Also vital to device behaviour is the choice of architecture employed in RRAM fabrication. The reason for this is the fact that the oxide layer in the MIM stack is normally a few tens of nanometres in thickness, which is of the same order of magnitude as the electrode thickness, meaning that is very easy to pierce all the layers by contacting the top layer with a micro probe. More importantly, during electrical characterisation, short-circuits (or devices with extremely low resistance) hide all other possible issues related to RRAM behaviour that are due to material properties further hindering development. In other words, a short-circuited device can be caused by an number of reasons: (1) the bottom contact roughness may be too high, with macroscopic particulates effectively bridging the two electrodes on a MIM stack, (2) the active layer has a very low resistivity, which is likely linked to deposition conditions, (3) the active layer is too thin, or deposition conditions gave rise to pin holes that will short-circuit the device once the top contact is deposited, or (4) during measurement, the micro probes pierced the resistive switching layer and contacted the bottom electrode. These phenomena, although different in nature, will give rise to the same electrical response, which is problematic. One way to overcome all issues that arise from using micro probes is preparing a "crossbar" array where the contacts pads are not on top of the active layer, meaning the probes cannot short-circuit the device under testing. The preparation of RRAM devices in a "crossbar" array was achieved, but not without overcoming a few challenges, as explained in detail in the results chapter. A second architecture was used for optimised RRAM devices, where the main difference is the ability of device patterning without a vacuum break between the Ti electrode and ZrO_2. This is of extreme importance, in order to link subtle differences found during EELS analysis solely to a RS mechanisms, and not due to fabrication. For the remainder of this thesis, RRAM devices presented on chapters 5 and 6 will be linked according to their architecture, and labelled as "round" or "crossbar" devices. Further information related to device design can be found in section 8.2

in the Appendix.

For the second part of the chapter, an in-depth study of bipolar amorphous ZrO_2 based RRAM is presented. The motivation for this study is linked to the inherent variability observed while characterising RRAM devices, which cannot be attributed to issues in fabrication or measurement. Several recent reports of device variability have highlighted deviations from the idealised mechanisms, described in chapter 1, for example, by suggesting their coexistence [34, 224]. In amorphous oxides in particular, it is possible that device cycling may cause enough Joule heating to induce local crystallisation. Amorphous layers will be easier to crystallise when compared to poly or single crystal ones, but so far the influence of such phenomena on electrical properties has not been thoroughly investigated. This is interesting as ongoing crystallisation with device cycling could account for some of the variability observed in amorphous devices. It will be shown that in zirconia based devices, two different types of SET and RESET transitions coexist, which give rise to different resistance states. Analysis of the conduction mechanisms shows that, essentially in the LRS, the conductive filament has very different conduction properties. STEM EELS was used to characterise the devices, focusing on differences found at the interfaces. Finally, a model that links the electrical characterisation with the EELS analysis, within the framework of valence change memories is proposed.

5.2 Experimental

Films characterised in the next section were grown with experimental conditions summarised on table 2.1 under IDs 7 and 8, presented on chapter 2 on page 44. Electrical characterisation on the probe station was performed under N_2. The platinum electrode was grounded for all measurements. For the forming and set processes, a current compliance (typically <5 mA) protected devices against hard breakdown of the initial high resistance state. No current compliance was used for the reset process. For pulsed measurements, a read voltage of 100 mV and write/erase voltage of 1.5 V was employed (unless stated otherwise).

5.3 Results

5.3.1 Development of a-ZrO_2 RRAM devices

Contact Roughness

Bottom contact roughness is a parameter of critical importance, regardless of the device architecture employed. If the contact is too rough it might give rise to localised and preferred conduction paths (that are especially problematic when Joule heating takes place) or even short-circuits that will hinder the overall RS response of the MIM structure. The AFM image in figure 5.1a shows an aluminium film deposited by thermal evaporation. It is covered in microscopic particulates that make it inadequate as a bottom electrode. In figure 5.1b, a bright field TEM image shows how damaging these microscopic particulates can be: the figure shows a similar films after subsequent deposition of ZrO_2 and Al, and where the ZrO_2 is interrupted causing a short-circuit between the top and bottom electrodes (highlighted with the red circle).

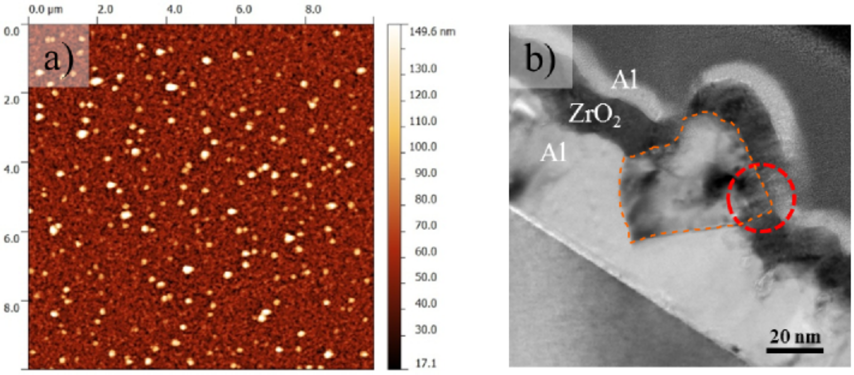

Figure 5.1: a) AFM image of the surface of a metallic Al bottom contact deposited using thermal evaporation. Clusters of material with inadequate roughness are easily observed with a peak-to-peak roughness in excess of 100 nm. b) TEM image of the obtained Al-ZrO_2-Al structure when thermal evaporation is used. It is clear that the active layer is interrupted due to the large grain that bridges the bottom and top metallic layers (highlighted in orange).

It is therefore critical to use deposition techniques that will yield thin films with the correct morphology. Best results were obtained when sputtering or/and e-beam deposition systems were used for the deposition of the metal thin films for the bottom contacts. With such techniques, the films are much smoother with no bigger sized particulates that are responsible for the short-circuits and with a peak-to-peak roughness of less than 5 nm. This is why PLD was used to deposit MIM stacks without a vacuum break, only in later stages of development, as droplets originated from PLD (described in chapter 3) would have the same effect as the microscopic particulates described herein.

“crossbar” Array

The fabrication of a “crossbar” array, as the example presented in chapter 1 (in figure 1.3 on 4), was a fundamental step towards RRAM device characterisation. Given that the smallest line width on our devices is 10 micrometres wide, patterning was done using photolithography. Normally the initial stages of device fabrication are the bottom contact deposition and patterning on a flat substrate. The standard experimental steps used in photolithography (and in e-beam lithography) are illustrated in 5.2.

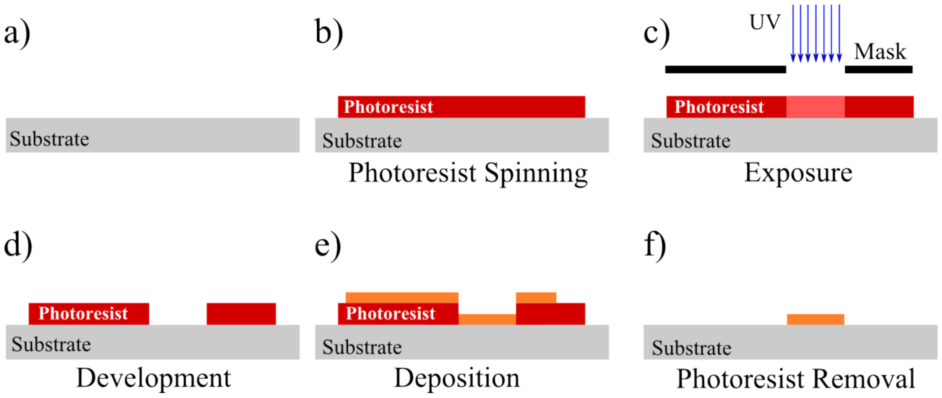

Figure 5.2: Experimental steps necessary for the patterning of thin films using photolithography. a) Spinning of photoresist onto a clean substrate b) exposure of the photoresist using a mask with the desired pattern c) development of the photoresist will remove the exposed region d) deposition of the thin film e) removing of the photoresist (striping) leaving the patterned thin film behind (lift-off procedure).

The deposition of the active layer is the second step and the depositions end with the deposition of the top contact. The bottom contact will therefore create several “ribs” across the substrate that will be coated with the active layer, as seen in figure 5.3. Depending on how conformal the active layer deposition technique is, the more or less pronounced these “ribs” will be. These “ribs” will have a huge influence on the overall performance figures of RRAM “crossbar” arrays, particularly when it comes to endurance, as reported by Xia et al. [225]. This happens because the coverage on the side walls cannot be avoided, giving rise to weaker regions or even short-circuits, as seen in the highlighted regions on figures 5.3a and 5.3b.

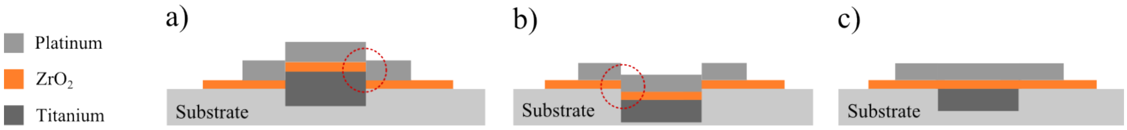

Figure 5.3: Layer deposition with the dry etching step before the bottom contact deposition. a) short-circuits or weaker conduction paths when bottom contact thickness is higher than etched region b) etched region is deeper than bottom contact thickness. c) Etching and contact thickness match perfectly.

This "ribbed" configuration proved to be inadequate by reducing the device's lifetime to very short periods or small number of electrical sweeps, due to short-circuits. This problem was overcome by embedding the lower contact within the substrate, leaving it flush with the substrate surface. For planar contacts the etching depth should be determined by the required contact thickness so that the substrate becomes flat again just prior to the deposition of the active layer. By carefully etching, determining the depth via AFM and depositing with accurate thickness control, bottom electrodes are virtually flushed with the surface, with steps generally lower than 1 nm. With the use of planar bottom contacts, it is possible to study remarkably thin resistive switching layers further contributing to the already very good scalability of RRAM technology. Figure 5.4a illustrates the RRAM "crossbar" developed herein. The darker features are the buried Ti electrodes and the lighter ones are the Pt electrodes. The ZrO_2 resistive switching layer (grey square) is sandwiched in between the electrodes.

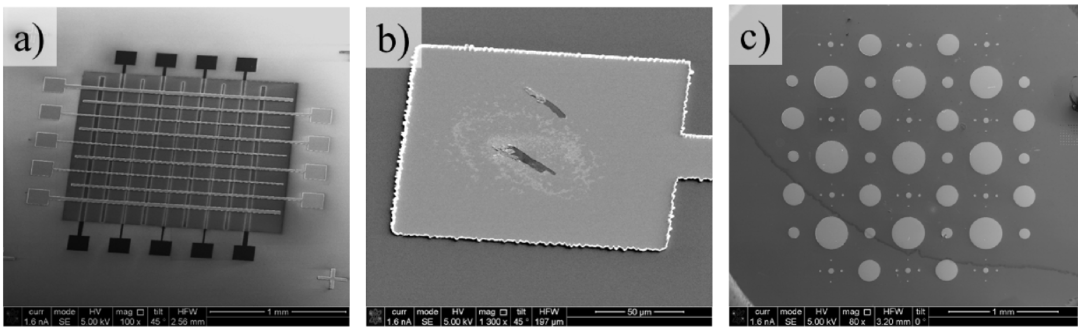

Figure 5.4: SEM images of a) fabricated planar "crossbar" array (used in "crossbar" devices) and b) damage caused by the micro probes during electrical characterisation. c) pattern used for the preparation of optimised or "round" devices.

Figure 5.4b shows way a "crossbar" array was necessary during early device development. The damage caused by the electrical characterisation probes is clearly visible, as the top electrode material is completely removed. If the RS layer and bottom electrode were underneath the damaged region, devices would probably be short-circuited. Figure 5.4c illustrates the second architecture used for optimised devices. For both architectures, devices have a range of areas so that its effect is investigated.

Flagging during Lift-off

Figure 5.5 illustrates a further problem with the lithography process. By observing the AFM image in figure 5.5 one can see that the edges of the patterned bottom contact are higher than the surface of the thin film (brighter lines on the edges of the pattern), an photolithographic artifact known as flagging [226]. These structures (or spikes) are so sharp that not even a conformal deposition technique would be able to effectively coat them and these features will always give rise to short-circuits in future fabrication stages.

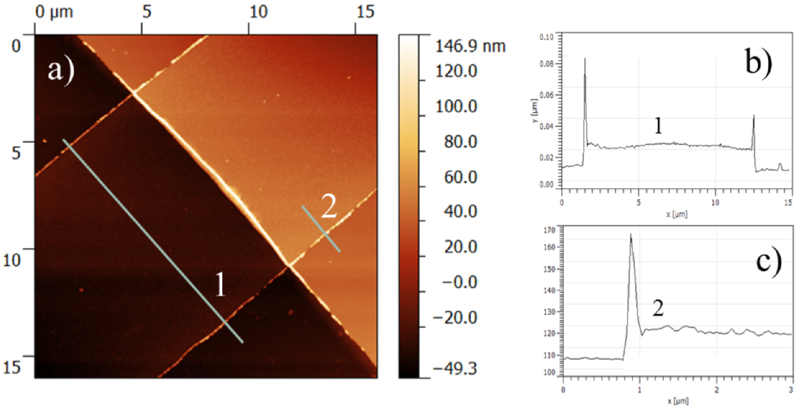

Figure 5.5: AFM image of the surface of the metallic bottom contact partially coated with the active layer. Lines a) and b) represent the regions where the line profiles were taken from.

The line profiles in figure 5.5 illustrate how sharp the spikes or flags are. Flagging happens because part of the photoresist sidewall is coated with the material one wants to remove. Once the lift-off is performed (hence photoresist is removed) the edges of the thin film will remain, giving rise to sharp features i.e. flags or spikes, as seen in figure 5.6a and 5.6b. To overcome this, the standard technique is the use of a two layer photoresist stack. The underlying photoresist will have a much higher development rate than the one on top originating a step with a negative profile. With this negative slope step, the metallic film will not be continuous on the pattern side and on the lift-off side as shown on figure 5.6b and 5.6c. The negative slope will promote an easier lift-off given that the two sides of the thin film are not connected nor are the photoresist sidewalls.

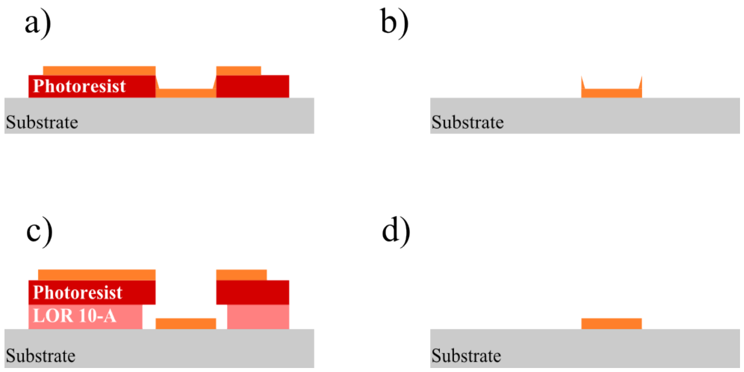

Figure 5.6: a) and b) schematic lift-off procedure that gives rise to flagging. c) and d) With the use of a second photoresist layer (LOR 10-A) that develops faster than the original a “negative profile” can be achieved. This “negative profile” will allow for a clean lift-off given that the sidewalls are not coated like on the previous example.

This was performed giving rise to planar electrodes without flagging, which made the “crossbar” architecture feasible. Figure 5.7 illustrates how the dry etching step and the deposition of electrodes without flagging can give rise to planar bottom electrodes, as shown in figure 5.3.

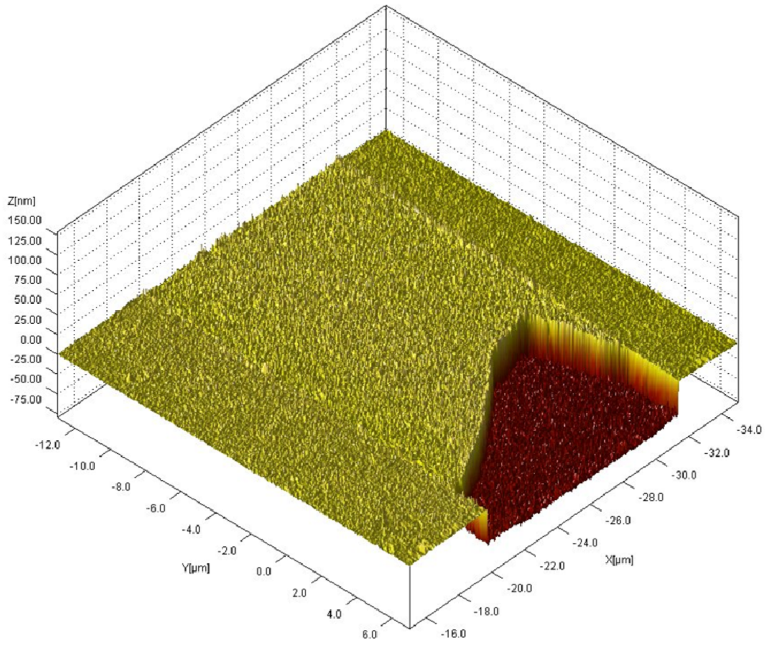

Figure 5.7: AFM image of the dry etched SiO_2/Si substrate partially filled with Ti deposited by the Plassys IV e-beam evaporator. The etched depth is 80 nm (determined by AFM between the dry etching and deposition stages) which matches the Ti deposition thickness measured by the quartz microbalance within the Plassys IV system.

This image was achieved by drawing a line, using a laboratory marker pen, after the dry etching stage but before the Ti e-beam evaporation. After the deposition is performed, lift-off of the pen line gives rise to regions where the etching and the Ti film are clearly visible. It should be mention that although the dry etching stage and undercut gave much better results, not all devices will have clean and extremely smooth electrodes exactly like those illustrated on figure 5.7.

Effect of Electrode Thickness - Electrical Characterisation

In this section, electrical results from zirconia based devices obtained during development stages will be presented and a correlation to the switching behaviour(s) will be made and explained. All the electrical characterisation presented will be regarding asymmetric devices where the one electrode is made of Ti and the other of Pt. To study the influence of electrode thickness, three different architectures were fabricated. These architectures were made with all the optimised fabrication steps described so far, and using the "crossbar" design. The rationale for this study is linked to the role Ti electrodes have in resistive switching, as covered in chapter 1. The oxygen gettering properties of Ti will be influenced by its thickness, hence, RS will be affected too. Sample 3 has a Ti insertion layer within the zirconia RS layer, to further Note that electrical results presented in this section are representative of a large number of devices:

Sample 1 – Pt/Ti (20 nm)/ZrO_2 (90 nm)/Pt
Sample 2 – Pt/Ti (90 nm)/ZrO_2 (100 nm)/Pt
Sample 3 – Pt/Ti (90 nm)/ZrO_2 (55 nm)/Ti (15 nm)/ZrO_2 (45 nm)/Pt

For all the electrical results presented here, the bias was always applied to the top Ti electrode whereas the bottom Pt electrode was grounded. Also, all devices presented in this study employed the "crossbar" architecture. Additional information regarding the electrical characterisation of RRAM devices (effect of temperature, influence of device size and voltage sweep rates) presented throughout the thesis can be found in section 8.3 in the Appendix. Figure 5.8 illustrates the unipolar behaviour of sample 1 where the device switches between a high resistance state (HRS) and a low resistance state (LRS) and vice-versa with a positive bias. Indeed, plots in figures 5.8a and 5.8b were obtained in sequence, during electroforming. The first interesting observation is that there are actually three states (HRS1, HRS2, and LRS) in the plots shown in figure 5.8. The semilog plot in figure 5.8c illustrates this phenomenon very clearly. In fact, the plot in figure 5.8c is similar to the example of unipolar switching presented in chapter 1, figure 1.10 (page 13), where RESET happens for lower voltages than SET, but for the same polarity.

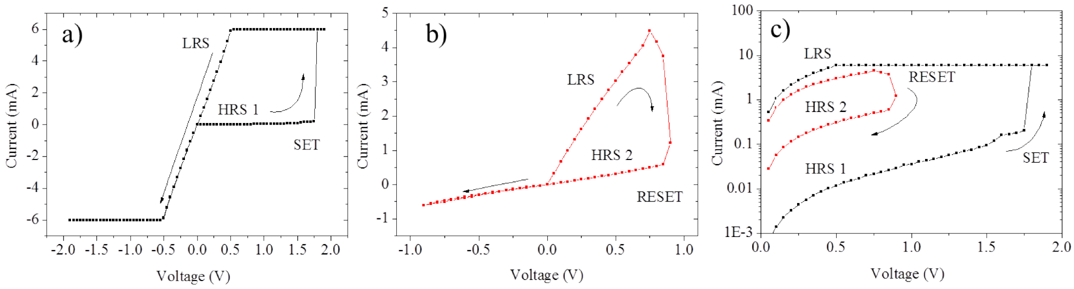

Figure 5.8: I-V curves obtained for sample 1 showing a clear unipolar behaviour. a) from HRS to LRS at 1.7 V (first sweep) and b) from LRS to HRS at 0.9 V (second sweep). c) Semilog plot comparing the two RS events. Active layer thickness is 90 nm and the architecture employed was the “crossbar” array.

Perhaps more surprising is the fact that, with continued measurements (tens of I-V sweeps, without increasing current limit), the same devices continues to show unipolar behaviour but the shape of sweeps is much different. Figure 5.9 illustrates this characteristic and also shows how the same device switches with similar voltages but with current values two orders of magnitude lower, which is surprising. This exemplifies just how careful one must be when measuring RRAM devices. The increase in resistance, seen by the magnitude of the current in figures 5.8 and 5.9, can perhaps be explained by some “breaking in” effect happening on a weaker region of the sample, due to some fabrication imperfection, which disappears after initial measurements.

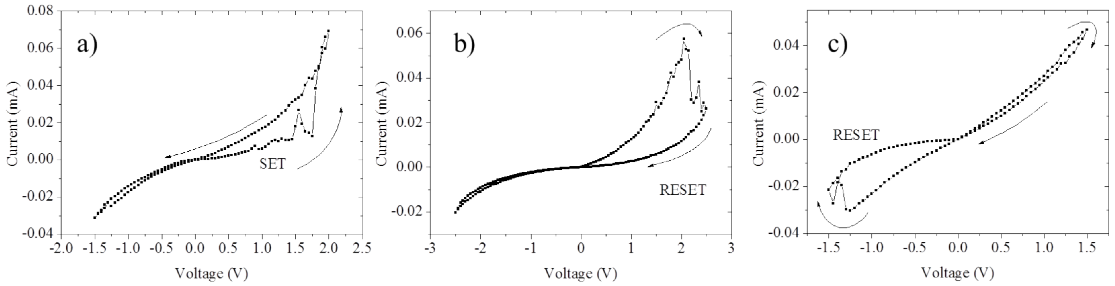

Figure 5.9: I-V curves obtained for sample 1. Note how the current values are now 100x lower than the ones obtained for previous sweeps (see figure 5.8).Active layer thickness is 90 nm and the architecture employed was the “crossbar” array.

Still in figure 5.9, notice how the device has a RESET transition for positive (5.9b) and negative bias (5.9c), which is curious. The reason behind this phenomenon is not unambiguously clear, but it suggests the existence of competing resistive switching mechanisms. Also, note how the SET transition is very different when comparing plots 5.8a and 5.9a. The very abrupt SET transition in 5.8a, which is characteristic of amorphous or polycrystalline systems, is not observed in 5.9a, which is also surprising [27]. Furthermore, the ohmic behaviour seen in both LRS and HRS on figure 5.8b, contrasts with the non-linear seen in figure 5.9b, for the same RESET transition. Such devices have not only very poor reproducibility, but also a short lifetime, which makes additional characterisation very challenging.

Behaviour obtained for the early sweeps on sample 2, which has the same oxide but a thicker Ti electrode, is shown in figure 5.10. In such devices, bipolar resistive switching was always observed, as well as an increase in the reproducibility. However, I-V sweep in figure 5.10a illustrates the typical variability during the SET operation, which happens in two distinct stages, indicated by the red dashed circle. A possible explanation for this behaviour is the competition between two conductive filaments (CF) being formed nearly at the same time but where the first one is unstable. Another interesting feature of such devices can be seen by the trend of the RESET transition, highlighted by the yellow circle. This phenomenon, where the voltage is increasing but the current decreasing, has been seen in the vast majority of RRAM devices and in many materials systems, always for the RESET transition. One possibility, is that such effect is a detrapping process [92], as explained in chapter 1 while discussing conduction mechanisms.

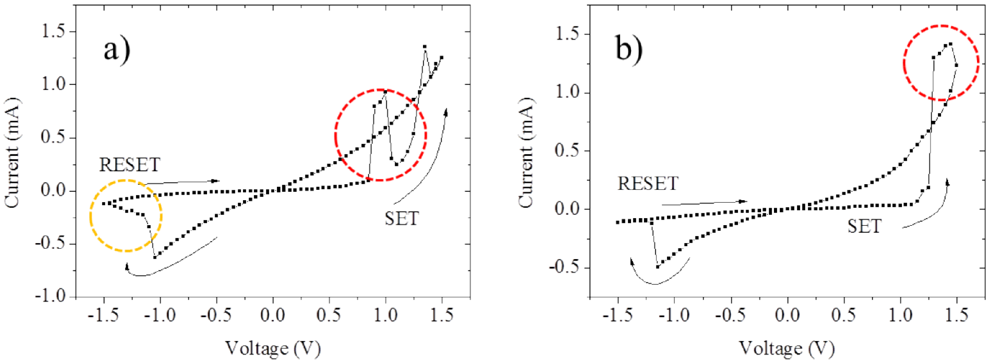

Figure 5.10: I-V curves obtained for sample 2, with a thicker Ti electrode. a) and b) Bipolar behaviour is evident even if the reproducibility of the devices is poor. b) Note the NDR region highlighted with the yellow circle. Active layer thickness is 100 nm and the architecture employed was the “crossbar” array.

Figure 5.10b shows I-V sweeps done in the same conditions as before, but after continued cycling, where the onset of complementary resistive switching (as illustrated in figure 1.10c on page 13) during SET is observed, highlighted by the red dashed circle. A reason for this behaviour is not so clear, but it likely suggests that the interface where RS is taking place changed, as explained by Balatti et al. [30, 66]. Generally speaking, these two situations point to the fact that there could be reproducible effects but also non-reproducible ones happening at the same time. However, after a few erratic sweeps, sample 2 devices showed clear and stable bipolar resistive switching for a significant amount of time. Figure 5.11 illustrates the best results obtained for such devices based on how reproducibly we could switch them and how reproducible the two resistance states are (i.e. how easily one can perform RS and get the same resistance values).

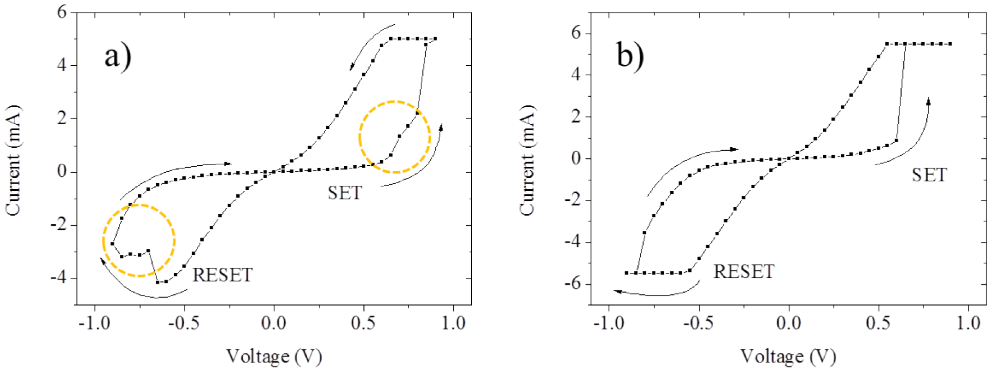

Figure 5.11: I-V curves obtained for sample 2. a) Note the regions highlighted with the yellow circle where the RS does not look like a single event. Active layer thickness is 100 nm and the architecture employed was the "crossbar" array.

Even with the use of a thicker Ti electrode and consequent improved reproducibility, the performance of sample 2 could still be enhanced. The main reason for this conclusion is that these devices can only be switched using voltage sweeps. As soon as voltage sweeps are changed to microsecond long voltage pulses (using voltages just above the switching thresholds) the devices stop behaving like RRAM devices, remaining in either one of the resistance states (i.e. LRS or HRS) and therefore not showing resistance bistability. However, the increase in performance between devices with thin and thick Ti electrodes is clear, by comparing figure 5.9 to 5.11. Such variation can be explained by devices with different concentration of oxygen vacancies, induced by the oxidation of the Ti by different amounts. In other words, a thin electrode may not introduce the required amount of oxygen vacancies because it oxidises completely. In contrast, a thicker electrode does not suffer from such effect, which clearly enhances RS behaviour, by easing conductive filament formation with a higher concentration of oxygen vacancies. To further investigate such an effect, a Ti insertion layer was deposited within the zirconia active layer in an effort to improve device reproducibility. Figure 5.12 illustrates the characteristic voltage sweep in linear and log scale for sample 3, as well as pulsed measurements. The semilog plot in figure 5.12b also illustrates how different the SET and RESET processes are, given the different shape of the plots at switching voltages.

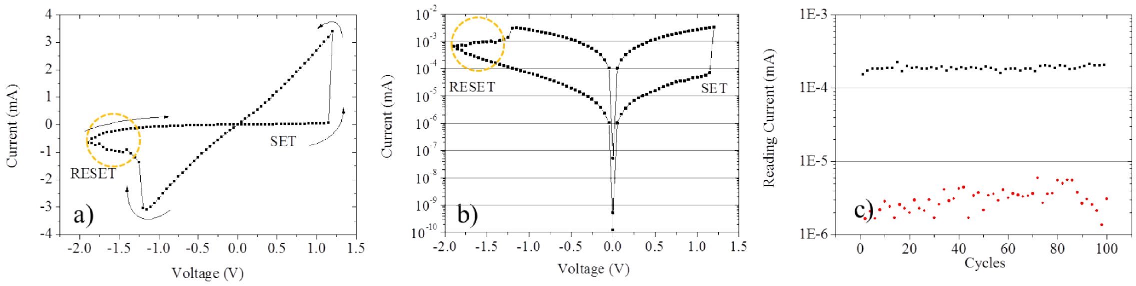

Figure 5.12: I-V curves obtained for sample 3. a) linear - best result obtained for ZrO2 based memristors b) logarithmic – on/off ratio of almost 2 orders of magnitude. Note how the NDR region is clearly visible (yellow circles). c) Current obtained for a read bias of 0.1 V. It is clear from plot that the lower resistance state is much more stable and reliable than the HRS. Active layer has an overall thickness of 100 nm with a Ti insertion layer of 15 nm and devices were patterned in a "crossbar" array.

Even if the plots clearly show an increase in the performance figures (on/off ratio, lower and stable switching voltages, enhanced reproducibility), perhaps the property that has improved most was the response to fast voltage pulses (as long as the voltages are above the threshold for switching, i.e. 1.3 V for SET and -1.9 V for RESET). The difference in voltages is very likely due to the asymmetric Pt/ZrO_2/Ti MIM stack, as suggested by Waser et al. [27]. Figure 5.12c illustrates the results obtained when sample 3 was measured using pulses. It is clear that the HRS is less reproducible (the current changes with cycle number for the same applied bias of 0.1 V) than the LRS where the current hardly changes with cycles. The stability observed for the LRS is, in theory, consistent with the metallic nature of the CF and can indicate that (1) only 1 filament is formed and (2) its dimensions (which are directly proportional to its resistivity) are unchanged. The next section presents the structural and chemical characterisation of sample 3 performed by TEM.

Effect of Electrode Thickness - TEM Characterisation

Figure 5.13a is a bright field image of a region of sample 3 (which has the insertion layer), where all the layers within the device are clearly resolved. Figure 5.13b is a diffraction pattern obtained from the same region of figure 5.13a and it was with this image that the dark-field images presented in 5.13c and 5.13d were obtained. It is clear even from 5.13a that the structure of the two zirconia layers is different, which is coherent with the fact that the deposition conditions were different i.e. the bottom zirconia layer was deposited at room-temperature, then effectively annealed during the deposition of the top layer, which was deposited directly at 500 °C.

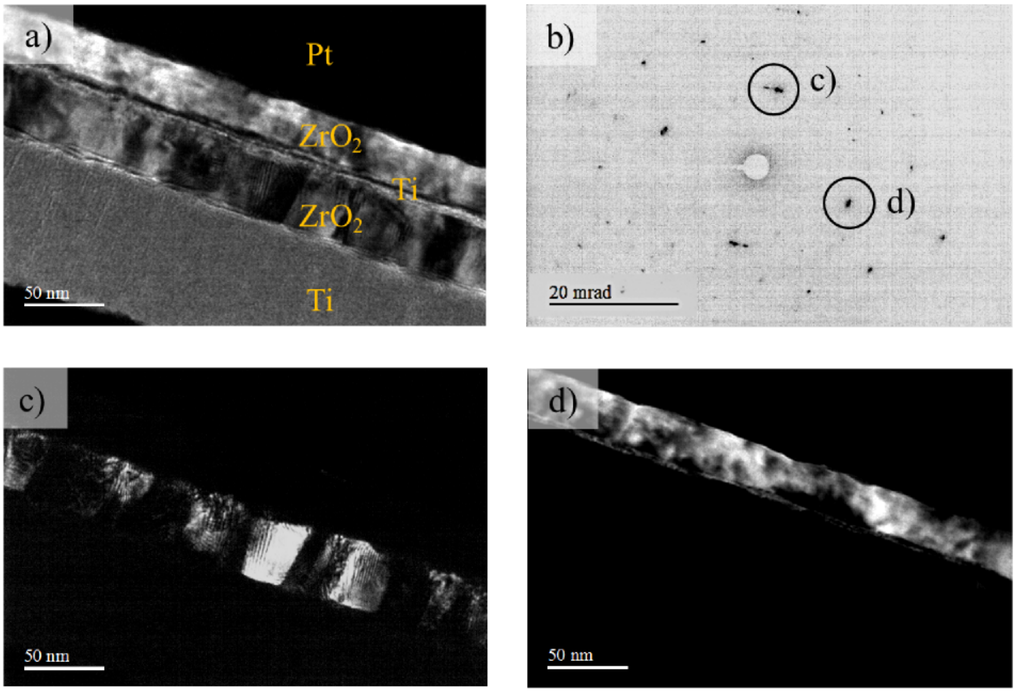

Figure 5.13: a) Bright field TEM image of sample 3 after electrical testing. b) Diffraction pattern obtained in exactly the same area. Highlighted circles illustrate where the following dark field images where obtained. c) Top ZrO_2 layer where columnar growth is clearly observable. d) Bottom ZrO_2 layer that was deposited at room-temperature and was annealed during the deposition of the top layer.

It is worth mentioning that there are no diffraction rings visible in the diffraction pattern of figure 5.13b which was, to some extent, unexpected. It appears that the deposition temperature used for the growth of the second zirconia layer (and its duration) was enough to crystallise to great extent the first layer. Figures 5.13c and 5.13d illustrates two dark field images of the layers: one image of each of the layers. The fact that the chosen diffraction spots are representative of the entire layers individually is interesting. Figure 5.13c is a good example of columnar growth, where the highlighted regions represent individual and highly crystalline domains. Indeed, additional TEM studies performed on zirconia films deposited with similar conditions gave similar results. The surprise is how crystalline the first layer is: note that the entire layer lights up in figure 5.13d in comparison to only a few columns in figure 5.13c. Another very interesting phenomenon is the fact that the insertion layer is visible in figure 5.13d. The insertion layer was also deposited at room-temperature and it is likely that it also crystallised during the deposition of the second zirconia layer. Figure 5.13d suggests that the thin Ti insertion layer appears to have the same crystallographic orientation as the underlying zirconia layer. Figure 5.14 illustrates energy filtered TEM images (EFTEM) of sample 3.

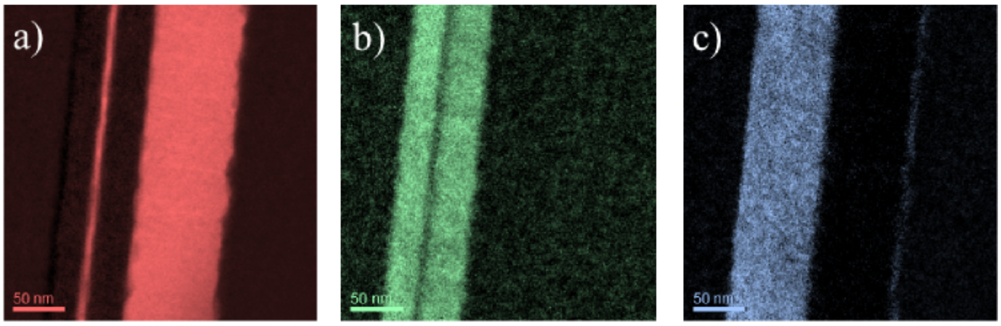

Figure 5.14: EFTEM images obtained for sample 3. a) Titanium map, b) Zirconium map and c) Oxygen map. The top contact is on the right side.

The Ti electrode and insertion layer are clearly resolved (figure 5.14a) as well as the two zirconia active layers (figure 5.14b). The oxygen map (figure 5.14c) clearly shows that the Ti insertion layer is oxidised, which is important. Oxidation of the Ti electrode implies that the zirconium layers are correspondingly reduced, as Ti was deposited at base pressure i.e. without any oxygen in the chamber. This being the case, it is clear that oxygen vacancies were introduced onto the zirconia layers, during oxidation of Ti, which very likely account for the increase in RS reproducibility. Later in this chapter, an extensive EELS analysis is presented were attention is focused on the interfaces, that were not characterised with the EFTEM analysis, shown on figure 5.14. The comparison of these 3 samples, proves that not only thicker Ti electrodes are favourable, but also that a Ti insertion layer further improves results. Such outcome suggest that the zirconia layer may have too few oxygen vacancies to start with, and hence RS is somewhat compromised. Alternatively, it may also suggest that the switching layer in use here, which is 90−100 nm thick, is too thick. Indeed, more recent reports on RRAM devices employ thinner oxide layers, like the one used for the bistability section presented next.

Poly-crystalline and Amorphous devices

A comparison between poly-crystalline and amorphous RRAM devices was made. The motivation behind this comparison has to do with advantage that amorphous devices have over crystalline ones, namely on scalability and reproducibility of very small devices [163, 227], as discussed in the introduction of chapter 3. Amorphous devices were deposited at room temperature whereas the crystalline devices were grown at 500 °C, this being the only difference in fabrication. Both batches of devices employed “round” electrode. Figure 5.15a illustrates a representative forming step on a crystalline device (red line).

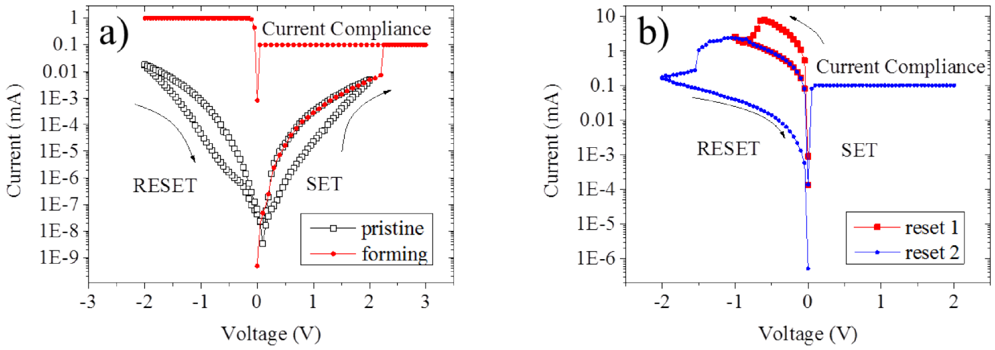

Figure 5.15: Forming I-V sweep for poly-crystalline zirconia RRAM in a) linear and b) semilog scale. $Pt/ZrO_2/Ti/SiO_2/Si$ stack, with an active layer thickness of 40 nm and patterned with “round” electrodes.

Without electroforming, poly-crystalline devices will show no evidence of stable RS and the small hysteretic sweep seen in figure 5.15a (white marker) represents the pristine resistance state (IRS). Electroforming ocurred at an applied bias of 2.2 V, as illustrated by the sharp red line in figure 5.15a. Interestingly, in the same sweep, no RESET transition was observed within the current compliance (CC), as depicted by the red flat line in figure 5.15a). To overcome this issue, and to induce stable RS in the device, two consecutive RESET transitions were performed (with higher CC), as illustrated in figure 5.15b. This phenomenon is interesting as it may suggest that the HRS is only achieved by (1) the dissolution of two different filaments or (2) the single filament dissolution takes place in discrete events with different voltage thresholds, represented by the red and blue RESET events. In contrast, amorphous devices required no additional RESET steps after forming, as seen in figures 5.16a and 5.16b. Also, amorphous devices required less current to perform the RESET transition. With the exception of these changes, during forming or initial DC sweeps, poly-crystalline and amorphous ZrO_2 based devices have very similar RS behaviour, as seen in figures 5.17a and 5.17b. Surprisingly, both threshold voltages are exactly the same, approximately 1 V and -0.6 V for SET and RESET, respectively. It was consistently observed that poly-crystalline devices have a more conductive ON state when compared to their amorphous counterparts.

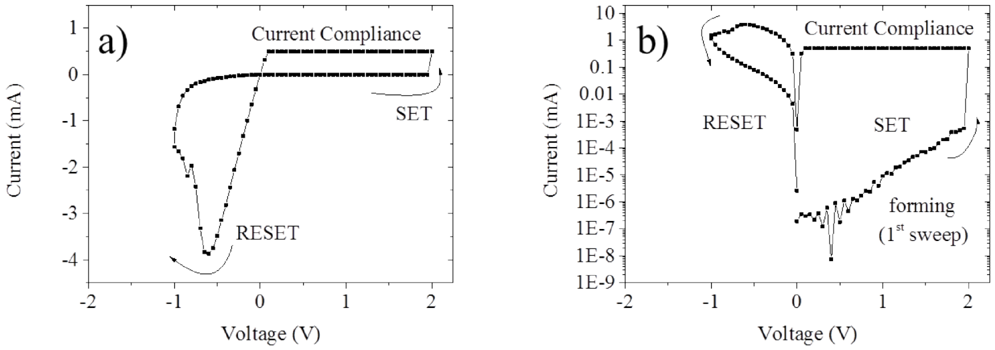

Figure 5.16: Forming I-V sweep for amorphous zirconia RRAM in a) linear and b) semilog scale. Pt/ZrO_2/Ti/SiO_2/Si stack, with an active layer thickness of 40 nm and patterned with "round" electrodes.

This observation corroborates the role that structure has on device properties. In fact, poly-crystalline devices presented here were prepared with very similar experimental parameters to those characterised by TEM in the previous section. Hence, it is very likely that the zirconia layer in these devices resembles the bottom layer of the devices with an insertion layer, shown on figure 5.13c. Grain boundaries that span across the oxide layer, effectively bridging the electrodes can explain more conductive LRS, as grain boundaries act like preferred fast migration paths, as discussed in chapter 1.

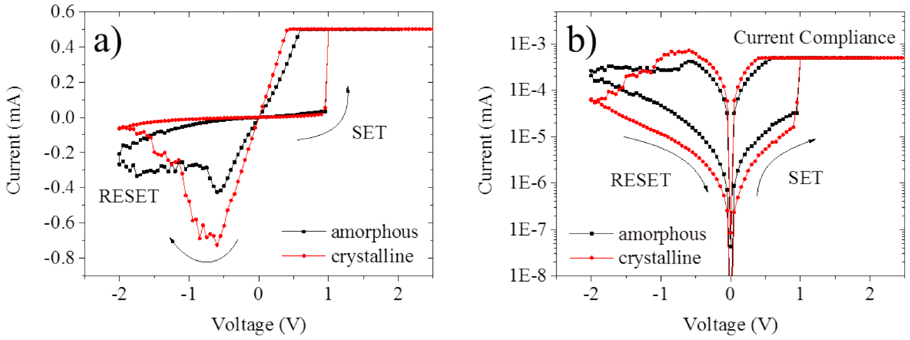

Figure 5.17: I-V sweeps comparing the behaviour of amorphous and crystalline zirconia based RRAM devices in a) linear and b) semilog scales. Pt/ZrO_2/Ti/SiO_2/Si amorphous and poly-crystalline stack, with an active layer thickness of 40 nm and patterned with "round" electrodes.

Furthermore, the OFF state is more resistive in the poly-crystalline case, making the ON/OFF ratio of crystalline devices marginally higher, which is in line with what was said about vacancies migrating faster along extended grain boundaries. This can easily be seen in figures 5.17a and 5.17b, that show the device response to fast write/erase pulses. The LRS (ON) in both sets of devices are stable, with almost no variation, but the HRS (OFF) is clearly more variable for crystalline devices.

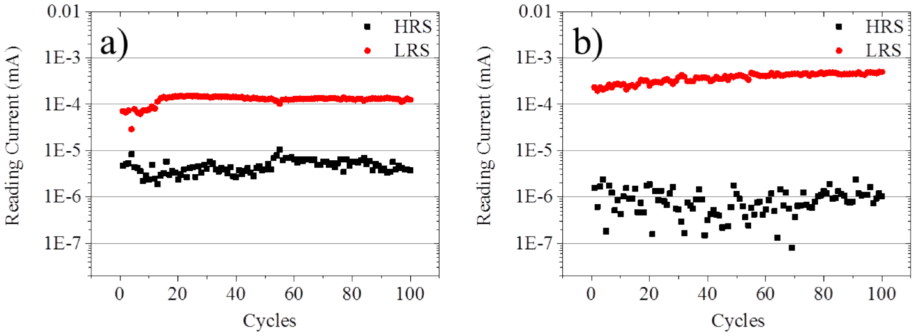

Figure 5.18: Write/Erase cycles comparing the behaviour of zirconia based RRAM devices a) amorphous Pt/ZrO_2/Ti/SiO_2/Si and b) crystalline Pt/ZrO_2/Ti/SiO_2/Si. Both batches have an active layer thickness of 40 nm and patterned with "round" electrodes.

The biggest difference found between both sets of devices was the overall number of pulsing cycles or DC sweeps each set could endure. It was observed that amorphous ZrO_2 have lower ON/OFF ratios, but are more reproducible, and essentially more durable, withstanding over 10^4 pulsed DC ON/OFF cycles. Generally speaking, amorphous ZrO_2 based devices described here, have low power operation, good durability, and very good prospects for scalability. Low voltage operation is important, as it is suggested to be on of the requirements for future technologies, as covered in the revision of emerging technologies in chapter 1. However, as referred in the introduction of this chapter and of chapter 3, some degree of instability and variability is described for RRAM devices in general, and those fabricated here are no exception. The next section will focus on linking the STEM EELS analysis with electrical response, proposing a RS model that accounts for all the observed phenomena.

5.3.2 Bistability and instability in ZrO_2 RRAM devices

Electron microscopy analysis of a typical optimised amorphous ZrO_2 device (after electrical switching) is summarised in figure 5.19. Figure 5.19a shows a cross-section in dark field STEM and indicates the layers to be smooth, continuous and structurally homogeneous. Electron diffraction (not shown) confirmed the ZrO_x layer to be amorphous and there is little diffraction contrast evident in the STEM image. The spectrum imaging technique [228] was used to assess compositional variations within the two marked regions. Elemental profiles across the first highlighted region are presented in figure 5.19b. Data were collected using EELS to map the Zr, O and Ti profiles and EDX to map the Pt. The integrated signals have been normalised in each case to aid comparisons. Our main interest is in the O profile across the active layer, since oxygen migration and variations in the oxidation state underpin both filamentary and interfacial switching mechanisms [27, 34, 43]. Figure 5.19b reveals an asymmetry in the ZrO_x – electrode interfaces. At the Pt/ZrO_x interface, the oxygen profile follows very closely that of zirconium, and the overlap of Pt and ZrO_x signals is consistent with interfacial roughness. Platinum is electrochemically inert, and there are no obvious interfacial reactions. However, at the ZrO_2/Ti interface there is instead a clear extension of the oxygen signal beyond Zr and into the Ti layer, suggesting that a thin interfacial region of Ti has oxidised. Variations in the EELS fine structure, illustrated in figures 5.19c and (d) and collected from the second region of figure 5.19a, confirm this oxidation.

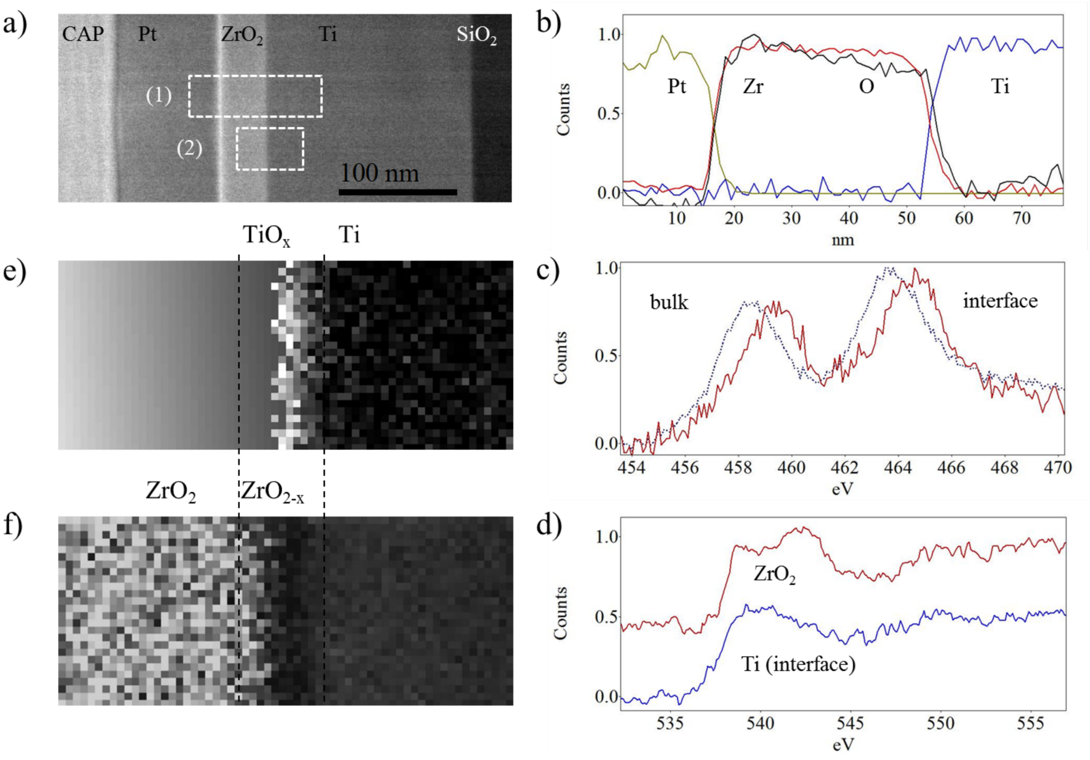

Figure 5.19: a) STEM dark field image of the RRAM stack. b) Normalised elemental composition given by EELS (Zr, O, Ti) and EDX (Pt) on the highlighted region 1 in a). c) Chemical shift in the Ti $L_{2,3}$ edge indicating localised oxidation shown in e). d) Comparison between oxygen K edge on the zirconia film and at the Ti interface. f) O/Zr ratio at the interface, indicating localised zirconia reduction. c) and d) obtained from region 2 in a).

Figure 5.19c presents normalised Ti $L_{2,3}$ EELS spectra obtained at the ZrO_2/Ti interface (full lines) and in the bulk of the titanium electrode (dashed lines), collected using the Dual EELS technique to allow the effects of plural scattering to be removed [229]. The spectra indicate a clear 1.0 eV chemical shift of the L_3 and L_2 main peaks, which is consistent with previous studies [230, 231] of oxidation and suggests specifically the formation of TiO. A lack of obvious crystal field splitting of the L_2 and L_3 features further suggests that the interfacial TiO is amorphous [232]. Higher resolution images (not shown here) did not reveal any evidence of crystallisation. Turning to the O K-edge, figure 5.19d compares the oxygen of bulk zirconia with that at the ZrO_2/Ti interface. The peak broadening of the ZrO_2 spectrum is consistent with the amorphous nature of the zirconia layer, whereas the spectrum obtained at the interface is in good agreement with previous results for amorphous TiO [231–233]. The changes in EELS fine structure are mapped in figures 5.19e and (f), allowing the width of the interfacial oxide to be estimated. Figure 5.19e shows that the chemical shift of the Ti $L_{2,3}$ edge is restricted to a thin region that is 2 nm thick. This is interesting because Ti films deposited via PLD have a peak-to-peak roughness of less than 0.5 nm (obtained from previous work), suggesting the oxidation is real and not a TEM image acquisition artifact due to interfacial roughness. Additionally, modification of the zirconia is similarly restricted: figure 5.19f shows that the Zr:O ratio is uniform until within 2 nm of the interface, where the ratio drops by 10 %. It is interesting that the change in zirconia stoichiometry illustrated in figure 5.19f is more spatially localised than the trends of figure 5.19b, which were collected in a separate region, but only 50 nm away. The statistical relevance of this variation is unclear but does suggest slight chemical inhomogeneities within the active zirconia layer that cannot be observed in STEM imaging alone but which could have notable implications in electrical switching. Irrespective, the drop in ZrO_2 oxygen content strongly suggests an interfacial reaction between ZrO_2 and Ti to form TiO, which is interesting. In fact, the formation of TiO, and not TiO_2 for instance, suggests the formation of a quasi-ohmic interface as TiO is known to be an electrical conductor. This suggestion is further corroborated with the fact that zirconia is reduced on that same interface. The low work function and high oxygen affinity of Ti are therefore likely to aid in the formation of a quasi-ohmic interface made from: ZrO_2/ZrO/TiO/Ti. The implication of such an interfacial redox reaction is twofold: first, it suggests the creation of oxygen vacancies within the initially insulating zirconia layer, and second (perhaps more important), it turns ZrO_2/Pt into the active interface i.e. RS will take place here, which has not been described before for ZrO_2 based devices [26, 27]. Interestingly, the existence of oxygen vacancies is corroborated by the lack of an electroforming step: all devices exhibited RS without the application of a higher voltage pre-treatment. Characteristic current-voltage (I-V) sweeps of a typical device are summarised in Figure 5.20. These were obtained after a small number of DC cycles.

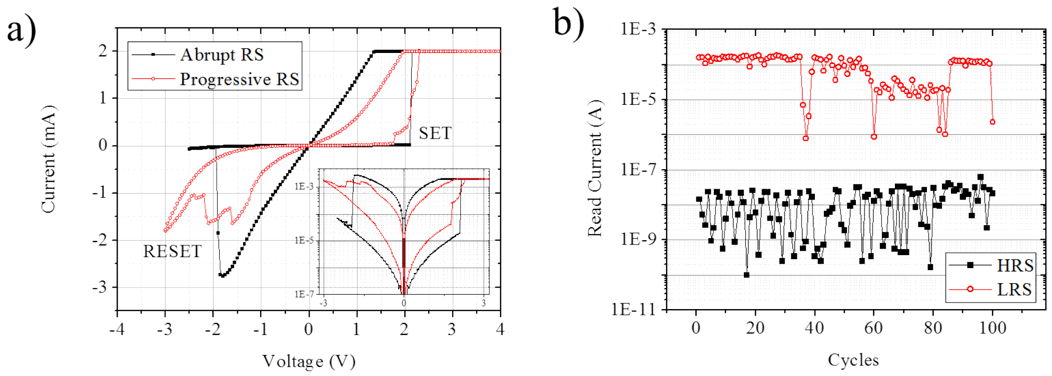

Figure 5.20: a) I-V sweeps illustrating two distinct resistive switching behaviours. b) pulse measurements which show discreet variability. Pt/ZrO_2/Ti/SiO_2/Si stack with 38 nm thick zirconia active layer and patterned with the “round” electrodes.

5.20a shows two bipolar switching modes, both of which were observed to occur within a single device. One trend would typically be observed for several voltage sweeps before changing, seemingly at random, to the second trend. Despite this variability, the devices showed good durability, withstanding $<10^4$ pulsed SET/RESET transitions. A 100-cycle subset of those transitions is presented in figure 5.20b, which illustrates the device variability during SET/RESET pulsing of a typical device. The device switched reliably in every cycle, with good reproducibility of the insulating, high resistance state (HRS). The on/off ratio was typically 10^4 but would periodically dip to values a“round” 10^3 and occasionally to as low as 10^1. We attribute this behaviour to the device switching between the two main modes of figure 5.20a. Following the literature, we term the first mode (figure 5.20, solid circles) “abrupt RS”, which exhibits ohmic behaviour in the low resistance state (LRS), abrupt SET/RESET transitions and a very favourable on/off ratio of 10^4. This contrasts with the second mode (figure 5.20, open circles), which we term “progressive RS” and which exhibits non-linear behaviour, progressive switching between states and an on/off ratio of 10^2 - 10^3. Both hysteresis modes have been described previously in the literature and have good on/off switching ratios that would be viable in a practicable memory element [26, 27, 36, 43]; however, their coexistence in a single device is surprising and not so well documented. Interestingly, SET and RESET transitions were observed for positive and negative voltages, respectively, which confirm that RS is happening at the Pt/ZrO_x interface, as oxygen vacancies are positively charged and therefore attracted by the negatively polarised Pt electrode (during SET). Conduction mechanisms can often be inferred from the slope of log(I)-log(V) curves [234–237], which are plotted in figures 5.21a and 5.21b for the set (positive voltage sweep) and reset (negative voltage sweep) operations, respectively. Conduction mechanisms for both resistance states were described in chapter 1, with special attention to space charge limited conduction (SCLC), which is experimentally described here. The LRS state of the abrupt mode is well described by a single, linear relationship, with unity gradient for both polarities, and indicates Ohmic conduction throughout. It has previously been argued [27, 36, 43] that an abrupt SET/RESET transition and an ohmic LRS is consistent with insulator to metal transition (IMT) of the conducting filament, probably in the vicinity of the Pt/ZrO_2 interface. This is consistent with other reports on Pt/ZrO_2/Ti devices, which also suggests that Ti electrodes enhance bipolar RS in ZrO_x based devices [238, 239], and crucially, show the same trend. However, such reports attribute the RS to sourcing/sinking of oxygen ions, and place the RS at the ZrO_2/Ti, which is not the case here. In the off state, i.e. when the device is not appreciably conductive, the trends of Figure 5.21 are more consistent with space-charge-limited conduction [236, 237] and are therefore bulk limited, as expected for an insulator [234, 235]. Considerable variability exists within this basic conduction mechanism for the abrupt RS mode and figure 5.22a illustrates five additional hysteresis loops recorded from the same device as that of figure 5.20.

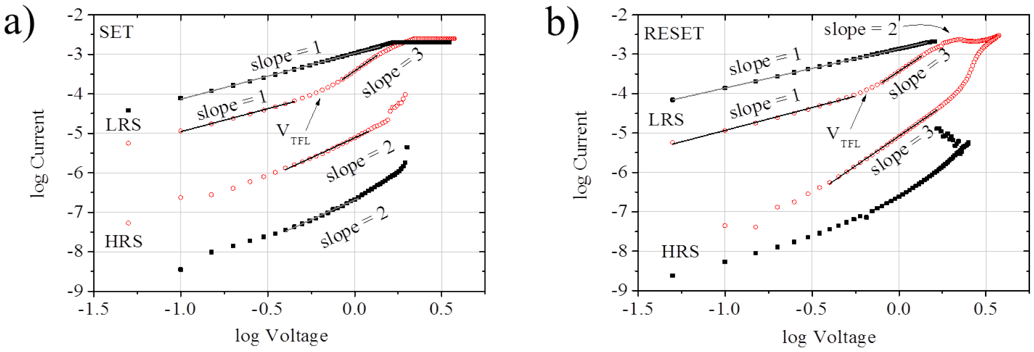

Figure 5.21: a) conduction mechanisms for the LRS and HRS for during a) SET and b) RESET transitions. Pt/ZrO_2/Ti/SiO_2/Si stack with 38 nm thick zirconia active layer and patterned with the "round" electrodes.

These loops were recorded during in an automated sequence of DC voltage sweeps and were observed to be "stable" for several cycles, before evolving. There did not appear to be any obvious degradation with time, and (as illustrated in figure 5.20b), the device would readily switch from a mode with low on/off ratio back to one with better performance; indeed, the hysteresis loops with low on/off ratios tended to be the least reproducible. All of the loops of figure 5.22a retain the abrupt RS characteristics seen in figure 5.20a with clear ohmic behaviour in the LRS. Typically, the RESET voltages and subsequent HRS characteristics hardly changed from sweep to sweep, whilst the SET transition was more variable. We propose that the variability in the LRS is due to the formation of conductive filaments with different geometries and therefore different resistances, but with similar activation energies given that the voltages at which switching happens, are very similar. The possibility that such variability is linked to ongoing crystallisation of the active or interfacial layers should be kept in mind. Turning to the progressive mode, a less abrupt SET followed by a progressive RESET transition suggests the formation of a CF that does not completely connect the electrodes during switching, so that the current is limited by a thin layer of dielectric, or perhaps by the formation of a semiconducting filament [26, 27, 43]. The fits illustrated in figures 5.21a and (b) indicate that two different conduction mechanisms operate in the LRS [234–237]. Conduction is Ohmic only at low voltages and the gradient in figure 5.21 departs from unity above 0.63 V (V_{TFL}), changing to a trend that suggests the presence of trap-filled states (characterised by a gradient of 3 in the log-log plot of figure 3) [236, 237].

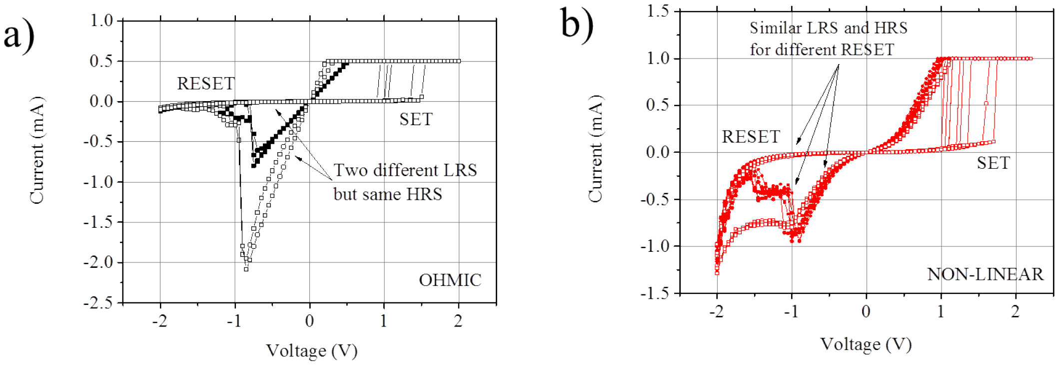

Figure 5.22: I-V sweeps of variability within main switching behaviours a) two discreet ohmic behaviours in 5 consecutive sweeps; b) two discreet non-linear behaviours in 10 consecutive sweeps. $Pt/ZrO_2/Ti/SiO_2/Si$ stack with 38 nm thick zirconia active layer and patterned with the “round” electrodes.

The high resistance state (HRS) is again consistent with the space-charge-limited conduction [235–237] expected for an insulator and is very reproducible from cycle to cycle. However, we again observe dynamic changes to the LRS, which will show good cycle-to-cycle reproducibility for some time, then change. Figure 5.22b illustrates a number of progressive RS hysteresis loops, all of which share the basic characteristics outlined above and which overlap remarkably well throughout the majority of the I-V cycle. However, there are notable differences in the SET and RESET characteristics. The SET process exhibits similar variability to that seen in figure 5.22a whilst the RESET process is in some cases a gradual variation (open circles) and in other cases is mediated by more abrupt step-changes in conductivity (filled circles). This variability on the non-linear behaviour can be explained by different trapping and de-trapping mechanisms taking place in slightly different regions of the Pt/ZrO_2 interface, and essentially, not in a localised region. The existence of two types of RESET transitions in progressive mode indicates different reactions taking place at the ZrO_2/Pt interface. It has been suggested that the existence of RESET transitions showing negative differential resistance (NDR) is explained by trapping/detrapping effects at a Schottky interface, as also seen on figure 5.10 on page 137. However, the use of the expression “NDR” is far from reaching scientific consensus, which is interesting, but essentially shows that additional characterisation is necessary. Depending on the electrical current values, DC cycling RRAM devices can reach temperatures in excess of 900 K [4]. The amount of electric current that passes through the resistive switching oxide on the LRS will promote Joule heating that can lead to its crystallisation, like suggested before. For both polycrystalline and single-crystal materials, additional crystallisation due to Joule heating might be negligible but that should not be the case with amorphous layers. Ongoing crystallisation promotes changes to grain boundaries that can explain the existence of several conduction or fast diffusion paths with competing activation energies [27, 240].

5.4 Conclusion

Fabrication and electrical characterisation techniques were optimised towards the preparation of RRAM devices based on polycrystalline ZrO_2 with good overall properties. It was shown that fabrication techniques directly affect not only which RS mechanism governs RRAM device response, but also dictate device yield, and essentially, device reproducibility and durability. Without the optimisation of fabrication techniques, for instance, it would have been very challenging (if not impossible) to understand why devices fail. Similarly, without a electrical characterisation probe station with a comprehensive and dedicated computer interface, obtaining fully optimised devices could not have been achieved.

Amorphous zirconia RRAM devices with very satisfactory overall properties fully prepared at room temperature were described. For these devices PLD was used to deposit the Ti electrode and ZrO_2 active layer, hence avoiding any vacuum breaks that would complicate EELS analysis. It was shown that the platinum electrode does not oxidise significantly, which contrast with the interfacial oxidation of the titanium electrode. The unambiguous oxidation of the titanium active electrode gives rise to an n-type conductive region that turns that interface ohmic, as well as introduces oxygen vacancies that are vital for RS. This being the case, it suggests that the RS is happening at the Pt/ZrO_2 interface, which has not been described before. Also, it has been suggested that further miniaturisation and continued scalability will require the use of amorphous metal-oxide materials deposited at low temperatures. Therefore, it is possible that scalability enhances the variability in the electrical response if the thickness of main oxide RS layer becomes comparable to the thickness of the oxidised electrode. In other words, it must be understood if the coexistence of two RS can be absolutely eliminated with the fabrication of smaller devices or if this is a fundamental material or technology limitation. Nevertheless, we propose that the coexistence of different RS modes is a characteristic of RRAM devices in general, rather than a specific property of ZrO_x. The coexistence of two RS modes in the same device, and the variability described in this work substantiate the importance of in-situ TEM atomic scale characterisation of RRAM devices, where mapping of interface oxidation states is closely monitored during device operation.

Bibliography

[4] Shimeng Yu, Byoungil Lee, and H S Philip Wong. *Functional Metal Oxide Nanostructures*. Ed. by Junqiao Wu, Jinbo Cao, Wei-Qiang Han, Anderson Janotti, and Ho-Cheol Kim. Vol. 149. Springer Series in Materials Science. New York, NY: Springer New York, 2012, pp. 303–335. DOI: `10.1007/978-1-4419-9931-3`.

[26] Rainer Waser and Masakazu Aono. "Nanoionics-based resistive switching memories." In: *Nature materials* 6.11 (Nov. 2007), pp. 833–40. DOI: `10.1038/nmat2023`.

[27] Rainer Waser, Regina Dittmann, Georgi Staikov, and Kristof Szot. "Redox-Based Resistive Switching Memories - Nanoionic Mechanisms, Prospects, and Challenges". In: *Advanced Materials* 21.25-26 (July 2009), pp. 2632–2663. DOI: `10.1002/adma.200900375`.

[30] F. Nardi, S. Balatti, S. Larentis, and D. Ielmini. "Complementary switching in metal oxides: Toward diode-less crossbar RRAMs". In: *2011 International Electron Devices Meeting* (Dec. 2011), pp. 31.1.1–31.1.4. DOI: `10.1109/IEDM.2011.6131647`.

[34] Ruth Muenstermann, Tobias Menke, Regina Dittmann, and Rainer Waser. "Coexistence of filamentary and homogeneous resistive switching in Fe-doped SrTiO3 thin-film memristive devices." In: *Advanced materials (Deerfield Beach, Fla.)* 22.43 (Nov. 2010), pp. 4819–22. DOI: `10.1002/adma.201001872`.

[36] R Tetzlaff. *Memristors and Memristive Systems*. Springer Science & Business Media, 2014, p. 5.

[43] J Joshua Yang, Dmitri B Strukov, and Duncan R Stewart. "Memristive devices for computing." In: *Nature nanotechnology* 8.1 (Jan. 2013), pp. 13–24. DOI: `10.1038/nnano.2012.240`.

[66] S Balatti, S Larentis, D C Gilmer, and D Ielmini. "Multiple memory states in resistive switching devices through controlled size and orientation of the conductive filament."

In: *Advanced materials (Deerfield Beach, Fla.)* 25.10 (Mar. 2013), pp. 1474–8. DOI: `10.1002/adma.201204097`.

[92] H. F. Tian et al. "Resistance switching effect in LaAlO3/Nb-doped SrTiO3 heterostructure". In: *Applied Physics A: Materials Science and Processing* 102.4 (2011), pp. 939–942. DOI: `10.1007/s00339-011-6276-5`.

[163] B. Govoreanu et al. "10 x 10 nm2 Hf/HfOx crossbar resistive RAM with excellent performance, reliability and low-energy operation". In: *Electron Devices Meeting (IEDM), 2011 IEEE International.* Dec. 2011, pp. 31.6.1–31.6.4. DOI: `10.1109/IEDM.2011.6131652`.

[224] Ming Liu et al. "Multilevel resistive switching with ionic and metallic filaments". In: *Applied Physics Letters* 94.23 (2009), p. 233106. DOI: `10.1063/1.3151822`.

[225] Qiangfei Xia et al. "Impact of geometry on the performance of memristive nanodevices." In: *Nanotechnology* 22.25 (June 2011), p. 254026. DOI: `10.1088/0957-4484/22/25/254026`.

[226] O. Ignatova, S. Thoms, W. Jansen, D. S. Macintyre, and I. Thayne. "Lithography scaling issues associated with III-V MOSFETs". In: *Microelectronic Engineering* 87.5-8 (2010), pp. 1049–1051. DOI: `10.1016/j.mee.2009.11.093`.

[227] Chia-Chun Lin, Yung-Hsien Wu, Tung-Hsuan Hung, and Chin-Yao Hou. "Impact of dielectric crystallinity on the resistive switching characteristics of ZrTiOx-based metal–insulator-metal devices". In: *Microelectronic Engineering* 109 (Sept. 2013), pp. 374–377. DOI: `10.1016/j.mee.2013.03.016`.

[228] J. a. Hunt and D. B. Williams. "Electron energy-loss spectrum-imaging". In: *Ultramicroscopy* 38 (1991), pp. 47–73. DOI: `10.1016/0304-3991(91)90108-I`.

[229] J Scott et al. "Near-simultaneous dual energy range EELS spectrum imaging". In: *Ultramicroscopy* 108.12 (2008), pp. 1586–1594. DOI: `10.1016/j.ultramic.2008.05.006`.

[230] L Soriano. "Chemical changes induced by sputtering in TiO , and some selected titanates as observed by X-ray absorption spectroscopy". In: 290 (1993), pp. 427–435.

[231] Pavel Potapov, Kevin Jorissen, Dominique Schryvers, and Dirk Lamoen. "Effect of charge transfer on EELS integrated cross sections in Mn and Ti oxides". In: *Physical Review B* 70.4 (July 2004), p. 045106. DOI: `10.1103/PhysRevB.70.045106`.

[232] G. Bertoni et al. “Quantification of crystalline and amorphous content in porous samples from electron energy loss spectroscopy”. In: *Ultramicroscopy* 106.7 (May 2006), pp. 630–635. DOI: `10.1016/j.ultramic.2006.03.006`.

[233] R.D. Leapman. “Study of the L23 edges in the 3d transition metals and their oxides by electron-energy-loss spectroscopy with comparisons to theory”. In: *Physical Review B* 26.1 (1982).

[234] Wan Shen, Regina Dittmann, Uwe Breuer, and Rainer Waser. “Improved endurance behavior of resistive switching in (Ba,Sr)TiO[sub 3] thin films with W top electrode”. In: *Applied Physics Letters* 93.22 (2008), p. 222102. DOI: `10.1063/1.3039809`.

[235] Yidong Xia, Weiye He, Liang Chen, Xiangkang Meng, and Zhiguo Liu. “Field-induced resistive switching based on space-charge-limited current”. In: *Applied Physics Letters* 90.2 (2007), p. 022907. DOI: `10.1063/1.2430912`.

[236] Ting Zhang, Jiang Yin, Yidong Xia, Weifeng Zhang, and Zhiguo Liu. “Conduction mechanism of resistance switching in fully transparent MgO-based memory devices”. In: *Journal of Applied Physics* 114.13 (2013), p. 134301. DOI: `10.1063/1.4821900`.

[237] Sungho Kim, Hu Young Jeong, Sung-Yool Choi, and Yang-Kyu Choi. “Comprehensive modeling of resistive switching in the Al/TiO[sub x]/TiO[sub 2]/Al heterostructure based on space-charge-limited conduction”. In: *Applied Physics Letters* 97.3 (2010), p. 033508. DOI: `10.1063/1.3467461`.

[238] Wan-Gee Kim and Shi-Woo Rhee. “Effect of the top electrode material on the resistive switching of TiO2 thin film”. In: *Microelectronic Engineering* 87.2 (Feb. 2010), pp. 98–103. DOI: `10.1016/j.mee.2009.05.023`.

[239] P. Zhou et al. “Resistance switching study of stoichiometric ZrO2 films for non-volatile memory application”. In: *Thin Solid Films*. Vol. 518. 20. 2010, pp. 5652–5655. DOI: `10.1016/j.tsf.2009.10.034`.

[240] M. Lanza et al. “Resistive switching in hafnium dioxide layers: Local phenomenon at grain boundaries”. In: *Applied Physics Letters* 101.19 (2012), p. 193502. DOI: `10.1063/1.4765342`.

Chapter 6

Crystalline RRAM devices

In contrast to the amorphous systems described in chapter 5, the majority of the literature considers crystalline RRAM devices. Such studies tend to be motivated by their amenability to modelling and the progressive nature of the SET and RESET transitions, which may enable devices with more than two resistance states. This chapter will cover the electrical and TEM characterisation of RRAM devices based on crystalline material systems, with a focus on electron energy loss spectroscopy (EELS). Two different material systems are investigated in this chapter, both incorporating zirconia within the active layer.

6.1 Introduction

For most n-conducting binary oxides, including ZrO_2, it has been demonstrated that resistive switching and the related redox processes do not take place homogeneously beneath the whole electrode area but are restricted to a spatially defined filament region that evolves during the electroforming process [26, 27, 43, 241–245]. In fact, all the devices characterised and presented in the previous chapter fall into this resistive switching category. As outlined in chapter 1, however, there is another class of bipolar resistive switching oxide systems, for which the high and low resistive state currents scale with the electrode area, implying that forming and switching events take place beneath the whole electrode [81, 246]. This RS mechanism is termed homogeneous or interfacial switching and is part of a larger class of RS called valence change memories (VCM). Such behaviour has been identified in many material systems, including perovskite manganites that are particularly promising for the development of multifunctional RRAM devices because of their largely tunable electric and magnetic properties [247]. Such properties are promising for multi-state memory, in which a single memory cell can store several bits of information, either encoded in multiple resistance states or, ideally, by incorporating additional functionality, such as ferromagnetism [247]. Moreover, the scalability of current with the electrode area might be advantageous for circuit design since it offers another degree of freedom. Perhaps more importantly, in most cases the switching has a gradual character: the resistance of a device changes continuously (not as the abrupt jump between two limiting values that was seen in the previous chapter). In fact, it has been suggested that RRAM devices that are governed by continuous or progressive RS are advantageous for advanced brain-like parallel computing, because the I-V characteristics resemble in some aspects those of neurons [248], as described in chapter 1. Hence, research on brain-inspired neuromorphic computing has attracted much attention due to its massive parallelism, adaptivity to complex input information, and tolerance to errors [249]. The synapse is a crucial element in a neural network, and due to their large number, it is highly desirable to realise the synaptic function with a simple device structure that has high density and low energy consumption [250], in which metal-oxide based resistive switching memory devices have demonstrated great advantages [251]. Multilevel ability is one of the key characteristics for synaptic application [250]. Although interfacial RRAM devices show multilevel resistive switching ability, which arises from the progressive RS behaviour, effectively controlling such behaviour remains challenging. In addition, progressive RS devices are perhaps more difficult to characterise because of the large number of interfacial electronic phenomena known to affect RS [27, 43, 252].

This chapter will focus on electrical and STEM EELS characterisation of two crystalline RRAM devices based on different material systems. The first is Ti/ZrO_2/Nb:STO/STO, prepared via PLD in Glasgow, as described in chapter 4. The second includes yttria stabilised zirconia (YSZ) and was prepared by collaborators in Jülich [244, 253]. Both devices employ zirconium oxide: undoped ZrO_2 was used in Ti/ZrO_2/Nb:STO devices and YSZ was used in conjunction with $PrCaMnO_3$ (PCMO) in Ni/YSZ/PCMO/SRO devices. The reason behind using YSZ and PCMO is related to previous results on devices with a Ti top electrode, where the formation of a thin TiO_x interfacial region upon fabrication, gives rise to a thin TiO_2 layer formed upon device cycling. In such devices, the RS can be explained by the amount of fully oxidised Ti ions in the stack, implying reversible redox reactions at the interface that governs the widening and narrowing of an insulating tunnel barrier [244, 253]. This model is very important as it proposes an alternative explanation for the resistive switching behaviour observed for a variety of material systems. In the devices characterised here, the 3 nm thick YSZ, is employed to act as a tunnelling barrier that governs RS, without the use of an easily oxidisable top electrode like Ti, which in this case is Ni. In other words, Ni/YSZ/PCMO/SRO devices characterised in the following sections were prepared to understand if in fact RS can be explained by changes in the width of a tunnel barrier. This being the case, it is expected that the two devices will have different RS properties, partly due to anticipated tunnel barrier and partly because of the use of PCMO, a p-type perovskite oxide, which contrasts with ZrO_2 an n-type binary oxide. Based on this, it is expected that SET/RESET polarities may be inverted when comparing the two types of RRAM device stacks because redox reactions will likely have opposite effects in such materials i.e oxidation will reduce the electrical conductivity in n-type materials but increase it in p-type materials. Still, it is likely that for both devices, the RS is not truly filamentary and it should also exhibit continuous transition between resistance states, being very different from devices presented in the previous chapter. STEM EELS data are correlated to electrical characterisation of devices, and in the case of Ni/YSZ/PCMO/SRO stacks allows for the direct comparison of IRS, LRS, HRS and “formed” states.

6.2 Experimental

Ti/ZrO_2/Nb:STO devices characterised in the next section were grown with experimental conditions summarised on table 2.1 on page 44. Electrical characterisation on the probe station was performed under N_2 to avoid oxidation due to Joule heating. The platinum electrode was grounded for all measurements. For the forming and set processes, a current compliance (typically <5 mA) protected devices against hard breakdown of the initial high resistance state. No current compliance was used for the reset process. For pulsed measurements, a read voltage of 100 mV and write/erase voltage of 1.5 V was employed (unless stated otherwise). Regarding the EELS analysis, a Multivariate Statistical Analysis (MSA) Digital Micrograph plug-in was utilised in order to perform Principal Component Analysis (PCA) on the datasets to separate the real signals from as many random noise components as possible and thereby produce low-noise spectra for mapping and quantitative evaluation [155, 254].

6.3 Results

6.3.1 Electrical Measurements on Ti/ZrO_2/Nb:STO devices

The electrical characterisation presented in this section was performed on devices that belong to the same sample, but have very different configurations: the first consists of a number of patterned "bulk" devices similar to those characterised in the previous chapter, wheres the second consists of a TEM lamella which is electrically connected to a conventional TEM membrane. Details of RRAM "TEM" specimen preparation and electrical connections was presented in detail in chapter 2, in the SEM and FIB section on page 70. The comparison between devices is useful because it allows some insight into the scalability of performance with device area. "Bulk" devices have an area of 31000 μm^2 whereas the TEM lamella has an area of 15 μm^2. Note that several "bulk" devices were measured and electrically stressed, but only one TEM specimen was analysed. For this reason, results presented for the "bulk" devices are representative of a much larger dataset, this not being the case for the "TEM" device. Starting with the "bulk" devices, it was observed that electroforming was not required for the majority of devices. Figures 6.1a and 6.1b illustrate the resistive switching behaviour observed for "formless" devices.

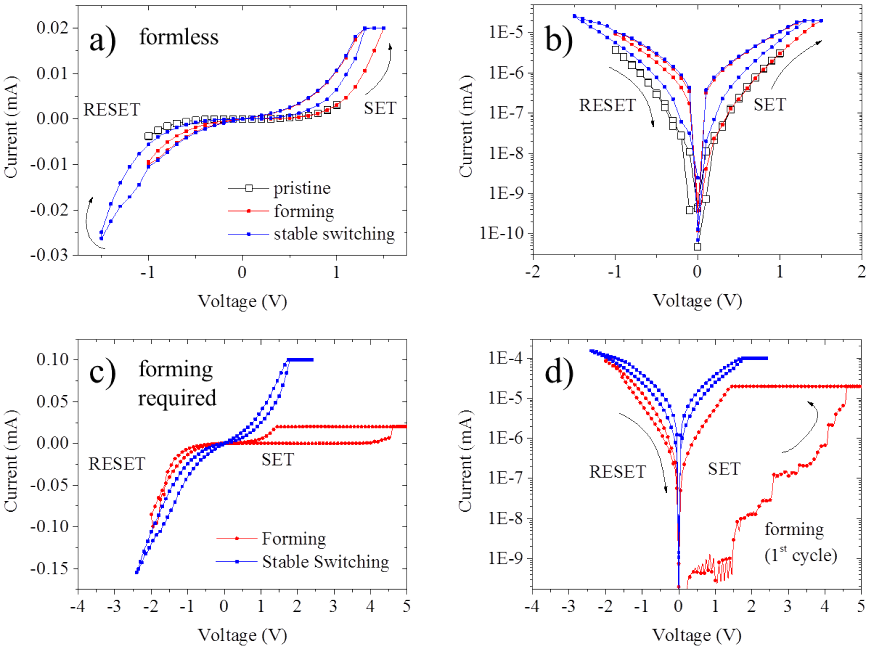

Figure 6.1: I-V characteristic of "bulk" crystalline RRAM devices during stable RS in a) formless, linear and b) formless, semilog scales. c) and d) illustrate electroforming step in linear and semilog scales, respectively. Ti/ZrO_2/Nb:STO stack with crystalline ZrO_2 38 nm thick and patterned with the "round" electrodes.

No RS is observed by applying 1 V (of either polarities) and the resistance measured is the pristine (IRS) MIM stack resistance, illustrated by the white markers on both plots on figure 6.1. With increasing SET voltage (up to 1.5 V) the device progressively switches from the pristine resistance state to the LRS and exhibits a small RESET transition (red circles). Note that the negative bias was kept at -1 V which very likely hindered a complete RESET transition. When higher voltages are applied (to both polarities), stable and reproducible RS is observed (blue squares). In contrast to "formless" devices, figures 6.1c and 6.1d illustrate a representative forming step that is obtained for devices that do not exhibit RS naturally. Note how the pristine resistance is approximately 10^3 times higher, as shown by the red circles, at 1 V, figure 6.1b and 6.1d, which can only be explained by variation within the fabrication procedure. Also, for such devices, the electroforming step takes place at much higher voltages than those required for RS transitions only. In fact, both SET and RESET voltages do not change by much: the voltage required to SET this device is approximately 1.5 V and it RESETS at -2 V. However, stable and reproducible RS involves currents approximately one order of magnitude higher, as can be seen by comparing figures 6.1b and 6.1d (blue squares). This phenomenon can be explained by permanent changes, possibly structural and chemical, that are induced by a forming step at significantly higher voltages than those used for RS. The concept of a controlled breakdown of the oxide layer during electroforming, covered in chapter 1, helps explain this phenomenon. Both types of devices showed good endurance, withstanding at least 10^4 cycles (not shown here) before starting to fail.

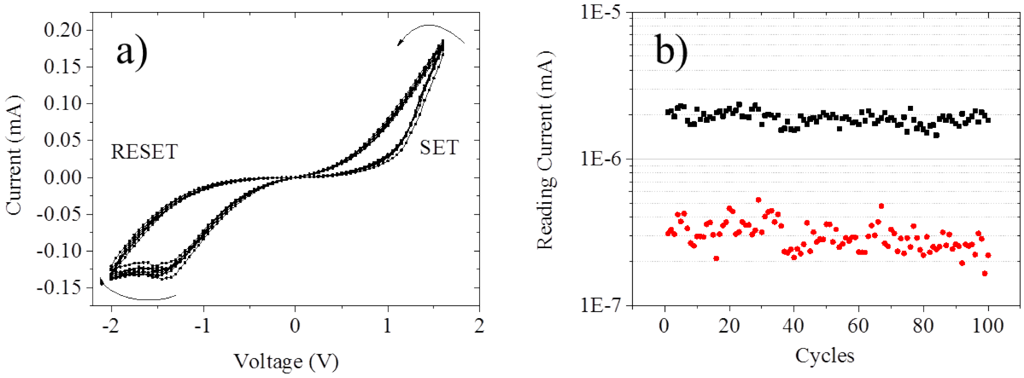

Figure 6.2: I-V characteristic of bulk sample a) 10 consecutive I-V sweep b) pulsing cycles. Ti/ZrO_2/Nb:STO stack with crystalline ZrO_2 38 nm thick and patterned with the "round" electrodes.

It was noticed that the current increases with cycling, normally during the first hundred

I-V sweeps, but stabilises soon after. The current-voltage sweeps shown in figure 6.2a and the switching cycles in figure 6.2b, illustrate the stable RS behaviour representative of Ti/ZrO$_2$/Nb:STO "bulk" devices, obtained after approximately 200 cycles. Additionally, the current required for RS is lower by approximately one order of magnitude, which is an advantage in the sense that less Joule heating might increase device lifetime. However, the ON/OFF ratio is also substantially lower, just under 10^1, which compares to ratios of 10^3 to 10^4 normally seen in amorphous systems. Figure 6.3 shows the same electrical characterisation, but obtained for the lamella.

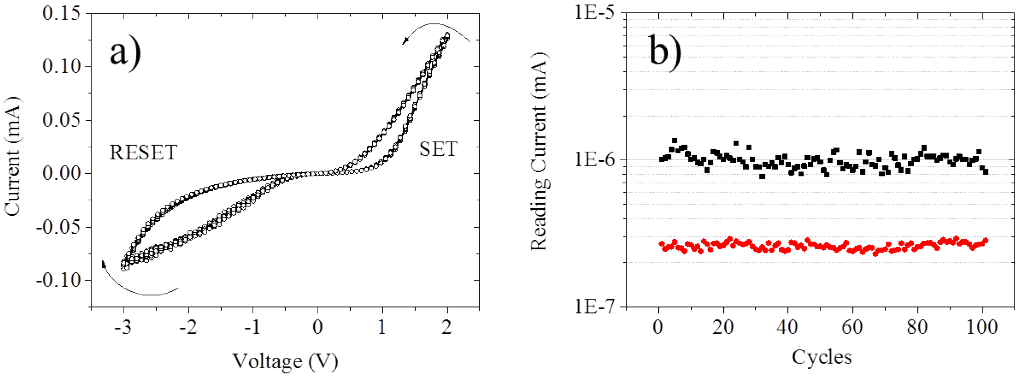

Figure 6.3: a) I-V characteristic of the lamella sample over 10 consecutive I-V sweeps b) No notable degradation in on/off ratio was noted over 100 pulsing cycles.Ti/ZrO$_2$/Nb:STO stack with crystalline ZrO$_2$ 38 nm thick. Device is now the entire TEM lamella.

Interestingly, both SET and RESET transitions take place for approximately the same voltages, 1.5 V and -3 V respectively, which suggests that there is no significant increase in the series resistance due to the electrical connections made to the lamella. Also, the magnitude of the current involved is in the same and no compliance is required, similarly to the "bulk" devices. Figure 6.3b shows the device's response to pulsing cycles. Although there is a decrease in the ON/OFF ratio, the most interesting feature is an increase in reproducibility of the HRS. Actually, the lamella exhibited the most reproducible HRS of all devices characterised, including the amorphous presented in chapter 5. The distribution of values for the LRS, on the other hand, shows no difference between lamella and "bulk" devices. For a comparison with devices of previous chapters, it is important to note that for both lamella and "bulk" cycle plots (figures 6.2b and 6.3b) the reading voltage was altered from 0.1 V to 0.3 V, respectively. This was performed because of the increased plateau over the origin, seen in the I-V sweeps on figure 6.3a, where the LRS and HRS are less distinguishable. The I-V sweeps in figure 6.4 illustrates the remarkable similarities between the lamella and "bulk" devices.

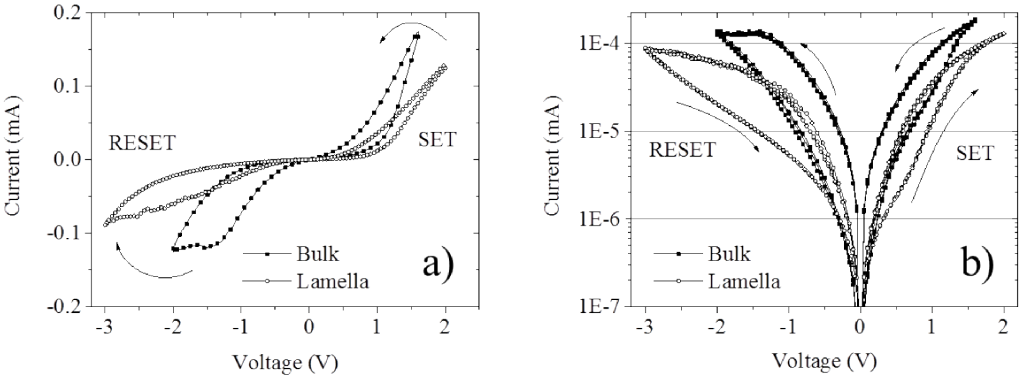

Figure 6.4: I-V characteristic comparing the bulk and lamella samples a) I-V sweep linear scale b) I-V sweep in semilog scale. Both samples originated from the same Ti/ZrO_2/Nb:STO stack with crystalline ZrO_2 38 nm thick and patterned with the "round" electrodes.

The first observation is that the device's resistances do not appear to scale with area, even if the increased reproducibility of the "TEM" device is likely attributed to its smaller dimensions. This is interesting because it suggests that RS in these devices cannot be solely interfacial, at least not over the entire device. In fact, the difference in device area is so big (ratio over 2×10^3), that the fact currents are in the same order of magnitude is completely unexpected. This observation would imply that these devices are filamentary in some way, even though other aspects, like the continuous shape of the I-V sweep and the lack of a current compliance are similar to the characteristics of interfacial switching described in the literature. One test that contributes to understanding which mechanism is governing RS is to compare the polarities of the SET and RESET transitions. For the majority of devices (in several material systems), polarities for filamentary-type and interfacial-type RS are opposite [34, 252]. This happens because RS will happen at opposite interfaces, were the polarity is inverted. Interestingly, for lamella and "bulk" devices the bipolar RS happens for the same polarity, which further complicates the analysis. Many models have been suggested for the conduction mechanisms, depending on the material system and device architecture, and where space-charged limited conduction (SCLC) is usually involved (as seen in the bistability section in chapter 5, page 148) [61, 92, 236, 255, 256]. Figure 6.5 shows log(I)-log(V) plots (similar to those found on page 148) for both devices for SET and RESET transitions. Plots are vertically grouped in respect to devices so that threshold voltages can be compared. Figure 6.5a illustrates the SET and figure 6.5b the RESET transition.

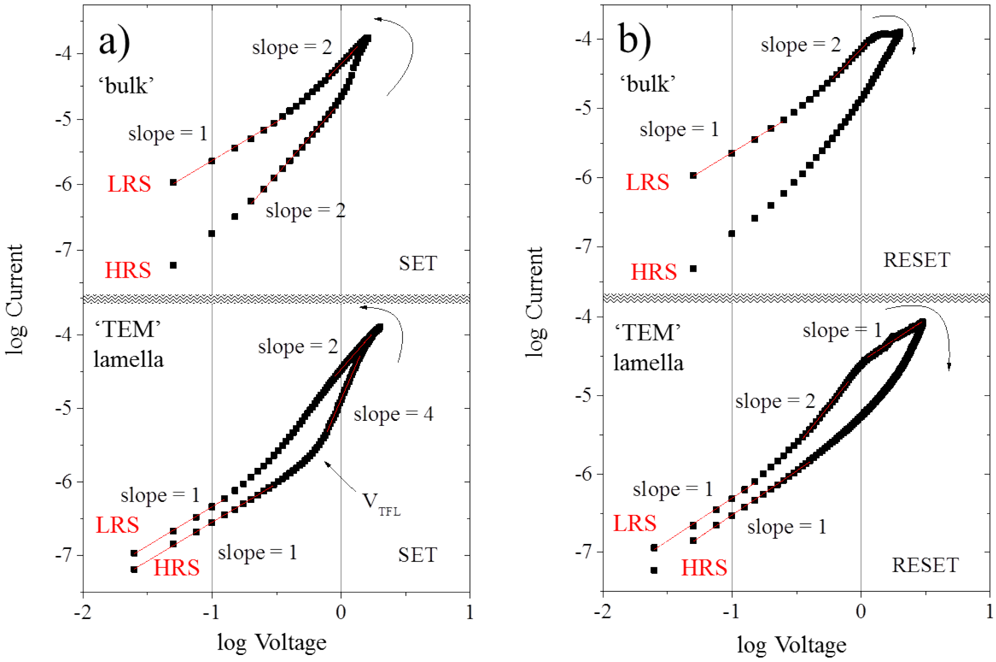

Figure 6.5: I-V log-log plots comparing the bulk and lamella conduction mechanisms a) during SET and b) RESET transitions. Both samples originated from the same Ti/ZrO_2/Nb:STO stack with crystalline ZrO_2 38 nm thick and patterned with the "round" electrodes.

Surprisingly lamella devices exhibits ohmic conduction at low voltages for both LRS and HRS, which is only achieved on the LRS for "bulk" devices. In fact, for the amorphous and polycrystalline devices characterised in the previous chapter, ohmic conduction was only seen on the LRS as well. This leads to another difference, seen in figure 6.5a during the SET transition, where the voltage threshold for the current increase (V_{TFL}) is only observed on the lamella device. This voltage threshold (where conduction departs from ohmic behaviour) is normally associated with a trap-filled state, as covered in chapter 1 and in the bistability section in chapter 5. This being the case, RS in the lamella device can be explained by a trapping/de-trapping process, where charge trapping happens at a positive (SET) and de-trapping at negative (RESET) voltages. One explanation for the existence of a threshold voltage (at V_{TFL}) when compared to "bulk" devices may arise from the much smaller volume of the device, and where scale dependence may account for the difference in electronic conduction. In the LRS shown in figure 6.5b, both devices show ohmic behaviour for lower voltages and switch to trap-filled SCLC (although not abruptly) at higher voltages. On the HRS, both devices seem to exhibit a quadratic decrease in current, characteristic of an insulator.

In summary, both devices agree with SCLC models described in the literature, even if with different characteristics. These findings corroborate the interfacial and homogeneous RS, or at very least, prove that a metallic conductive filament is not formed (compare figure 6.5 with 5.21 on page 148). In other words, crystalline Ti/ZrO_2/Nb:STO devices seem to be consistent with interfacial RS that does not scale with area, which is very intriguing. On possibility is that the overall concentration of structural defects in these devices is low (much lower when compared to amorphous or polycrystalline) and restricts the electromigration of oxygen ions that are responsible for RS, as suggested by Shibuya [252]. The lack of scalability with device area needs to be explained by a filamentary process, but where (1) only semiconducting filaments are formed or (2) filaments do not entirely bridge the top and bottom electrodes, meaning current will need to go through a thin oxide layer.

To further characterise crystalline Ti/ZrO_2/Nb:STO devices, STEM EELS analysis was performed. Figure 6.6a shows the elemental distribution of a pristine device.

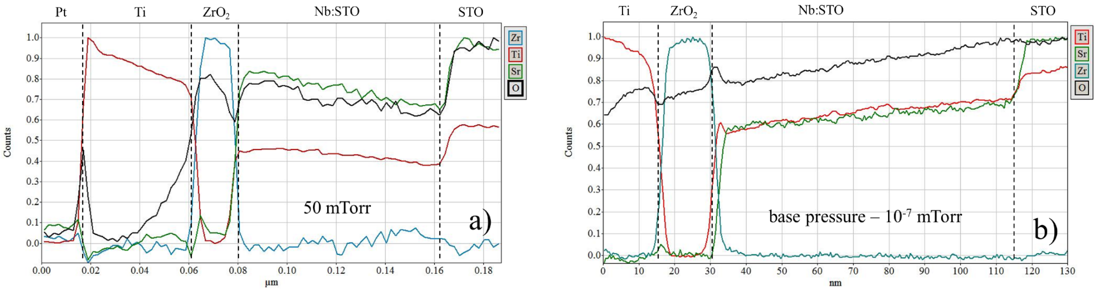

Figure 6.6: Elemental distribution obtained by STEM EELS on crystalline Ti/ZrO_2/Nb:STO devices.

Under applied positive bias to the Pt/Ti electrode, it is expected that oxygen ions drift towards that interface, injecting oxygen vacancies into the zirconia layer. This can be seen by the existence of oxygen signal well within Ti electrode, as shown in figure 6.6a. These vacancies will drift in the opposite direction, forming a filament with lower resistance. By applying reverse bias, oxygen ions will drift from the Ti into the zirconia, extinguishing the vacancies as well as the filament, hence increasing electrical resistance. It is possible that with the crystalline zirconia layer (which has less structural defects, when compared to amorphous layers) the oxygen vacancies will not be able to form a metallic filament that abruptly switches devices to a lower resistance state. Nevertheless, EELS results suggest that both interfaces are ohmic and hence these play a lesser role in RS. This comment about the interfaces is linked to partial oxidation of the Ti electrode and to the dip, on the oxygen profile, at the ZrO_2/Nb:STO interface. A gradual oxidation from a metallic Ti to TiO_y and a reduction from ZrO_2 to ZrO_{x-y} gives rise to ohmic interfaces, as explained in chapter 1. Analogously, a reduction in the oxygen content of zirconia in between ZrO_2 and Nb:STO will have the same effect. In fact the symmetric behaviour on the I-V sweeps presented before, corroborate this observation.

It is important to note, before drawing any conclusions, that there was a vacuum break at the Ti/ZrO_2 interface, used to pattern the devices. The sharp spike, seen on the oxygen profile at the Pt/Ti interface on figure 6.6a, is likely due to another vacuum break when changing the sputtering targets. However, the partial oxidation of the Ti electrode and the dip in the oxygen profile at the ZrO_2/Nb:STO interface can still be attributed to the oxygen gathering properties of titanium. More importantly, figure 6.6b illustrates a stack which comprises the same layers, but where the Nb:STO electrode was grown at base pressure, as described in chapter 4. Although there are many differences between samples, like the ratio of Sr to Ti and the overall oxidation of the Nb:STO, for the analysis described in this section the difference found at the interfaces are more important. The ZrO_2/Nb:STO interface is very different, as depicted by the oxygen profile, that shows an opposite behaviour. The dip in figure 6.6a gives rise to a pronounced bump, seen in figure 6.6b. This difference can be explained by the growth of Nb:STO at base pressure and with an oxygen pressure of 50 mTorr. Because ZrO_2 is deposited at 2 mTorr, it represents a decrease or an increase depending on the pressure used for the Nb:STO electrode. Furthermore, figure 6.6b also shows that the oxygen bump closely matches a bump on the oxygen profile, which suggests the formation of a thin TiO_x region, that may influence RS behaviour. In other words, this analysis proves that fine control of fabrication protocols is a requirement in the preparation of RRAM devices, and why so much attention was given to it.

6.3.2 YSZ/PCMO based RRAM devices

This section presents STEM EELS analysis performed on Ni/YSZ/PCMO/SRO devices prepared by collaborators in Jülich. These devices make use of a tunnelling oxide layer (YSZ) that accounts for RS behaviour, a mechanisms different from those presented in chapters 5 and in the previous section.

Resistive switching is explained by oxygen being pushed and pulled from the YSZ, where PCMO acts as an oxygen reservoir, similarly to what was described for Ti/PCMO devices [244, 253], and covered in the introduction of this chapter. An oxidised YSZ will have a higher resistance than a reduced one and hence resistance can be switched by applying different biases to the top Ni electrode. In these RRAM devices, Ni and SRO are the top and bottom electrodes respectively, and PCMO and YSZ the RS switching layers. Figure 6.7 illustrates electrical characterisation of these devices.

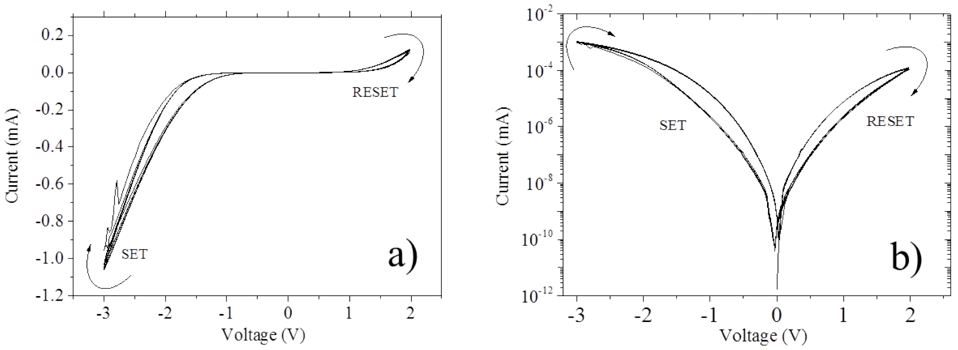

Figure 6.7: I-V sweeps of Ni/YSZ/PCMO/SRO devices in a) linear and b) semilog scales. Note how different the RS behaviour is when compared to those on the previous section and those presented on chapter 5.

The first observation is the different polarity for the SET and RESET transitions, when compared to all other devices presented in this work. SET happens for negative voltages and RESET for positive. Also, both transitions are more progressive than those observed for Ti/ZrO_2/Nb:STO devices characterised in the previous section, which is interesting as YSZ/PCMO devices have resistance states that scale with electrode area.

STEM EELS analysis of Ni/YSZ/PCMO/SRO devices is performed on four different TEM specimens representative of the resistance state of the devices: pristine, formed, ON and OFF. Different experimental conditions during STEM EELS acquisition mean that samples are grouped: in the next sections, “pristine” will be compared to “formed”, and “ON” will be compared to “OFF”. Figure 6.8a is a CTEM image of the entire stack of layers, illustrating the epitaxial growth of crystalline SRO and PCMO, polycrystalline YSZ and Ni layers. The fact that YSZ is poly-crystalline, seen from the lattice fringes of the inset in figure 6.8a, is interesting as YSZ was deposited at room temperature. However the use of PLD during preparation of samples may help explain the poly-crystalline nature of YSZ, similarly to what was presented for amorphous ZrO_2 layers in chapter 3. Alternatively, electron beam induced crystallisation cannot be ruled out, even if TEM was performed at 80 kV. However, it is surprising how the poly-crystalline YSZ still gives rise to RS that scales with area, which contrasts clearly with results obtained for poly-crystalline ZrO_2 based devices prepared in Glasgow.

Figure 6.8b is a dark field STEM image where all the layers are more clearly seen. Analysis

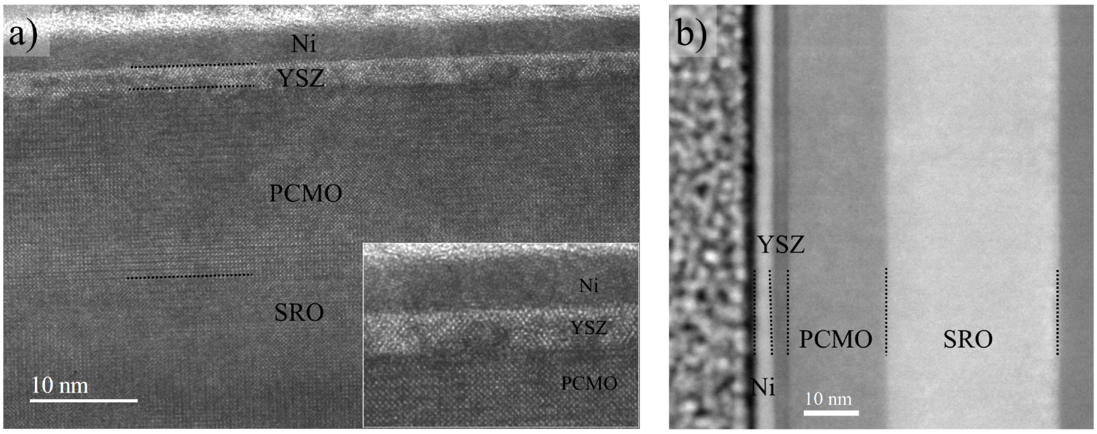

Figure 6.8: a) CTEM image illustrating all the layers that form the RRAM device to be analysed and b) dark field STEM image where all layer are more clearly visible.

will begin with a line profile indicating the elemental distribution across the SI. Additionally, several regions where analysed in detail: middle of the Ni top contact, middle of YSZ and middle of PCMO layer.

Starting with the "pristine" and "formed", both spectra were obtained with a dispersion value of 0.5 eV and a step size of 0.1 nm, and it is important to mention that SI "pristine" has a substantial carbon signal, decreasing in intensity throughout the specimen (higher in Ni and lower in PCMO). The carbon signature makes it very challenging to compare with precision the Ca L and Zr M edges, in the vicinity of the C K edge and, because of this, the elemental profiles of Ca and Zr, in figure 6.9 should be assessed at qualitatively. Higher energy loss edges, O K, Mn L, Ni L and Pr M show less of an influence and a comparison between both specimens is more accurate.
Perhaps the biggest observation is how similar the elemental profiles of both specimens are. However, the oxygen profile shows some subtle differences at the YSZ/PCMO interface, being higher for the formed specimen. Also, the Ca terrace observed within the YSZ, implies that it diffuses easier when compared to Pr and Mn, and likely to happen during fabrication as it does not change significant with forming. Also worth noticing that Mn and Pr signals cross-over at the YSZ/PCMO interface, and although by not much, this effect is very likely real because both edges are significantly away from the C K edge, and because this was also observed for the ON and OFF specimens. The Zr M edge signal was not found within Ni or PCMO, and the progression of Zr profile into the PCMO is due to difficulties during background fitting and removal, and should be ignored. Further investigation was performed by analysing line shape of EELS edges from the elements

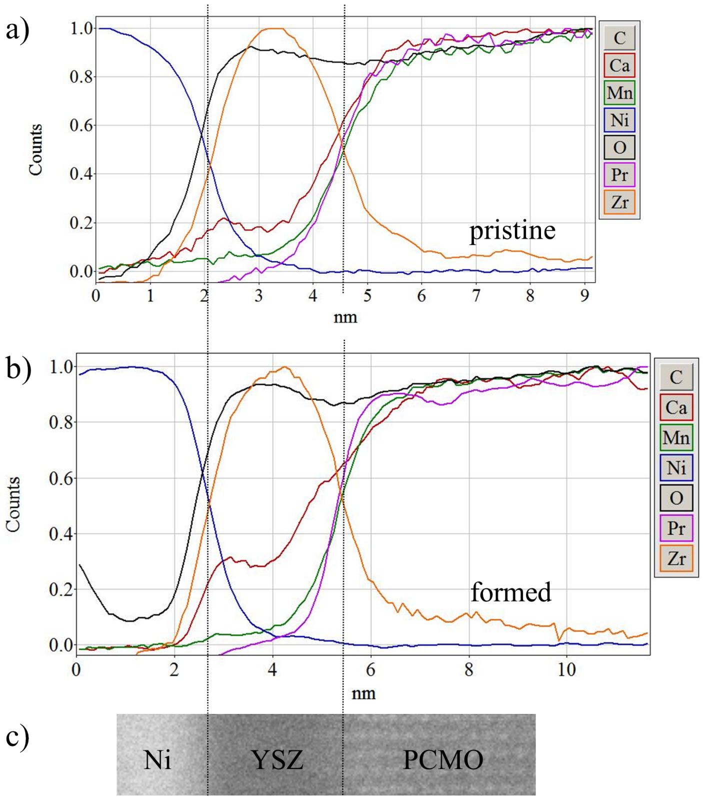

Figure 6.9: Elemental distribution of a) "pristine" and b) "formed devices". c) HAADF image aligned with spectra.

present in the sample. Figure 6.10 shows a dark field image representative of specimens "pristine" and "formed" illustrating where the edge spectra are extracted from.

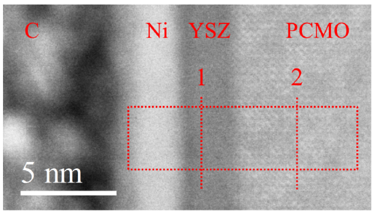

Figure 6.10: Dark field image indicating where O K, Mn L, Ca L and Pr M edge spectra is extracted from.

Region 1 covers the YSZ layer and regions 2 the PCMO layer. Starting with the oxygen, figures 6.11a and 6.11b illustrates O K edges extracted from regions 1 and 2 for "pristine" (blue) and "formed" (red). The O K edges presented are not vertically scaled, as both specimens have approximately the same t/λ, and because the difference between both samples is easier to see.

Within the YSZ (region 1), the oxygen K edge shows a small difference between specimens, in the fine structure. These differences, are very consistent and also found for specimens

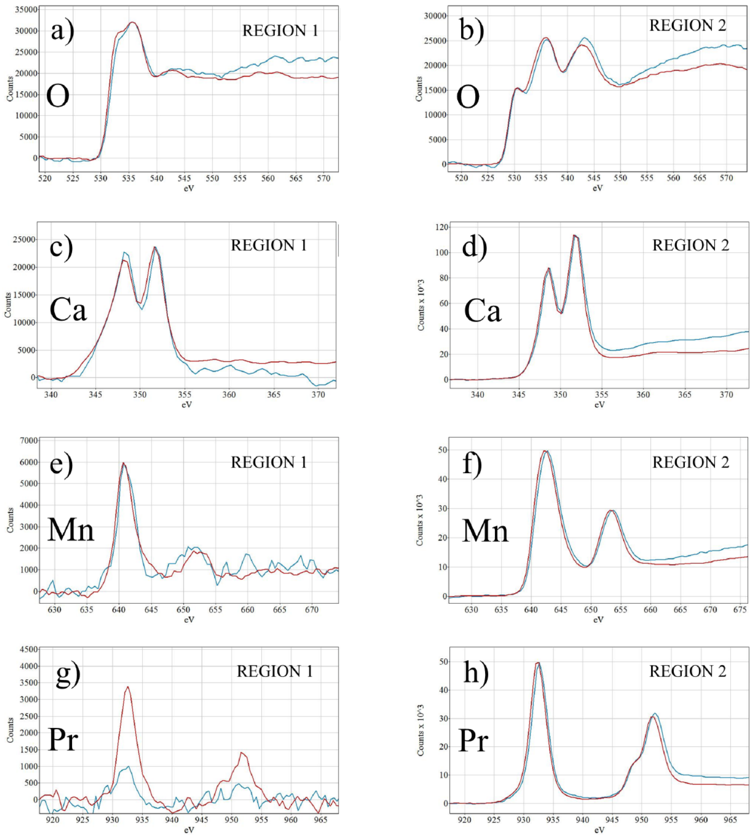

Figure 6.11: O K, Ca M, Mn M and Pr N edges for regions 1 and 2, indicated in figure 6.10. “Pristine” and “formed” in blue and red lines respectively. The SI is 11.7 nm in length.

ON and OFF. They are further analysed in the next section. Also, oxygen K edge line shape from spectra extracted from YSZ is also consistent with that obtained from ZrO_2, presented in chapter 3 on figure 3.16a. This being the case, it is likely that the YSZ layer is fully oxidised. In the PCMO layer, the line shape is consistent with that collected from other PCMO perovskites [257]. It edge shows some variation in the intensity of the third feature. The alignment between maxima and minima in the first two features suggest that the variation is likely real.

Figures 6.11c and 6.11d illustrates Ca L edge spectra extracted from regions 1 and 2, since it was not found within the Ni electrode. In this case, the interesting differences are between the spectra from two regions, rather than between “pristine” and “formed” devices. The ratio of Ca L_{23} edges is clearly different, possibly indicating a different oxidation state of calcium within YSZ and PCMO. However, comparing both specimens no difference is seen. Figures 6.11e and 6.11f shows the Mn L edge spectra extracted from within YSZ and PCMO layers. As seen for Ca L edge, it appears that there is some difference in the ratio of the L_{23} features for Mn as well, but not seen when comparing specimens. The second feature is relatively more intense for spectra extracted from region 3. Additionally, there is a small but measurable chemical shift towards lower energies on spectra extracted from within the YSZ layer (region 2). This chemical shift will be analysed in more detail while presenting the results comparing ON and OFF devices. Finally, figures 6.11g and 6.11h presents the Pr M edges extracted from within YSZ and PCMO layers. For this edge, it was observed that there is a variation in intensity of Pr within YSZ between the "pristine" and "formed" devices, as seen in 6.11g. In contrary, Pr M spectra extracted from PCMO shows no distinguishable differences in either white line ratio or chemical shift, which suggests that Pr does not change its oxidation state between YSZ and PCMO layers. In summary, EELS highlights subtle differences between the "pristine" and "formed" devices. These are: (1) the line shape of the O K edge within the YSZ layer and (2) a chemical shift in Mn L edge when comparing spectra extracted from the YSZ to PCMO layers. Both differences were also found for ON and OFF devices and will be analysed together, at the end of this section. Also, Ni was found in the bulk of the PCMO layer and Ca, Mn and Pr were found within the YSZ layer even at the interface with Ni. This is especially important because these findings originated on the "pristine" device, and hence cannot be explained by electromigration, suggesting that diffusion happened naturally during fabrication.

Moving on to the second sets of specimens, figure 6.12 shows the elemental distribution obtained for "ON" and "OFF" devices.

The main difference between the distribution is related to the shape of oxygen within YZS and at the YSZ/PCMO interface. It appears that oxygen is spatially more localised in the ON specimen than in the OFF specimen within YSZ. There is also a difference in the oxygen gradient in the PCMO layer. In the OFF specimen the oxygen almost follows the Pr and Mn profiles, detaching slightly in the vicinity of the YSZ/PCMO interface. This effect is greatly enhanced for the ON specimen, where the oxygen profile is very different at the YSZ/PCMO interface. Interestingly, such an effect was also observed for formed Ti/PCMO/SRO devices, and attributed to oxidation of the Ti electrode [253, 258]. However, there is a contradictory behaviour in the sense that such an effect is observed for ON devices, which are obtained by applying a negative bias to the top Ni electrode. As seen in the previous "pristine" and "formed" datasets, Mn and Pr profile cross-over at the YSZ/PCMO interface for ON and OFF, implying a greater diffusion and greater mobility. It is important to note that the spectra presented for such devices differs from the ones presented before: dispersion is 0.25 eV which gives better energy resolution (and hence more information about the fine structure), but covers less elements. Because of this,

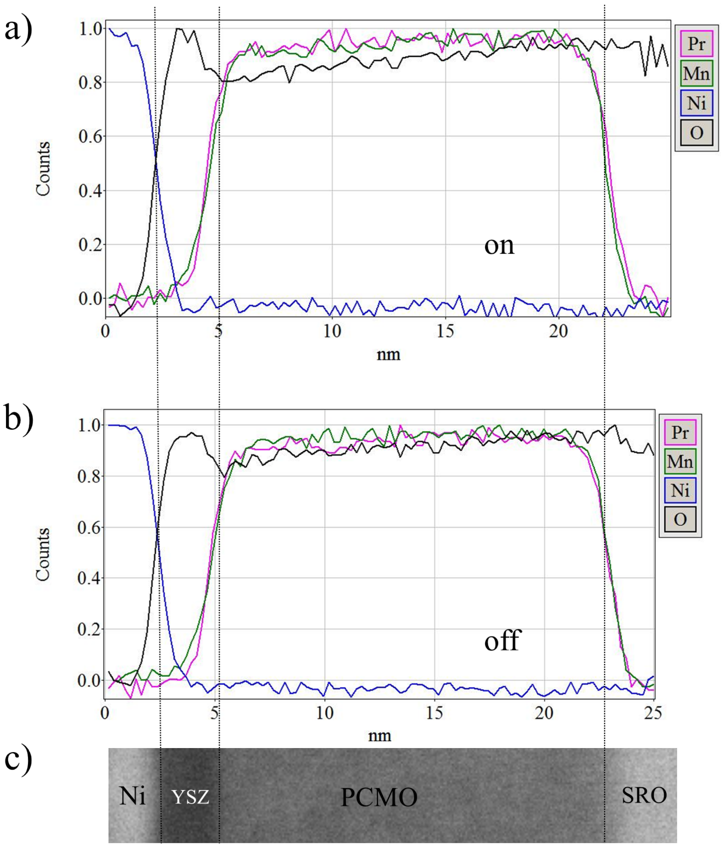

Figure 6.12: Elemental distribution of a) "ON" and b) "OFF" devices. c) HAADF image aligned with spectra.

there is no information about the Ca and Zr for ON and OFF devices, and the analysis is limited to oxygen, manganese and praseodymium. Figure 6.13 shows the dark field STEM image representative of specimens ON and OFF illustrating where the edge spectra are extracted from.

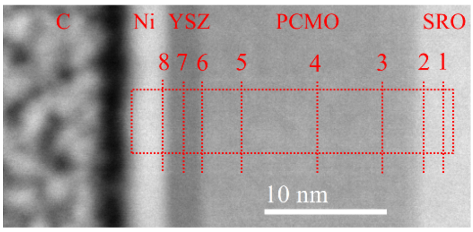

Figure 6.13: Dark field image illustrating where individual spectra is extracted from.

It is important to mention that for the "ON/OFF" comparison, the EELS datasets were experimentally acquired in exactly the same conditions. More importantly, the length of the SI and the t/λ values are very similar, which makes the direct comparison very robust to EELS processing. Because of this, spectra were not scaled. Figure 6.14 shows Mn L edge spectra extracted from regions 3-8, spanning from PCMO to the Ni/YSZ interface.

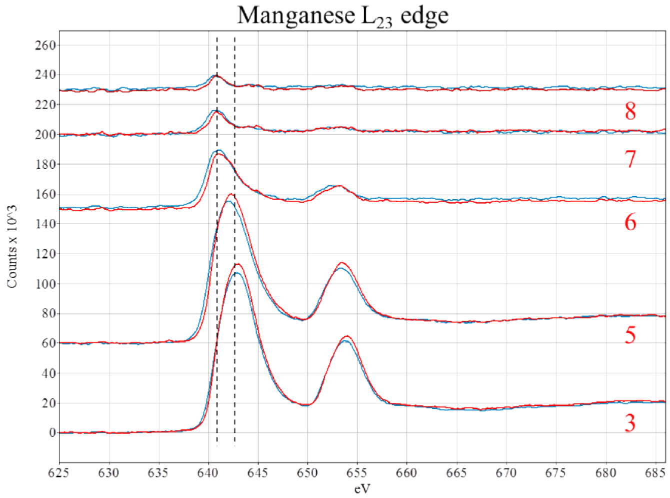

Figure 6.14: Manganese L_{23} edge for regions of interest 3-8 indicated in figure 6.13. "ON" and "OFF" in red and blue lines respectively.

It is clear from figure 6.14 that there is a clear shift to lower energies when comparing spectra extracted from regions 3, 5 with those extracted from 6-8. This is interesting because it suggests different oxidation states of Mn within YSZ and PCMO. In fact, a chemical shift in Mn was also observed for Ti/PCMO/SRO devices, although smaller than the one seen herein [258]. More importantly, it is suggested that such a progressive shift can be interpreted as a change from Mn^{4+} species (found within PCMO) to lower valence Mn^{3+}, due to chemical reduction at the interface and within YSZ [253, 258, 259].

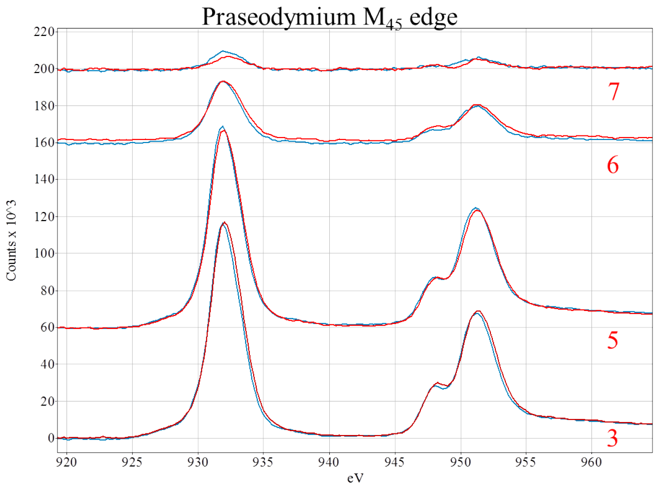

Figure 6.15: Praseodymium M_{45} edge for regions of interest 3-7 indicated in the previous figure. ON and OFF in red and blue lines respectively.

Yasuhara et al. also attributed such change to a reduction, but from $\text{Mn}^{3.3+}$ to Mn^{2+} [259, 260]. In contrast, Pr has shows no chemical shift or change in white line ratio, as can be seen in figure 6.15. This result is different to that obtained from Ti/PCMO/SRO devices, which showed a small chemical shift to higher energies for the Pr M edge, implying a subtle chemical oxidation [253]. Figure 6.16 shows O K edge spectra extracted from both specimens ("ON", red and "OFF", blue) from regions 1-8, which show a number of differences. The first observation is linked to the chemical shift gradually seen between spectra 1 and 8, which spans over 3 eV. This is attributed to the different ELNES signatures from SRO, PCMO and YSZ.

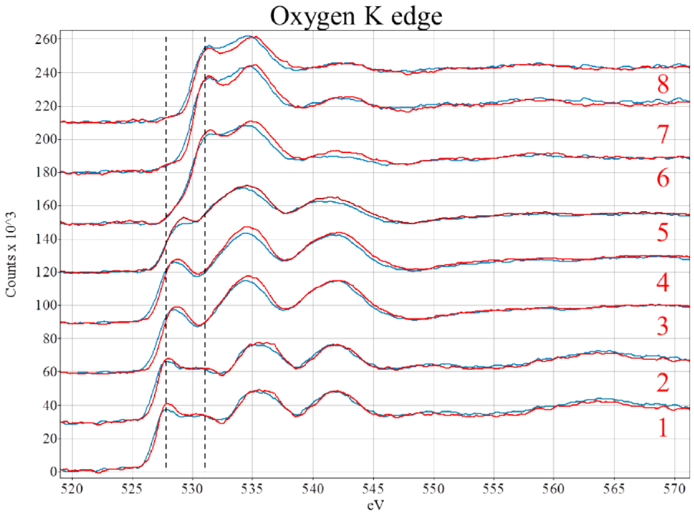

Figure 6.16: Oxygen K edge for all the regions of interest indicated in the previous figure, for "ON" and "OFF" devices. Profiles are offset vertically for clarity. "ON" and "OFF" in red and blue lines respectively.

There is little difference between ON and OFF in the SRO and PCMO layers (regions 1-5), but spectra extracted from within the YSZ layer (6-8) show increased differences. In figure 6.17, a direct comparison between O K edge extracted from within the YSZ layer (regions 6-8) is presented, illustrating the differences in line shape for specimens "ON" (red) and "OFF" (blue).

Figure 6.17, shows spectra from regions 6-8, but grouped by devices, so that a comparison is clearer. The changes are subtle, but very reproducible (and also found for specimens "pristine" and "OFF", as seen before), which suggest that this is not due to experiential error or incorrect background fitting and removal. The first feature on the O K edge has a higher intensity for specimen "OFF" (indicated by the arrow), whereas the second feature has the same intensity for both specimens. The difference in the peak intensities of O K

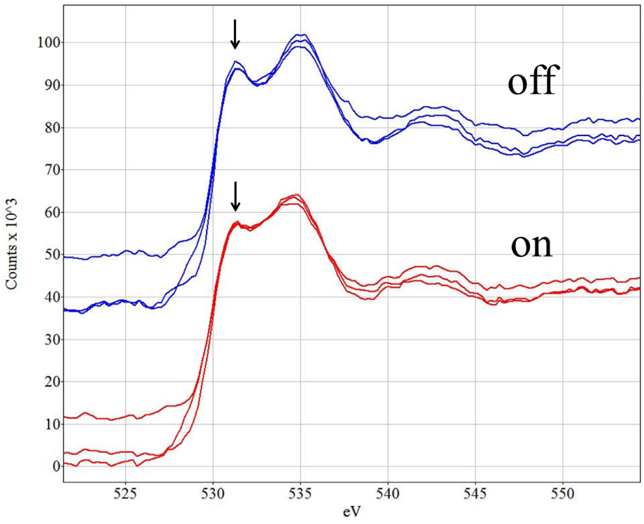

Figure 6.17: Oxygen K edge grouped by devices, and extracted from within YSZ (6-8). Profiles are vertically offset for clarity.

edge was also reported by McComb et al and was attributed to differences in structure, specifically between cubic and tetragonal stabilised zirconia, CSZ and TSZ respectively, which are two anion deficient phases [186]. According to figure 6.17, devices in the OFF state appear to match TSZ whereas devices in the ON state match CSZ. Very little is known about the structural properties of YSZ, but the CTEM image on figure 6.8, suggests some structure. Interestingly, it is suggested that the change in structure of YSZ (from TSZ to CSZ) is mostly linked to the concentration of oxygen vacancies [186, 187, 261]. The presence of oxygen vacancies within the YSZ reduces the average Zr cation coordination number from 8 to 7, in other words, ZrO_7 polyhedra are formed alongside ZrO_8 and YO_8 polyhedra [186, 187]. This link is important in RRAM devices, as oxygen vacancies are key in resistive switching mechanisms, as explained in chapters 1 and 5. In fact, differences found on the O K edge, and linked to different stabilised structures, may well indicated that RS changes the concentration of oxygen vacancies within the YSZ, possibly changing its structure which is what figure 6.17 is possibly suggesting. This hypothesis is similar to that of Fabris et al, that suggested that the electronic and structural properties of stabilised zirconia can be controlled by the structural disorder around the oxygen vacancies [262]. However, the effect that a change from TSZ (low oxygen vacancies concentration) to CSZ (high concentration) has on the measured change in electrical resistance is challenging to interpret, and may very well be linked to other elements. To further investigate the role that oxygen vacancies have on RRAM devices, attention was drawn towards the low-loss region of the EELS spectra. Figures 6.18a and 6.18b illustrate the low loss spectra obtained from the centre of the Ni and SRO layers respectively, and are shown for reference.

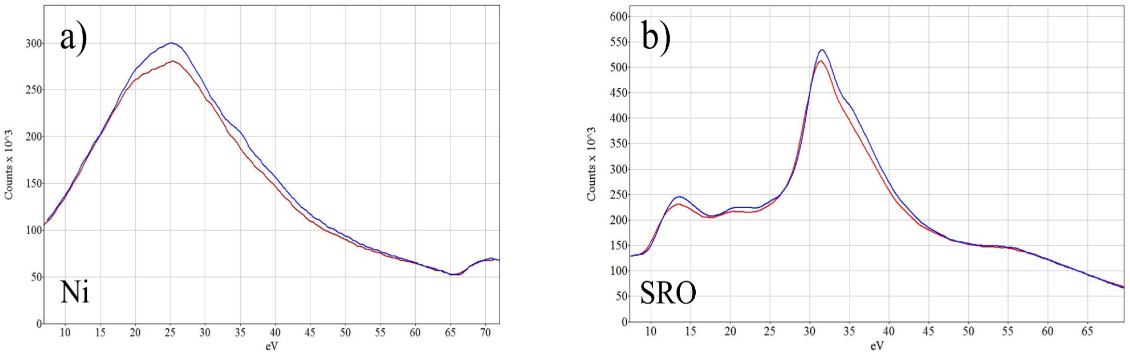

Figure 6.18: Low loss EELS spectra for a) Ni and b) SRO from in-house reference and [263]. “ON” and “OFF” in red and blue lines respectively.

Both plots show good agreement with metallic Ni and SRO low loss spectra found in the literature [263] and in house referenced spectra. Also, for both plots, the ON and OFF traces show almost no difference. However, the small differences found are for both cases restricted to an energy loss region ranging from 20 eV to 40 eV. This is interesting because such differences are within the energy loss range attributed to collective excitations between the valence and conduction bands [186]. In contrary, plots show almost no difference in features below 20 eV and above 40 eV. Figures 6.19a and 6.19b illustrate the low loss spectra obtained for YSZ and PCMO respectively.

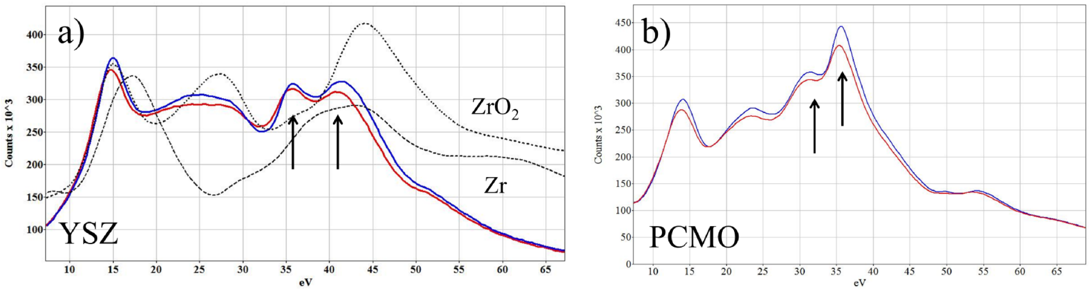

Figure 6.19: Low loss EELS spectra for a) YSZ and b) PCMO from in-house reference and literature [264]. “ON” and “OFF” in red and blue lines respectively.

In this case, plots show increased differences between the two specimens, also in the 20-40 eV region, when compared to the Ni and SRO presented on figure 6.18. More importantly, it is shown that the spectra obtained for YSZ, figure 6.18a, does not match the reference spectra obtained from (1) earlier ZrO_2 EELS study (presented in chapter 3 on figure 3.16b), (2) Zr and ZrO_2 spectra obtained in house by colleagues and (3) spectra found in literature [264]. This is unexpected as the O K edge from YSZ showed remarkable similarities with the one from ZrO_2, as referred when discussing "pristine" and "formed" specimens. However, the YSZ spectra seems to match ZrO_2 on the first and second features, but a match with PCMO is seen for higher energy loss features, with a small chemical shift towards higher energies (indicated by the arrows). Hence, the YSZ low loss signature is in agreement with the findings from the high loss analysis, that suggest intermixing between YSZ and PCMO, illustrated by the presence of Ca, Mn and Pr within YSZ. Interestingly, McComb *et al.* [186], Surnev *et al.* [265], French *et al.* [266] and Kobayashi *et al.* [267] have showed that the low loss EELS features between 5 and 35 eV are oxygen related. In fact, the energy loss features at approximately 15, 18, 21 and 24 eV have been attributed to interband transitions between O 2s/2p to Zr 4d/5s states [266, 267]. It is possible that transitions from the oxygen valence band to Ca, Mn and Pr conduction bands take place at approximately the same energy range. However, because transition between Zr p and d states happens at very similar energies, care should be taken when making assumptions regarding the low loss region. Also, it is worth mentioning that such transitions may not give rise to a clear and sharp features in the low loss spectra, which comprise many other electronic effects, including plasmons [268, 269]. Figure 6.20a-c are line profiles obtained using different energy windows, from spectra illustrated on figure 6.19a, for both "ON" and "OFF" specimens. The first interesting observation is how similar all plots are to the oxygen profile obtained from the high-loss SI, shown in figure 6.12. This appears to confirm that energy losses in the range of 10-50 eV are in fact related to oxygen interband transitions. Figure 6.20a was obtained by using a 2.5 eV signal window centred around 14.25 eV and without any background subtraction. It is clear that at the Ni top electrode, both profiles show almost no difference with the exception of a small increase for the "ON" specimen. This is important as the shape is exactly like the one obtained for the O K edge and presented in figure 6.12. Within the YSZ region, profiles not only show a substantial difference in intensity, but also on the shape, where the OFF specimen appears to shift towards the YSZ/PCMO interface. In the PCMO layer, both profiles match almost perfectly, with the exception of the region in the vicinity of the YSZ interface, where OFF specimen shows a subtle decrease in intensity. At the YSZ/SRO interface there is a significant offset, and as seen for the YSZ, the OFF specimen is also shifted towards the bulk of the specimen.

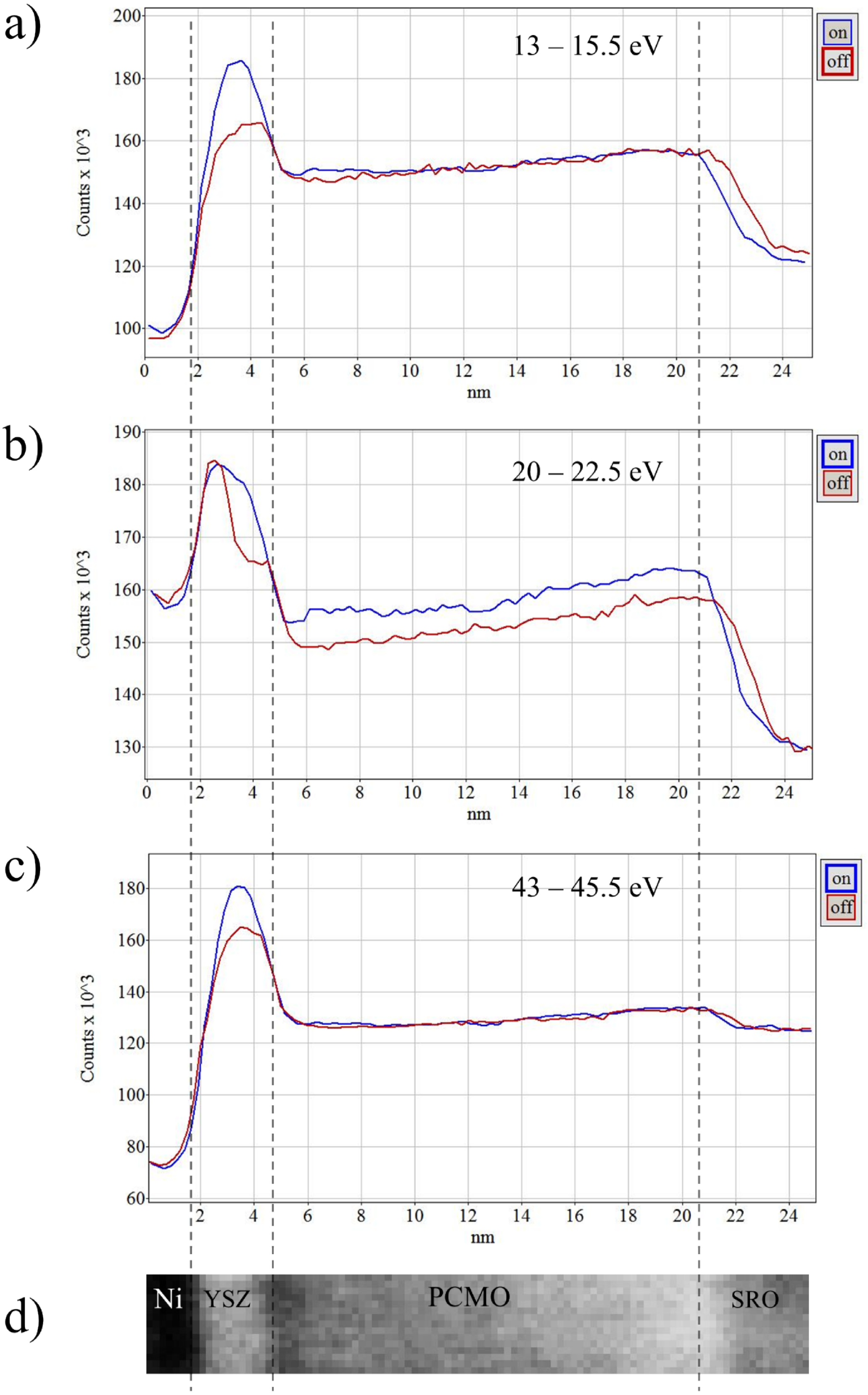

Figure 6.20: Spectrum images obtained at different energy losses. a) 13-15.5 eV b) 20-22.5 eV and c) 43-45.5 eV on specimens "ON" (red) and "OFF" (blue). Zero-loss peak was extracted and no background was used before extracting signal.

Figure 6.20b shows the biggest difference between "ON" and "OFF" EELS spectra of all the results in this chapter. There is a very clear difference in the shape of the profiles within the YSZ layer, where specimen OFF appears to have two distinct regions. Furthermore, the profiles show a clear intensity offset between OFF and ON within the PCMO layer, being higher for the ON specimen. This is important as PCMO is a p-type material, hence, a higher oxygen content likely indicates a more conducting PCMO layer during the ON state. Interestingly, at the YSZ/SRO interface there are also some differences: the ON specimen appears to have a sharper decrease, which also happens 1 nm before the OFF It is important to highlight that both profiles show very good agreement at the beginning (Ni electrode) and at the end (SRO) of the SI, which validates this comparison. Finally, figure 6.20c was obtained for higher energy losses, and shows less differences. There is an intensity difference within the YSZ layer, but both profile shapes agree perfectly. Also, no differences were seen for the PCMO layer, and only a very subtle offset was observed at the PCMO/SRO interface. In fact, energy losses in the range of 44 eV have been attributed to transitions between Zr 4p to Zr 4d/5s states [267], which is possibly why such differences are only seen on the YSZ layer. The analysis of figures 6.20a-c suggests that in fact it is possible to map oxygen with the low loss EELS spectra, and more importantly, it is possible to obtain more information about oxidation states than that given by the high loss O K edge. More importantly, it strongly suggests that three regions may be responsible for the resistive switching in YSZ/PCMO devices: the Ni/YSZ interface, the PCMO layer and the PCMO/SRO interface, as these regions were shown to have the biggest differences between ON and OFF devices. One scenario that explains the RS behaviour in these devices is that a positive bias on the top Ni electrode will cause an oxygen drift towards it, which needs to be compensated by the oxygen in the PCMO layer, and in turn by the SRO film. By applying the reverse polarity, oxygen drifts towards the bulk of the stack, and less of a difference is seen. As a matter of fact, on figure 6.20b, spectra for the OFF specimen is shifted towards the Ni electrode within YSZ, which is positively biased and will attract oxygen ions. In addition, the signal for the OFF specimen is much lower within the PCMO layer which can be explained by a supply of oxygen ions to the YSZ layer, and possibly explaining its shape too. Hence, a change in resistance can be interpreted by different concentrations of oxygen ions within the YSZ, that modulates the tunnelling barrier, increasing and decreasing its resistance. Analysis of the O K edge suggest that the YSZ changes its structure from TSZ to CSZ, for "OFF" and "ON" specimens, which also implies a change in the concentration of oxygen vacancies. The interpretation is more complicated for the change observed on the PCMO region, as an increase in oxygen should reduce its conduction being p-type. Alternatively, the changes within PCMO may be too small compared to those taking place within the YSZ tunnel layer, that effectively governs RS. Finally, it is curious that such chemical differences are still measurable after considerable time after electrical characterisation, which possibly indicates that such processes are non-volatile, and if this is the case, so are the electrical properties.

6.4 Conclusion

The preparation of crystalline resistive switching devices based on ZrO_2 was achieved on bulk and on a TEM lamella. Electrical characterisation performed on such devices showed that they do not scale with area. Moreover, crystalline ZrO_2 devices exhibited very continuous RS transitions, good stability and reproducibility, but significant lower on/off ratios when compared to the amorphous samples presented in chapter 5. EELS analysis performed in these devices showed that the Ti top electrode oxidises, shifting the oxygen content of the ZrO_2 layer towards the interface with Ti. This analysis was performed on a “pristine” specimen hence giving a clear picture about naturally formed interfaces. Additionally, the ZrO_2 interface appears to be reduced, as seen by the dip in the oxygen profile at the same interface. Resistive switching can be explained by oxygen ions drifting in and out of the Ti top electrode under a positive or negative bias, respectively. In this scenario, the oxidation of the Ti electrode induces oxygen vacancies within the ZrO_2 layer that will be responsible for forming a lower resistance path between the top and bottom electrodes. The difference between these and the devices presented in the previous chapter has to do with the crystalline nature of the ZrO_2 and Nb:STO layers. It is possible that a higher structural order will hinder the formation of a metallic filament as there are less defects within the film that are known to act as preferential fast diffusion paths.

For the Ni/YSZ/PCMO/SRO devices, it was shown that bipolar RS takes place for opposite polarities when compared to Ti/ZrO_2/Nb:STO. Furthermore, SET and RESET transitions are completely progressive, and resistance states scale with device area. By mapping the electronic transitions, with low loss EELS, between the oxygen valence band and zirconium (and possibly other cations) conduction band it was possible to infer that three regions may be involved in resistive switching. It was shown that the YSZ geometry, the oxygen content within the PCMO and finally the PCMO/SRO interface, all change considerably between ON and OFF devices. RS can be explained by different concentration of oxygen within localised regions of the YSZ, compensated by the PCMO. High loss EELS analysis showed that all four specimens (“pristine”, “formed”, “ON” and “OFF”) are very similar. In fact, differences for the high loss region showed only subtle differences, and was mostly useful for understanding intermixing and how fabrication techniques alter the intended device geometries.

EELS characterisation performed on YSZ/PCMO devices proves that there are spectroscopic differences between the “ON” and “OFF” resistance states which is of critical importance. So far, analysis of RRAM devices comprised only electrical measurements that showed the existence of *electronic* effects, like SCL conduction models in chapter 5 and in the previous section on this chapter, that do no explain of the voltage-time dilemma is overcome. The EELS analysis on YSZ/PCMO devices proves that redox reactions are also involved which can help explain why the voltage-dilemma is not a problem in such devices.

Bibliography

[26] Rainer Waser and Masakazu Aono. "Nanoionics-based resistive switching memories." In: *Nature materials* 6.11 (Nov. 2007), pp. 833–40. DOI: `10.1038/nmat2023`.

[27] Rainer Waser, Regina Dittmann, Georgi Staikov, and Kristof Szot. "Redox-Based Resistive Switching Memories - Nanoionic Mechanisms, Prospects, and Challenges". In: *Advanced Materials* 21.25-26 (July 2009), pp. 2632–2663. DOI: `10.1002/adma.200900375`.

[34] Ruth Muenstermann, Tobias Menke, Regina Dittmann, and Rainer Waser. "Coexistence of filamentary and homogeneous resistive switching in Fe-doped SrTiO3 thin-film memristive devices." In: *Advanced materials (Deerfield Beach, Fla.)* 22.43 (Nov. 2010), pp. 4819–22. DOI: `10.1002/adma.201001872`.

[43] J Joshua Yang, Dmitri B Strukov, and Duncan R Stewart. "Memristive devices for computing." In: *Nature nanotechnology* 8.1 (Jan. 2013), pp. 13–24. DOI: `10.1038/nnano.2012.240`.

[61] F. Yang, M. Wei, and H. Deng. "Bipolar resistive switching characteristics in CuO/ZnO bilayer structure". In: *Journal of Applied Physics* 114.13 (2013), p. 134502. DOI: `10.1063/1.4821237`.

[81] Akihito Sawa. "Resistive switching in Rapid advances in information technology rely on high-speed and". In: *Materials Today* 11.6 (2008), pp. 28–36.

[92] H. F. Tian et al. "Resistance switching effect in LaAlO3/Nb-doped SrTiO3 heterostructure". In: *Applied Physics A: Materials Science and Processing* 102.4 (2011), pp. 939–942. DOI: `10.1007/s00339-011-6276-5`.

[155] Joanna Bobynko, Ian MacLaren, and Alan J Craven. "Spectrum imaging of complex nanostructures using DualEELS: I. digital extraction replicas". In: *Ultramicroscopy* 149 (Nov. 2015), pp. 9–20. DOI: `10.1016/j.ultramic.2014.10.014`.

[186] Dw McComb. “Bonding and electronic structure in zirconia pseudopolymorphs investigated by electron energy-loss spectroscopy.” In: *Physical review. B, Condensed matter* 54.10 (Sept. 1996), pp. 7094–7102.

[187] S Ostanin et al. “Effect of relaxation on the oxygen K -edge electron energy-loss near-edge structure in yttria-stabilized zirconia”. In: *Physical Review B* 62.22 (2000), pp. 728–735. DOI: `10.1103/PhysRevB.62.14728`.

[236] Ting Zhang, Jiang Yin, Yidong Xia, Weifeng Zhang, and Zhiguo Liu. “Conduction mechanism of resistance switching in fully transparent MgO-based memory devices”. In: *Journal of Applied Physics* 114.13 (2013), p. 134301. DOI: `10.1063/1.4821900`.

[241] J Joshua Yang et al. “Memristive switching mechanism for metal/oxide/metal nanodevices.” In: *Nature nanotechnology* 3.7 (2008), pp. 429–433. DOI: `10.1038/nnano.2008.160`.

[242] Y B Nian, J Strozier, N J Wu, X Chen, and a Ignatiev. “Evidence for an oxygen diffusion model for the electric pulse induced resistance change effect in transition-metal oxides.” In: *Physical review letters* 98.14 (2007), p. 146403.

[243] Hong-Sub Lee, Sun Gyu Choi, Hye-jung Choi, Sung-Woong Chung, and Hyung-Ho Park. “A study of resistive switching property in Pr0.7Ca0.3MnO3, CaMnO3, and their bi-layer films”. In: *Thin Solid Films* 529 (2013), pp. 347–351. DOI: `10.1016/j.tsf.2012.07.075`.

[244] Anja Herpers et al. “Spectroscopic proof of the correlation between redox-state and charge-carrier transport at the interface of resistively switching Ti/PCMO devices”. In: *Advanced Materials* (2014), pp. 2730–2735. DOI: `10.1002/adma.201304054`.

[245] M. J. Rozenberg et al. “Mechanism for bipolar resistive switching in transition-metal oxides”. In: *Physical Review B - Condensed Matter and Materials Physics* 81.11 (2010), pp. 20–23. DOI: `10.1103/PhysRevB.81.115101`. arXiv: `1001.0703`.

[246] John Paul Strachan et al. “Structural and chemical characterization of TiO2 memristive devices by spatially-resolved NEXAFS.” In: *Nanotechnology* 20.48 (2009), p. 485701. DOI: `10.1088/0957-4484/20/48/485701`.

[247] Yuriy V. Yv Pershin, Massimiliano Di Ventra, and Massimiliano Di Ventra. “Memory effects in complex materials and nanoscale systems”. In: *Advances in Physics* 60.2 (2011), pp. 145–227. DOI: `10.1080/00018732.2010.544961`. arXiv: `arXiv:1011.3053v1`.

[248] Bin Gao, Lifeng Liu, and Jinfeng Kang. “Investigation of the synaptic device based on the resistive switching behavior in hafnium oxide”. In: *Progress in Natural Science: Materials International* 25.1 (2015), pp. 47–50. DOI: `10.1016/j.pnsc.2015.01.005`.

[249] C. Mead. “Neuromorphic electronic systems”. In: *Proceedings of the IEEE* 78.10 (Oct. 1990), pp. 1629–1636. DOI: `10.1109/5.58356`.

[250] Duygu Kuzum, Shimeng Yu, and H-S Philip Wong. “Synaptic electronics: materials, devices and applications”. In: *Nanotechnology* 24.38 (2013), p. 382001. DOI: `10.1088/0957-4484/24/38/382001`.

[251] Shimeng Yu et al. “A low energy oxide-based electronic synaptic device for neuromorphic visual systems with tolerance to device variation”. In: *Advanced Materials* 25.12 (2013), pp. 1774–1779. DOI: `10.1002/adma.201203680`.

[252] Keisuke Shibuya, Regina Dittmann, Shaobo Mi, and Rainer Waser. “Impact of defect distribution on resistive switching characteristics of Sr2TiO4 thin films.” In: *Advanced materials (Deerfield Beach, Fla.)* 22.3 (Jan. 2010), pp. 411–4. DOI: `10.1002/adma.200901493`.

[253] Francesco Borgatti et al. “Chemical insight into electroforming of resistive switching manganite heterostructures.” In: *Nanoscale* 5.9 (2013), pp. 3954–60. DOI: `10.1039/c3nr00106g`.

[254] G Lucas, P Burdet, M Cantoni, and C Hébert. “Multivariate statistical analysis as a tool for the segmentation of 3D spectral data.” In: *Micron (Oxford, England : 1993)* 52-53 (2013), pp. 49–56. DOI: `10.1016/j.micron.2013.08.005`.

[255] Yongdan Zhu et al. “Fabrication and mechanism of high performance bipolar resistive switching device based on SrTiO3/NiO stacked heterostructure”. In: *Microelectronic Engineering* 104 (Apr. 2013), pp. 85–89. DOI: `10.1016/j.mee.2012.11.023`.

[256] F. Pan, S. Gao, C. Chen, C. Song, and F. Zeng. “Recent progress in resistive random access memories: Materials, switching mechanisms, and performance”. In: *Materials Science and Engineering R: Reports* 83.1 (2014), pp. 1–59. DOI: `10.1016/j.mser.2014.06.002`.

[257] Jonas Norpoth, Stephanie Mildner, Malte Scherff, Jörg Hoffmann, and Christian Jooss. “In situ TEM analysis of resistive switching in manganite based thin-film heterostructures”. In: *Nanoscale* 6.16 (2014), pp. 9852–9862. DOI: `10.1039/C4NR02020K`.

[258] Anja Herpers. “Electrical characterization of manganite and titanate heterostructures”. In: *PhD Thesis* Julich (2014).

[259] Laurence A. J. Garvie, Alan J. Craven, Brydson, and Rik. “Use of electron-energy loss near-edge fine structure in the study of minerals”. In: *American Mineralogist* 79 (1994), pp. 411–425.

[260] R. Yasuhara, T. Yamamoto, I. Ohkubo, H. Kumigashira, and M. Oshima. “Interfacial chemical states of resistance-switching metal/Pr0.7 Ca0.3MnO3 interfaces”. In: *Applied Physics Letters* 97.13 (2010), pp. 18–21. DOI: `10.1063/1.3496033`.

[261] S. Ostanin et al. “Electron energy-loss near-edge shape as a probe to investigate the stabilization of yttria-stabilized zirconia”. In: *Physical Review B* 65.22 (June 2002), p. 224109. DOI: `10.1103/PhysRevB.65.224109`.

[262] Stefano Fabris, Anthony T. Paxton, and Michael W. Finnis. “A stabilization mechanism of zirconia based on oxygen vacancies only”. In: *Acta Materialia* 50.20 (2002), pp. 5171–5178. DOI: `10.1016/S1359-6454(02)00385-3`. arXiv: `0206080 [cond-mat]`.

[263] P A Cox, R G Egdell, J B Goodenough, A Hamnett, and C C Naish. *The metal-to-semiconductor transition in ternary ruthenium (IV) oxides: a study by electron spectroscopy.* 1983. DOI: `10.1088/0022-3719/16/32/014`.

[264] L.O. Prieto-López, F. Yubero, R. Machorro, and W. De La Cruz. “Optical properties of Zr and ZrO2 films deposited by laser ablation”. In: *Microelectronics Journal* 39.11 (Nov. 2008), pp. 1371–1373. DOI: `10.1016/j.mejo.2008.01.048`.

[265] L. Surnev and G. Rangelov. *EELS study of a clean and an oxygen covered Ru(001) surface.* 1985. DOI: `10.1016/0038-1098(85)90285-6`.

[266] R. French, S. Glass, F. Ohuchi, Y. Xu, and W. Ching. *Experimental and theoretical determination of the electronic structure and optical properties of three phases of ZrO2.* 1994. DOI: `10.1103/PhysRevB.49.5133`.

[267] Shoji Kobayashi, Atsushi Yamasaki, and Takeo Fujiwara. “Electronic Structure and Dielectric Properties of Cubic Zirconia”. In: *Japanese Journal of Applied Physics* 42.Part 1, No. 11 (Nov. 2003), pp. 6946–6950. DOI: `10.1143/JJAP.42.6946`.

[268] G. Marletta and S. Pignataro. “Electronic excitations in solid ZrO2 from reflection EELS and ESCA multipeak structures”. In: *Chemical Physics Letters* 124.5 (1986), pp. 414–419. DOI: `10.1016/0009-2614(86)85045-X`.

[269] Gregory R. Corallo, Douglas A Asbury, Richard E Gilbert, and Gar B Hoflund. "Electron-energy-loss study of clean and oxygen-exposed polycrystalline zirconium". In: *Physical Review B* 35.18 (1987), pp. 9451–9459. DOI: `10.1103/PhysRevB.35.9451`.

Chapter 7

Conclusions and Outlook

The work presented in this thesis contributed to advancing the current understanding of resistive switching mechanisms that govern valence change memories. Zirconium oxide resistive switching devices were prepared via PLD and characterised electrically and by transmission electron microscopy. This section summarises the main results obtained in all chapters and presents possible RS models that explain the electrical behaviour of the RRAM devices presented.

7.1 Conclusions

The formation of droplets was greatly reduced by the use of an aperture on the laser beam path, and by optimising target movement under ablation. Lower flux tails of the beam profile were removed as they are responsible for melting target regions close to where plasma expansion and sputtering occur, contributing to droplet formation. The reduction in droplet density contributed to the preparation of RRAM devices, because the risk of short-circuits in MIM stacks is linked to the density of droplets. Amorphous ZrO_2 thin films were deposited at different oxygen partial pressures and morphological, structural and optoelectronic characterisation was performed. Increase in partial pressure, from 1 mTorr to 30 mTorr, increases surface roughness from 0.25 nm to 0.5 nm and with surface features increasing from 7 nm to 27 nm in diameter. Even though films are generally smooth, the use of higher partial pressures may hinder the fabrication of RRAM devices with ultra-thin resistive switching layers, like 5 nm or less, as peak-to-peak roughness of films deposited at 30 mTorr is in the same order of magnitude. CTEM analysis showed that films deposited at the lower end of the pressure range comprise bigger crystallites when compared to those grown at higher pressures. In addition, zirconia films deposited onto the KBr single crystal substrates showed evidence of texturing, which is not expected for films deposited onto amorphous substrates or poly-crystalline layers. EELS indicated that films have a very approximate stoichiometry, suggesting that the minimum oxygen partial pressure employed here is enough to fully oxidise zirconium films during growth. Although a precise stoichiometry value was not determined with the O K and Zr M edges, the shape of the low loss spectra matches that of ZrO_2 obtained from in-house reference and those found in literature. The direct band-gap was calculated, ranging from 5.45 to 5.90 eV for films deposited deposited at 1 and 30 mTorr with the Zr and ZrO_2 targets, respectively. Even if the band-gap value did not show a significant evolution, the more abrupt onset of absorption suggests that such films may have band gaps with less traps when compared to those deposited with the Zr target. The optimal oxygen partial pressure was found to be 2 mTorr, as it yields devices that have the best compromise between on/off ratios and reproducibility and durability. The study linking that deposition partial pressure with film properties strongly suggests that the differences seen in device behaviour are better explained by different morphologies and the existence of nanocrystallites within the switching oxide layer, rather than differences in its stoichiometry.

Preparation of $SrTiO_3$ substrates with a single termination was achieved by annealing in the presence of oxygen at 1150 °C for 1 hour. Acidic and deionised water etching recipes gave rise to substrates where SrO is found on the surface, which is undesirable in our case. In addition, it was shown that as-received substrates are very different, and where the miscut angle changes significantly. Epitaxial deposition of Nb:STO was achieved, as given by the RHEED oscillations during growth and by the unit-cell steps on film's surface shown by AFM. Films have good electrical conduction, which makes them adequate for being used as bottom electrodes for the preparation of fully crystalline RRAM devices. Oxygen partial pressure during epitaxial Nb:STO and crystalline ZrO_2 deposition is responsible for changing the interfaces very substantially, where thin interfacial layers may be formed naturally. The formation of interfacial layers, namely TiO or TiO_2, should be avoided as it induces changes in the resistive switching behaviour of devices, especially by increasing variability.

Optimisation of fabrication procedures was essential, in order to achieve reliable RRAM devices with good performance figures. During device development stages, it was critical to decouple variability that arises from fabrication and measurement effects from that normally attributed to resistive switching mechanisms. Amorphous and poly-crystalline RRAM devices fabricated with Ti electrodes with a range of thicknesses clearly show different resistive switching behaviour. Devices with thinner electrodes show very unreliable switching characteristics, especially illustrated by the occurrence of unipolar and complementary switching events. With the use of thicker Ti electrodes, or with the introduction of an insertion layer, stable bipolar resistive switching is obtained. The explanation for the different behaviour can be interpreted by the concentration of oxygen vacancies, that are created within the zirconia switching layer when Ti oxidises. A thinner electrode may not be able to introduce the required concentration of vacancies, hence unreliable switching can be better explained by a controlled partial breakdown of the ZrO_2 layer. Instability and bistability seen for amorphous zirconia based RRAM devices can be explained by two different and competing mechanisms: first, electron trapping and de-trapping, characterised by having non-ohmic LRS and progressive SET and RESET transitions. Second, an insulator-to-metal transition explains the very abrupt SET and RESET transitions, as well as the ohmic LRS. The coexistence of two resistive switching mechanisms is possibly attributed to the as-deposited amorphous nature of the zirconia switching layer. Device operation leads to Joule heating that induces crystallisation, more likely to happen in the vicinity of the conductive filament, or where the localised resistive switching is taking place. From all the devices characterised in this work, amorphous are the only with a clear bistability. However, the coexistence of two mechanisms was not linked to device failure or further instability, as such devices were shown to withstand more than 10^4 cycles without degrading their performance. Crystalline devices based on ZrO_2 and Nb:STO do not show any evidence of bistability and are characterised by having extremely progressive resistive switching, as well as non-ohmic behaviour in the LRS. Analysis of the conduction mechanisms that govern such devices clearly indicate that space-charge limited conduction and trapping and de-trapping play a significant role in device switching. The preparation of a RRAM devices on a TEM lamella provided the most stable and reliable device operation, indicating that even though RRAM performance does not scale with electrode area, scalability if not a concern in RRAM technology. Similarly to what was observed for amorphous and poly-crystalline devices, analysis of crystalline ZrO_2/Nb:STO devices suggests that resistive switching is spatially localised, and therefore likely to be filamentary. For all ZrO_2 based devices presented in this work, the RS can be explained by the introduction of oxygen vacancies into the insulating oxide by the oxidation of the Ti electrode. Filamentary bipolar RS is taking place at the ZrO_2/Pt or ZrO_2/Nb:STO interfaces, depending on the device type, and not at the ZrO_2/Ti interface as often reported in the literature. Amorphous, poly-crystalline and crystalline devices have different bipolar switching characteristics depending on (1) concentration of oxygen vacancies within the as-deposited zirconia layer introduced during deposition or by the Ti electrode oxidation, and (2) existence of structural defects that act like preferential migration paths that ease filament formation.

On the contrary, Ni/YSZ/PCMO/SRO devices prepared by collaborators in Jülich are not filamentary, where performance figures scale with electrode area thus providing an additional degree of freedom when designing more complex architectures. Also, for such devices the SET and RESET polarities are inverted when compared to ZrO_2 devices. This can be explained by the use of PCMO, which contrary to ZrO_2, is a p-type material. Furthermore, both resistance state transitions are extremely progressive, and the analysis of the conduction mechanisms shows no evidence of electron trapping and de-trapping. STEM EELS analysis of such devices, performed for 'on' and 'off' specimens showed differences on the YSZ, PCMO and PCMO/SRO interface, suggesting that RS induces spectroscopic changes in these three regions. Switching can be explained by different concentration of oxygen anions within the YSZ that acts as a tunnelling layer. Oxygen anions are supplied by the neighbouring PCMO, which is why differences are also found within it and at the interface with SRO. On this basis, the resistive switching in Ni/YSZ/PCMO/SRO devices is homogeneous, being fundamentally different to all other devices presented in this work.

A comparison between the behaviour of ZrO_2 and YSZ indicates that different RS mechanisms govern both types of devices. Filamentary switching describes ZrO_2 based devices, whereas homogeneous RS describes YSZ ones. However, for ZrO_2 based devices STEM EELS was only performed for pristine devices, hence it was only possible to characterise such devices from a fabrication point of view, where naturally formed layers can be identified. Preparing TEM specimens that show evidence of the conductive filament is very challenging because of (1) its nanoscopic dimensions and (2) there is no indication whatsoever as to where the filament is formed which makes it characterisation impossible. On the contrary, YSZ devices have homogeneous RS that can be characterised anywhere on the device. Another advantage of the YSZ devices relates to the use of single crystal perovskite layers, that are model materials, characterised extensively over the years. Finally, it is important to note that spectroscopic evidence of RS was only seen for YSZ based devices. Devices based on ZrO_2 were characterised electrically, and it was shown that SCLC and trapping and de-trapping governs RS, but no redox evidence was obtained.

7.2 Outlook and Future Work

For the implementation of RRAM devices in everyday-life technologies, work could focus on two separate fields: very fast non-volatile binary memories, and more advanced computing approaches based on neuromorphic-like RRAM devices. In the first case, RRAM devices based on amorphous binary oxides should be considered as they offer the best potential for scalability, and because properties like low power consumption, fast switching and good on/off ratios have been reported. For the latter case, the use of crystalline material systems with extremely progressive switching as given promising results when mimicking brain synapses. Another interesting possibility is the development of resistive switching layers, based on perovskites oxides like LSMO, where additional material properties, like its magnetic state, can be controlled and used as additional data bits. However, the use of materials with controllable magnetic properties creates challenges due to the small size of the devices. In other words, it is experimentally very difficult to actually determine the magnetic state of a single RRAM device. One way to achieve such characterisation is to perform in-situ TEM measurements were the TEM sample if effectively a single "pristine" RRAM device.

Hence, future work should be aimed at preparing TEM lamellae which can be electrically connected so that "TEM" RRAM devices can be cycled in-situ and STEM EELS characterisation can be performed. For filamentary type devices, not necessarily based on ZrO_2, in situ measurements are critical as it is likely to be the only technique that allows for a clear picture about the driving forces that govern each of the RS mechanisms reported. In addition to STEM EELS, in-situ devices also open the possibility to magnetically characterise LSMO active layers, for instance. Techniques like Lorentz differential phase contrast (DPC) allow for magnetic characterisation of very small volumes to be performed within the TEM. However, correct preparation of such lamellae devices is very challenging and is possible that the high vacuum environment of the TEM may have very damaging effects, inducing vaporisation with Joule heating due to device operation. In this regard, TEM lamellae vapourisation can possibly be avoided by the use of TEM rod with a cryostat that allows for TEM samples to be cooled to very low temperatures using liquid N_2. In fact, the use of cooling TEM rods may also be beneficial as it may help prevent sample crystallisation under the electron beam. Another source of problems may arise from the use of sourcemeters connected to the "TEM" RRAM device which may interfere with the electron beam or magnetic lenses and spectrometer. In summary, future work should focus on the optimisation of in-situ TEM sample preparation and on the additional in-situ TEM characterisation techniques that were only very recently made available or are under development.

Chapter 8

Appendix

The following sections expand on the results presented in chapter 3 regarding the PLD system characterisation, as well as results regarding the electrical characterisation of the epitaxial Nb:STO bottom electrodes presented in chapter 4. Additional results regarding device design and patterning, as well as the electrical characterisation of RRAM devices covered in chapters 5 and 6 will also be presented. The first three sections describe the experimental challenges and techniques whereas the fourth presents the MATLAB codes used for the data analysis.

8.1 PLD Commissioning

This section starts with a description of how the PLD laser ablation plume and shutter fine control were characterised. Also it describes how the density of macroscopic droplets on film surface was determined using SEM images and a MATLAB image processing code. As mentioned in throughout the thesis, the commissioning of the PLD system was performed during the very initial stages of the experimental work.

8.1.1 Plume Characterisation

Nb:STO was deposited at room temperature and with an oxygen pressure of 1 mTorr, and was used essentially because of its significantly higher growth rate when compared to metals. The 2" wafer was not rotating so that a thickness profile of the ablation plume could be obtained. AFM thickness measurements were performed after lift-off of the Nb:STO film over the grid shown in figure 3.7 on page 86. Such grid was drawn using a conventional laboratory marker pen and the lift-off was performed in acetone. Figure

8.1 illustrates where the thickness measurement were performed on the 2” wafer coated with Nb:STO for the PLD ablation plume characterisation presented on page 86. The X-Y coordinates of each measurement were given by the scanning stage of the AFM itself, as all measurements where performed without moving the 2” wafer. A MATLAB code (see next section) interpolates the film thickness across the entire 2” wafer and determines the optimal position to place the samples, in a rotating sample holder inside the PLD system, to maximise thickness uniformity.

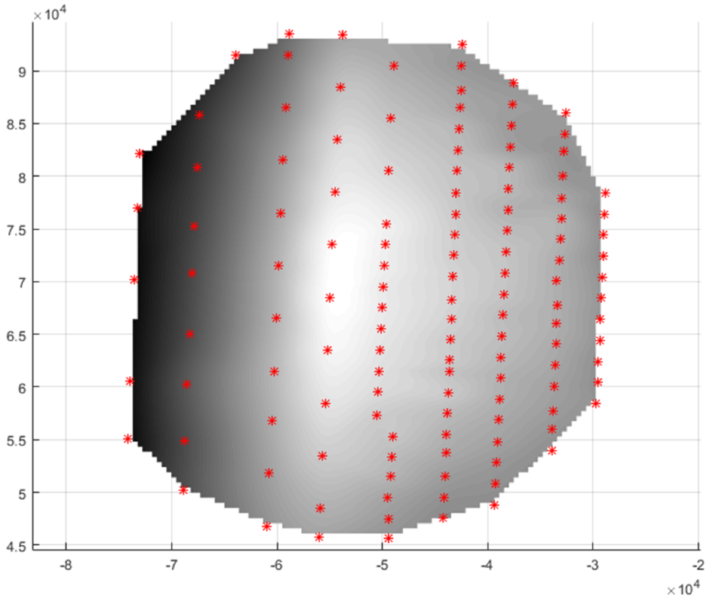

Figure 8.1: Position of thickness measurements taken for the interpolation presented on figure 3.7 on page 86. Scale in micrometres. Colour code in this image is grayscale.

The colour code in figure 3.7a was adjusted to match the photograph in figure 3.7b on page 86, and where the green circle indicates the optimal position for a 10 × 10 mm^2 rotating substrate.

8.1.2 Shutter Masking

The PLD system has a shutter system inside the chamber, between the target and the sample, to shield the sample during, for example, cleaning of the target. The shutter can also be used to mask specific regions of the substrate, to produce stepped or wedge deposition profiles. For all devices where the “round” architecture was employed, the shutter was used to mask the bottom electrode for accessing later without the need of post-deposition lift-off or etching processes, and more importantly, without breaking the vacuum. Fine control over the shutter position is essential as some of the RRAM devices were prepared on 5 × 5 mm^2 substrates. The characterisation consisted on a Nb:STO thin film (same conditions as before) deposited with 6 different thicknesses onto a 10 × 10 mm^2 c-Si chip by moving the substrate 2 mm every 1500 shots, while keeping the shutter fixed in the half-open position. This was most beneficial because the substrate movement can be done with greater precision, while keeping the shutter fixed in relation to the plume profile characterised previously, thus yielding better results. Figure 8.2 is a photograph of the substrate after deposition. Each colour indicates a different thickness and the diagonal white line is the lift-off line where the AFM thickness measurements took place.

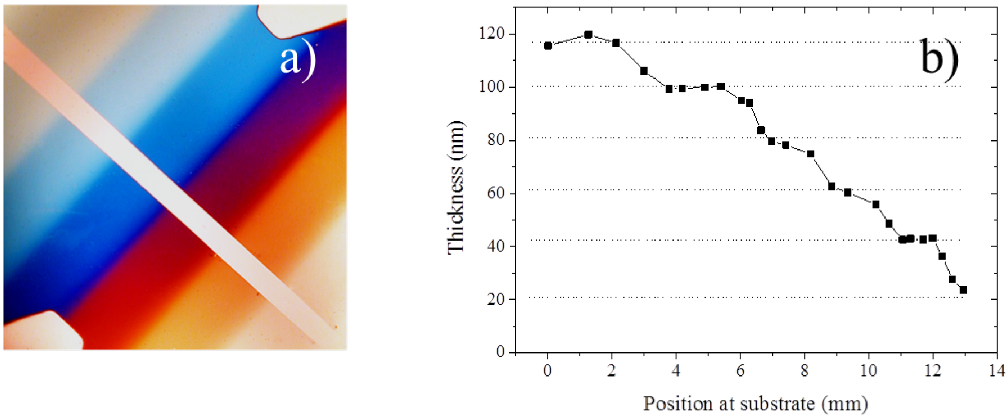

Figure 8.2: a) Photograph of the 10 x 10 mm^2 c-Si chip with 6 different thicknesses, decreasing from top left to bottom right. The two other features are caused by the pins holding the c-Si chip during deposition. The thicknesses can also be estimated using the colour code presented in figure 3.7 on page 86. b) Thickness profile across the lift-off line, illustrating the thickness steps.

The step height is in the range of 20 nm but even though the steps are clearly distinguishable visually they're not sharp enough for a direct AFM thickness measurement because they extend across a distance of several tenths of micrometres. Instead, a sharp step was created by lift-off (the diagonal white line in figure 8.2a) for AFM measurement of film thickness. Figure 8.2b shows the thickness profile obtained with this study using the lift-off line for all the thickness measurements.

8.1.3 Droplet Analysis

A MATLAB code (see next section) was developed for the correct analysis of the influence of the aperture on the density of particulates or droplets. The script consists of several instructions that process SEM images using threshold and edge-finding functions to identify high contrast regions. The regions are then stored and their area is calculated so that density versus particulate size density calculations can be inferred. For all the materials, five images (with a SEM magnification of 1000×) of the films with and without the aperture were analysed with the MATLAB script for averaging purposes. All the parameters in the SEM were the same when acquiring the images with the exception of the contrast and brightness which were adjusted afterwards.

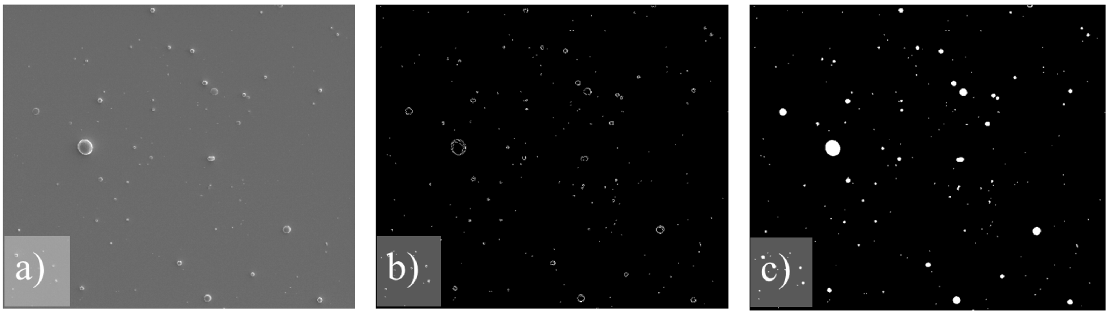

Figure 8.3: Illustration of some of the steps taken during image processing with MATLAB: a) and b) cropping images and converting from grayscale to binary with threshold and edge-finding followed by c) closing and filling of the areas. Magnification of all SEM images is 1000 ×.

Figure 8.3 illustrates some of the steps in image processing done with the MATLAB script. Figure 8.4 illustrates the accuracy of the MATLAB script in identifying particulates in the SEM images provided for this study. Once the images are in binary format and with the particulates correctly identified, their sizes can be determined accurately.

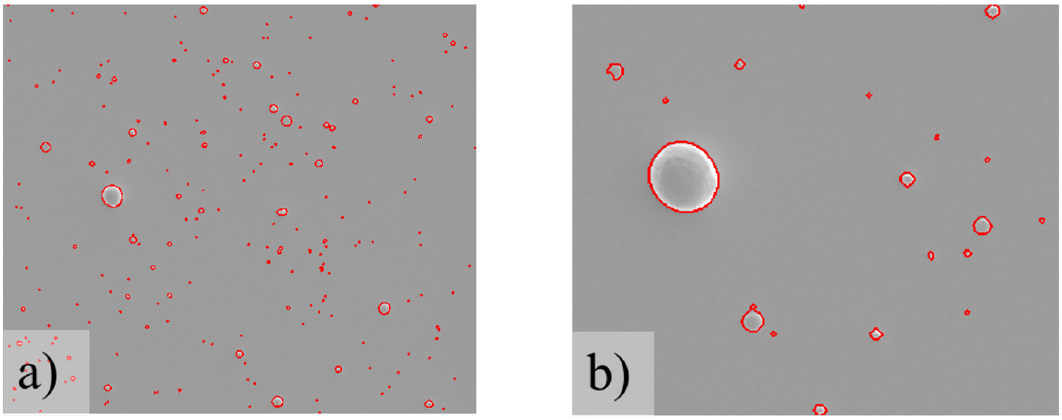

Figure 8.4: Particulate identification a) entire image b) close-up. This process step was mainly used to verify if the threshold and edge-finding function values were adequate for the contrast/brightness settings of the SEM images i.e. make sure the script correctly identifies macroscopic ejecta.

The histograms presented in figure 3.12 on page 91 were constructed with the result from the MATLAB image analysis shown above.

8.2 Photolithography and Device Design

All devices presented in this thesis were patterned either on a “crossbar” architecture or employed “round” electrodes, as explained on page 132. This section extends the discussion behind the use of the two different device designs and comments on how device areas influence device behaviour.

8.2.1 Device Design

As mentioned in chapter 5, the “crossbar” architecture was used during the development phase of the RRAM device fabrication and material selection. After fine optimisation of the zirconia deposition conditions and electrode material selection, device design changed to “round” electrodes. The main benefit of such change is the ability to prepare devices without a vacuum break between the active electrodes and the active layer.

Starting with the “crossbar” architecture, figure 8.5a and 8.5b illustrate the two photolithography masks required for the preparation of crossbar devices. Device patterning starts with mask 1 before the substrate dry-etching, Ti deposition and lift-off. The process continues with mask 2, that is used to delimit the zirconia active area, always using lift-off. Upon deposition of the zirconia active layer, the top electrodes are obtained using mask 1 rotated by 90°, in relation to the orientation of the bottom electrodes.

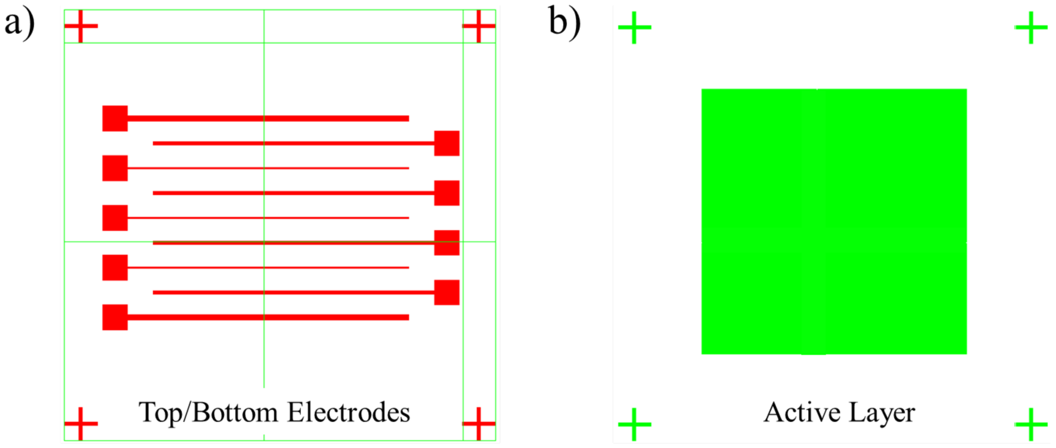

Figure 8.5: Photolithography masks employed for the “crossbar” devices. a) Mask 1 used for the electrodes and b) mask 2 used for the active layer. The “crossbar” design is finally achieved with the deposition of the top electrodes by rotating mask 1 by 90° in relation to the bottom electrodes. Square pads are 150 × 150 μm^2, lines are 1.8 mm in length and have three different widths: 10, 20 and 30 μm.

The fabrication of devices with different areas was achieved given the electrode lines on mask 1 have different widths, specifically, 10, 20 and 30 μm. Hence, with such pattern, device areas range from 100 to 900 μm^2. The length of the electrode lines is 1.8 mm which is shorter than the active layer square is 2 × 2 mm^2. The square pads at the end of each line are 150 × 150 μm^2 which is more than enough to accommodate the tungsten probes that have a diameter of about 30 μm.

Moving on to the second device design, figure 8.6a and 8.6b illustrate the photolithography masks design used to pattern "round" devices. In such design, patterning is achieved using a single photolithography step. Access to the bottom electrodes is accomplished by using the PLD system shutter as a shadow mask during active layer deposition.

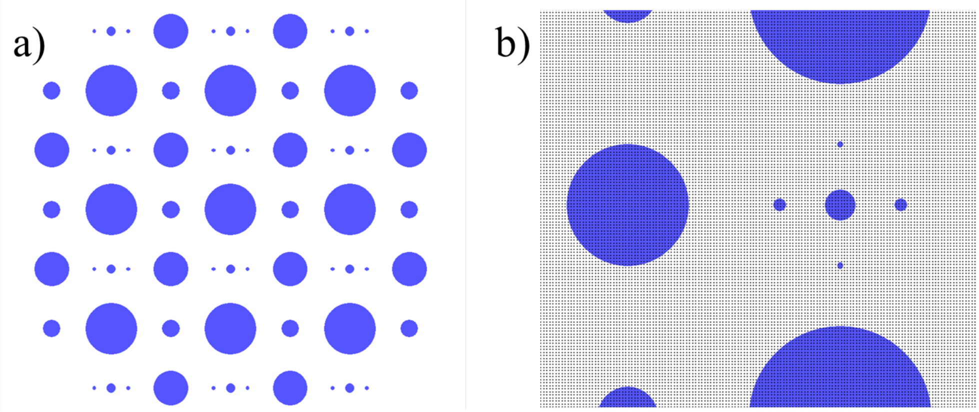

Figure 8.6: Photolithography mask design used for the preparation of "round" devices. a) Entire mask and b) close-up of the smaller dimension devices. Device diameters are: 5, 10, 30, 100 and 150 μm.

By avoiding the vacuum break, it is possible to investigate the oxidation and reduction reactions at the active electrode/oxide interface with greater detail, as the Ti electrode surface would otherwise oxidise during photolithography. Device areas using the "round" design range from 20 to 18000 μm^2, but for the majority of the results presented in chapters 5 and 6 devices with areas of about 700 μm^2 were used (having 30 μm in diameter).

A final comment regarding the two device architectures employed in this work is necessary: as mentioned in chapter 5, the reason behind using two device designs is linked to RRAM device development. It was evident that the "crossbar" design provided some assurances that the measured I-V response and observed resistive switching in early devices was not due to short-circuits caused by the tungsten probes or any other effects linked to fabrication (flagging, electrode roughness, active layer pin-holes, etc). In addition, such design makes electrical characterisation possible on very small devices. However, the "crossbar" design has its own major limitation. Specifically, unless great care is taken during electrical measurements to make sure devices are switched “OFF”, parallel switching is likely to occur. In other words, if devices are in the LRS or are damaged (short-circuited), it is possible that a voltage bias is applied to more than one device with unpredictable outcomes. This unwanted effect limits the number of devices that is possible to measure without suffering from “parallel” effects. Because of this, as soon as device yield became acceptable, “round” devices were always preferred, not only due to the lack of vacuum break during fabrication, but because such design enables the characterisation of single devices regardless of what happened to neighbouring ones.

8.3 Electrical Measurements and data Filtering

This section expands on the resistivity measurements performed during the optimisation of the PLD parameters for the epitaxial growth of the Nb:STO bottom electrodes presented in chapter 4, on page 121. These electrodes were then used for the preparation of the crystalline ZrO_2 devices presented in chapter 6, on page 163. The section continues with the presentation of additional electrical characterisation performed on “crossbar” Ti electrodes and on the amorphous ZrO_2 devices presented in chapter 5, on page 149.

8.3.1 Nb:STO resistance measurements

Resistance measurements using the Van der Pauw method were used to electrically characterise the epitaxial Nb:STO bottom electrodes used for Ti/ZrO_2/Nb:STO/STO devices presented on page 121. Measurements were performed for all Nb:STO films deposited during the development stages, when the optimal O_2 pressure during growth was being determined. For such electrical measurements, the Keithley sourcemeter normally used for 2 probe RRAM I-V sweeps and pulses was used in 4 probe mode. Figure 8.7b illustrates the electrode configuration used for all the Van der Pauw measurements performed in this work.

Platinum electrodes were deposited with a sputter coater and the patterning of the electrodes on the corner of the 5×5 μm^2 substrate was performed with another substrate rotated by 45°. Although the optimal configuration was not employed, resistance results across the contact permutations showed very good agreement. It is worth pointing out that the STO substrates are insulating which makes the resistance measurements on the Nb:STO films easier. In fact, more recent Van der Pauw measurements were performed without the platinum contact deposition, instead, silver paste was used in exactly the same

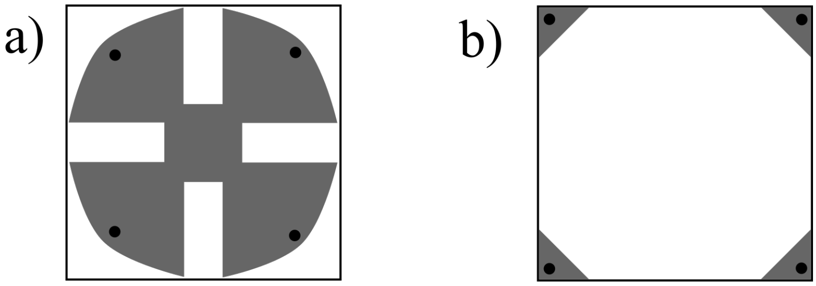

Figure 8.7: Electrode patterning for Van der Pauw resistance measurements. a) Optimal Van der Pauw pattern and b) pattern used for the resistance measurements performed throughout the thesis.

geometry. Resistivity values ranged between 3 × 10^{-4} to 9 × 10^{-4} ohm.cm for all the Nb:STO films measured. Interestingly, it was observed that the electrical resistivity is not so much affected by different oxygen pressures during growth when compared, for instance, with film growth modes.

8.3.2 RRAM devices - "Crossbar" electrode characterisation

Electrical characterisation was also performed on buried Ti bottom electrodes used in the "crossbar" architecture. The reason for this test has to do with understanding what is the minimum resistance that "crossbar" devices may exhibit i.e. resistance is governed by the electrodes when devices are in the LRS or "ON" state. Figure 8.8 illustrates the I-V response obtained for such electrodes.

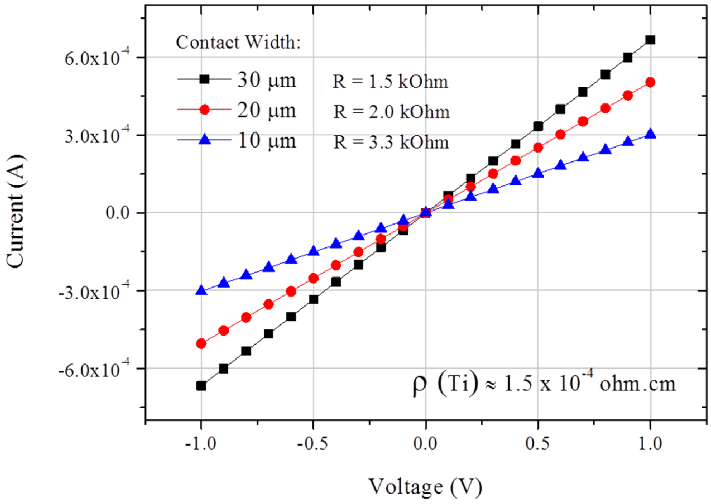

Figure 8.8: Ti electrode resistance as a function of line width. For all the electrode lines measured, Ti resistivity is approximately 1.5 × 10^{-4} ohm.cm.

The resistance measurement was performed on SiO_2/Si substrates prior to the deposition of the zirconia active layer. One of the tungsten probes was placed on a square pad and the other on the end of the electrode lines. This test was repeated twice during the course of device optimisation and results were always consistent with the ones presented here.

The effect that device area has on amorphous RRAM devices was also investigated using the “crossbar” architecture. Such tests was performed on amorphous zirconia based devices with an active layer thickness of 60 nm. Figure 8.9 illustrates how different device areas influence device electrical behaviour. Resistance measurements were originally performed on “pristine” devices, that do show an area dependence as shown by the blue markers in figure 8.9. However, once amorphous RRAM devices are electroformed and electrically stressed, the dependence on area is no longer observed, as illustrated by the red markers (right axis) on figure 8.9. Interestingly, the resistance values of stressed devices match those obtained for the Ti bottom electrode lines alone, as discussed above. The important outcome of this observation is that the resistance of amorphous RRAM devices in the LRS must be much smaller than the electrodes themselves. In other words, such electrode resistance can be used to limit the amount of current going through the devices without the use of additional current compliance on the sourcemeter.

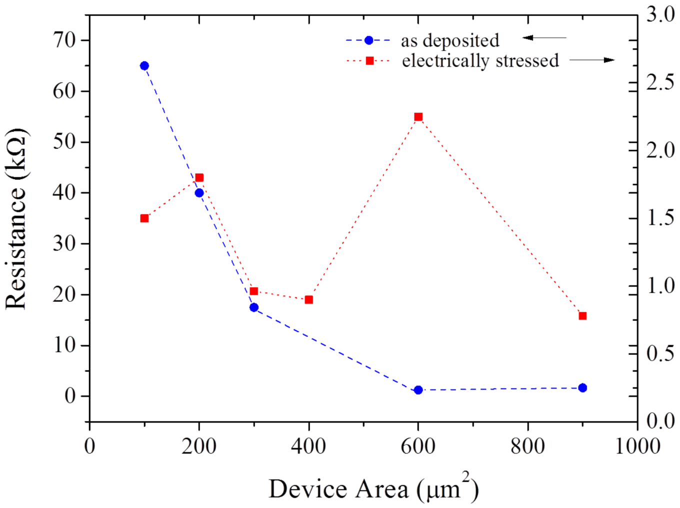

Figure 8.9: Resistance as a function of device areas for a) “pristine” and b) electrically stressed devices.

The lack of dependence on area is not surprising given the highly localised nature of the filamentary resistive switching mechanism that governs amorphous zirconia based RRAM devices. In fact, all the devices presented in this thesis did not show any dependence with area once electrically cycled or stressed. One particularly good example of the lack of dependence on area is presented in chapter 5, when describing the “TEM lamella” device, that effectively is the smallest device ever characterised in this work. Remarkably, it shows a similar electrical response when compared to its “bulk” counterparts.

8.3.3 RRAM devices - Effect of temperature

The effect of temperature on the electrical behaviour of amorphous ZrO_2 based RRAM devices (presented on page 149) was also investigated, as illustrated in figure 8.10. It is worth noticing that such tests were performed more recently i.e. not done during the RRAM device development stage. Heating of the devices was achieved with a Peltier heater as described in chapter 2, and for all tests thermal paste was used between the substrate and the Peltier stage, and the temperature was allowed to stabilise before electrical characterisation.

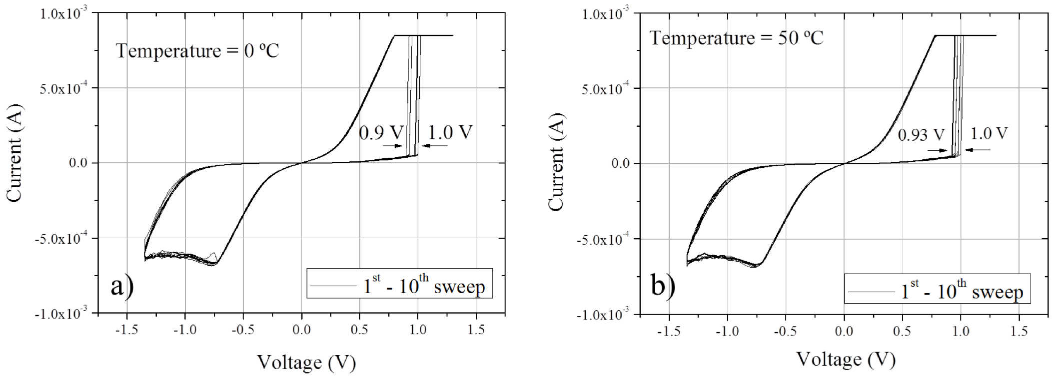

Figure 8.10: 10 consecutive I-V sweeps performed a) at 0 °C and b) 50 °C. Note how little influence temperature has RRAM devices. Measurements showed no influence on temperature, even at 85 °C which was the maximum achievable temperature. Performing measurements at 0 ° or lower is challenging because condensation forms on top of the samples very easily, even within the glovebox purged with N_2.

For all the temperature tests performed, zirconia based RRAM devices showed hardly any variation when performed at different temperatures. One reason that can explain such observation is the fact that in filamentary RS the current density generates much higher temperatures by Joule heating than the “low” temperatures achieved by the Peltier during this test.

8.3.4 RRAM devices - Effect of sweep rate

In addition to temperature tests, the use of different sweep rates was also investigated, as shown in figure 8.11. The different sweep rate was controlled by the LabVIEW interface running the Keithley sourcemeter, where the wait time changed from 0 ms to 500 ms per voltage step. For the two plots presented in figure 8.11 the voltage step was the same, 50 mV/step, and although devices have different areas, they are from the same batch. A complete I-V sweep changes from 2 seconds to about 50 seconds when the wait time changes from 0 ms to 500 ms. Although some variation is observed, the overall behaviour remains somewhat unchanged, and where the SET and RESET voltages hardly change.

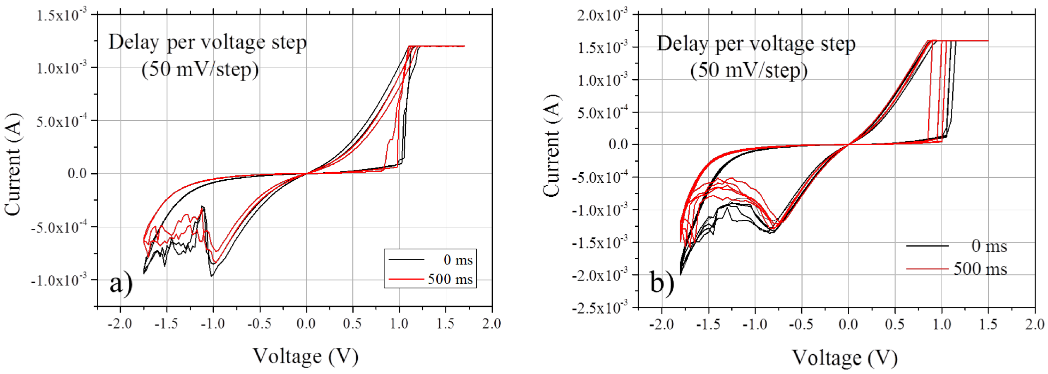

Figure 8.11: 10 consecutive I-V sweeps performed at different voltage sweep rates, 0 ms wait time and 500 ms wait time per voltage step. a) 10 × 10 μm^2 and b) 30 × 30 μm^2 devices.

One possible explanation for the small variation observed has to do with Joule heating of the device under test. Keeping the device on the ON state for a few seconds (with a current limit of 1.5 mA) will heat up the devices substantially more than what was achieved by an external heat supply. Still, devices based on amorphous ZrO_2 showed remarkable tolerance to the use of different characterisation temperatures and DC sweep rates.

8.3.5 RRAM devices - Data filtering

The electrical characterisation of RRAM devices, during development and with optimised devices, generates a very large number of data files. The specific RRAM LabVIEW interface outputs a .csv file for every measurement, which means that literally hundreds (sometimes thousands) of files are created. To overcome this difficulty, a MATLAB code (presented in the next section) was developed to filter the .csv files depending on a given criteria, usually on/off ratios. Figures 8.12 and 8.13 illustrate what the MATLAB code outputs as a result of the data filtering and analysis process. The datasets under analysis are related to ZrO_2 devices with an insertion layer, presented in chapter 5 on page 139.

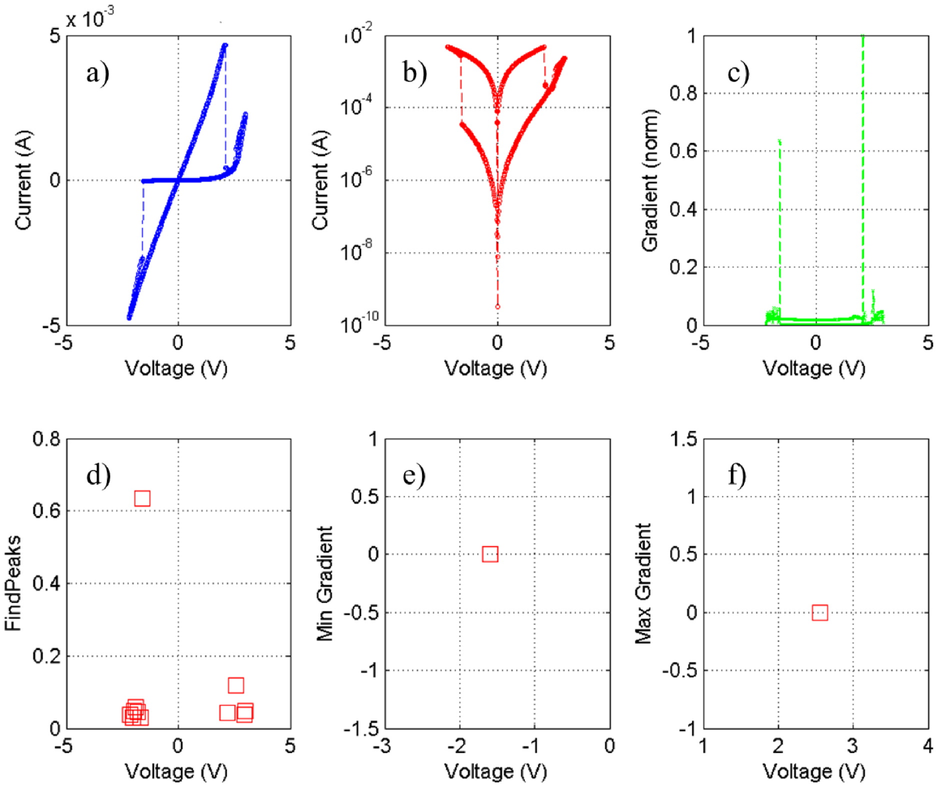

Figure 8.12: a) liner plot I-V sweep data b) semilog plot of I-V sweep data c) gradient of the I(V) data d) switching voltages determined by the *findpeaks* function e) and f) switching voltages determined using maximum and minimum *gradient* function.

In simple terms, the code identifies where on the I-V plane the gradient is maximised or minimised. The code achieves this using the *gradient* function and the *findpeaks* function. Figures 8.12a and 8.12b plot the I-V data in linear and log scales respectively, whereas figure 8.12c plots the gradient of I(V). Figures 8.12d-f illustrate how the code identifies the switching voltages according to the *gradient* and *findpeaks* functions. Normally, the code runs through an entire data folder and filters the I-V sweeps that have an on/off ratio higher than a pre-determined ratio (say, 10×) and distributes the switching events depending on the transition voltages, building a histogram as illustrated in figure 8.13. As can be seen in figures 8.13a and 8.13b show different distributions for exactly the same dataset. Starting with figure 8.13a, one of the most interesting features of the code was its ability to identify two resistance switching modes, as can be seen by the different voltage distribution for the RESET transition for "Control" devices. These two resistance

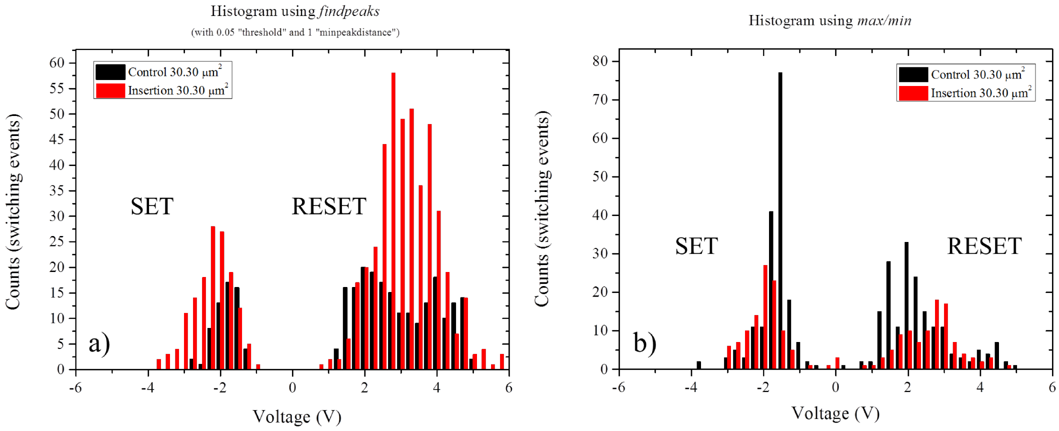

Figure 8.13: Histograms constructed using the results from the MATLAB filtering code a) using the *findpeaks* and b) *gradient* functions.

switching modes are explained in chapter 5 when describing the bistability in ZrO_2 RRAM devices. Figure 8.13b on the other hand, simply determines the “main” switching events in each cycle. From the analysis of the results, it is clear that both functions (*gradient* and *findpeaks*) are useful, and not interchangeable. In conclusion, the MATLAB code was an invaluable tool in not only filtering the results, but also in identifying trends during the electrical characterisation of RRAM devices that would’ve been otherwise more difficult to identify.

8.4 MATLAB Codes

This section presents all the MATLAB codes developed during the course of the work presented in this thesis.

8.4.1 Droplet Analysis

```
function ParticulatesSEMfiles

    [image pathname] = uigetfile(’*.*’);
    cd(pathname);
    whos allFiles
    imshow(image);
these commands ask for an image file to be opened

    imageread = imread(image);
    imagecrop = imcrop(imageread,[1 1 1024 883]);
    imshow(imageread), figure, imshow(imagecrop)
these commands crop the bottom part (with the SEM info)

    THRES = 0.04;
    imagedrop = edge(imagecrop,’sobel’,THRES);
droplet detection threshold
lower number is higher sensitivity
    figure, imshow(imagedrop)

    SIZE = 4;
    imagedropprocessed1 = bwareaopen(imagedrop,SIZE);
    figure, imshow(imagedropprocessed1)
this is particulate size threshold
higher cuts smaller particulates

    se = strel(’disk’,2);
    imagedropprocessed2 = imclose(imagedropprocessed1,se);
    figure, imshow(imagedropprocessed2)
this closes any “open” areas

    imagedropfinal = imfill(imagedropprocessed2,’holes’);
```

```
imshow(imagedropfinal)
```

fills areas with solid white

```
imagedroplets = imfindcircles(imagedropfinal, [5 50]);
figure, viscircles(imagedroplets, ’EdgeColor’, ’b’);
```

8.4.2 RRAM device filtering

ReRam Filter Hist - Version 3.0 - Jan 2014

Filters by ON/OFF - Plots histogram of all switching events

```
clear;
```

Opens and determines number of files selected

```
[filename, pathname] = uigetfile(’*.csv’,’MultiSelect’, ’on’);
filename = cellstr(filename);
destfolderimp = input(’Destination Folder?’, ’s’);
destfolder = strcat(pathname,destfolderimp,’\’);
mkdir(destfolder);
minthresholdonoff = str2num(input(’MINIMUM threshold for flagging?
(on/off ratio)’,’s’));
maxthresholdonoff = str2num(input(’MAXIMUM threshold for flagging?
(on/off ratio)’,’s’));
totaltime = clock;
```

Starts clock, creates preview folder for output, filter criteria

```
svoltagehist = cell(1, 2000);
s = 0;
```

Pre-allocates and initiates variable “svoltagehist” for histogram at end

```
for i = 1:length(filename);
processtime = clock;
file = char(filenamei);
fh = fopen(file);

p = 1;
header = cell(0);
```

```
while(true)
k = fgetl(fh);
if( isempty(k) ); break; end
header(p) = cellstr(k);
p=p+1;
end

acolheader = fgetl(fh);
fclose( fh );
```

Reads all files selected in gui.

Reads headers and determines in which row DATA starts

```
numdata = csvread(file, p+1,0);

IndexMeasurementType = strfind(header, ’Measurement’);
if size(IndexMeasurementType) < 1
else
[rowm,colm] = find(not(cellfun(’isempty’, IndexMeasurementType)));
measurementtypeinfo = (headerrowm,colm);
ameasurement = regexp(measurementtypeinfo,’,’,’split’);
measurementtype = str2double(ameasurement(1,2));
end
```

Determines where “Measurement” string is and outputs cell address.

Reads “Measurement type” allowing CASE STRUCTURE ahead

```
IndexRepCount = strfind(header, ’Repeats’);
if size(IndexRepCount) == 0
else
[rowr,colr] = find(not(cellfun(’isempty’, IndexRepCount)));
if size(rowr) > 0
repcountinfo = (headerrowr(1,1),colr);
arep = regexp(repcountinfo,’,’,’split’);
repcount = str2double(arep(1,2));
else
end
```

```
end
```

Determines where ”Repeats” string is and outputs cell address

```
IndexRepCounta = strfind(header, ’Repeatsactual’);
if size(IndexRepCounta) == 0
else
[rowra,colra] = find(not(cellfun(’isempty’, IndexRepCounta)));
if size(rowra) > 0
repcountainfo = (headerrowra(1,1),colra);
arepa = regexp(repcountainfo,’,’,’split’);
repcounta = str2double(arepa(1,2));
else
end
end
```

Determines where “Repeatsactual” string is and outputs cell address

---

Creates exceptions allowing for multiple .csv files to be selected even without headers allowing the program to process only the “good” files. So far this is the same code as the other scripts. File handling bit.

START OF CASE STRUCTURE

```
acolheader = regexp(acolheader,’,’,’split’);
```

Separates the header into individual cells that can be addressed individually

Starts CASE STRUCTURE to process only “Arbitrary Sweeps”, Measurement Type 1

```
switch measurementtype
case 1
IndexSource = strfind(acolheader, ’Source(specified)’);
if size(IndexSource) == 0
else
[rowsi,colsi] = find(not(cellfun(’isempty’, IndexSource)));
if size(rowsi) > 0
sourcev = numdata(:,colsi);
else
end
```

```
end
```

Looks up Source(specifield), which is X

```
IndexMeasure = strfind(acolheader, ’Measure 00’);
if size(IndexMeasure) == 0
else
[rowm,colm] = find(not(cellfun(’isempty’, IndexMeasure)));
if size(rowm) > 0 & size(rowra) > 0
if repcounta<repcount
measure = (numdata(:,colm:colm+repcounta-1));
else
measure = (numdata(:,colm:colm+repcount-1));
end
else
measure = (numdata(:,colm:colm+repcount-1));
end
end
```

Measure 00 is Y. Current columns are dependent on repcount or repcounta

```
readvpos = find(sourcev == 0.2);
```

Change to INTERP or TRISCATTEREDINTERP??

```
readvneg = find(sourcev == -0.2);
```

Change to INTERP or TRISCATTEREDINTERP??

```
readipos = measure(readvpos,:);
readineg = measure(readvneg,:);
flagipos = max(readipos)/min(readipos);
flagineg = min(readineg)/max(readineg);
```

Creates flagging variables to allow filtering.

MUST CHANGE 0.2 to TRISCATTEREDINTERP 0.2 in case there is no 0.2 in source values.

```
if (flagipos > minthresholdonoff |flagineg > minthresholdonoff)
&(flagipos < maxthresholdonoff |flagineg < maxthresholdonoff)
```

Filters by on/off ratio and processes for switching voltage

```
sourcevpos = find(sourcev>0);
sourcevneg = find(sourcev<0);
measurepos = measure(sourcevpos,:);
measureneg = measure(sourcevneg,:);

measurelog = abs(measure);
measuregrad = gradient(measure);
measuregradabs = (abs(gradient(measure)));
maxgrad = max(measuregradabs);
measuregradnorm = measuregradabs/maxgrad;
[peaks,svoltage] = findpeaks(measuregradnorm,’threshold’,0.005,’minpeakdistance’,1);
[maxg, gvmax] = max(gradient(measurepos));
[ming, gvmin] = min(gradient(measureneg));
```

Calculates abs and gradient of measurement to identify switching voltages (X)

1 - Uses findpeaks to map several gradient peaks that represent switching

2 - Calculates max and min gradient that represent MAIN switching events

```
figure;
set(gcf,’Color’,’w’);
hold on;
suptitle(file);
subplot(2,3,1),plot(sourcev,measure,’–bo’,’MarkerSize’,2); grid on;
xlabel(’Voltage (V)’); ylabel(’Current (A)’,’fontsize’,10);
subplot(2,3,2),semilogy(sourcev,measurelog,’–ro’,’MarkerSize’,2); grid on;
xlabel(’Voltage (V)’); ylabel(’Current (A)’,’fontsize’,10);
subplot(2,3,3),plot(sourcev,measuregradnorm,’–gx’,’MarkerSize’,2); grid on;
xlabel(’Voltage (V)’); ylabel(’Gradient (norm)’,’fontsize’,10);
subplot(2,3,4),plot(sourcev(svoltage),peaks,’rs’,’MarkerSize’,10); grid on;
xlabel(’Voltage (V)’); ylabel(’FindPeaks’,’fontsize’,10);
subplot(2,3,5),plot(sourcev(sourcevneg(gvmin)),ming,’rs’,’MarkerSize’,10); grid on;
xlabel(’Voltage (V)’); ylabel(’Min Gradient’,’fontsize’,10);
subplot(2,3,6),plot(sourcev(sourcevpos(gvmax)),maxg,’rs’,’MarkerSize’,10); grid on;
xlabel(’Voltage (V)’); ylabel(’Max Gradient’,’fontsize’,10);
dest = strcat(destfolder,file(1:length(file)-4));
```

```
print(gcf,’-dpng’,dest);
close(gcf);
```

Creates a 6 plot figure/window where all data is displayed

```
s = s+1;
svoltagea = sourcev(svoltage);
svoltagehists = svoltagea;
svoltagemins = sourcev(sourcevneg(gvmin),:);
svoltagemaxs = sourcev(sourcevpos(gvmax),:);
else
end
```

This creates a 3D matrix with all the voltages where switching occured

This uses the pre-allocated and pre-initialised variable ‘s’ for speed

```
otherwise
end

processftime = clock;
processtime = etime(processftime,processitime);
processtimestr = num2str(processtime);
info = strcat(file, ’ |processed in: ’,processtimestr,’ s’)
```

Prints “info” onto console to understand if program is running

“info” gives processed time per file and prints current filename

```
end

histdest = strcat(destfolder,’hist’);
histdestminmax = strcat(destfolder,’histminmax’);
```

Concatenates address strings for histogram data files

Address is pathname\destfolder from start

```
hista = [];
histmin = [];
histmax = [];
```

```
status = (’Filtered... not enough data points for histogram.’);
```

Pre-allocates variables for “if statement” ahead. This skips the histogram thing when selected files do not meet filter criteria.

```
for z = 1:s

hista = svoltagehist1,z;
histmin = svoltagemin1,z;
histmax = svoltagemax1,z;
dlmwrite(histdestminmax, histmin, ’-append’);
dlmwrite(histdestminmax, histmax, ’-append’);
dlmwrite(histdest, hista, ’-append’);

end
```

Reads each cell of the 3D matrix in append mode to create a 2D array

New 2D array is saved into current path

Maybe try SQUEEZE in future versions (3D to 2D function)

```
windowmin = -10;
windowmax = 10;
windowstep = 0.25;
histwindow = windowmin:windowstep:windowmax;

if size(hista) == 0 |size(histmin) == 0 |size(histmax) == 0
status
```

Skips files that do not meet filter criteria

```
else
hist = dlmread(histdest);
histmm = dlmread(histdestminmax);

switchinghistmm = histc(histmm, histwindow);
switchinghist = histc(hist,histwindow);
figure;
subplot(1,2,1),bar(histwindow,switchinghist,’r’);
xlabel(’Voltage (V)’); ylabel(’Counts (findpeaks)’,’fontsize’,10);
subplot(1,2,2),bar(histwindow,switchinghistmm,’b’);
xlabel(’Voltage (V)’); ylabel(’Counts (min/max)’,’fontsize’,10);
```

Sets up the conditions for histogram and outputs the 2 histograms obtained

One with the findpeaks and other with max/min gradient filters

```
    end

    totalftime = clock;
    totaltime = etime(totalftime,totalitime)
```

Stops clock and shows total process time

8.4.3 Plume Characterisation

```
function totaldeposition = DepCalc(Cx,Cy,R,x,y,z)

    hold off
    xlin=linspace(min(x),max(x),100);
    ylin=linspace(min(y),max(y),100);
    [X,Y]=meshgrid(xlin,ylin);
    Z=griddata(x,y,z,X,Y,’cubic’);
    theta=(0:360);
```

these commands generate the mesh grid where the experimental points are going to be mapped

```
    Cx=-22661;
    Cy=70000;
    R=2.5E5;
```

here one sets up the position of the centre of the substrate and its size, given by a radius

```
    surf(X,Y,Z);view([0,90]),shading interp
    hold on
    z=200*ones(1,length(x));
    plot3(x,y,z,’*’)
```

here the interpolation is performed and displayed as well as the experimental data points

```
    totaldeposition=zeros(size(Cx));
    for i=1:length(Cx)
    px=Cx(i)+R(i)*cosd(theta);
    py=Cy(i)+R(i)*sind(theta);
```

```
pz=interp2(X,Y,Z,px,py);
plot3(px,py,pz,’g*’,’MarkerSize’,2)
totaldeposition(i)=sum(pz( isnan(pz)));
```

here the integration over the substrate area is performed according to the thickness map generated beforehand

```
end
```

8.5 Vacuum Diagram

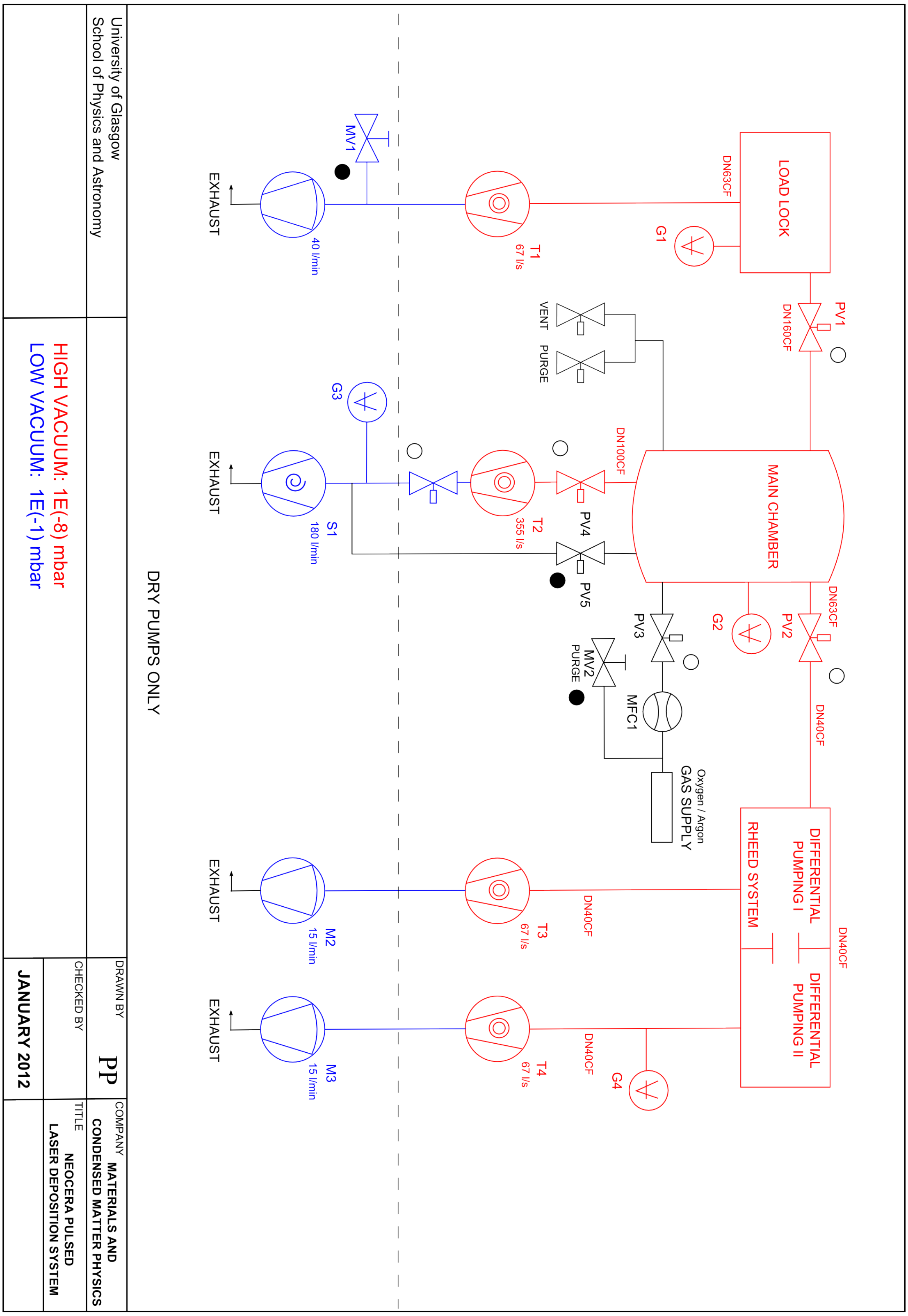

Figure 8.14: Vacuum diagram of the Neocera Pulsed Laser Deposition system.